

The physics of climate variability and climate change

Michael Ghil¹

*Geosciences Department and Laboratoire de Météorologie Dynamique (CNRS and IPSL),
Ecole Normale Supérieure and PSL University, F-75231 Paris Cedex 05, France
and Department of Atmospheric and Oceanic Sciences, University of California,
Los Angeles, California 90095-1565, USA*

Valerio Lucarini²

*Department of Mathematics and Statistics, University of Reading,
Reading RG66AX, United Kingdom,
Centre for the Mathematics of Planet Earth, University of Reading,
Reading RG66AX, United Kingdom,
and CEN—Institute of Meteorology, University of Hamburg, Hamburg 20144, Germany*

(published 31 July 2020)

The climate is a forced, dissipative, nonlinear, complex, and heterogeneous system that is out of thermodynamic equilibrium. The system exhibits natural variability on many scales of motion, in time as well as space, and it is subject to various external forcings, natural as well as anthropogenic. This review covers the observational evidence on climate phenomena and the governing equations of planetary-scale flow and presents the key concept of a hierarchy of models for use in the climate sciences. Recent advances in the application of dynamical systems theory, on the one hand, and nonequilibrium statistical physics, on the other hand, are brought together for the first time and shown to complement each other in helping understand and predict the system's behavior. These complementary points of view permit a self-consistent handling of subgrid-scale phenomena as stochastic processes, as well as a unified handling of natural climate variability and forced climate change, along with a treatment of the crucial issues of climate sensitivity, response, and predictability.

DOI: [10.1103/RevModPhys.92.035002](https://doi.org/10.1103/RevModPhys.92.035002)

CONTENTS

| | | | |
|---|----|--|----|
| I. Introduction and Motivation | 2 | 2. Bifurcation diagrams for GCMs | 29 |
| A. Basic facts of the climate sciences | 2 | D. Bistability, oscillations, and bifurcations | 31 |
| B. More than “just” science | 4 | 1. Bistability and steady-state bifurcations | 31 |
| 1. The Intergovernmental Panel on Climate Change | 4 | 2. Oscillatory instabilities and Hopf bifurcations | 32 |
| 2. Hockey stick controversy and climate blogs | 5 | E. Main modes of variability | 33 |
| C. This review | 5 | 1. Modes of variability and extended-range prediction | 33 |
| II. Introduction to Climate Dynamics | 7 | 2. Coupled atmosphere-ocean modes of variability | 34 |
| A. Climate observations: Direct and indirect | 7 | 3. Atmospheric low-frequency variability | 34 |
| 1. Instrumental data and reanalyses | 7 | F. Internal variability and routes to chaos | 36 |
| 2. Proxy data | 10 | 1. A simple model of the double-gyre circulation | 37 |
| B. Climate variability on multiple Timescales | 11 | 2. Bifurcations in the double-gyre problem | 38 |
| 1. A survey of climatic timescales | 12 | a. Symmetry-breaking bifurcation | 38 |
| 2. Atmospheric variability in mid-latitudes | 13 | b. Gyre modes | 38 |
| C. Basic properties and fundamental equations | 16 | c. Global bifurcations | 39 |
| 1. Governing equations | 16 | G. Multiple scales: Stochastic and memory effects | 40 |
| 2. Approximate balances and filtering | 17 | 1. Fast scales and their deterministic parametrization | 40 |
| a. Hydrostatic balance | 17 | 2. An example: Convective parametrization | 41 |
| b. Geostrophic balance | 18 | 3. Stochastic parametrizations | 41 |
| 3. Quasigeostrophy and weather forecasting | 19 | 4. Modeling memory effects | 42 |
| D. Climate prediction and climate model performance | 20 | a. The Mori-Zwanzig formalism | 43 |
| 1. Predicting the state of the system | 22 | b. EMR methodology | 43 |
| 2. Predicting the system's statistical properties | 23 | c. Role of memory effects in EMR | 43 |
| 3. Metrics for model validation | 24 | d. EMR applications | 44 |
| III. Climate Variability and the Modeling Hierarchy | 25 | e. Explicit derivation of the parametrized equations | 45 |
| A. Radiation balance and energy balance models | 25 | IV. Climate Sensitivity and Response | 46 |
| B. Other atmospheric processes and models | 28 | A. A simple framework for climate sensitivity | 46 |
| C. Oscillations in the ocean's thermohaline circulation | 28 | | |
| 1. Theory and simple models | 28 | | |

| | |
|--|----|
| B. Climate sensitivity: Uncertainties and ambiguities | 47 |
| C. Transient climate response (TCR) | 48 |
| D. Beyond climate sensitivity | 49 |
| E. A general framework for climate response | 50 |
| 1. Pullback attractors (PBAs) | 50 |
| 2. Fluctuation dissipation and climate change | 51 |
| 3. Ruelle response theory | 51 |
| 4. Climate change prediction via Ruelle response theory | 53 |
| 5. Slow correlation decay and sensitive parameter dependence | 54 |
| V. Critical Transitions and Edge States | 56 |
| A. Bistability for gradient flows and EBMs | 56 |
| B. Finding the edge states | 58 |
| C. Invariant measures and noise-induced transitions | 59 |
| D. Nearing critical transitions | 60 |
| E. Chaos-to-chaos transition | 60 |
| VI. Conclusions | 62 |
| List of Symbols and Abbreviations | 64 |
| Acknowledgments | 64 |
| References | 65 |

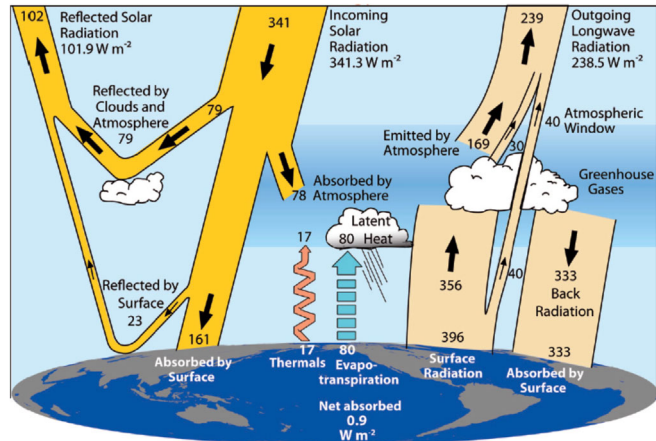


FIG. 1. Globally averaged energy fluxes in the Earth system (W m^{-2}). The fluxes on the left represent solar radiation in the visible and the ultraviolet, those on the right represent terrestrial radiation in the infrared, and those in the middle represent nonradiative fluxes. From Trenberth, Fasullo, and Kiehl, 2009.

I. INTRODUCTION AND MOTIVATION

A. Basic facts of the climate sciences

The climate system is forced, dissipative, chaotic, and out of equilibrium; its complex natural variability arises from the interplay of positive and negative feedbacks, instabilities, and saturation mechanisms. These processes span a broad range of spatial and temporal scales and include many chemical species and all of the most common physical phases. The system's heterogeneous phenomenology includes the mycrophysics of clouds, cloud-radiation interactions, atmospheric and oceanic boundary layers, and several scales of turbulence (Ghil, 2019); it evolves, furthermore, under the action of large-scale agents that drive and modulate its evolution, mainly differential solar heating and the Earth's rotation and gravitation.

As is often the case, the complexity of the physics is interwoven with the chaotic character of the dynamics. Moreover, the climate system's large natural variability on different timescales is strongly affected by relatively small changes in the forcing, anthropogenic as well as natural (Ghil and Childress, 1987; Peixoto and Oort, 1992; Lucarini, Blender *et al.*, 2014).

On the macroscopic level, climate is driven by differences in the absorption of solar radiation throughout the depth of the atmosphere, as well as in a narrow surface layer of the ocean and of the soil; the system's actual governing equations are given in Sec. II.C. The prevalence of absorption at the surface and in the atmosphere's lower levels leads through several processes to compensating vertical energy fluxes, most notably, fluxes of infrared radiation throughout the atmosphere and convective motions in the troposphere; see Fig. 1.

More solar radiation is absorbed in the low latitudes, leading to horizontal energy fluxes as well. The atmosphere's large-scale circulation is to first order a result of these horizontal and vertical fluxes arising from the gradients in solar radiation absorption, in which the hydrological cycle plays a key role as well. The ocean circulation, in turn, is set into motion by surface or near-surface exchanges of mass,

momentum, and energy with the atmosphere: the so-called wind-driven component of the circulation is due mainly to the wind stress and the thermohaline one is due mainly to buoyancy fluxes (Dijkstra, 2005; Dijkstra and Ghil, 2005; Kuhlbrodt *et al.*, 2007). The coupled atmospheric and oceanic circulation reduces the temperature differences between the tropics and polar regions with respect to that on an otherwise similar planet with no horizontal energy transfers (Lorenz, 1967; Peixoto and Oort, 1992; Held, 2001; Lucarini and Ragone, 2011). At steady state, the convergence of enthalpy transported by the atmosphere and the ocean compensates for the radiative imbalance at the top of the atmosphere; see Fig. 2.

The classical theory of the general circulation of the atmosphere (Lorenz, 1967) describes in further detail how the mechanisms of energy generation, conversion, and dissipation produce the observed circulation, which deviates substantially from the highly idealized, zonally symmetric picture sketched so far. According to Lorenz (1955), atmospheric large-scale flows result from the conversion of available potential energy, which is produced by the atmosphere's differential heating, into kinetic energy, and the Lorenz (1967) energy cycle is completed by energy cascading to smaller scales to eventually be dissipated. McWilliams (2019) provided an up-to-date criticism of and further perspective on this theory.

Overall, the climate system can be seen as a thermal engine capable of transforming radiative heat into mechanical energy with a given, highly suboptimal efficiency given the many irreversible processes that make it less than ideal (Pauluis and Held, 2002; Kleidon and Lorenz, 2005; Lucarini, 2009b; Lucarini, Blender *et al.*, 2014). This conversion occurs through genuinely three-dimensional (3D) baroclinic instabilities (Charney, 1947; Eady, 1949) that are triggered by large temperature gradients and would break zonal symmetry even on a so-called aqua planet, with no topographic or thermal asymmetries at its surface. These instabilities give rise to a negative feedback, as they tend to reduce the temperature

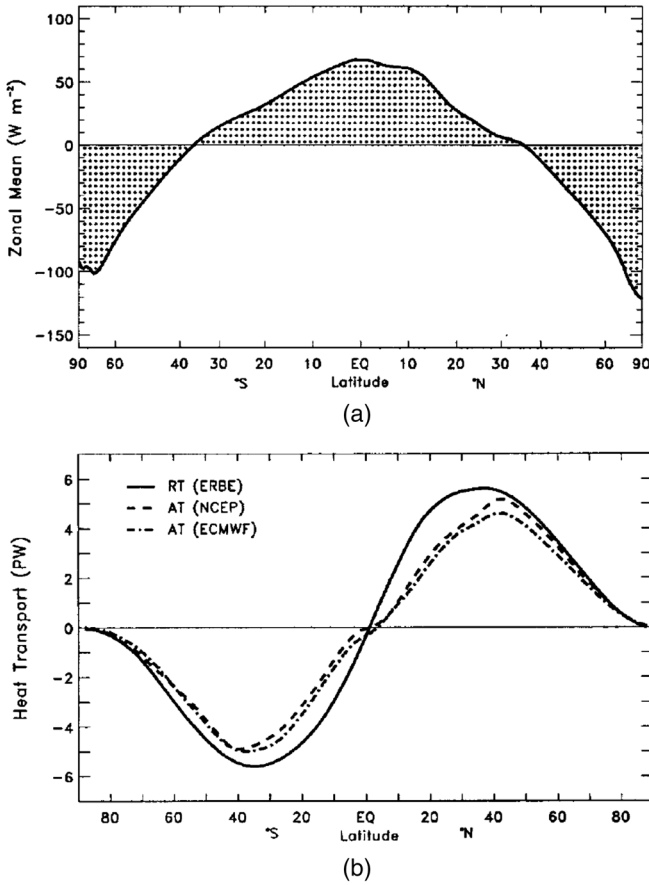


FIG. 2. Meridional distribution of net radiative fluxes and of horizontal enthalpy fluxes. (a) Observed zonally averaged radiative imbalance at the top of the atmosphere from the ERBE experiment (1985–1989). (b) Inferred meridional enthalpy transport from ERBE observations (solid line) and estimate of the atmospheric enthalpy transport from two reanalysis datasets (ECMWF and NCEP). From Trenberth and Caron, 2001.

gradients they feed upon by favoring the mixing between masses of fluids at different temperatures.

Note that while these baroclinic and other large-scale instabilities do act as negative feedbacks they cannot be treated as diffusive, Onsager-like [Onsager (1931)] processes. Faced with the Earth system's complexity discussed herein and illustrated in Fig. 3, the closure of the coupled thermodynamical equations governing the general circulation of the atmosphere and ocean would provide a self-consistent theory of climate. Such a theory should be able to connect instabilities and large-scale stabilizing processes on longer spatial and temporal scales, and to predict its response to a variety of forcings, both natural and anthropogenic (Ghil and Childress, 1987; Lucarini, 2009b; Lucarini, Blender *et al.*, 2014; Ghil, 2015). This goal is being actively pursued but is still out of reach at this time; see, e.g., Ghil (2019) and the references therein, and also Secs. IV and V. The observed persistence of spatial gradients in chemical concentrations and temperatures, as well as the associated mass and energy fluxes, is a basic signature of the climate system's intrinsic disequilibrium.

Figure 3 emphasizes, moreover, that the fluid and the solid parts of the Earth system are coupled on even longer

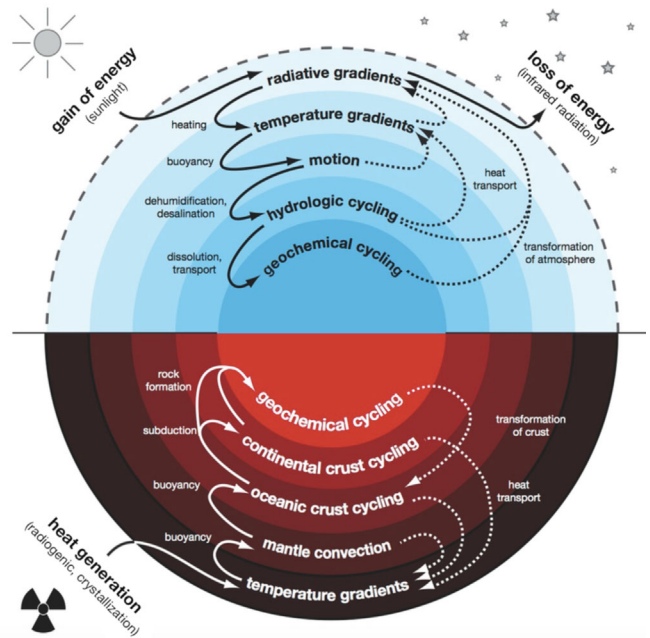


FIG. 3. Schematic diagram representing forcings, dissipative and mixing processes, gradients of temperature and chemical species, and coupling mechanisms across the Earth system. Blue (red) areas refer to the fluid (solid) Earth. From Kleidon, 2010.

timescales, on which geochemical processes become of paramount importance (Rothman, Hayes, and Summons, 2003; Kleidon, 2009). In contrast, closed, isolated systems cannot maintain disequilibrium and have to evolve toward homogeneous thermodynamical equilibrium as a result of the second law of thermodynamics (Prigogine, 1961).

Studying the climate system's entropy budget provides a good global perspective on this system. Earth as a whole absorbs shortwave radiation carried by low-entropy solar photons at $T_{\text{Sun}} \simeq 6000$ K and emits infrared radiation to space via high-entropy thermal photons at $T_{\text{Earth}} \simeq 255$ K (Peixoto and Oort, 1992; Lucarini, Blender *et al.*, 2014). Besides the viscous dissipation of kinetic energy, many other irreversible processes, such as turbulent diffusion of heat and chemical species, irreversible phase transitions associated with various hydrological processes, and chemical reactions involved in the biogeochemistry of the planet, contribute to the total material entropy production (Goody, 2000; Kleidon, 2009).

These and other important processes appear in the schematic diagram of Fig. 3. In general, in a forced dissipative system, entropy is continuously produced by irreversible processes, and at steady state this production is balanced by a net outgoing flux of entropy at the system's boundaries (Prigogine, 1961; de Groot and Mazur, 1984); in the case at hand, this flux leaves mainly through the top of the atmosphere (Goody, 2000; Lucarini, 2009b). Thus, on average, the climate system's entropy budget is balanced, just like its energy budget.

The phenomenology of the climate system is commonly approached by focusing on distinct and complementary aspects that include the following:

- Wavelike features such as Rossby waves or equatorially trapped waves [see, e.g., Gill (1982)], which play a key

role in the transport of energy, momentum, and water vapor, as well as in the study of atmospheric, oceanic, and coupled-system predictability.

- Particlelike features such as hurricanes, extratropical cyclones, and oceanic vortices [see, e.g., [Salmon \(1998\)](#) and [McWilliams \(2019\)](#)], which strongly affect the local properties of the climate system and its subsystems and subdomains.
- Turbulent cascades, which are of crucial importance in the development of large eddies through the mechanism of geostrophic turbulence ([Charney, 1971](#)), as well as in mixing and dissipation within the planetary boundary layer ([Zilitinkevich, 1975](#)).

Each of these points of view is useful, and they do overlap and complement each other ([Ghil and Robertson, 2002](#); [Lucarini, Blender et al., 2014](#)), but neither by itself provides a comprehensive understanding of the properties of the climate system. It is a key objective of this review to provide the interested reader with the tools for achieving such a comprehensive understanding with predictive potential.

While much progress has been achieved ([Ghil, 2019](#)), understanding and predicting the dynamics of the climate system faces, on top of all the difficulties that are intrinsic to any nonlinear, complex system out of equilibrium, the following additional obstacles that make it especially hard to grasp fully:

- The presence of well-defined subsystems, the atmosphere, the ocean, the cryosphere, characterized by distinct physical and chemical properties and widely differing timescales and space scales.
- The complex processes coupling these subsystems.
- The continuously varying set of forcings that result from fluctuations in the incoming solar radiation and in the processes, both natural and anthropogenic, that alter the atmospheric composition.
- The lack of scale separation between different processes, which requires a profound revision of the standard methods for model reduction and calls for unavoidably complex parametrization of subgrid-scale processes in numerical models.
- The lack of detailed, homogeneous, high-resolution, and long-lasting observations of climatic fields that leads to the need for combining direct and indirect measurements when trying to reconstruct past climate states preceding the industrial era.
- The fact that we only have one realization of the processes that give rise to climate evolution in time.

For all of these reasons, it is far from trivial to separate the climate system's response to various forcings from its natural variability in the absence of time-dependent forcings. More simply, and as noted already by [Lorenz \(1979\)](#), it is hard to separate forced and free climatic fluctuations ([Lucarini and Sarno, 2011](#); [Lucarini, Blender et al., 2014](#); [Lucarini, Ragone, and Lunkeit, 2017](#)). This difficulty is a major stumbling block on the road to a unified theory of climate evolution ([Ghil, 2015, 2017](#)), but some promising ideas for overcoming it are emerging and are addressed in Secs. IV and V; see also [Ghil \(2019\)](#).

B. More than “just” science

1. The Intergovernmental Panel on Climate Change

Besides the strictly scientific aspects of climate research, much of the recent interest in it has been driven by the accumulated observational and modeling evidence on the ways humans influence the climate system. To review and coordinate the research activities carried out by the scientific community in this respect, the United Nations Environment Programme (UNEP) and the World Meteorological Organization (WMO) established in 1988 the Intergovernmental Panel on Climate Change (IPCC); its assessment reports (ARs) are issued every 4–6 yr. By compiling systematic reviews of the scientific literature relevant to climate change, the ARs summarize the scientific progress, the open questions, and the bottlenecks regarding our ability to observe, model, understand, and predict the climate system's evolution.

More specifically, it is the IPCC Working Group I that focuses on the physical basis of climate change; see [IPCC \(2001, 2007, 2014a\)](#) for the three latest reports in this area: AR3, AR4, and AR5. Working Groups II and III are responsible for the reports that cover the advances in the interdisciplinary areas of adapting to climate change and of mitigating its impacts; see [IPCC \(2014b, 2014c\)](#) for the contributions of Working Groups II and III, respectively, to AR5. AR6 is currently in preparation.¹

Moreover, the IPCC supports the preparation of special reports on themes that are of interest across two of the working groups, e.g., climatic extremes ([IPCC, 2012](#)), or across all three of them. The IPCC experience and working group structure is being replicated for addressing climate change at the regional level, as in the case for the Hindu Kush Himalayan region, sometimes called the “third pole” ([Wester et al., 2019](#)).

The IPCC reports are based on the best science available and are policy relevant but not policy prescriptive. Their multistage review is supposed to guarantee neutrality but the reports are still inherently official, UN-sanctioned documents and have to bear the imprimatur of the IPCC's 195 member countries. Their release thus leads to considerable and often adversarial debates involving a variety of stakeholders from science, politics, civil society, and business; they also affect media production, cinema, video games, and art at large and are more and more reflective of them.

Climate change has thus become an increasingly central topic of discussion in the public arena, involving all levels of decision-making, from local through regional and on to global. In recent years, climate services have emerged as a new area at the intersection of science, technology, policy making, and business. They emphasize tools to enable climate change adaptation and mitigation strategies, and they have benefited from large public investments like the European Union's Copernicus Programme.²

The lack of substantial progress made by national governments and international bodies tackling climate change has

¹See <https://www.ipcc.ch/assessment-report/ar6/>.

²See <https://climate.copernicus.eu>.

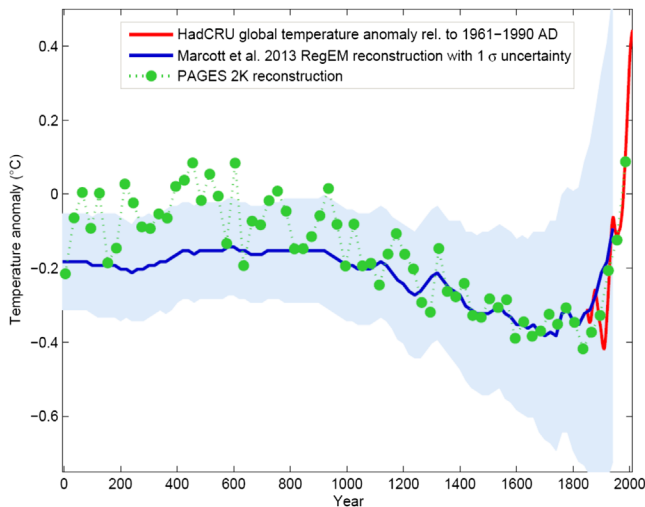


FIG. 4. Surface air temperature record for the last two millennia. Green dots show the 30-yr average of the latest PAGES 2k reconstruction (PAGES, 2013), while the red curve shows the global mean temperature, according to HadCRUT4 data from 1850 onward; the original “hockey stick” of Mann, Bradley, and Hughes (1999) is plotted in blue and its uncertainty range in light blue. Graph by Klaus Bitterman.

recently led to the rapid growth of global, young-people-driven grassroots movements like Extinction Rebellion³ and FridaysForFuture.⁴ Some countries, like the United Kingdom, have declared a state of climate emergency,⁵ and some influential media outlets have started to use the expression *climate crisis* instead of climate change.⁶ While such socio-economic and political issues are of great consequence, this review does not dwell on them.

2. Hockey stick controversy and climate blogs

Mann, Bradley, and Hughes (1999) produced in Fig. 3(a) of their paper a temperature reconstruction from proxy data (see Sec. II.A) for the last 1000 years, shown as part of the blue (dark gray) curve in Fig. 4. This curve was arguably the most striking, and hence controversial, scientific result contained in the AR3 report (IPCC, 2001), and it was dubbed for obvious reasons the hockey stick. The AR3 report combined into one figure, Fig. 1(b) of the Summary for Policy Makers (SPM), the blue curve and the red curve shown in Fig. 4, which was based on instrumental data over the last century and a half; see Fig. 1(a) of the SPM. This superposition purported to demonstrate that the recent temperature increase was unprecedented over the last two millennia, in both values attained and rate of change.

Figure 1(b) of the AR3’s SPM received an enormous deal of attention from the social and political forces wishing to underscore the urgency of tackling anthropogenic climate change. For opposite reasons, the paper and its authors were the subject of intense political and judicial scrutiny and attack

by other actors in the controversy, claiming that the paper was both politically motivated and scientifically unsound.

McIntyre and McKittrick (2005), among others, strongly criticized the results of Mann, Bradley, and Hughes (1999), claiming that the statistical procedures used for smoothly combining the diverse proxy records used, including tree rings, coral records, ice cores, and long historical records, with their diverse sources and ranges of uncertainty, into a single multiproxy record, and the latter with instrumental records, were marred by bias and underestimation of the actual statistical uncertainty. Later papers criticized in turn the statistical methods of McIntyre and McKittrick (2005) and confirmed the overall correctness of the hockey stick reconstruction; see, e.g., Huybers (2005), Mann *et al.* (2008), Taricco *et al.* (2009), and PAGES (2013). NRC (2006) provided a review of the state of our knowledge concerning the last two millennia of climate change and variability.

This controversy included the notorious “Climategate” incident, in which data hacked from the computer of a well-known UK scientist were used to support the thesis that scientific misconduct and data falsification had been routinely used to support the hockey stick reconstruction. These claims were later dismissed but they did lead to an important change in the relationship between the climate sciences, society, and politics, and in the way climate scientists interact among themselves and with the public. In certain countries, e.g., the UK and the United States, stringent rules have been imposed to ascertain that scientists working in governmental institutions have to publicly reveal the data they use in the preparation of scientific work if formally requested to do so.

Faced with the confusion generated by the polemics, several leading scientists started blogs⁷ in which scientific literature and key ideas are presented for a broader audience and debated outside the traditional media of peer-reviewed journals or public events, such as conferences and workshops. Most contributions are of high quality, but sometimes arguments appear to sink to the level of bitter strife between those in favor and those against the reality of climate change and of the anthropogenic contribution to its causes.

C. This review

The main purpose of this review is to bring together a substantial body of literature published over the last few decades in the geosciences, as well as in mathematical and physical journals, and provide a comprehensive picture of climate dynamics. Moreover, this picture should appeal to a readership of physicists and help stimulate interdisciplinary research activities.

For decades meteorology and oceanography, on the one side, and physics, on the other side, have had a relatively low level of interaction, with by-and-large separate scientific gatherings and scholarly journals. Recent developments in dynamical systems theory, both finite and infinite dimensional, as well as in random processes and statistical mechanics, have created a common language that makes it possible at

³See <https://rebellion.earth/>.

⁴See <https://www.fridaysforfuture.org>.

⁵See <https://www.bbc.co.uk/news/uk-politics-48126677>.

⁶See <https://tinyurl.com/y2v2jwzy>.

⁷See, e.g., <http://www.realclimate.org>, <http://www.ClimateAudit.org>, <http://www.climate-lab-book.ac.uk>, and <http://judithcurry.com>.

this time to achieve a higher level of communication and mutual stimulation.

The key aspects of the field that we tackle here are the natural variability of the climate system, the deterministic and random processes that contribute to this variability, its response to perturbations, and the relations between internal and external causes of observed changes in the system. Moreover, we present tools for the study of critical transitions in the climate system, which could help us to understand and possibly predict the potential for catastrophic climate change.

In Sec. II, we provide an overview for nonspecialists of the way climate researchers collect and process information on the state of the atmosphere, the land surface, and the ocean. Next the conservation laws and the equations that govern climatic processes are introduced.

An important characteristic of the climate system is the already mentioned coexistence and nonlinear interaction of multiple subsystems, processes, and scales of motion. This state of affairs entails two important consequences that are also addressed in Sec. II. First is the need for scale-dependent filtering: on the positive side, this filtering leads to simplified equations; on the negative one, it calls for so-called parametrization of unresolved processes, i.e., for the representation of subgrid-scale processes in terms of the resolved, larger-scale ones. Second is the fact that no single model can encompass all subsystems, processes, and scales; hence the need for resorting to a hierarchy of models. Section II ends with a discussion of present-day standard protocols for climate modeling and the associated problem of evaluating the models' performance in a coherent way.

Section III treats climate variability in greater depth. We describe the most important modes of climate variability and provide an overview of the coexistence of several equilibria in the climate system, and of their dependence on parameter values. While the study of bifurcations and exchange of stability in the climate system goes back to the work of E. N. Lorenz, H. M. Stommel, and G. Veronis in the 1960s [see, e.g., [Ghil and Childress \(1987\)](#), [Dijkstra \(2013\)](#), and [Ghil \(2019\)](#)], a broadened interest in these matters has been stimulated by the borrowing from the social sciences of the term *tipping points* ([Gladwell, 2000](#); [Lenton et al., 2008](#)).

Proceeding beyond multiple equilibria, we show next how complex processes give rise to the system's internal variability by successive instabilities setting in, competing, and eventually leading to the quintessentially chaotic nature of the evolution of climate. Section III concludes by addressing the need to use random processes to model the faster and smaller scales of motion in multiscale systems, and by discussing Markovian and non-Markovian approximations for the representation of the neglected degrees of freedom. We also discuss top-down versus data-driven approaches.

Section IV delves into the analysis of climate response. The response to the external forcing of a physicochemical system out of equilibrium is the overarching concept we use in clarifying the mathematical and physical bases of climate change. We critically appraise climate models as numerical laboratories and review ways to test their skill at simulating past and present changes, as well as at predicting future ones. The classical concept of equilibrium climate

sensitivity is critically presented first, and we discuss its merits and limitations.

We present next the key concepts and methods of nonautonomous and random dynamical systems, as a framework for the unified understanding of intrinsic climate variability and forced climate change, and emphasize the key role of pullback attractors in this framework. These concepts have been introduced only quite recently into the climate sciences, and we show how pullback attractors and the associated dynamical systems machinery provide a setting for studying the statistical mechanics of the climate system as an open system.

This system is subject to variations in the forcing and in its boundary conditions on all timescales. Such variations include, on different timescales, the incoming solar radiation, the position of the continents, and the sources of aerosols and greenhouse gases. We further introduce time-dependent invariant measures on a parameter-dependent pullback attractor, and the Wasserstein distance between such measures, as the main ingredients for a more geometrical treatment of climate sensitivity in the presence of large and sudden changes in the forcings.

We then outline, in the context of nonequilibrium statistical mechanics, Ruelle's response theory as an efficient and flexible tool for calculating climate response to small and moderate natural and anthropogenic forcings, and we reconstruct the properties of the pullback attractor from a suitably defined reference background state. The response of a system near a tipping point is studied, and we emphasize the link between properties of the autocorrelation of the unperturbed system and its vicinity to the critical transition, along with their implications in terms of telltale properties of associated time series.

Section V is devoted to discussing multistability in the climate system and the critical transitions that occur in the vicinity of tipping points in systems possessing multiple steady states. The corresponding methodology is then applied to the transitions between a fully frozen so-called snowball state of our planet and its warmer states. These transitions have played a crucial role in modulating the appearance of complex life forms. We introduce the concept of an edge state, a dynamical object that has helped explain bistability in fluid mechanical systems, and argue that such states will also yield a more complete picture of tipping points in the climatic context. Finally, we present an example of a more exotic chaos-to-chaos critical transition that occurs in a delay-differential-equation model for the tropical Pacific Ocean.

In Sec. VI, we briefly summarize this review's main ideas and introduce complementary research lines that are not discussed herein, as well as a couple of the many still open questions. The [List of Symbols and Abbreviations](#) contains a list of scientific and institutional acronyms that are used throughout the review.

We started this section by characterizing the climate system and giving a broad-brush description of its behavior. But we have not defined the concept of climate as such since we do not have as yet a consensual definition of what the climate, as opposed to weather, really is. An old adage states that "climate is what you expect, weather is what you get."

This implies that stochastic and ergodic approaches must play a role in disentangling the proper types of averaging on the multiple timescales and space scales involved. A fuller understanding of the climate system's behavior should eventually lead to a proper definition of climate. Mathematically rigorous work aimed at such a definition is being undertaken but is far from complete.⁸

II. INTRODUCTION TO CLIMATE DYNAMICS

A. Climate observations: Direct and indirect

A fundamental difficulty in the climate sciences arises from humanity's insufficient ability to collect data of standardized quality, with sufficient spatial detail, and of sufficient temporal coverage. Instrumental datasets have substantial issues of both synchronic and diachronic coherence. Moreover, such datasets extend, at best, only about one to two centuries into the past. In this section, we first cover instrumental datasets and then so-called historical and proxy datasets, which use indirect evidence on the value of meteorological observables before the industrial era.

1. Instrumental data and reanalyses

Since the establishment of the first meteorological stations in Europe and North America in the 19th century, the extent and quality of the network of observations and the technology supporting the collection and storage of data have rapidly evolved. Still, at any given time, the spatial density of data changes dramatically across the globe, with much sparser observations over the ocean and over land areas characterized by low population density or a low degree of technological development; see, e.g., Ghil and Malanotte-Rizzoli (1991), Fig. 1.

Starting in the late 1960s, polar-orbiting and geostationary satellites have led to a revolution in collecting weather, land surface, and ocean surface data. Spaceborne instruments are now remotely sensing many climatic variables from the most remote areas of the globe; for instance, they measure the overall intensity and spectral features of emitted infrared and reflected visible and ultraviolet radiation, and complex algorithms relate their raw measurements to the actual properties of the atmosphere, such as temperature and cloud cover.

Figure 5 represents schematically the evolution of the observational network for climatic data, while Fig. 6 portrays the instruments that today compose the Global Observing System of the WMO, the United Nations agency that coordinates the collection and quality check of weather and climate data over the entire globe.

Since the early 20th century, the daily measurements have grown in number by many orders of magnitude and now more regularly cover the entire globe, even though large swaths of Earth still feature relatively sparse observations. Figures 7 and 8 illustrate the coverage and variety of the observing systems available at present to individual researchers and

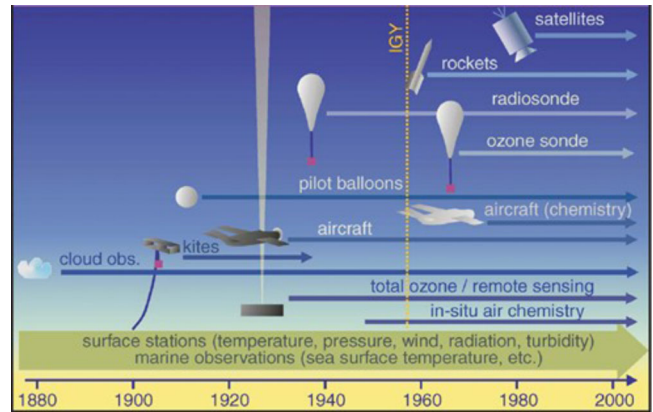


FIG. 5. Schematic diagram representing the evolution of the observing network for weather and climate data. The dotted vertical line corresponds to the International Geophysical Year (IGY). Courtesy of Dick Dee.

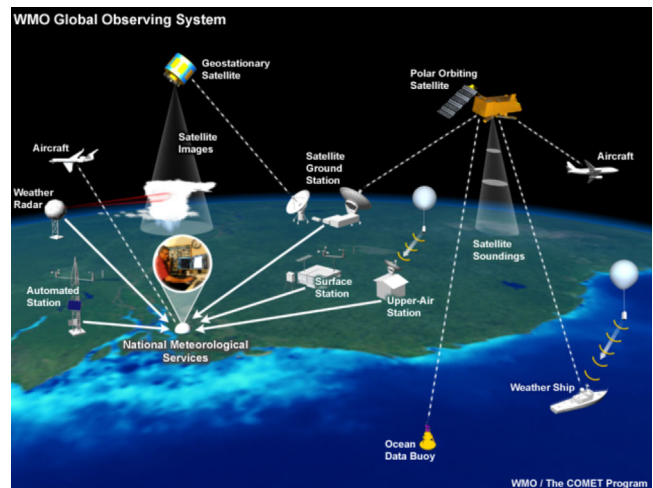


FIG. 6. An illustration of the instruments and platforms that compose the World Meteorological Organization's (WMO's) Global Observing System (GOS). From the COMET website⁹ of the University Corporation for Atmospheric Research (UCAR), sponsored in part through a cooperative agreement with the National Oceanic and Atmospheric Administration (NOAA), U.S. Department of Commerce (DOC).

practitioners, as well as to environmental and civil-protection agencies. Note that the so-called conventional network of ground-based weather stations and related observations has evolved since the Global Weather Experiment in the late 1970s [see Fig. 1 in Bengtsson, Ghil, and Källén (1981)], but only marginally so: it is the remote-sensing observations that have increased tremendously in number, variety, and quality.

The number and quality of oceanographic observations was several orders of magnitude smaller than that of meteorological ones in the 1980s (Munk and Wunsch, 1982; Ghil and Malanotte-Rizzoli, 1991). Here the advent of spaceborne altimetry for sea-surface heights, scatterometry for surface winds, and other remote-sensing methods has revolutionized

⁸See, e.g., F. Flandoli, Lectures at the Institut Henri Poincaré, Paris, October 2019, http://users.dma.unipi.it/flandoli/IHP_contribution_Flandoli_Tonello_v3.pdf.

⁹See <http://meted.ucar.edu/>.

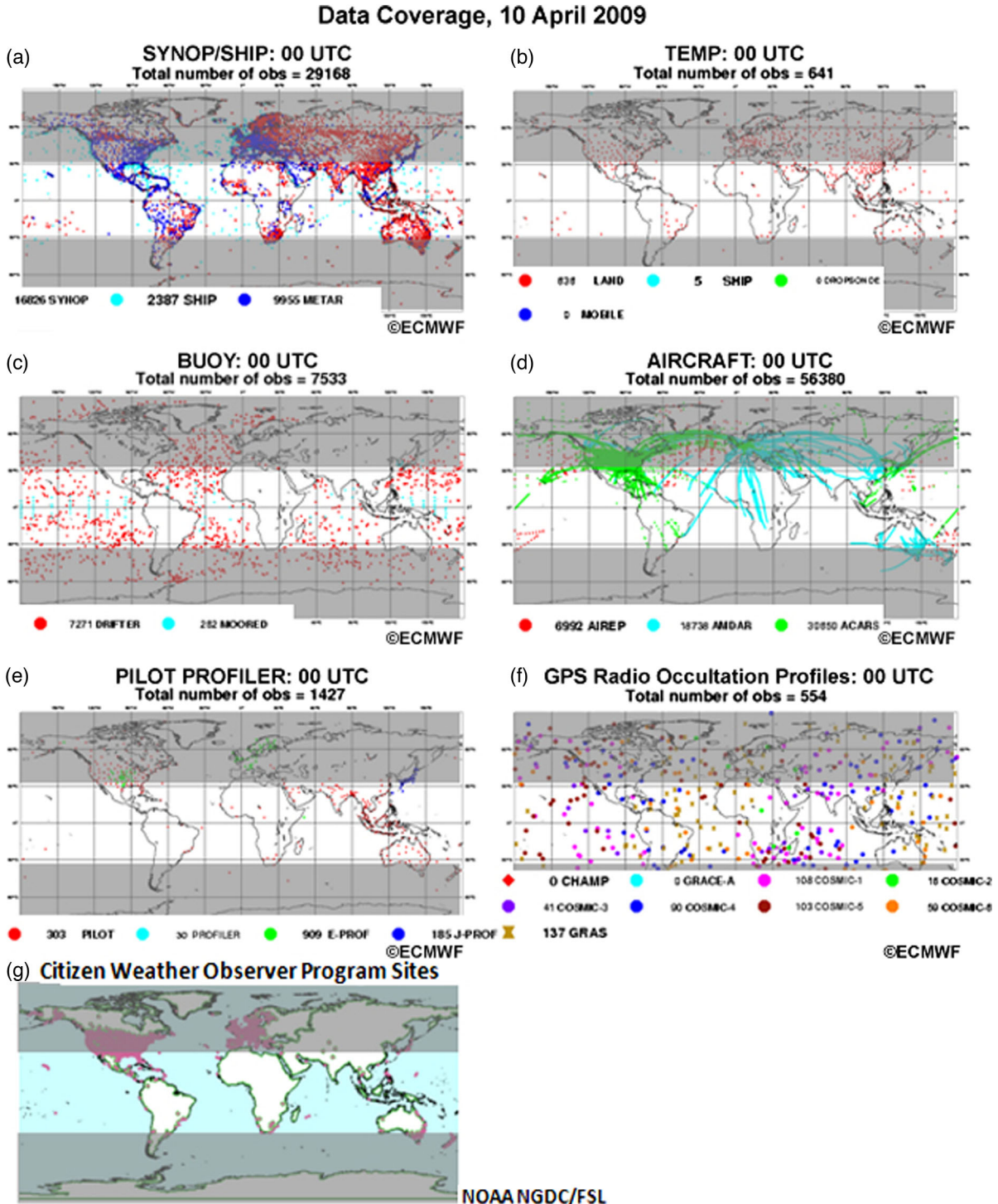


FIG. 7. Maps of point observations from the WMO's GOS on 10 April 2009: (a) synoptic weather station and ship reports, (b) upper-air station reports, (c) buoy observations, (d) aircraft wind and temperature, (e) wind profiler reports, (f) temperature and humidity profiles from Global Positioning System (GPS) radio occultation, and (g) observations from citizen weather observers. The tropics are the bright areas bordered by $\pm 30^\circ$ latitude. From the COMET website¹⁰ of the UCAR, sponsored in part through cooperative agreements with the NOAA, U.S. DOC.

the field; see, e.g., Robinson (2010). This number, however, is still smaller by at least 1 order of magnitude than that of atmospheric observations since, as pointed out by Munk and

Wunsch (1982), the ocean's interior is not permeable to exploration by electromagnetic waves. This is a fundamental barrier hindering our ability to directly observe the deep ocean.

Observational data for the atmosphere and ocean are at any rate sparse, irregular, and of different degrees of accuracy, while in many applications one has to obtain the best estimate,

¹⁰See <http://meted.ucar.edu/>.

Data Coverage, 10 April 2009

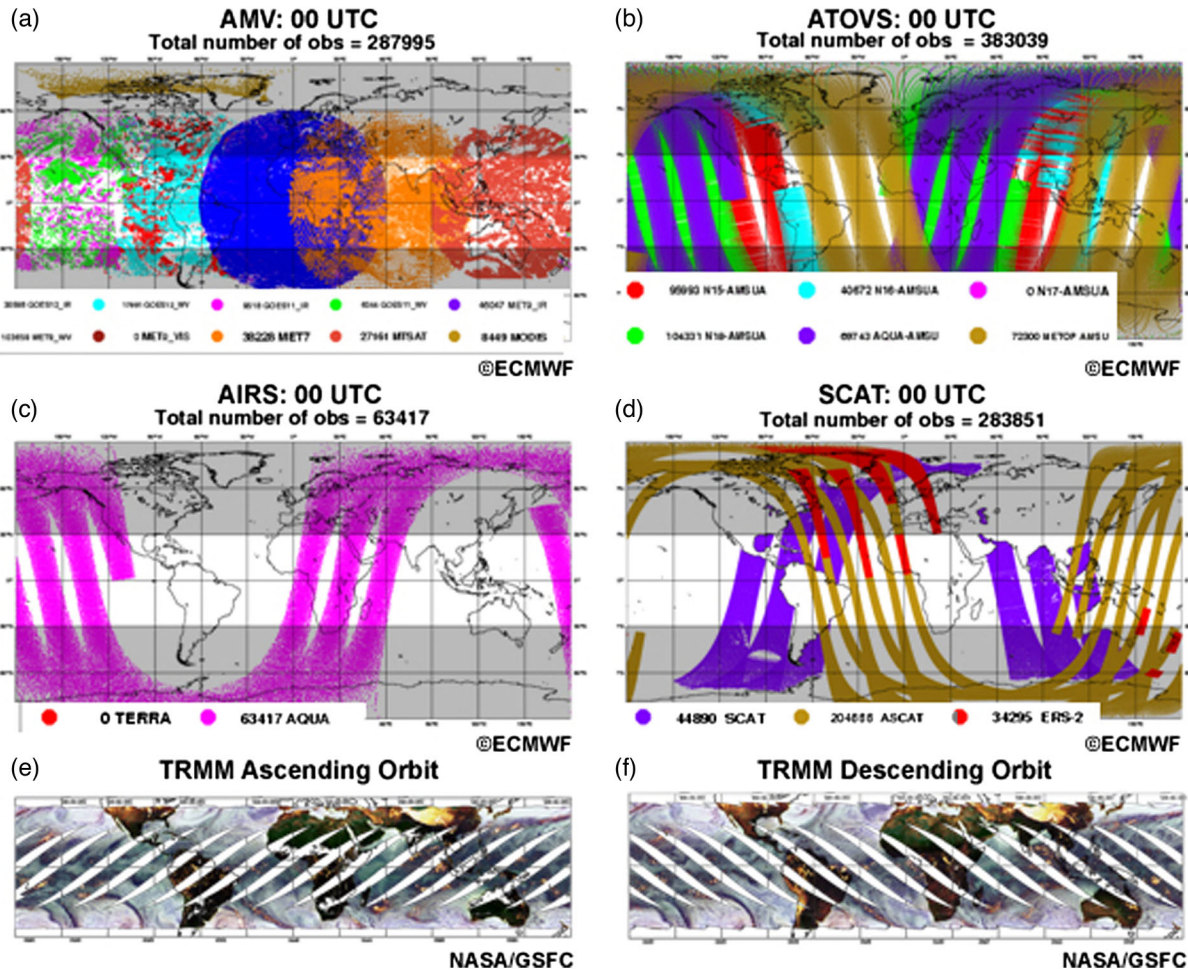


FIG. 8. Geographic distribution of observing systems: (a) geostationary satellite observations, (b),(c) polar-orbiting satellite soundings, (d) ocean surface scatterometer-derived winds, and (e),(f) Tropical Rainfall Measuring Mission (TRMM) Microwave Imager orbits. Each color represents the coverage of a single satellite. Observations in (b) and (c) represent vertical layers and area-averaged values. The tropics are marked by the lighter areas bordered by $\pm 30^\circ$ latitude. From the same source as Fig. 7.

with known error bars, of the state of the atmosphere or ocean at a given time and with a given, uniform spatial resolution. More often than not, this estimate also needs to include meteorological, oceanographic, or coupled-system variables, such as vertical wind velocity and surface heat fluxes, that can be observed only either poorly or not at all.

The active field of *data assimilation* has been developed to bridge the gap between the observations that are, typically, discrete in both time and space and the continuum of the atmospheric and oceanic fields. Data assimilation, as distinct from polynomial interpolation, statistical regression, or the inverse methods used in solid-earth geophysics, first arose in the late 1960s from the needs of numerical weather prediction (NWP), on the one hand, and the appearance of time-continuous data streams from satellites, on the other hand (Charney, Halem, and Jastrow, 1969; Ghil, Halem, and Atlas, 1979). NWP is essentially an initial-value problem for the partial differential equations (PDEs) governing large-scale atmospheric flows (Richardson, 1922) that needed a complete and accurate initial state every 12 or 24 hours.

Data assimilation combines partial and inaccurate observational data with a dynamic model, based on physical laws, that governs the evolution of the continuous medium under study to provide the best estimates of the state of the medium. This model is also subject to errors, due to incomplete knowledge of the smaller-scale processes, numerical discretization errors, and other factors. Given these two sources of information, observational and physicmathematical, there are three types of problems that can be formulated and solved given measurements over a time interval $\{t_0 \leq t \leq t_1\}$: filtering, smoothing, and prediction; see Fig. 9.

Filtering involves obtaining a best-possible estimate of the state $\mathbf{X}(t)$ at $t = t_1$, *smoothing* at all times $t_0 \leq t \leq t_1$, and *prediction* at times $t > t_1$. Filtering and prediction are typically used in NWP and can be considered the generation of short “video loops,” while smoothing is typically used in climate studies and resembles the generation of long “feature movies” (Ghil and Malanotte-Rizzoli, 1991).

Figure 10 illustrates a so-called forecast-assimilation cycle, as used originally in NWP: at evenly spaced, preselected times $\{t_k : k = 1, 2, \dots, K\}$, one obtains an analysis of the state

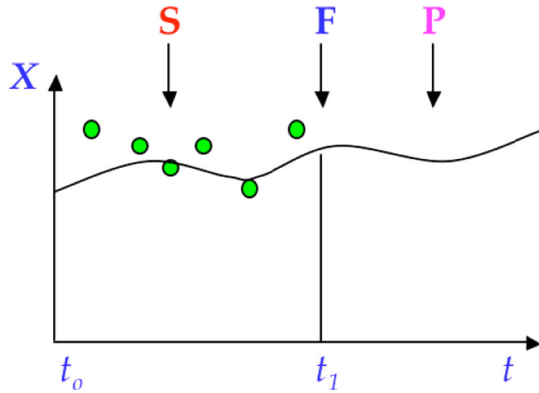


FIG. 9. Schematic diagram of filtering **F**, smoothing **S**, and prediction **P**; green solid circles are observations. From Wiener, 1949.

$\mathbf{X}(t_k)$ by combining the observations over some interval preceding the time t_k with the forecast from the previous state $\mathbf{X}(t_{k-1})$ (Bengtsson, Ghil, and Källén, 1981; Kalnay, 2003). Many variations on this relatively simple scheme have been introduced in adapting it to oceanographic data [see Ghil and Malanotte-Rizzoli (1991) and references therein] and space plasmas [see, e.g., Merkin *et al.* (2016)] or to using the time-continuous stream of remote-sensing data (Ghil, Halem, and Atlas, 1979). Carrassini *et al.* (2018) provided a comprehensive review of data assimilation methodology and applications.

Analyses are routinely used for numerical weather forecasts and take advantage of the continuous improvements of models and observations. But climate studies require data of consistent spatial resolution and accuracy over long time intervals, over which an operational NWP center might have changed its numerical model or its data assimilation scheme, as well as its raw data sources. To satisfy this need, several NWP centers have started in the 1990s to produce so-called reanalyses that use the archived data over multidecadal time intervals, typically since World War II, as well as the best model and data assimilation method available at the time of the reanalysis project. For obvious reasons of computational cost, reanalyses are often run at a lower spatial resolution than the latest version in operational use at the time.

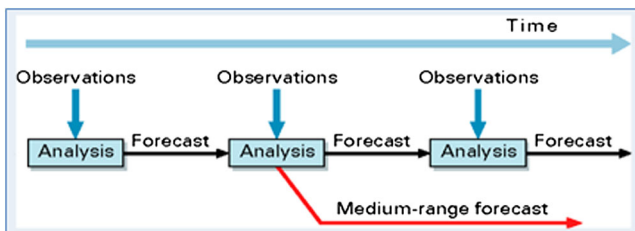


FIG. 10. Schematic diagram of a forecast-assimilation cycle that is used for constructing the best estimates of the state of the atmosphere, ocean, or both through the procedure of data assimilation. Observational data are dynamically interpolated using the a meteorological, oceanographic, or coupled model to yield the analysis products. The red arrow corresponds to a longer forecast, made only from time to time. Greater detail for the case of operational weather prediction appears in Ghil (1989), Fig. 1.

Some leading examples of such diachronically coherent reanalyses for the atmosphere are those produced by the European Centre for Medium-Range Weather Forecasts (ECMWF) (Dee *et al.*, 2011), the NCEP-NCAR reanalysis produced as a collaboration of the U.S. National Centers for Environmental Prediction (NCEP) and the National Center for Atmospheric Research (NCAR) (Kistler *et al.*, 2001), and the JRA-25 reanalysis produced by the Japan Meteorological Agency (Onogi *et al.*, 2007). While these reanalyses agree fairly well for fields that are relatively well observed, such as the geopotential field (see Sec. II.C) over the continents of the Northern Hemisphere, substantial differences persist in their fields over the Southern Hemisphere or those that are observed either poorly or not at all (Dell'Aquila *et al.*, 2005, 2007; Kharin, Zwiers, and Zhang, 2005; Marques *et al.*, 2009; Marques, Rocha, and Corte-Real, 2010; Kim and Kim, 2013).

Compo *et al.* (2011) produced a centennial reanalysis from 1871 to the present by assimilating only surface pressure reports and using observed monthly sea-surface temperature and sea-ice distributions as boundary conditions, while Poli *et al.* (2016) provided a similar product for the time interval 1899–2010, where the surface pressure and the surface winds were assimilated. These enterprises are motivated by the need to provide a benchmark for testing the performance of climate models for the late 19th and the 20th century.

A similar need has arisen for the ocean: on the one hand, several much more sizable data sources have become available through remote sensing and have led to detailed ocean modeling; on the other hand, the study of the coupled climate system requires a more uniform dataset, albeit one less accurate than for the atmosphere alone. Thus, the equivalent of a reanalysis for the ocean had to be produced, in spite of the fact that the equivalent of NWP for the ocean did not exist. A good example of a diachronically coherent dataset for the global ocean is the Simple Ocean Data Assimilation (Carton and Giese, 2008). More recently the community of ocean modelers and observationalists delivered several ocean reanalyses able to provide a robust estimate of the state of the ocean (Lee *et al.*, 2009; Balmaseda *et al.*, 2015).

Finally, by relying on recent advances in numerical methods and in the increased availability of observational data, as well as of increased performance of computing and storage capabilities, coupled atmosphere-ocean data assimilation systems have been constructed; see, e.g., Penny and Hamill (2017). Vannitsem and Lucarini (2016) provided a theoretical rationale for the need of coupled data assimilation schemes to be able to deal effectively with the climate system's multiscale instabilities. These coupled systems play a key role in efforts to produce seamless weather, subseasonal-to-seasonal (S2S), seasonal, and interannual climate predictions (Palmer *et al.*, 2008; Robertson and Vitart, 2018); they have already been used for constructing climate reanalyses; see, e.g., Karspeck *et al.* (2018) and Laloyaux *et al.* (2018).

2. Proxy data

As already mentioned repeatedly and discussed in greater detail in Sec. II.B, climate variability covers a vast range of timescales, and the information we can garner from the instrumental record is limited to the last century or two.

Even so-called historical records extend only to the few millennia of a literate humanity (Lamb, 1972). To extend our reach beyond this eyeblink of the planet's life, it is necessary to resort to indirect measures of past climatic conditions able to inform us about its state thousands or even millions of years ago.

Climate proxies are physical, chemical, or biological characteristics of the past that have been preserved in various natural repositories and that can be correlated with the local or global state of the atmosphere, ocean, or cryosphere at that time. Paleoclimatologists and geochemists currently take into consideration multiple proxy records, including coral records (Boiseau, Ghil, and Juillet-Leclerc, 1999; Karamperidou *et al.*, 2015) and tree rings (Esper, Cook, and Schweingruber, 2002) for the last few millennia, as well as marine-sediment (Duplessy and Shackleton, 1985; Taricco *et al.*, 2009) and ice-core (Jouzel *et al.*, 1993; Andersen *et al.*, 2004) records for the last 2×10^6 yr of Earth's history, the Quaternary. Glaciation cycles, i.e., an alternation of warmer and colder climatic episodes, dominated the latter era. The chemical and physical characteristics, along with the accumulation rate of the samples, require suitable calibration and dating and are used thereafter to infer some of the properties of the climate of the past; see, e.g., Ghil (1994) and Cronin (2010) and references therein.

Proxies differ enormously in terms of precision, uncertainties in the values and dating, and spatiotemporal extent, and they do not homogeneously cover Earth. It is common practice to combine and cross-check many different sources of data to have a more precise picture of the past (Imbrie and Imbrie, 1986; Cronin, 2010). Recently data assimilation methods have started to be applied to this problem as well, using simple models and addressing the dating uncertainties in particular; see, e.g., Roques *et al.* (2014). Combining the instrumental and proxy data with their extremely different characteristics of resolution and accuracy is a complex and sometimes controversial exercise in applied statistics. An important example is that of estimating the globally averaged surface air temperature record well before the industrial era; see Fig. 4 and the previous discussion of the hockey stick controversy in Sec. I.B.2.

B. Climate variability on multiple Timescales

The presence of multiple scales of motions in space and time in the climate system can be summarized through so-called Stommel diagrams. Figure 11(a) presents the original Stommel (1963) diagram, in which a somewhat idealized spectral density associated with the ocean's variability was plotted in logarithmic spatial and temporal scales while characteristic oceanic phenomena whose variance exceeds the background level were identified. Stommel diagrams describe the spatial-temporal variability in a climatic sub-domain by associating different, phenomenologically well-defined dynamical features, such as cyclones and long waves in the atmosphere or meanders and eddies in the ocean, with specific ranges of scales; they emphasize relationships between spatial and temporal scales of motion. Usually, specific dynamical features are associated with specific

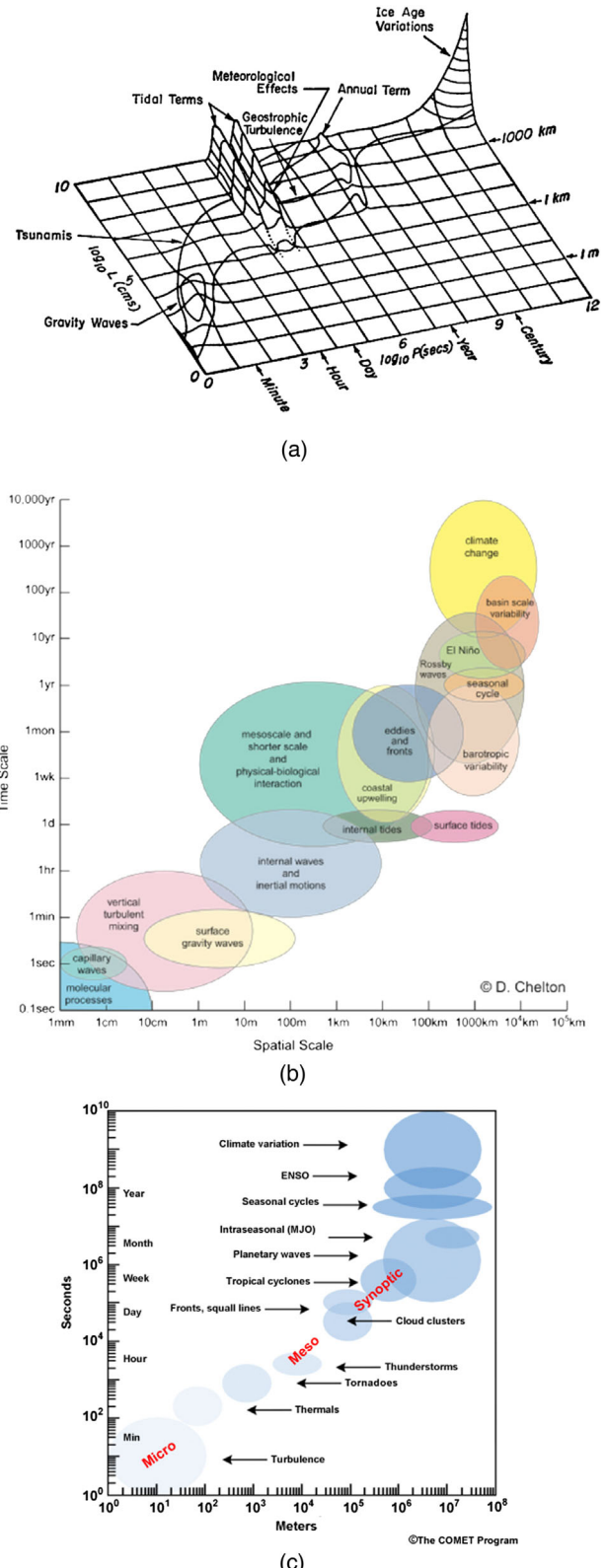


FIG. 11. Idealized wavelength-and-frequency power spectra for the climate system. (a) The original Stommel diagram representing the spectral density (vertical coordinate) of the ocean's variability as a function of the spatial and temporal scale. From Stommel, 1963(b) Diagram qualitatively representing the main features of ocean variability. Courtesy of D. Chelton. (c) The same as (b), describing here the variability of the atmosphere.

approximate balances governing the properties of the evolution equations of the geophysical fluids; see Sec. II.C.2.

In Figs. 11(b) and 11(c), a qualitative Stommel diagram portrays today's estimates of the main range of spatial and temporal scales in which variability is observed for the ocean and the atmosphere, respectively. One immediately notices that larger spatial scales are typically associated with longer temporal scales, in both the atmosphere and the ocean. The two plots show that for both geophysical fluids a “diagonal” of high spectral density in the wavelength-frequency plane predominates. As the diagonal reaches the size of the planet in space, the variability can no longer maintain this proportionality of scales and keeps increasing in timescales, which are not bounded, while the spatial ones are.

Both extratropical cyclones in the atmosphere and eddies in the ocean are due to baroclinic instability, but their characteristic spatial extent in the ocean is 10 times smaller and their characteristic duration is 100 times longer than in the atmosphere. In Fig. 11(c), three important meteorological scales are explicitly mentioned: the microscale (small-scale turbulence), the mesoscale (e.g., thunderstorms and frontal structures), and the synoptic scale (e.g., extratropical cyclones).

Given the different dynamical variability ranges in space and time, different classes of numerical models based on different dynamical balances can simulate explicitly only one or a few such dynamical ranges. The standard way of modeling processes associated with a particular range of scales is to “freeze” processes on slower timescales or to prescribe their slow quasiadiabatic effect on the variability being modeled to handle the processes that are too large or too slow in scale to be included in the model.

As for the faster processes, these are “parametrized”; i.e., one attempts to model their net effect on the variability of interest. Such parametrizations have been, until recently, purely deterministic but have started over the last decade or so to be increasingly stochastic; see Palmer and Williams (2009) and references therein. We discuss the mathematics behind parametrizations and provide a few examples in Sec. III.G.

To summarize, there are about 15 orders of magnitude in space and in time that are active in the climate system, from continental drift at millions of years to cloud processes at hours and shorter increments. The presence of such a wide range of scales in the system provides a formidable challenge for its direct numerical simulation. There is no numerical model that can include all the processes that are active on the various spatial and temporal scales and can run for 10^7 simulated years. Occam's razor and its successors, including Poincaré's parsimony principle (Poincaré, 1902), suggest that if we had one, it would not necessarily be such a good tool for developing scientific insight. It would instead just be a gigantic simulator not helping scientists to distinguish the forest from the trees.

Still, there are increasing efforts for achieving “seemless prediction” across timescales and space scales; see, e.g., Palmer *et al.* (2008) and Robertson and Vitart (2018). Merryfield *et al.* (2020) provided a comprehensive review of the most recent efforts for bridging the gap between S2S and seasonal-to-decadal predictions.

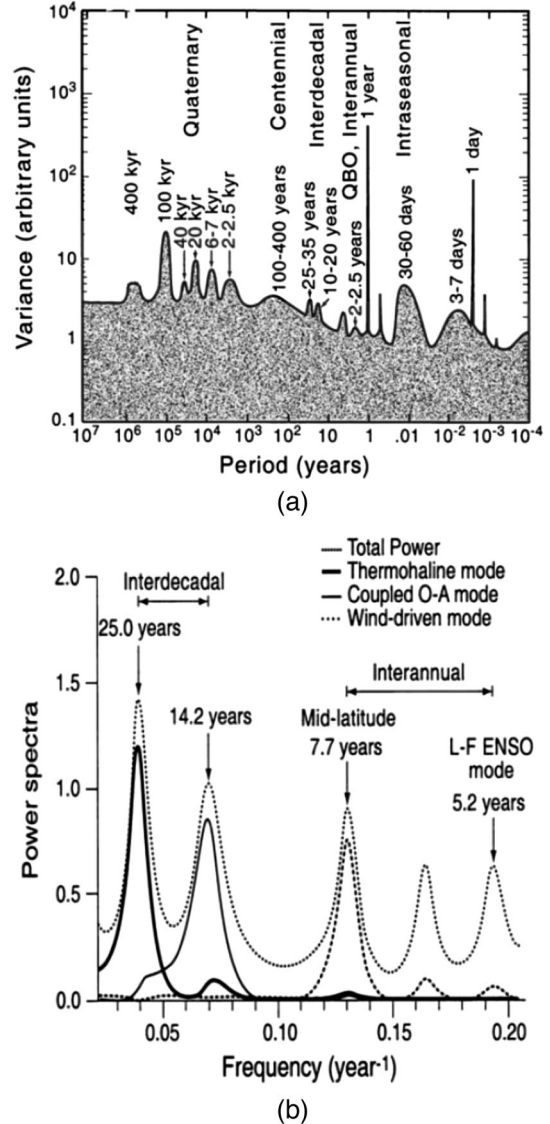


FIG. 12. Power spectra of climate variability across timescales. (a) An artist's rendering of the composite power spectrum of climate variability for a generic climatic variable, from hours to millions of years; it shows the amount of variance in each frequency range. (b) Spectrum of the Central England temperature time series from 1650 to the present. Each peak in the spectrum is tentatively attributed to a physical mechanism; see Plaut, Ghil, and Vautard (1995) for details. From Ghil, 2002.

1. A survey of climatic timescales

Combining proxy and instrumental data allows one to gather information not only on the mean state of the climate system but also on its variability on many different scales. An artist's rendering of climate variability in all timescales is provided in Fig. 12(a). The first version of this figure was produced by Mitchell (1976), and many versions thereof have circulated since. The figure is meant to provide semiquantitative information on the spectral power $S = S(\omega)$, where the angular frequency ω is 2π times the inverse of the oscillation period; $S(\omega)$ is supposed to give the amount of variability in a given frequency band for a generic climatic variable, although one typically has in mind the globally averaged surface air

temperature. Unlike in the Stommel diagrams of Fig. 11, there is no information on the spatial scales of interest.

This power spectrum is not computed directly by spectral analysis from a time series of a given climatic quantity, such as local or global temperature; indeed, there is no single time series that is 10^7 yr long and has a sampling interval of hours, as the figure would suggest. Figure 12(a) instead includes information obtained by analyzing the spectral content of many different time series, for example, the spectrum of the 335-yr-long record of Central England temperatures in Fig. 12(b). This time series is the longest instrumentally measured record of temperatures; see Kondrashov, Feliks, and Ghil (2005) for Nile River water levels. Given the lack of earlier instrumental records, one can imagine but not easily confirm that the higher-frequency spectral features might have changed in amplitude, frequency, or both over the course of climatic history.

With all due caution in its interpretation, Fig. 12(a) reflects three types of variability: (i) sharp lines that correspond to periodically forced variations, at 1 day and 1 yr, (ii) broader peaks that arise from internal modes of variability, and (iii) a continuous portion of the spectrum that reflects stochastically forced variations, as well as deterministic chaos (Ghil, 2002). We provide a mathematical framework to support this interpretation in Sec. IV.E.

Between the two sharp lines at 1 day and 1 yr lies the synoptic variability of midlatitude weather systems, concentrated at 3–7 days, as well as intraseasonal variability, i.e., variability that occurs on the timescale of one to three months. The latter is also called low-frequency atmospheric variability, a name that refers to the fact that this variability has lower frequency or longer periods than the life cycle of weather systems. Intraseasonal variability comprises phenomena such as the Madden-Julian oscillation of winds and cloudiness in the tropics or the alternation between episodes of zonal and blocked flow in midlatitudes (Ghil and Childress, 1987; Ghil, Kimoto, and Neelin, 1991; Ghil and Mo, 1991; Haines, 1994; Molteni, 2002).

Immediately to the left of the seasonal cycle in Fig. 12(a) lies interannual, i.e., year-to-year, variability. An important component of this variability is the El Niño phenomenon in the tropical Pacific Ocean: once about every 2–7 yr, the sea-surface temperatures (SSTs) in the eastern tropical Pacific increase by one or more degrees over a time interval of about 1 yr. This SST variation is associated with changes in the trade winds over the tropical Pacific and in sea level pressures (Bjerknes, 1969; Philander, 1990); an east-west seesaw in the latter is called the Southern Oscillation. The combined El Niño–Southern Oscillation (ENSO) phenomenon arises through large-scale interaction between the equatorial Pacific and the atmosphere above. Equatorial wave dynamics in the ocean plays a key role in setting ENSO’s timescale (Cane and Zebiak, 1985; Neelin, Latif, and Jin, 1994; Neelin *et al.*, 1998; Dijkstra and Burgers, 2002).

The greatest excitement among climate scientists, as well as the public, has more recently been generated by interdecadal variability, i.e., climate variability on the timescale of a few decades, the timescale of an individual human’s life cycle (Martinson *et al.*, 1995). Figure 12(b) represents an enlargement of the interannual-to-interdecadal portion of Fig. 12(a). The broad peaks are due to the climate system’s internal

processes: each spectral component can be associated, at least tentatively, with a mode of interannual or interdecadal variability (Plaut, Ghil, and Vautard, 1995). Thus, the rightmost peak, with a period of 5.5 yr, can be attributed to the remote effect of ENSO’s low-frequency mode (Ghil and Robertson, 2000; Ghil *et al.*, 2002), while the 7.7-yr peak captures a North Atlantic mode of variability that arises from the Gulf Stream’s interannual cycle of meandering and intensification; see Dijkstra and Ghil (2005) and references therein. The two interdecadal peaks, near 14 and 25 yr, are also present in global records, instrumental as well as paleoclimatic (Kushnir, 1994; Mann, Bradley, and Hughes, 1998; Moron, Vautard, and Ghil, 1998; Delworth and Mann, 2000; Ghil *et al.*, 2002).

Finally, the leftmost part of Fig. 12(a) represents paleoclimatic variability. The information summarized here comes exclusively from proxy indicators of climate; see Sec. II.A.2.

The presence of near cyclicity is manifest in this range in the broad peaks present in Fig. 12(a) between roughly 10^3 and 10^6 yr. The two peaks at about 2×10^4 and 4×10^4 yr reflect variations in Earth’s orbit, while the dominant peak at 10^5 yr remains to be convincingly explained (Imbrie and Imbrie, 1986; Ghil, 1994; Gildor and Tziperman, 2001). Quaternary glaciation cycles provide a fertile testing ground for theories of climate variability for two reasons: (i) they represent a wide range of climatic conditions, and (ii) they are much better documented than earlier parts of paleoclimatic history.

Within these glaciation cycles, there is higher-frequency variability prominent in North Atlantic paleoclimatic records. These are the Heinrich events (Heinrich, 1988), marked by a sediment layer that is rich in ice-raftered debris whose near periodicity is of $(6 - 7) \times 10^3$ yr, and the Dansgaard-Oeschger cycles (Dansgaard *et al.*, 1993) that provide the peak at around $(1 - 2.5) \times 10^3$ yr in Fig. 12(a). Rapid changes in temperature of up to half of the amplitude of a typical glacial-interglacial temperature difference occurred during Heinrich events and somewhat smaller ones over a Dansgaard-Oeschger cycle. Progressive cooling through several of the latter cycles, followed by an abrupt warming, defines a Bond cycle (Bond *et al.*, 1997). None of these higher-frequency phenomena can be directly connected to orbital or other cyclic forcings.

In summary, climate variations range from the large-amplitude climate excursions of past millennia to smaller-amplitude fluctuations on shorter timescales. Several spectral peaks of variability can be clearly related to forcing mechanisms; others cannot. In fact, even if the external forcing were constant in time, i.e., if no systematic changes in insolation or atmospheric composition, such as trace gas or aerosol concentrations, would occur, the climate system would still display variability on many timescales. This statement is clearly true for interannual ENSO variability in the equatorial Pacific, as discussed earlier. We seek to understand multiscale climate variability better in Secs. III and IV, where we look in greater detail at natural climate variability and climate response to forcings, respectively.

2. Atmospheric variability in mid-latitudes

Midlatitude atmospheric variability during boreal winter, when the winds are stronger and the variability is larger in the

Northern Hemisphere, has long been a major focus of dynamic meteorology. The intent of this section is to motivate the reader to appreciate the complexity of large-scale atmospheric dynamics by focusing on a relatively well understood aspect thereof. We see that fairly diverse processes contribute to the spectral features discussed in connection with Fig. 12.

The synoptic disturbances that are most closely associated with midlatitude weather have characteristic timescales of the order of 3–10 days, with a corresponding spatial scale of the order of 1000–2000 km (Holton and Hakim, 2013). They roughly correspond to the familiar eastward-propagating cyclones and anticyclones and emerge as a result of the process of baroclinic instability, which converts available potential energy of the zonal flow into eddy kinetic energy.

This conversion is a crucial part of the Lorenz energy cycle (Lorenz, 1955, 1967), and it occurs through the lowering of the center of mass of the atmospheric system undergoing an unstable development. Baroclinic instability (Charney, 1947; Vallis, 2006; Holton and Hakim, 2013) is active when the meridional temperature gradient or, equivalently, the vertical wind shear is strong enough. These conditions are more readily verified in the winter season, which features a large equator-to-pole temperature difference and a strong midlatitude jet (Speranza, 1983; Holton and Hakim, 2013).

The space-time spectral analysis introduced by Hayashi (1971) and refined by Pratt (1976) and Fraedrich and Bottger (1978) builds upon the idea of the Stommel diagrams in Fig. 11. In addition, it provides information about the direction and speed at which the atmospheric eddies move and associates with each range of spatial and temporal scales a corresponding weight in terms of spectral power. This information may be obtained in the first instance by Fourier analysis of a one-dimensional spatial field, and it allows one to reconstruct the propagation of atmospheric waves. This analysis is usually carried out in the so-called zonal, i.e., west-to-east, direction; see Sec. II.C.

Next one can compute the power spectrum in the frequency domain for each spatial Fourier component and then average the results across consecutive winters to derive a climatology of winter atmospheric waves. The difficulty here lies in the fact that straightforward space-time decomposition does not distinguish between standing and traveling waves: a standing wave gives two spectral peaks corresponding to waves that travel eastward and westward at the same speed and with the same phase. This problem can be circumvented only by making assumptions regarding a given wave's nature. For instance, we may assume complete coherence between the eastward and westward components of standing waves and attribute the incoherent part of the spectrum to actual traveling waves.

Figure 13 shows the spectral properties of the winter 500-hPa geopotential height field meridionally averaged across the midlatitudes of the northern hemisphere (specifically, between 30° and 75° N) for the time interval 1957–2002. The properties of all waves, as well as the standing, eastward-traveling, and westward-traveling waves, appear in panels Figs. 13(a)–13(d), respectively. As discussed later, the 500-hPa height field provides a synthetic yet comprehensive picture of the atmosphere's synoptic to large-scale dynamics.

Figure 13(c) shows that the eastward-propagating waves are dominated by synoptic variability, concentrated over 3–12-day periods and zonal wave numbers 5–8; note that a single cyclone or anticyclone counts for half a wavelength. In addition, the slanting high-variability ridge in \bar{H}_E indicates the existence of a statistically defined dispersion relation that relates frequency and wave number, which is in agreement with the basic tenets of baroclinic instability theory (Holton and Hakim, 2013).

When looking at the westward-propagating variance in Fig. 13(d), one finds that the dominant portion of the variability is associated with low-frequency, planetary-scale Rossby waves. Finally, Fig. 13(b) shows the contribution to the variance given by standing waves, which correspond to large-scale, geographically locked, and persistent phenomena like blocking events. Note that westward-propagating and stationary waves provide the lion's share of the overall variability of the atmospheric field; see also Kimoto and Ghil (1993a), Fig. 7.

The dynamics and energetics of planetary waves are still under intensive scrutiny. Descriptions and explanations of several highly nonlinear aspects thereof are closely interwoven with those of blocking events, identified as persistent, large-scale deviations from the zonally symmetric general circulation (Charney and DeVore, 1979; Legras and Ghil, 1985; Benzi *et al.*, 1986; Ghil and Childress, 1987; Benzi and Speranza, 1989; Kimoto and Ghil, 1993a). Weeks *et al.* (1997) provided a fine example of contrast between a blocking event and the climatologically more prevalent zonal flow.

Persistent blocking events strongly affect the weather for up to a month over continental-size areas. Such persistence offers some hope for extended predictability of large-scale flows, and of the associated synoptic-scale weather, beyond the usual predictability of the latter, which is believed not to exceed 10–15 days; see Lorenz (1996) and references therein.

Today, the most highly resolved and physically detailed NWP models are reasonably good at predicting the persistence of a blocking event once the model's initial state is within that event, but not at predicting the onset of such an event or its collapse (Ferranti, Corti, and Janousek, 2015). Likewise, the capability of necessarily lower-resolution climate models to simulate the spatiotemporal statistics of such events is far from perfect; in fact, relatively limited improvement has been realized in the last two decades (Davini and D'Andrea, 2016). Weeks *et al.* (1997) reproduced successfully in the laboratory key features of the dynamics and statistics of blocking events.

Ghil and Robertson (2002) reviewed several schematic descriptions of the midlatitude atmosphere's low-frequency variability (LFV) as jumping between a zonal regime and a blocked one or, more generally, a small number of such regimes. This coarse graining of the LFV's phase space and Markov chain representation of the dynamics continues to inform current efforts at understanding what atmospheric phenomena can be predicted beyond 10–15 days and how. Recently analyses based on dynamical-systems theory have associated blocked flow configurations with higher instability of the atmosphere as a whole (Schubert and Lucarini, 2016;

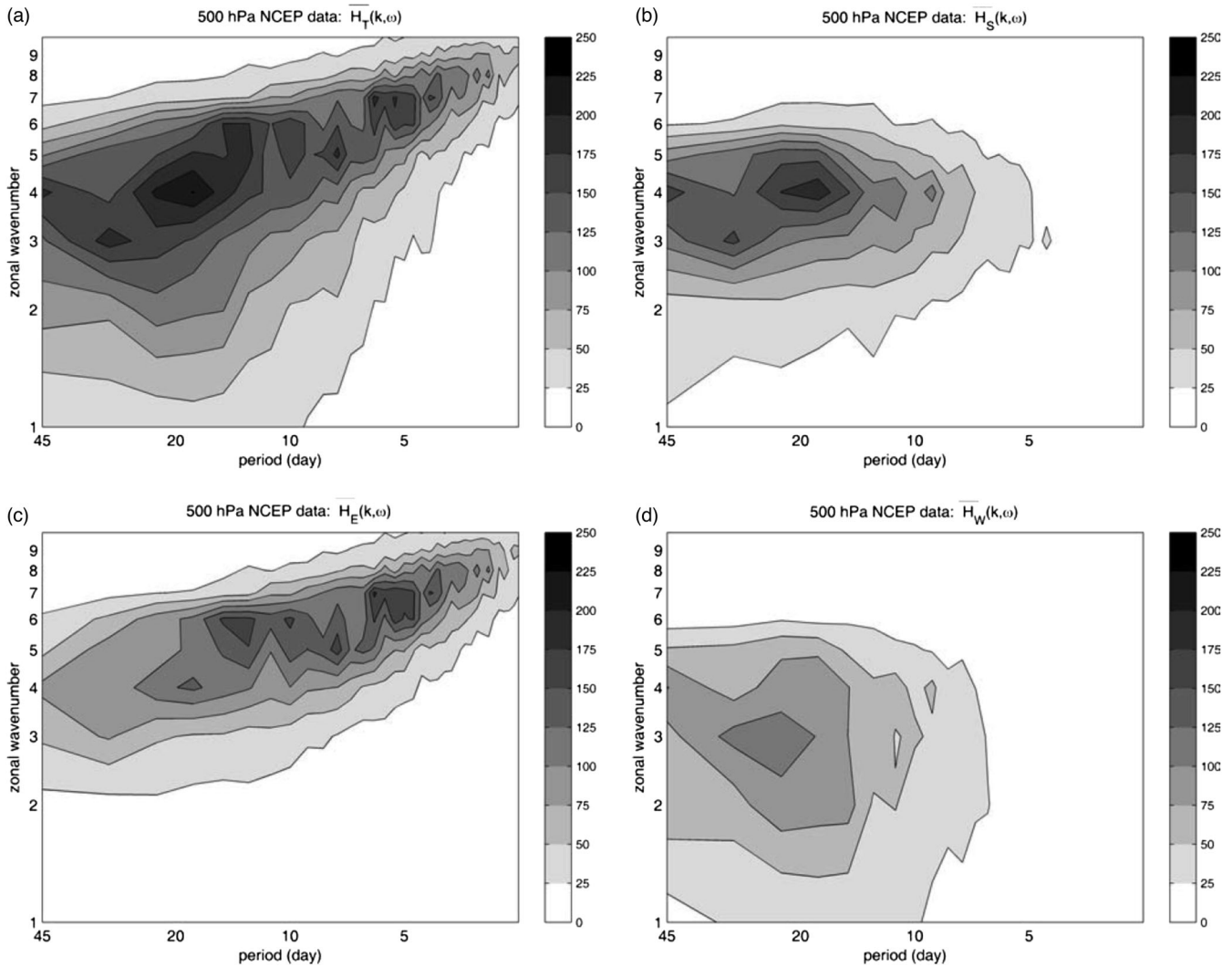


FIG. 13. Variance \bar{H} of the winter (December–February) atmospheric fields in the midlatitudes of the Northern Hemisphere. (a) Total variance \bar{H}_T . (b) Variance associated with standing waves \bar{H}_S . (c) Variance associated with eastward-propagating waves \bar{H}_E . (d) Variance associated with westward-propagating waves \bar{H}_W . Based on NCEP-NCAR reanalysis data (Kistler *et al.*, 2001). See the text for details. From Dell’Aquila *et al.*, 2005.

Faranda, Messori, and Yiou, 2017; Lucarini and Gritsun, 2020), as predicted by Legras and Ghil (1985).

The effect of global warming on the statistics of blocking events has recently become a matter of considerable controversy. The sharper increase of near-surface temperatures in the Arctic than near the Equator is fairly well understood [see, e.g., Ghil (1976), Fig. 7] and has been abundantly documented in recent observations; see, e.g., Walsh (2014), Fig. 8. This decrease in pole-to-equator temperature difference ΔT is referred to as polar amplification of global warming.

Francis and Vavrus (2012) and Liu *et al.* (2012) suggested that reduced ΔT slows down the prevailing westerlies and increases the north-south meandering of the subtropical jet stream, resulting in more frequent blocking events. This suggestion seems to agree with fairly straightforward arguments of several other authors on the nature of blocking (Charney and DeVore, 1979; Legras and Ghil, 1985; Ghil and Childress, 1987), as illustrated, for instance, by Ghil and Robertson (2002) in their Fig. 2): The strength ψ_A^* of the

driving jet in the figure is proportional to ΔT , in accordance with standard quasigeostrophic flow theory,¹¹ and lower jet speeds ψ_A favor blocking. Ruti *et al.* (2006) also presented observational evidence for a nonlinear relation between the strength of the subtropical jet and the probability of occurrence of blocking events, in agreement with the bent-resonance theory of midlatitude LFV proposed by Benzi *et al.* (1986).

Considerable evidence against the apparently straightforward argument for global warming as the cause of an increase in midlatitude blocking has accumulated too from both observational and modeling studies; see Hassanzadeh, Kuang, and Farrell (2014), Barnes and Screen (2015), and references therein. The issue is far from settled, as are many questions about other regional effects of global warming.

¹¹See Secs. II.C.2 and II.C.3 for geostrophic balance, quasigeostrophy, and their consequences.

C. Basic properties and fundamental equations

1. Governing equations

The evolution of the atmosphere, the ocean, the soil, and the ice masses can be described by using the continuum approximation, in which these subsystems are represented by field variables that depend on three spatial dimensions and time. For each of the climatic subdomains, we consider the following field variables: the density ρ and the heat capacity at constant volume C , with the specific expression for ρ and C defining the thermodynamics of the medium; the concentration of the chemical species $\{\xi_k : 1 \leq k \leq K\}$ contained in the medium and present in different phases, e.g., the salt dissolved in the ocean or the water vapor in the atmosphere; the three components $\{v_i : 1 \leq i \leq 3\}$ of the velocity vector; the temperature T ; the pressure p ; the heating rate J ; and the gravitational potential Φ .

Note that by making the thin-shell approximation $H/R \ll 1$, where H is the vertical extent of the geophysical fluid and R is the radius of Earth, we can assume that the gravitational potential at the local sea level is zero and can thus safely use the approximation $\Phi = gz$, where Φ is then called the geopotential, g is the gravity at the surface of Earth, and z is the geometric height above sea level. Moreover, one has to take into account the fact that the climate system is embedded in a noninertial frame of reference that rotates with an angular velocity Ω with components $\{\Omega_i : 1 \leq i \leq 3\}$.

The PDEs that govern the evolution of the field variables are based on the budget of mass, momentum, and energy. When the fluid contains several chemical species, their separate budgets also have to be accounted for (Vallis, 2006). To have a complete picture of the Earth system, one should in principle also consider the evolution of biological species. Doing so, however, is well beyond our scope here, even though present Earth system models do attempt to represent biological processes, albeit in a simplified way; see the discussion in Sec. II.D.

The mass budget equations for the constituent species can be written as follows:

$$\partial_t(\rho\xi_k) = -\partial_i(\rho\xi_k v_i) + D_{\xi_k} + L_{\xi_k} + S_{\xi_k}. \quad (1)$$

Here ∂_t is the partial derivative in time and ∂_i is the partial derivative in the x_i direction; D_{ξ_k} , L_{ξ_k} , and S_{ξ_k} are the diffusion operator, phase changes, and local mass budget due to other chemical reactions that are associated with k .

The momentum budget's i th component is written as

$$\begin{aligned} \partial_t(\rho v_i) &= -\partial_j(\rho v_j v_i) - \partial_i p + \rho \partial_i \Phi \\ &\quad - 2\rho \epsilon_{ijk} \Omega_j v_k + T_i + F_i. \end{aligned} \quad (2)$$

Here the Levi-Civita antisymmetric tensor ϵ_{ijk} is used to write the Coriolis force; T_i indicates direct mechanical forcings, e.g., those resulting from lunisolar tidal effects; $F_i = -\partial_j \tau_{ij}$ corresponds to friction, with $\{\tau_{ij}\}$ the stress tensor; and summation over equal indices is used. Equation (2) is just a forced version of the momentum equation in the Navier-Stokes equations (NSEs), written in a rotating frame of reference.

A general state equation valid for both fluid envelopes of Earth, i.e., the atmosphere and the ocean, is

$$\rho = g(T, p, \xi_1, \dots, \xi_K). \quad (3)$$

As a first approximation, one can take $K = 1$, where $\xi_1 = \xi$ is, respectively, moisture in the atmosphere and salinity of the ocean. For brevity, we restrict ourselves here to the atmosphere.

In general, one can write the specific energy of the climate system as the sum of the specific internal, potential, and kinetic energies, also taking into account the contributions coming from chemical species in different phases. To get manageable formulas, some approximations are necessary; see, e.g., Peixoto and Oort (1992).

Neglecting reactions other than the phase changes between the liquid and gas phases of water, the expression of the specific energy in the atmosphere is

$$e = c_v T + \Phi + v_j v_j / 2 + L q,$$

where c_v is the specific heat at constant volume for the gaseous atmospheric mixture, L is the latent heat of evaporation, and $q = \rho \xi$ is the specific humidity. In this formula, we neglect the heat content of the liquid and solid water and the heat associated with the phase transition between solid and liquid water. Instead, the approximate expression for the specific energy in the ocean is

$$e = c_w T + \Phi + v_j v_j / 2,$$

where c_w is the specific heat at constant volume of water, while neglecting the effects of salinity and of pressure. Finally, for the specific energy of soil or ice, we can take $e = c_{\{S,I\}} T + \Phi$, respectively.

After some nontrivial calculations, one derives the following general equation for the local energy budget:

$$\begin{aligned} \partial_t(\rho e) &= -\partial_j(\rho e v_j) - \partial_j Q_j^{\text{SW}} - \partial_j Q_j^{\text{LW}} \\ &\quad - \partial_j J_j^{\text{SH}} - \partial_j J_j^{\text{LH}} - \partial_j(v_i \tau_{ij}) + v_i T_i, \end{aligned} \quad (4)$$

where e is the energy per unit mass and $\epsilon = e + p/\rho$ is the enthalpy per unit mass. The energy source and sink terms can be written as the sum of the work done by the mechanical forcing $v_i T_i$ and of the respective divergences of the shortwave (solar) and longwave (terrestrial) components of the Poynting vector Q_j^{SW} and Q_j^{LW} , of the turbulent sensible and latent heat fluxes J_j^{SH} and J_j^{LH} , and of the scalar product of the velocity field with the stress tensor $v_i \tau_{ij}$.

Equation (4) is written in a conservative form, with the right-hand side containing only the sum of flux divergences, except for the last term, which is negligible. By taking suitable volume integrals of Eq. (4) and assuming steady-state conditions, one derives meridional enthalpy transports from the zonal budgets of energy fluxes (Ghil and Childress, 1987; Peixoto and Oort, 1992; Lucarini and Ragone, 2011; Lucarini, Blender *et al.*, 2014); recall Figs. 2(a) and 2(b). The presence of inhomogeneous absorption of shortwave radiation due to the geometry of the Sun-Earth system and of the physico-chemical properties of the climatic subdomains determines the

presence of nonequilibrium conditions for the climate system, as already discussed in Sec. I.A.

Various versions of Eqs. (1)–(4) have been studied for over a century, and well-established thermodynamical and chemical laws accurately describe the phase transitions and reactions of the climate system's constituents. Finally, quantum mechanics allows one to calculate in detail the interaction between matter and radiation.

Still, despite the fact that climate dynamics is governed by well-known evolution equations, it is way beyond our scientific ability to gain a complete picture of the mathematical properties of the solutions. In fact, many fundamental questions are still open regarding the basic NSEs in a homogeneous fluid without phase transitions and rotation (Temam, 1984, 1997). In particular, even for the basic NSEs, providing analytical, closed-form solutions is possible only in some highly simplified cases that are either linear or otherwise separable (Batchelor, 1974).

As discussed, Eqs. (1)–(4) can simulate a range of phenomena that spans many orders of magnitude in spatial and temporal scales. Hence, it is virtually impossible to construct numerical codes able to explicitly represent all ongoing processes at the needed resolution in space and time. It is thus necessary to parametrize the processes that occur at subgrid scales and cannot, therewith, be directly represented. Among the most important processes of this type are cloud-radiation interactions and turbulent diffusion. We discuss the theoretical framework behind the formulation of parametrizations in Sec. III.G.

2. Approximate balances and filtering

Equations (1)–(4) are too general and contain too many wave propagation speeds and instabilities to properly focus on certain classes of phenomena of interest. For instance, the fluid's compressibility plays a role only in the propagation of extremely fast acoustic waves, whose energy is negligible, compared to that of the winds and currents we are interested in here.

Therefore, starting with Charney (1947), more-or-less-systematic approximations have been introduced to filter out undesirable waves from the equations of motion and to study particular classes of phenomena and processes. Depending on the climate subsystem and the range of scales of interest, different approximations can be adopted. For example, if one considers ice sheets and bedrock on the timescale of millennia, it is reasonable to assume that $v_j \simeq 0$, i.e., to remove the flow field from the evolution equation; see Ghil (1994), Saltzman (2001), and references therein. This approximation is not valid if one wants to describe explicitly the motion of the ice sheets on shorter timescales (Paterson, 1981).

More precisely, the filtering process consists of applying a set of mathematical approximations to the fundamental governing equations, usually considered to be a suitable generalization of the classical NSEs like Eqs. (1)–(4). The purpose of this filtering is to exclude from the filtered system certain physical processes that are heuristically assumed to play only a minor role in its dynamics at the timescale and space scale under investigation. The magnitudes of all

terms in the governing equations for a particular type of motion are estimated by dimensional analysis (Barenblatt, 1987), and various classes of simplified equations have been derived by considering distinct asymptotic regimes in the associated scales (Ghil and Childress, 1987; Pedlosky, 1987; McWilliams, 2006; Klein, 2010).

The approximations adopted rely on assuming that the continuous medium, whether fluid or solid, obeys suitably defined time-independent relations or undergoes only small departures from such relations, and that these relations result from the balance of two or more dominating forces. Imposing such balances leads to reducing the number of independent field variables of the system that obey a set of evolution equations. Additionally, the imposition of dynamical balances leads to removing specific wave motions from the range of allowed dynamical processes.

In meteorological terminology, a *prognostic* variable whose tendency, i.e., time derivative, appears in the full equations may thus become a *diagnostic* variable, which appears in a nondifferentiated form only in the filtered equations. Next we see two of the most important examples of filtering, which, among other things, are essential for the practical implementation of numerical models of the atmosphere and ocean (Vallis, 2006; Cushman-Roisin and Beckers, 2011; Holton and Hakim, 2013).

a. Hydrostatic balance

A classical example of filtering is the hydrostatic approximation. In a local Cartesian coordinate system (x, y, z) , we define by $\hat{z} = \nabla\Phi/|\nabla\Phi|$ the direction perpendicular to a geopotential isosurface $\Phi \equiv \text{const}$. An obvious stationary solution of the NSEs is given in these coordinates by the time-independent hydrostatic balance equation

$$\rho_h g = -\partial_z p_h, \quad (5)$$

where the subscript h denotes this solution.

On sufficiently large spatial and temporal scales, many geophysical flows, e.g., atmospheric and oceanic, as well as continental surface and ground water, are near hydrostatic equilibrium. In general, stable hydrostatic equilibrium is achieved when fluid with lower specific entropy lies below fluid with higher specific entropy; in this case, Eq. (5) is obeyed for all (x, y, z) within the domain occupied by the fluid.

When this condition is broken because of external forcing or internal heating, say, the stratification is not stable and the fluid readjusts so as to reestablish the hydrostatic equilibrium. This readjustment is achieved by vertical convective motions, in which available potential energy is transformed into kinetic energy responsible for vertical motions that can locally be much faster than the large-scale flow. Violations of hydrostatic balance thus exist only on short timescales and space scales.

A large class of models used in studying, simulating, and attempting to predict climate variability and climate change is based on a particular simplification of the full set of Eqs. (1)–(4). This simplification leads to the so-called primitive equations, which filter out nonhydrostatic motions. As a result, sound waves are excluded from the solutions, a

fact that facilitates the numerical implementation of such models (Washington and Parkinson, 2005; Cushman-Roisin and Beckers, 2011).

The primitive equations are derived by assuming that the time-independent hydrostatic balance given in Eq. (5) does apply at all times, even when the flow is time dependent. One thus assumes that the vertical acceleration of the fluid is everywhere much smaller than gravity. Neglecting the vertical acceleration altogether leads to a monotonic relationship between the vertical coordinate z and pressure p .¹²

One can hence replace z with p as a vertical coordinate and rewrite the modified Eqs. (1)–(4) using a new coordinate system in which one also replaces, typically, the horizontal coordinates (x, y) by the longitude λ and the latitude ϕ , respectively. In such a coordinate system, $v_3 \equiv \omega \equiv \partial_t p$ is the change of pressure with time, the 3D velocity field is non-divergent $\partial_j v_j = 0$, and the density is automatically constant and set to 1 (Vallis, 2006; Holton and Hakim, 2013).

Despite the use of primitive equations, climate models aim at simulating a system that nonetheless features nonhydrostatic motions. Additionally, geophysical flows obeying primitive equations can lead to unstable vertical configurations of the fluids. Typical climate models are formulated to quickly eliminate local nonhydrostatic conditions and to parametrize the balanced condition that is thus recovered in terms of variables that are explicitly represented in the model, following the idea of convective adjustment originally proposed by Manabe and Strickler (1964). Finding optimal ways to parametrize the effect of convection on hydrostatic climate models has become a key research area in climate dynamics; see Emanuel (1994) for a classical treatise on the problem of atmospheric convection and Plant and Yano (2016) for a recent overview.

The primitive equations were at the core of both climate models and weather prediction models for three decades, from about the 1970s through the 1990s. Nonhydrostatic models, constructed through discretization of the full NSEs with forcing and rotation, have become increasingly available over the last decade, first as limited-area models and more recently even as global ones; see, e.g., Marshall *et al.* (1997).

These models require extremely high resolution in space and time and are computationally quite expensive; as they start to enter operational use, they require state-of-the-art hardware and software, in terms of both computing and storage, as well as sophisticated postprocessing of the output. Moreover, for all practical purposes sufficiently detailed initial and boundary data are not available, and methodological problems reappear in connection with formulating such data. Still, the use of nonhydrostatic models allows, in principle, for bypassing the key problem of parametrizing convection.

b. Geostrophic balance

Another important example of filtering is the one associated with time-independent purely horizontal balanced flows, in

which the horizontal components of the pressure gradient force and the Coriolis force cancel out in the NSEs. Such flows are termed geostrophic; etymologically, this means Earth turning. The nondimensional parameter that determines the validity of this approximation is the Rossby number $\text{Ro} = U/f_0 L$, where U is a characteristic horizontal velocity, L is a characteristic horizontal extent, and $f_0 = 2\Omega \sin \phi_0$; here Ω is the modulus of Earth's angular frequency of rotation around its axis and ϕ_0 is a reference latitude.

The geostrophic approximation provides a good diagnostic description of the flow when $\text{Ro} \ll 1$. Such small Ro values prevail for the atmosphere on synoptic and planetary scales, such as those of extratropical weather systems, say poleward of 30° , where f_0 is large enough, and in the free atmosphere, i.e., above the planetary boundary layer, where frictional forces can be comparable to the Coriolis force. In the ocean, this approximation is extremely accurate everywhere except close to the equator. The smallness of the Rossby number in the ocean arises from oceanic currents being orders of magnitude slower than atmospheric winds, so Ro nears unity only where f_0 is extremely small.

Purely geostrophic flow fields are obtained via a zeroth-order expansion in Ro of the NSEs. Fluid motion is introduced by considering small perturbations ρ_g and p_g that break the translation symmetry of the basic, purely hydrostatic density and pressure fields ρ_h and p_h but preserve the geostrophic balance, i.e., one sets $\rho = \rho_h + \rho_g$ and $p = p_h + p_g$, respectively.

Letting \hat{x} be locally the zonal direction and \hat{y} be locally the meridional direction, one can write (Holton and Hakim, 2013) the geostrophic balance at each height z as

$$\rho_h u f_0 = -\partial_y p_g, \quad (6a)$$

$$\rho_h v f_0 = \partial_x p_g, \quad (6b)$$

where the derivatives are taken at constant z , $(u, v) = (v_1, v_2)$ and, furthermore, the geostrophic perturbation itself is in hydrostatic equilibrium, i.e., $g\rho_g = -\partial_z p_g$. The combined hydrostatic and geostrophic balance constrains atmospheric and oceanic motions so that the velocity field is uniquely determined by the pressure field. In such doubly balanced flows, the winds or currents are parallel to the isobars at a given geopotential height z , as shown in Fig. 14(a) rather than perpendicular to the isobars, as in nonrotating fluids. Moreover, the vertical component of the velocity field vanishes $w = v_3 \equiv 0$.

Using the pressure coordinate system (x, y, p) described previously, where p plays the role of the vertical coordinate, it is possible to express the geostrophic balance as follows (Holton and Hakim, 2013):

$$f_0 u_g = -\partial_y \Phi, \quad (7a)$$

$$f_0 v_g = \partial_x \Phi, \quad (7b)$$

where this time derivatives are taken at constant p . The vertical derivative $\partial_p \Phi$ can, furthermore, be expressed in terms of ρ_g . For the atmosphere, one can make the simplifying

¹²The validity of this approximation, even locally in space and at most times, explains Pascal's experimental observation during the famed 1648 Puy-de-Dôme ascension that a barometer's reading decreases monotonically with altitude.

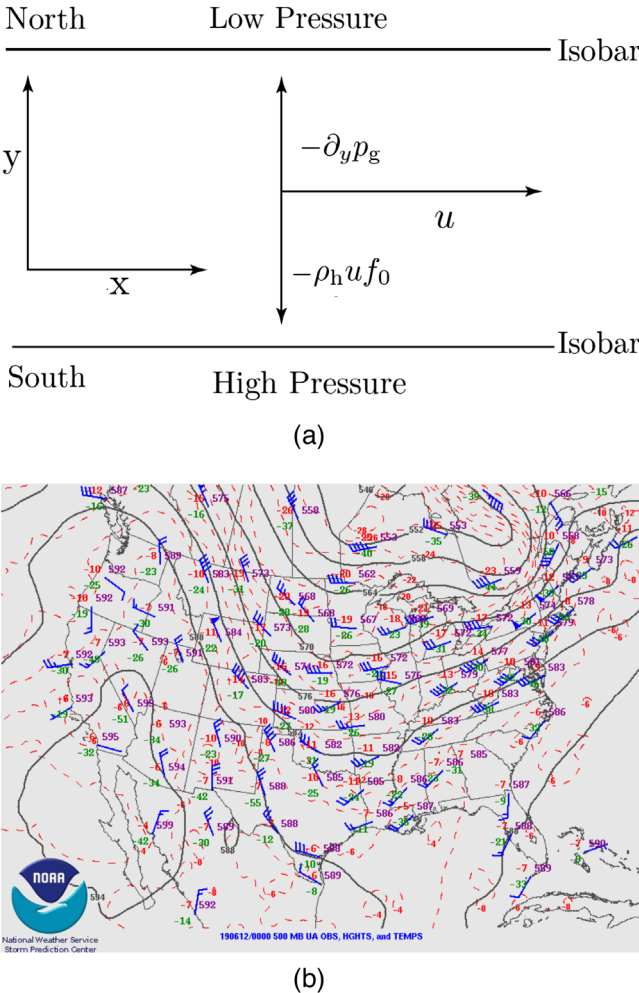


FIG. 14. Geostrophic balance. (a) Schematics of geostrophically balanced flow in the Northern Hemisphere. At a given z level, the pressure gradient force (upward-pointing arrow) and Coriolis force (downward-pointing arrow) cancel out and the flow (horizontal arrow) is parallel to the isolines. (b) Synoptic conditions for the 500-hPa level over the United States at 0000 Greenwich Mean Time (GMT) on 12 July 2019. The dark gray lines indicate the isolines of geopotential height $z = \Phi/g$ (in units of 10 m), and the barbed blue arrows indicate the direction of the wind; the bars indicate the wind speed, with each short (long) bar corresponding to a speed of 5 knots (10 knots), with 2 knots = 1.03 ms^{-1} . From the NOAA-National Weather Service.¹³

assumption of dry conditions, for which the equation of state is described by the gas constant R and the heat capacity at constant pressure C_p .

Assuming, moreover, a horizontally homogeneous background state with $T_h = T_h(p)$, introducing the potential temperature $\Theta_h = T_h(p/p_s)^{R/C_p}$, with $p_s = \text{const}$ the reference surface pressure, and letting $\sigma := -RT_h d \ln \Theta_h / dp$, which defines the stratification of the background state, one obtains

$$\partial_p \Phi = -\frac{Rp}{\sigma} T_g. \quad (8)$$

¹³See <https://www.spc.noaa.gov/obswx/maps/>.

Thus, in the geostrophic approximation the scalar field Φ provides complete diagnostic information on the state of the fluid: its horizontal derivatives give us the velocity field, while the vertical derivative gives us the geopotential, or mass field, via perturbations with respect to the background temperature field (Holton and Hakim, 2013).

Essentially, geophysical fluid dynamics (GFD) is the study of large-scale flows dominated by the combined hydrostatic and geostrophic balances. The former is a consequence of the shallowness of the planetary flows, the latter is a consequence of their rotation (Ghil and Childress, 1987; Pedlosky, 1987; McWilliams, 2006; Cushman-Roisin and Beckers, 2011). Section II.C.3 introduces the more complex situation of finite-but-small perturbations from this combined balance.

Although modern computers allow a fully ageostrophic (beyond geostrophic approximation) description of most geophysical fluids, geostrophic balance remains a fundamental tool of theoretical research, and it is also used for practical applications in everyday weather prediction. Figure 14(b) illustrates a typical midlatitude synoptic situation: at a given pressure level, the winds blow, to a good approximation, parallel to the isolines of geopotential height, and the speed of the wind is higher where the gradient of geopotential height is stronger. An appendix in Ghil, Halem, and Atlas (1979) describes the extent to which diagnostic relations based on the geostrophic approximation are still used in the analysis and prediction of midlatitude weather, as simulated by advanced numerical models. Indeed, geostrophic approximation is implicit in the day-to-day reading of weather maps on synoptic-to-planetary scales.

3. Quasigeostrophy and weather forecasting

The diagnostic, i.e., time-independent nature of the geostrophic balance, implies that the ageostrophic terms, although relatively small, are important for the time evolution of the flow. A planetary flow that evolves slowly in time compared to $1/f_0$ can be described using quasigeostrophic theory, namely, a perturbative theory that expands the NSEs in Ro and truncates at first order.

The use of the quasigeostrophic approximation effectively filters out solutions that correspond to higher-speed atmospheric or oceanic inertia-gravity waves; the latter, also called Poincaré waves, are gravity waves modified by the presence of rotation (Ghil and Childress, 1987; Pedlosky, 1987; McWilliams, 2006; Vallis, 2006; Cushman-Roisin and Beckers, 2011; Holton and Hakim, 2013). This approximation breaks down, though, near frontal discontinuities and in other situations in which the ageostrophic component of the velocity field plays an important advective role, and it has to be improved upon by retaining higher-order terms.

In quasigeostrophic theory, a fundamental role is played by the quasigeostrophic potential vorticity¹⁴

$$q = \frac{1}{f_0} \Delta_2 \Phi + f + \partial_p \left(\frac{f_0}{\sigma} \partial_p \Phi \right). \quad (9)$$

¹⁴More general formulations of potential vorticity are also quite important in GFD; see, e.g., Hoskins, McIntyre, and Robertson (1985).

Here Δ_2 is the horizontal Laplacian in p coordinates, the first term $\zeta_g = \Delta_2 \Psi / f_0$ is the relative vorticity of the geostrophic flow, f is the planetary vorticity, and the last term is the stretching vorticity; the static stability σ , which measures the stratification of the fluid, was introduced in Eq. (8).

The potential vorticity q thus combines dynamical and thermodynamical information on the fluid flow. In more abstract terms, one can write

$$q - f = \mathcal{L}\Phi, \quad (10)$$

where \mathcal{L} is a modified three-dimensional Laplacian operator. Using suitable boundary conditions, one can invert Eq. (10) and derive the geopotential field from the vorticity field

$$\Phi = \mathcal{L}^{-1}(q - f). \quad (11)$$

In the absence of forcing and dissipation, q is conserved by geostrophic motions so that

$$\partial_t q + J\left(\frac{\Phi}{f_0}, q\right) = 0, \quad (12)$$

where $J(A, B) = \partial_x A \partial_y B - \partial_y A \partial_x B$ is the Jacobian operator, so $J(\Phi/f_0, q) = (1/f_0)(\partial_x \Phi / \partial_y q - \partial_y \Phi / \partial_x q)$ describes vorticity advection by the geostrophic velocity field (u_g, v_g) ; see Eq. (6). Note that in the limit $\sigma \rightarrow \infty$, i.e., if one assumes infinitely stable stratification, the third term on the right-hand side of Eq. (9) drops out and Eq. (12) describes the conservation of the absolute vorticity in a barotropic two-dimensional flow.

Quasigeostrophic theory, as introduced by Charney (1947), arguably provided a crucial advance for the understanding of the dynamics of planetary flows and provided the foundation for the successful start of NWP (Charney, Fjørtoft, and von Neumann, 1950). The filtering associated with this theory was, in particular, instrumental in eliminating the numerical instability that marred the pioneering weather forecast experiment of Richardson (1922).

In fact, L.F. Richardson used a more accurate set of equations of motion for the atmosphere than the set of Eqs. (9)–(12). Somewhat counterintuitively, the quasigeostrophic model eventually provided a more accurate prediction tool because it represented more robustly the dynamical processes at the scales of interest. The inconclusive result of Richardson's one-step, 6-h numerical experiment was received by the meteorological community at the time as proof that NWP, as proposed by Bjerknes (1904), was not possible.

We outline herewith how the quasigeostrophic potential-vorticity equations can be used to perform stable numerical weather forecasts. Assume that at time $t = t_0$ we have information on the geopotential height field $\Phi_0 = \Phi(t_0)$.

- Step 0: Using Eq. (10), one computes the corresponding potential vorticity field $q_0 = q(t_0)$.
- Step A: Equation (12) is used next to predict the potential vorticity field at time t_1 as follows: $q_1 = q(t_1) = q(t_0) + J(\Phi_0/f_0, q_0)\Delta t$, where $\Delta t = t_1 - t_0$.
- Step B: Equation (11) is used now to infer Φ_1 .
- Step C: Go to step A and predict q_2 , etc.

Three decades after Richardson (1922), Charney, Fjørtoft, and von Neumann (1950) performed the first successful numerical weather forecasts on the ENIAC computer in Princeton by using essentially the same procedure detailed previously for the simpler case of barotropic two-dimensional flow. In this case, the standard absolute vorticity is given by the sum of relative and planetary vorticity, and it plays a role analogous to potential vorticity in quasigeostrophic three-dimensional flow. The procedure was adapted to describe the evolution of the 500-hPa field, which deviates the least from the behavior of an idealized atmosphere of homogeneous density with no vertical velocities. The simulation was performed on a limited domain that covered North America and the adjacent ocean areas.

Charney, Fjørtoft, and von Neumann investigated the issues associated with horizontal boundary conditions, as well as with the numerical stability of the integration. Their success (Charney, Fjørtoft, and von Neumann, 1950) paved the way for the theory's successive applications to physical oceanography and climate dynamics as a whole (Ghil and Childress, 1987; Pedlosky, 1987; Dijkstra, 2005). The saga of this scientific and technological breakthrough was told many times; see Lynch (2008) for a good recent account.

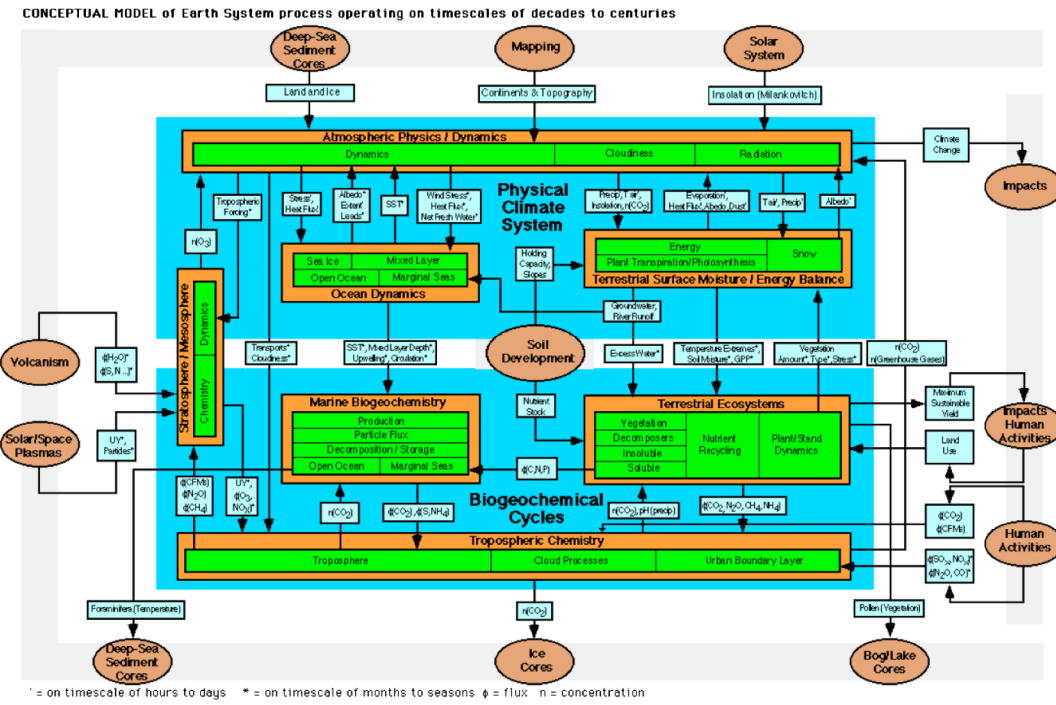
D. Climate prediction and climate model performance

A key area of interest in the climate sciences is the development and testing of numerical models used for simulating the past, present, and future of the climate system. As discussed later in the review, climate models differ enormously in terms of scientific scope, computational cost, and flexibility, so one has to consider systematically a hierarchy of climate models rather than one model that could incorporate all subsystems, processes, and scales of motion (Ghil and Robertson, 2000; Ghil, 2001; Lucarini, 2002; Held, 2005).

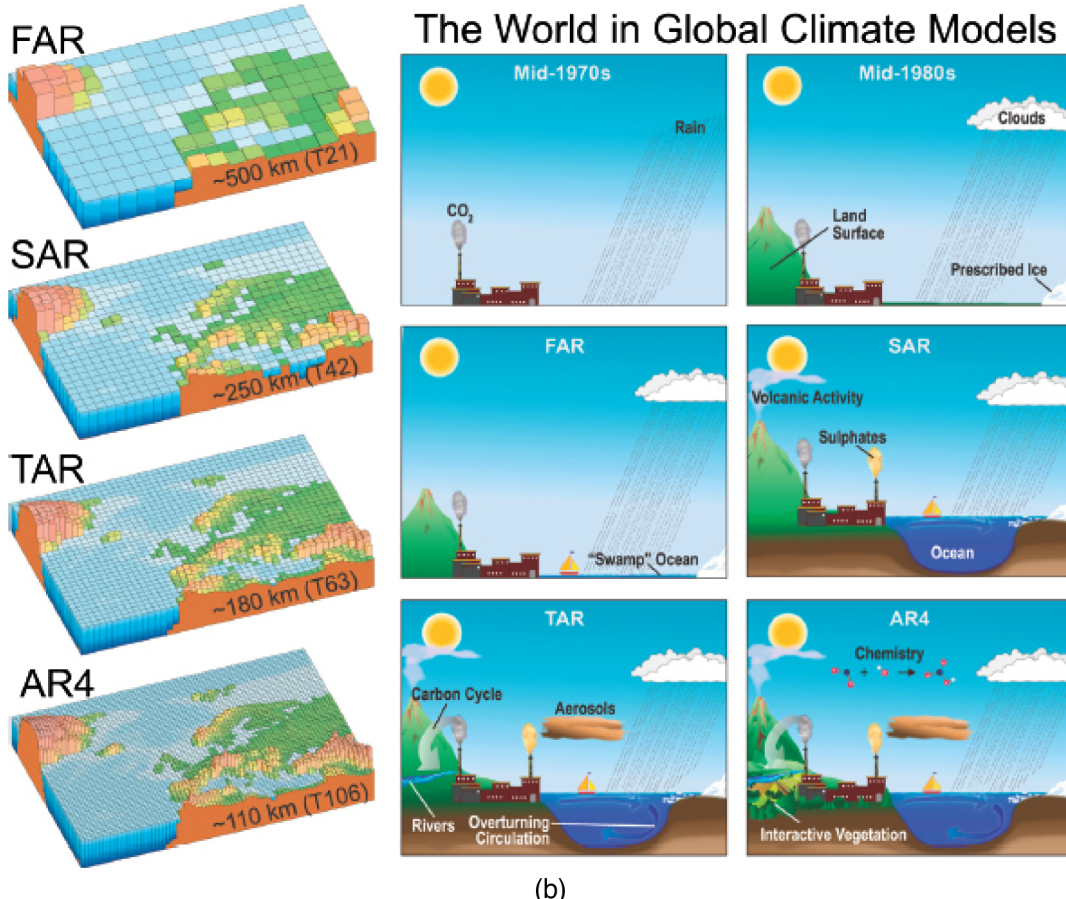
Figure 15(a) shows the so-called Bretherton horrendogram (NAC, 1986), which displays the full range of subsystems one needs to deal with when addressing the Earth system as a whole, along with some of the many interactions among these subsystems. The climate modeling community has slowly caught up with the complexities illustrated by F. Bretherton and his colleagues in this diagram three decades ago.

Models of different levels of complexity and detail are suited for addressing different kinds of questions, according, in particular, to the main spatial and temporal scales of interest. At the top of the hierarchy, one finds global climate models, known in the 1970s and 1980s as general circulation models. The two phrases share the acronym GCM, with the change in name reflecting a change in emphasis from understanding the planetary-scale circulation, first of the atmosphere, then of the ocean, to simulating and predicting the global climate. GCMs aim to represent, at the highest computationally achievable resolution, the largest number of physical, chemical, and biological processes of the Earth system; see Randall (2000) for an early overview.

The atmosphere and ocean, whose modeling relies on the equations discussed in Sec. II.C.1, are still at the core of the Earth system models being developed today. Following improvements in basic scientific knowledge, as well as in



(a)



(b)

FIG. 15. The Earth system, its components, and its modeling. (a) The NAC (1986) horrendogram that illustrates the main components of the Earth system and the interactions among them. (b) Evolution of climate models across the first four IPCC assessment reports, ranging from the early 1990s to the mid-2000s (IPCC, 2007).

computing and data storage capabilities, the latter models include an increasing number of physical, chemical, and biological processes. They also rely on a much higher spatial and temporal resolution of the fields of interest.

Figure 15(b) illustrates the process of model development schematically across the last three decades, from the first to the fourth assessment report: FAR, SAR, TAR, and AR4. The graph does not cover the developments of the last 5–10 yr, which has largely been spent dealing with the inclusion of ecobiological modules and the previously mentioned non-hydrostatic effects. Currently available state-of-the-art models resulted from the cumulative efforts of generations of climate scientists and coding experts, with hundreds of individual researchers contributing to different parts of the code. As in the early stages of post-WWII NWP, climate modeling exercises now are some of the heaviest users of civilian high performance computing.

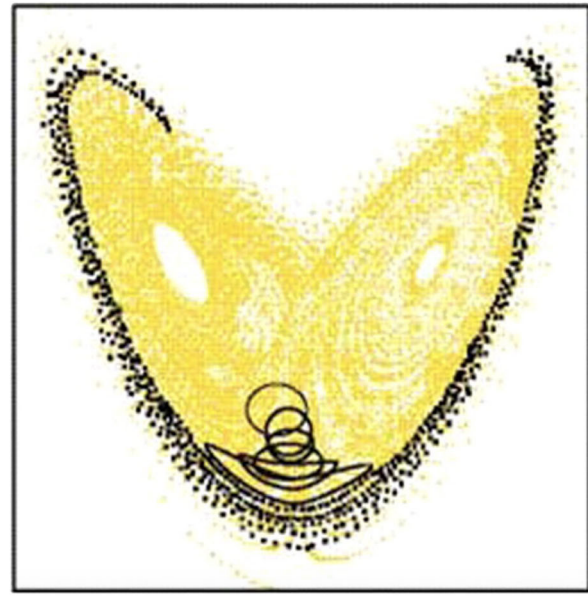
1. Predicting the state of the system

In spite of its remarkable progress, climate modeling and prediction face several kinds of uncertainties: first, uncertainties in predicting the state of the system at a certain lead time given the uncertain knowledge of its state at the present time. Geophysical flows are typically chaotic, as are other processes in the system. Hence, as discussed in Secs. III and IV, the climate system depends sensitively on its initial data, as suggested by Poincaré (1908) and recognized more fully by Lorenz (1963). Following up on terminology introduced by Lorenz (1976), these are *uncertainties of the first kind*, namely, small errors in the initial data that can lead at later times to large errors in the flow pattern.

Assume that two model runs start from nearby initial states. In a nearly linear regime, in which the phase space distance between the system's orbits is small, their divergence rate can be studied by considering the spectrum of Lyapunov exponents and, in particular, the algebraically largest ones. A chaotic system has at least one positive Lyapunov exponent, and physical instabilities that act on distinct spatial and temporal scales are related to distinct positive exponents (Eckmann and Ruelle, 1985). These instabilities can be described by using the formalism of covariant Lyapunov vectors (Ginelli *et al.*, 2007).

Addressing the uncertainties of the first kind and providing good estimates for the future state of the system is the classical goal of NWP. After the initially exponential increase of errors, nonlinear effects kick in and the orbits in the ensemble populate the attractor of the system so that any predictive skill is lost. In such an ensemble, several simulations using the same model are started with slightly perturbed initial states, and the ensemble of orbits produced is used to provide a probabilistic estimate of how the system will actually evolve (Palmer, 2017).

Figure 16(a) illustrates the main phases of error growth from an ensemble of initial states in the Lorenz (1963) model, and Fig. 16(b) outlines how an ensemble forecast system actually works. Obvious limitations are related to the computational difficulties of running a sufficient number of ensemble members to obtain an accurate estimate, as well as with the fact that an initial ellipsoid of states tends to become flattened



(a)

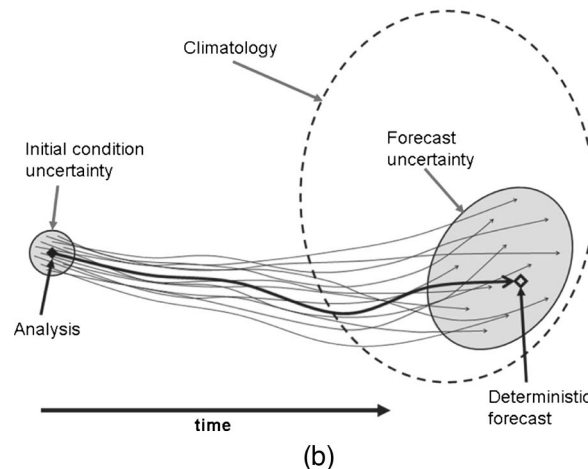


FIG. 16. Schematic diagram of the evolution of an ensemble of initial states in a chaotic system. (a) A small ball of initial states in the Lorenz (1963) model evolves initially in phase space according to the stretching and contracting directions associated with positive and negative Lyapunov exponents, until nonlinear effects become important and the set of initial states propagated by the system's vector field populates its attractor. From Slingo and Palmer, 2011. (b) Evolution in time of such an initial ball in a generic chaotic system. *Deterministic forecast* refers to the prediction obtained using one reference model run, *forecast uncertainty* describes the propagation of an ensemble of initial conditions, and *climatology* refers to the whole attractor of the system. From Swinbank, Friederichs, and Wahl, 2016.

out in time, making the error estimate more laborious. Thus, care has to be exercised in the choice of the initial states, which is done in practice by taking advantage of the reanalyses described in Sec. II.A.1.

Recently similar methods have been used on longer time-scales to perform experimental climate predictions, seen as an initial-value problem (Eade *et al.*, 2014). These predictions were performed on seasonal (Doblas-Reyes *et al.*, 2013) to decadal (Meehl *et al.*, 2014) timescales; they aimed not only

to reach a better understanding of the multiscale dynamics of the climate system but also to help achieve the many potential benefits of skillful medium-term to long-term predictions. One interesting example of such an application is the wind energy market (Torralba *et al.*, 2017).

The World Climate Research Programme (WCRP) has created an encompassing project focusing on the challenges of S2S predictions.¹⁵ We delve more specifically into extended-range forecasting in Sec. III.E.1 and see how its performance depends on a model's ability to capture the natural modes of variability of the climate system on different timescales.

2. Predicting the system's statistical properties

A key goal of climate modeling is to capture the system's statistical properties, i.e., its mean state and its variability, and its response to forcings of a different nature. These problems are treated thoroughly in the next two sections but are rendered quite difficult by a second set of uncertainties. Uncertainties in model formulation, as well as an unavoidably limited knowledge of the external forcings are referred to as *uncertainties of the second kind* (Lorenz, 1967, 1976; Peixoto and Oort, 1992) and intrinsically limit the possibility of providing realistic simulations of the statistical properties of the climate system; in particular, they affect severely the modeling of abrupt climate changes and of the processes that may lead to such changes.

These deficiencies are related to uncertainties in many key parameters of the climate system, as well as to the fact that each model may represent incorrectly certain processes that are relevant on the temporal and spatial scales of interest or that it may miss them altogether. These types of uncertainty are termed parametric and structural uncertainties, respectively (Lucarini, 2013).

A growing number of comprehensive climate models are available to the international scientific community for studying the properties of the climate system and predicting climate change; currently there are about 50 such models (IPCC, 2014a). Still, many of these models have in common a substantial part of their numerical code, as they originate from a relatively small number of models, atmospheric and oceanic, that were originally developed in the 1960s and 1970s. Figure 17 illustrates this family tree for the case of atmospheric GCMs. Hence, there is the widely noted fact that the climate simulations produced by this large number of models often fall into classes that bear marked similarities and do not necessarily resemble to a desired extent the observed climate evolution over the last century or so.

IPCC's evolution over three decades has led to a coordination and restructuring of modeling activities around the world. To improve comparisons among distinct models and the replicability of investigations aimed at climate change, the Program for Climate Model Diagnostics and Intercomparison (PCMDI), through its climate model intercomparison projects (CMIPs), defines standards for the modeling exercises to be performed by research groups that

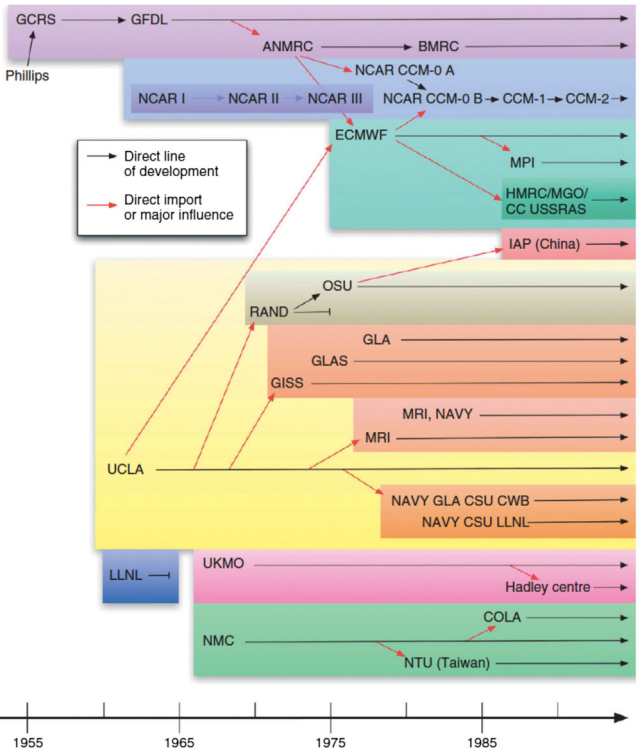


FIG. 17. Family tree of the main atmospheric general circulation models. The tree clearly shows that many of today's state-of-the-art models share a smaller or larger portion of their *genes*, i.e., of the basic ideas and parameter values that went into the coding. From Edwards, 2010.

wish to participate in a given AR and provide projections of future climate change.¹⁶

The PCMDI's CMIPs have also supported a single website that gathers climate model outputs contributing to the IPCC-initiated activities, thereby providing a unique opportunity to evaluate the state-of-the-art capabilities of climate models in simulating the climate system's past, present, and future behavior. A typical IPCC-style package of experiments includes simulating the climate system under various conditions, such as the following:

- A reference state, e.g., a statistically stationary preindustrial state with fixed parameters.
- Industrial era and present-day conditions, including known natural and anthropogenic forcings.
- Future climate projections, performed by using a set of future scenarios of greenhouse gas and aerosol emissions and land-use change with some degree of realism, as well as idealized ones (e.g., instantaneous doubling of CO₂ concentration).

The latter changes of greenhouse gas, aerosol concentrations, and land use follow a prescribed evolution over a given time window, and they are then fixed at a certain value to observe the relaxation of the system to a new stationary state. Each such evolution of the forcing is defined as a "scenario" in

¹⁵See <https://www.wcrp-climate.org/s2s-overview> and Robertson and Vitart (2018).

¹⁶See http://cmip-pcmdi.llnl.gov/cmip5/data_portal.html for CMIP5 and <https://www.wcrp-climate.org/wgcm-cmip/wgcm-cmip6> for CMIP6.

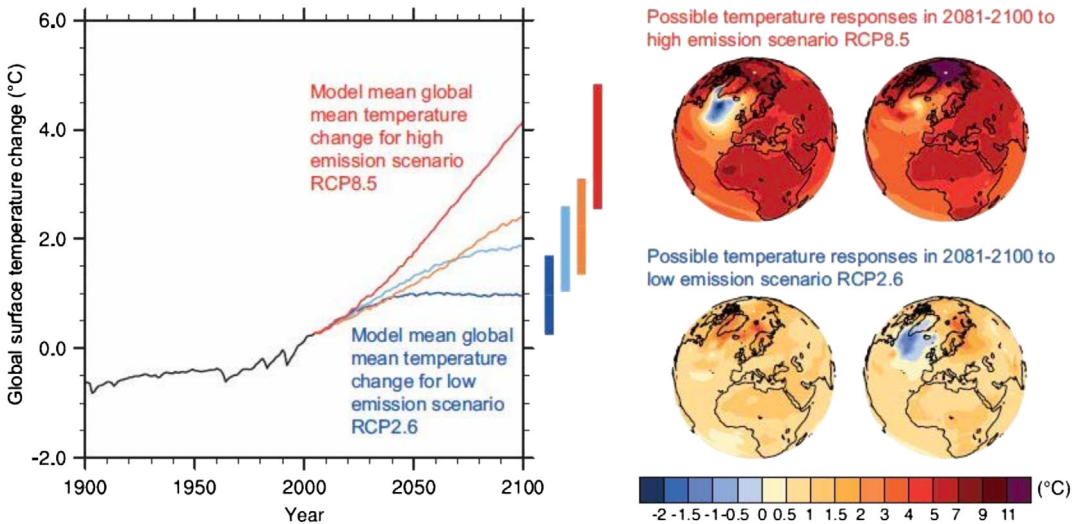


FIG. 18. State-of-the-art climate model outputs for various climate change scenarios. (Left panel) Change in the globally averaged surface temperature as simulated by climate models included in IPCC (2014a). Vertical bands indicate the range of model outputs, and the colors correspond to different representative concentration pathways (RCPs). (Right panel) Spatial patterns of temperature change, i.e., a 2081–2100 average with respect to the present, for the two most extreme RCPs. From IPCC, 2014a.

ARs 1–4 (IPCC, 2001; IPCC, 2007), and as a representative concentration pathway (RCP) in AR5 (IPCC, 2014a). Note that each succeeding AR involved an increasing number of models, people (reaching many hundreds by the latest AR), and hence acronyms.

Each scenario or RCP is a representation of the expected greenhouse gas and aerosol concentrations resulting from a specific path of industrialization and change in land use, as provided by Working Groups II and III to Working Group I; see Fig. 18 for AR5's simulations of the 20th and 21st century with two extreme RCPs. At the same time, the attribution of unusual climatic conditions to specific climate forcing is far from a trivial matter (Allen, 2003; Hannart, Pearl *et al.*, 2016).

In the most recent CMIP exercise CMIP6, the scope of model intercomparisons has grown beyond just testing future climate response to specific forcing scenarios or RCPs. To more comprehensively test the performance of climate models, various standardized intercomparison projects focus on the analysis of specific subsystems, processes, or timescales.¹⁷ Eyring, Bony *et al.* (2016) provide a useful summary of the strategy for PCMDI's CMIP6 project and the scientific questions it addresses.

3. Metrics for model validation

The standardization of climate model outputs promoted by the CMIPs has also helped address a third major uncertainty in climate modeling: what are the best metrics for analyzing a model's outputs and evaluating its skill? Note that in this context the term *metric* does not have its usual mathematical meaning of a distance in function space but refers instead to a statistical estimator of model performance, whether quadratic or not.

The validation, or auditing, i.e., the overall evaluation of the faithfulness, of a set of climate models is a delicate operation

that can be decomposed into two distinct but related procedures. The first one is model intercomparison, which aims to assess the consistency of different models in the simulation of certain physical phenomena in a certain time frame. The second procedure is model verification, whose goal is to compare a model's outputs with corresponding observed or reconstructed scalar quantities or fields (Lucarini, 2008b).

In principle, there are numerous ways to construct a metric by taking any reasonable function of a climate model's variables. Nevertheless, even if several observables are mathematically well defined, their physical relevance and robustness can differ widely. There is no *a priori* valid criterion for selecting a good climatic observable, even though taking basic physical properties of the climate system into account can provide useful guidance.

There is thus no unique recipe for testing climate models, a situation that is in stark contrast with more traditional areas of physics. For instance, in high-energy physics, the variables mass, transition probability, or cross section are suggested by the very equations that one tries to solve or to study experimentally.

In the absence of dissipation and of sources and sinks, certain scalars, such as the atmosphere's or the ocean's total mass, energy, and momentum, are also conserved by the fundamental equations of Sec. II.C.1. Local quantities, like the total rain over India during the summer monsoon or the intensity of the subtropical jet over North America during a given winter month, often matter in evaluating a climate model's skill: current models still have substantial difficulties in simulating the statistics of major regional processes, such as ENSO in the tropical Pacific (Bellenger *et al.*, 2014; Lu *et al.*, 2018), the Indian monsoon (Turner and Annamalai, 2012; Boos and Hurley, 2013; Hasson, Lucarini, and Pascale, 2013), and midlatitude LFV associated with blocking (Davini and D'Andrea, 2016; Woollings *et al.*, 2018).

From the end user's point of view, it is important to check how realistic the modeled fields of practical interest are. But if the aim is to define strategies for the radical improvement of

¹⁷See <https://search.es-doc.org>.

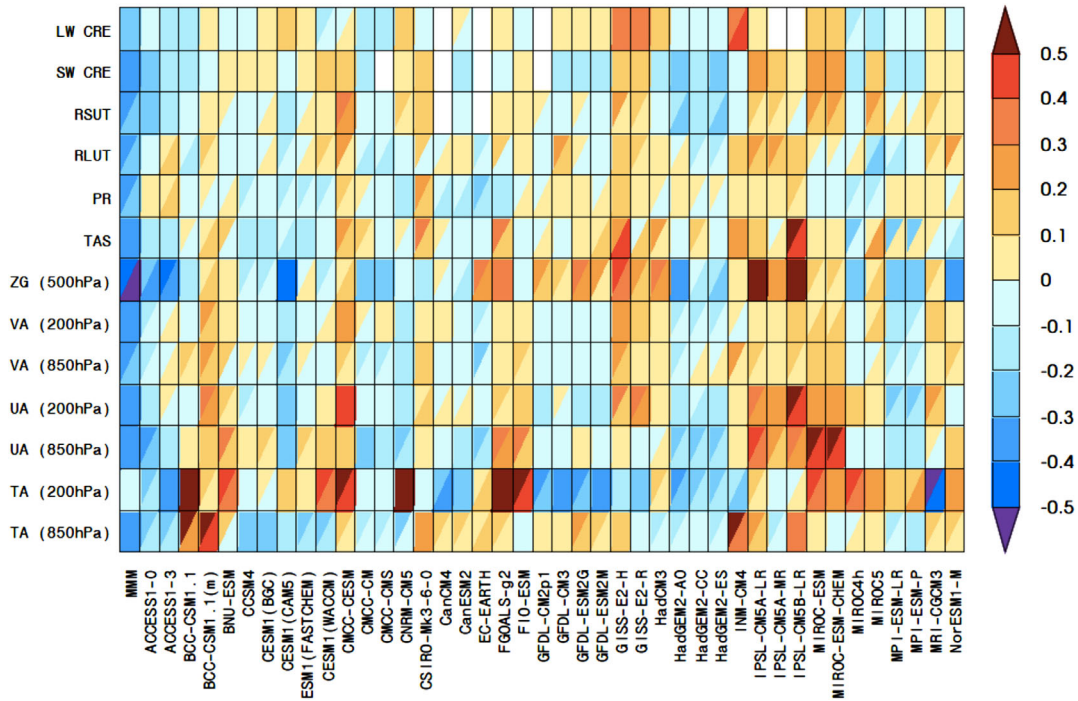


FIG. 19. Example of model performance evaluation. This diagram shows how 42 models participating in the Fifth Climate Model Intercomparison Project (CMIP5) fared in terms of representation of the seasonal cycle during the time interval 1980–2005 for 13 climate variables. Values are normalized, and perfect agreement with the observations is given by 0. See the text for details. From [IPCC, 2014](#).

model performance, beyond incremental advances often obtained at the price of large increases in computer power, it is crucial to fully understand the differences among models in their representation of the climate system, and to decide whether specific physical processes are correctly simulated by a given model.

Additional issues, practical as well as epistemological, emerge when we consider the actual process of comparing theoretical and numerical investigations with observational or reanalysis data. Model results and approximate theories can often be tested only against observational data from a sufficiently long history, which may pose problems for both accuracy and coverage, as mentioned in Sec. II.A.1.

To summarize, difficulties emerge in evaluating climate model performance because (i) we always have to deal with three different kinds of attractors: the attractor of the real climate system, its reconstruction from observations, and the attractors of the climate models, and (ii) because of the high dimensionality of both the phase space and the parameter space of these attractors.

To address these issues, multivariable metrics are currently used to try to assess the skill of available climate models. Figure 19 shows a diagram describing the performance of the 42 models participating in PCMDI’s CMIP5. Even superficial analysis of the diagram indicates that no model is the best for all variables under consideration. An improved assessment package is given by PCMDI’s metrics package ([Gleckler et al., 2016](#)) and the ESMValTool package ([Eyring et al., 2016](#)). Recently [Lembo, Lunkeit, and Lucarini \(2019\)](#) released TheDiato, a flexible diagnostic tool able to evaluate comprehensively the energy, entropy, and water budgets and their transports for climate models. This package will become part of

the second generation of the ESMValTool package ([Eyring et al., 2019](#)).

Finally, to describe the outputs of a growing number of climate models synthetically and comprehensively, it has become common to consider multimodel ensembles and focus attention on the ensemble mean and the ensemble spread. Mean and spread have been taken as the possibly weighted first two moments of the model’s outputs for the metric under study ([Tebaldi and Knutti, 2007](#)); see Fig. 18.

This approach merges information from different attractors, and the resulting statistical estimators cannot be interpreted in the standard way, with the mean approximating the true field and the standard deviation describing its uncertainty. Such a naive interpretation relies on an implicit assumption that the set is a probabilistic ensemble formed by equivalent realizations of a given process, and that the underlying probability distribution is unimodal; see [Parker \(2010\)](#) for a broader epistemological discussion of the issues.

While the models in such an “ensemble of opportunity” may be related to each other, as shown in Fig. 17, they are by no means drawn from the same distribution. A number of alternative approaches for uncertainty quantification in climate modeling have been proposed, but they go beyond the scope of this review.

III. CLIMATE VARIABILITY AND THE MODELING HIERARCHY

A. Radiation balance and energy balance models

The concepts and methods of the theory of deterministic dynamical systems ([Andronov and Pontryagin, 1937](#); [Arnold,](#)

1983; Guckenheimer and Holmes, 1983) were first applied to simple models of atmospheric and oceanic flows, starting about half a century ago (Stommel, 1961; Lorenz, 1963; Veronis, 1963). More powerful computers now allow their application to fairly realistic and detailed models of the atmosphere, the ocean, and the coupled atmosphere-ocean system. We start by presenting such a hierarchy of models.

This presentation is interwoven with that of the successive bifurcations that lead from simple to more complex solution behavior for each climate model. Useful tools for comparing model behavior across the hierarchy and with observations are provided by ergodic theory (Eckmann and Ruelle, 1985; Ghil, Chekroun, and Simonnet, 2008). Among these tools, advanced methods for the analysis and prediction of univariate and multivariate time series play an important role; see Ghil *et al.* (2002) and references therein.

The concept of a modeling hierarchy in climate dynamics was introduced by Schneider and Dickinson (1974). Several other authors have discussed in greater detail the role of such a hierarchy in the understanding and prediction of climate variability (Ghil and Robertson, 2000; Saltzman, 2001; Lucarini, 2002; Dijkstra and Ghil, 2005; Held, 2005). At present, the best-developed hierarchy is for atmospheric models. These models were originally developed for weather simulation and prediction on a timescale of hours to days. Currently they serve, in a stand-alone mode or coupled to oceanic and other models, to address climate variability on all timescales.

The first rung of the modeling hierarchy for the atmosphere is formed by zero-dimensional (0D) models, where the number of dimensions, from 0 to 3, refers to the number of independent space variables used to describe the model domain, i.e., to physical-space dimensions. Such 0D models essentially attempt to follow the evolution of the globally averaged air temperature at surface as a result of changes in global radiative balance:

$$c \frac{d\bar{T}}{dt} = R_i - R_o, \quad (13a)$$

$$R_i = \mu Q_0 \{1 - \alpha(\bar{T})\}, \quad (13b)$$

$$R_o = \sigma m(\bar{T})(\bar{T})^4. \quad (13c)$$

Here R_i and R_o are incoming solar radiation and outgoing terrestrial radiation. The heat capacity c is that of the global atmosphere plus that of the global ocean or some fraction thereof, depending on the timescale of interest: one might only include in c the ocean mixed layer when interested in subannual timescales, but the entire ocean when studying paleoclimate; see, e.g., Saltzman (2001).

The rate of change of \bar{T} with time t is given by $d\bar{T}/dt$, while Q_0 is the solar radiation received at the top of the atmosphere, also called the solar constant, σ is the Stefan-Boltzmann constant, and μ is an insolation parameter equal to unity for present-day conditions. To have a closed, self-consistent model, the planetary reflectivity or albedo α and grayness factor m have to be expressed as functions of \bar{T} ; $m = 1$ for a

perfectly black body and $0 < m < 1$ for a gray body like Earth.

There are two kinds of one-dimensional (1D) atmospheric models, for which the single spatial variable is latitude or height, respectively. The former are so-called energy balance models (EBMs), which consider the generalization of model (13a) for the evolution of surface air temperature $T = T(x, t)$, say,

$$c(x) \frac{\partial T}{\partial t} = R_i - R_o + D. \quad (14)$$

The terms R_i and R_o are similar to those given in Eqs. (13b) and (13c) for the 0D case but can now be functions of the meridional coordinate x , latitude, colatitude, or sine of latitude, as well as of time t and temperature T . The horizontal heat-flux term D describes the convergence of the heat transport across latitude belts; it typically contains first and second partial derivatives of T with respect to x , while $c(x)$ represents the system's space-dependent heat capacity.

Thus, Eq. (14) corresponds physically to a nonlinear heat or reaction-diffusion equation, and mathematically to a nonlinear parabolic PDE. Hence, the rate of change of local temperature T with respect to time also becomes a partial derivative $\partial T(x, t)/\partial t$. Two such models were introduced independently by Budyko (1969) in the then Soviet Union and by Sellers (1969) in the United States.

The first striking results of theoretical climate dynamics were obtained in showing that Eq. (14) could have two stable steady-state solutions, depending on the value of the insolation parameter μ ; see Eq. (13b).¹⁸

This multiplicity of stable steady states, or physically possible stationary climates of our planet, can be explained in its simplest form by the 0D model of Eq. (13). Note that the time derivative of the global temperature \bar{T} in Eq. (13a) can be written as minus the derivative of a potential $V(\bar{T}) = - \int \{R_i(\bar{T}) - R_o(\bar{T})\} d\bar{T}$, viz., $d\bar{T}/dt = -dV(\bar{T})/d\bar{T}$. In the case of bistability, the two local minima of V correspond to the stable solutions, or fixed points, and the local maximum of V corresponds to the unstable solution; see Fig. 20.

The physical explanation lies in the fact that for a fairly broad range of μ values around $\mu = 1.0$ the curves for R_i and R_o as a function of \bar{T} intersect at three points. One of these points corresponds to the present climate (highest \bar{T} value), and another one corresponds to an ice-covered planet (lowest \bar{T} value); both are stable, while the third one, i.e., the intermediate \bar{T} value, is unstable.

To obtain this result, it suffices to make two assumptions: (i) that $\alpha = \alpha(\bar{T})$ in Eq. (13b) is a piecewise-linear function of

¹⁸After the publication of the Budyko (1969) and Sellers (1969) models, it became apparent that massive nuclear explosions could induce a nuclear winter: namely, reducing the incoming solar radiation by a dramatic increase in atmospheric particulate matter could potentially trigger an even greater disaster for life on Earth than nuclear war itself; see, e.g., Turco *et al.* (1983). Studies to this effect were influential in reducing the size of nuclear arsenals at the end of the Cold War. Strikingly, the two contributions came almost simultaneously from scientists belonging to the Cold War's two opposing geopolitical blocks.

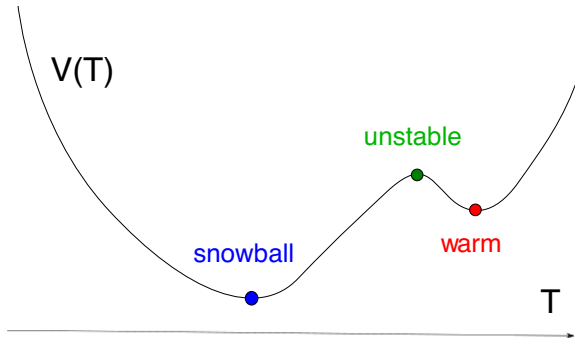


FIG. 20. Scalar double-well potential function $V(T)$. The warm and “deep-freeze” or snowball states correspond to the system’s two stable fixed points, separated by an unstable one.

\bar{T} , or, more generally, a monotonically increasing one with a single inflection point, with high albedo at low temperature due to the presence of snow and ice, and low albedo at high \bar{T} due to their absence; and (ii) that $m = m(\bar{T})$ in Eq. (13c) is a smooth, increasing function of \bar{T} that captures in its simplest form the “greenhouse effect” of trace gases and water vapor.

The EBM modelers (Held and Suarez, 1974; North, 1975; Ghil, 1976) called the ice-covered state a deep freeze. The possibility of such a state in Earth’s history was met with considerable incredulity by much of the climate community for being incompatible with existing paleoclimatic evidence at the time. Geochemical evidence led in the early 1990s to the discovery of a snowball or, at least, slush-ball Earth prior to the emergence of multicellular life, 6×10^8 yr ago (Hoffman *et al.*, 1998; Hoffman and Schrag, 2002). This discovery did not lead, however, to more enthusiasm for the theoretical prediction of such a state almost two decades earlier.

The bifurcation diagram of a 1D EBM, like the one of Eq. (14), is shown in Fig. 21. It displays the model’s mean temperature \bar{T} as a function of the fractional change μ in the insolation $Q_0 = Q_0(x)$ at the top of the atmosphere. The S-shaped curve in the figure arises from two back-to-back saddle-node bifurcations. Bensid and Diaz (2019) recently provided a mathematically rigorous treatment of the bifurcation diagram of a Budyko-type 1D EBM.

The normal form of the first saddle-node bifurcation is

$$\dot{X} = \mu - X^2. \quad (15)$$

Here X stands for a suitably normalized form of \bar{T} and \dot{X} is the rate of change of X , while μ is a parameter that measures the stress on the system, in particular, a normalized form of the insolation parameter in Eq. (13b).

The uppermost branch corresponds to the steady-state solution $X = +\mu^{1/2}$ of Eq. (15), and it is stable. This branch matches Earth’s present-day climate well for $\mu = 1.0$; more precisely the steady-state solution $T = T(x; \mu)$ of the full 1D EBM (not shown) closely matches the annual mean temperature profile from instrumental data over the last century (Ghil, 1976).

The intermediate branch starts out at the left as the second solution $X = -\mu^{1/2}$ of Eq. (15), and it is unstable. It blends smoothly into the upper branch of a coordinate-shifted and mirror-reflected version of Eq. (15), say,

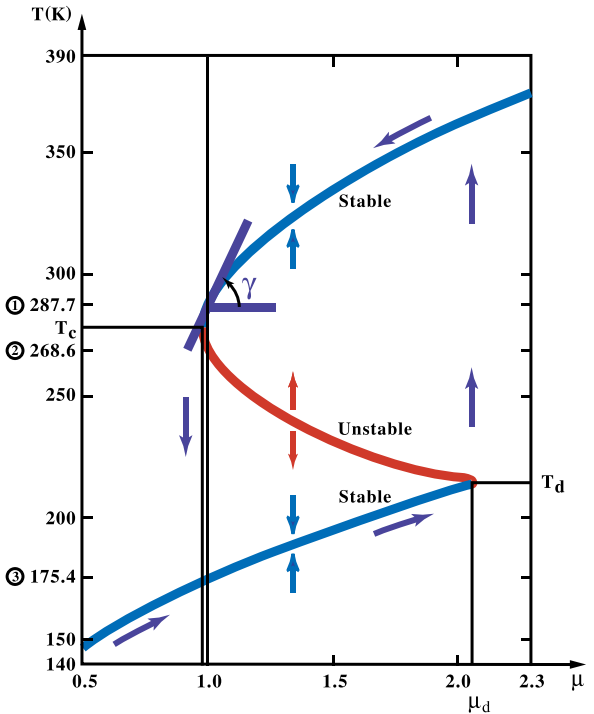


FIG. 21. Bifurcation diagram for the solutions of an energy balance model (EBM), showing the global mean temperature \bar{T} vs the fractional change μ of insolation at the top of the atmosphere. The arrows pointing up and down at about $\mu = 1.4$ indicate the stability of the branches: toward a given branch if it is stable and away from it if it is unstable. The other arrows show the hysteresis cycle that global temperatures would have to undergo for transition from the upper stable branch to the lower one and back. The angle γ gives the measure of the present climate’s sensitivity to changes in insolation. From Ghil and Childress, 1987.

$$\dot{X} = (\mu - \mu_0) + (X - X_0)^2. \quad (16)$$

This branch $X = X_0 + (\mu_0 - \mu)^{1/2}$ is also unstable. Finally, the lowermost branch in Fig. 21 is the second steady-state solution of Eq. (16) $X = X_0 - (\mu_0 - \mu)^{1/2}$, and it is stable like the uppermost branch. The lowermost branch corresponds to an ice-covered planet at the same distance from the Sun as Earth.

The fact that the upper-left bifurcation point (μ_c, T_c) in Fig. 21 is so close to present-day insolation values created great concern in the climate dynamics community in the mid 1970s, when these results were obtained. Indeed, much more detailed computations (discussed later) confirmed that a reduction of about 2%–5% of insolation values would suffice to precipitate Earth into a deep freeze. The great distance of the lower-right bifurcation point (μ_d, T_d) from present-day insolation values, on the other hand, suggests that one would have to nearly double atmospheric opacity, say, for Earth’s climate to jump back to more comfortable temperatures.

These results follow Ghil (1976), Held and Suarez (1974) and North (1975) obtained similar results, and a detailed comparison between EBMs appears in Chapter 10 of Ghil and Childress (1987). Ghil (1976) rigorously, then North *et al.*

(1979) numerically pointed out that a double-well potential, like the one sketched in Fig. 20, does exist for higher-dimensional (North *et al.*, 1979) and even infinite-dimensional (Ghil, 1976) versions of an EBM. In higher-dimensional cases, the maximum of the potential shown in Fig. 20 is replaced by a saddle, or “mountain pass”; see, e.g., Ghil and Childress (1987), Sec. 10.4. In this case, dimensionality refers to phase space rather than physical space; see Sec. V for a more detailed discussion.

B. Other atmospheric processes and models

The 1D atmospheric models in which the details of radiative equilibrium are investigated with respect to a height coordinate z (geometric height, pressure, etc.) are often called radiative-convective models (Ramanathan and Coakley, 1978). This name emphasizes the key role that convection plays in vertical heat transfer. While these models historically preceded EBMs as rungs on the modeling hierarchy, it was only recently shown that they too could exhibit multiple equilibria (Li *et al.*, 1997). The word *equilibrium*, here and in the rest of this review, refers simply to a stationary state of the model rather than a true thermodynamic equilibrium.

Two-dimensional (2D) atmospheric models are also of two kinds, according to the third space coordinate that is not explicitly included. Models that explicitly resolve two horizontal coordinates, on the sphere or on a plane tangent to it, tend to emphasize the study of the dynamics of large-scale atmospheric motions. They often have a single layer or two. Those that explicitly resolve a meridional coordinate and height are essentially combinations of EBMs and radiative-convective models and emphasize therewith the thermodynamic state of the system rather than its dynamics.

Yet another class of “horizontal” 2D models is the extension of EBMs to resolve zonal as well as meridional surface features, in particular, land-sea contrasts. We see in Sec. III.C.2 how such a 2D EBM is used when coupled to an oceanic model.

Schneider and Dickinson (1974) and Ghil and Robertson (2000) discussed additional types of 1D and 2D atmospheric models, along with some of their main applications. Finally, to encompass and resolve the main atmospheric phenomena with respect to all three spatial coordinates, as discussed in Sec. II.D, GCMs occupy the pinnacle of the modeling hierarchy; see, e.g., Randall (2000).

The mean zonal temperature’s dependence on the insolation parameter μ , as obtained for 1D EBMs and shown in Fig. 21, was confirmed to the extent possible by using a simplified GCM coupled to a “swamp” ocean model (Wetherald and Manabe, 1975). More precisely, forward integrations with a GCM cannot confirm the presence of the intermediate, unstable branch. Nor was it possible in the mid 1970s, when this numerical experiment was carried out, to reach the deep-freeze stable branch, as it was called at the time, because of the GCM’s computational limitations.

Still, the normal form of the saddle-node bifurcation, given by Eq. (15), suggests a parabolic shape of the upper, present-day-like branch near the upper-left bifurcation point in our figure, namely, (μ_c, T_c) . This parabolic shape is characteristic of the dependence of a variable that represents the model solution on a parameter that represents the intensity of the

forcing in several types of bifurcations; moreover, this shape is not limited to the bifurcation’s normal form, like Eqs. (15) and (16), but instead is much more general. The GCM simulations support quite well a similar shape for the globally averaged temperature profiles of the GCM’s five vertical layers; see Wetherald and Manabe (1975), Fig. 5. See the discussion in Secs. IV.E.5 and V.

Ghil and Robertson (2000) also described the separate hierarchies that have grown over the last quarter century in modeling the ocean and the coupled ocean-atmosphere system. More recently an overarching hierarchy of Earth system models that encompass all subsystems of interest (atmosphere, biosphere, cryosphere, hydrosphere, and lithosphere) has been developing. Eventually, the partial results about each subsystem’s variability, outlined in this section and Sec. 4, will have to be verified from one rung to the next of the full Earth system modeling hierarchy.

C. Oscillations in the ocean’s thermohaline circulation

1. Theory and simple models

Historically, the thermohaline circulation (THC) [see, e.g., Dijkstra and Ghil (2005) and Kuhlbrodt *et al.* (2007)] was first among the climate system’s major processes to be studied using a simple mathematical model. Stommel (1961) formulated a two-box model and showed that it possesses multiple equilibria.

A sketch of the Atlantic Ocean’s THC and its interactions with the atmosphere and cryosphere on long timescales is shown in Fig. 22. These interactions can lead to climate oscillations with multimillennial periods, such as the Heinrich events [see, e.g., Ghil (1994) and references therein], and are summarized in the figure’s caption. An equally schematic view of the global THC is provided by the widely known “conveyor-belt” (Broecker, 1991) diagram. The latter diagram captures greater horizontal, 2D detail, but it does not commonly include the THC’s interactions with water in both its gaseous and solid phases, which Fig. 22 does include.

Basically, the THC is due to denser water sinking, lighter water rising, and water mass continuity closing the circuit through near-horizontal flow between the areas of rising and sinking effects of temperature T and salinity S on the ocean water’s density $\rho = \rho(T, S)$ oppose each other: the density ρ decreases as T increases, and it increases as S increases. It is these two effects that give the *thermohaline* circulation its name, from the Greek words for T and S . In high latitudes, ρ increases as the water loses heat to the air above and, if sea ice is formed, as the water underneath is enriched in brine. At low latitudes, ρ increases due to evaporation but decreases due to sensible heat flux into the ocean.

For the present climate, the temperature effect is stronger than the salinity effect, and ocean water is observed to sink in certain areas of the high-latitude North Atlantic and Southern Ocean, with limited areas of deep-water formation elsewhere, and to rise everywhere else. Thus, in a thermohaline regime T is more important than S and hence comes before it.

During certain remote geological times, deep water may have formed in the global ocean near the equator; such an overturning circulation of opposite sign to that prevailing

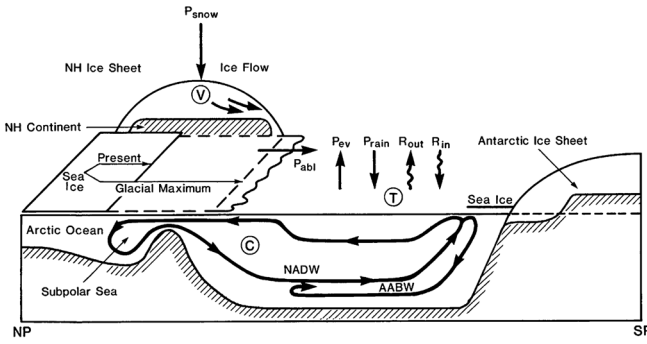


FIG. 22. Schematic diagram of an Atlantic meridional cross section from North Pole (NP) to South Pole (SP) showing mechanisms likely to affect the thermohaline circulation (THC) on various timescales. Changes in the radiation balance $R_{in} - R_{out}$ are due, at least in part, to changes in extent of Northern Hemisphere (NH) snow and ice cover V , and to how these changes affect the global temperature T ; the extent of Southern Hemisphere ice is assumed to be constant to a first approximation. The change in hydrologic cycle expressed in the terms $P_{rain} - P_{evap}$ for the ocean and $P_{snow} - P_{abl}$ for the snow and ice is due to changes in ocean temperature. Deep-water formation in the North Atlantic subpolar sea (North Atlantic deep water, NADW) is affected by changes in ice volume and extent and regulates the intensity C of the THC; changes in Antarctic bottom water (AABW) formation are neglected in this approximation. The THC intensity C in turn affects the system's temperature and is also affected by it. From Ghil, Mulhaupt, and Peltiaux, 1987.

today was named *halothermal*, S before T . The quantification of the relative effects of T and S on the oceanic water mass's buoyancy at high and low latitudes is far from complete, especially for paleocirculations; the association of the latter with salinity effects that exceed the thermal ones [e.g., during the Palaeocene, $\approx 5.7 \times 10^7$ yr ago; see Kennett and Stott (1991)] is thus rather tentative.

To study the reversal of the abyssal circulation due to the opposite effects of T and S , Stommel (1961) considered a model with two pipes connecting two boxes. He showed that the system of two nonlinear, coupled ordinary differential equations that govern the temperature and salinity differences between the two well-mixed boxes has two stable steady-state solutions; these two steady states are distinguished by the direction of flow in the upper and the lower pipe.

Stommel was primarily concerned with distinct local convection regimes, and hence vertical stratifications, in the North Atlantic and the Mediterranean or the Red Sea, say. Today we mainly think of one box as representing the low latitudes and the other one the high latitudes in the global THC; see Marotzke (2000) and references therein. Subsequently, many other THC models that used more complex box-and-pipe geometries have been proposed and studied; see, e.g., Rooth (1982), Scott, Marotzke, and Stone (1999), Titz *et al.* (2002), and Lucarini and Stone (2005).

The next step in the hierarchical modeling of the THC is that of 2D meridional-plane models, in which the temperature and salinity fields are governed by coupled nonlinear PDEs with two independent space variables, say, latitude and depth; see, e.g., Cessi and Young (1992), Quon and Ghil (1992), and

Lucarini, Calmant, and Artale (2005, 2007). Given boundary conditions for such a model that are symmetric about the Equator, like the equations themselves, one expects a symmetric solution, in which water either sinks near the poles and rises everywhere else (thermohaline) or sinks near the Equator and rises everywhere else (halothermal). These two symmetric solutions correspond to the two equilibria of the Stommel (1961) two-box model; see Thual and McWilliams (1992) for a discussion of the relationship between 2D and box models.

In fact, symmetry breaking can occur, leading gradually from a symmetric two-cell circulation to an antisymmetric one-cell circulation. In between, all degrees of dominance of one cell over the other are possible. A situation lying somewhere between the two seems to resemble most closely the meridional overturning diagram of the Atlantic Ocean in Fig. 22.

The gradual transition is illustrated by Fig. 23, and it can be described by a *pitchfork bifurcation*; see Dijkstra and Ghil (2005):

$$\dot{X} = f(X; \mu) = \mu X - X^3. \quad (17)$$

Here X measures how asymmetric the solution is, so $X = 0$ is the symmetric branch, and μ measures the stress on the system, in particular, a normalized form of the buoyancy flux at the surface. For $\mu < 0$ the symmetric branch is stable, while for $\mu > 0$ the two branches $X = \pm\mu^{1/2}$ inherit its stability.

In the 2D THC problem, the left cell dominates on one of the two branches, while the right cell dominates on the other: for a given value of μ , the two stable steady-state solutions, on the $\{X = +\mu^{1/2}\}$ branch and the $\{X = -\mu^{1/2}\}$ branch, respectively, are mirror images of each other. The idealized THC in Fig. 22, with the North Atlantic deep water extending to the Southern Ocean's polar front, corresponds to one of these two branches. In theory, therefore, a mirror-image circulation, with the Antarctic bottom water extending to the North Atlantic's polar front, is equally possible.

A complementary point of view to the one taken thus far suggests that surface winds and tides play a major role in the driving and maintenance of the large-scale ocean circulation (Wunsch, 2002, 2013). In particular, Cessi (2019) argued that the meridional overturning is actually powered by momentum fluxes and not buoyancy fluxes. Because of the ongoing arguments on this topic, the THC is increasingly termed the meridional overturning circulation (MOC).

2. Bifurcation diagrams for GCMs

Bryan (1986) was the first to document transition from a two-cell to a one-cell circulation in a simplified ocean GCM with idealized, symmetric forcing. In Sec. III.B, atmospheric GCMs essentially confirmed the EBM results. Results of coupled ocean-atmosphere GCMs, however, have led to questions about whether the presence of more than one stable THC equilibrium is actually realistic. The situation with respect to the THC's pitchfork bifurcation (17) is thus subtler than it was with respect to Fig. 21 for radiative equilibria.

Dijkstra (2007) showed, however, by comparing observational and reanalysis data with high-end ocean GCMs that the Atlantic Ocean's current THC is actually in its multiple-equilibrium regime. Climate models of intermediate complexity

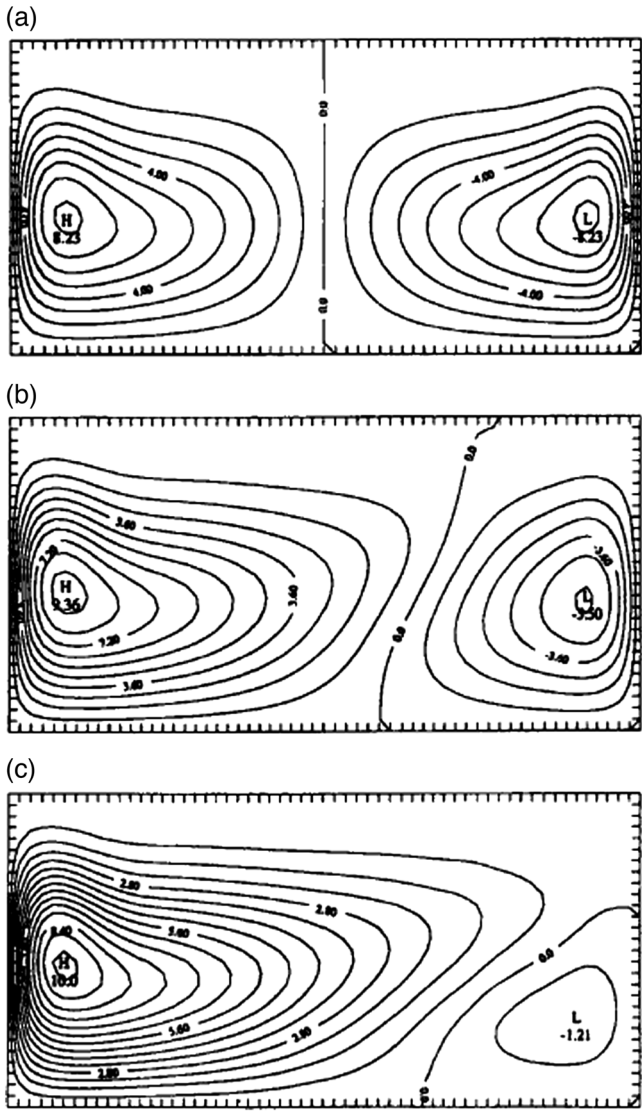


FIG. 23. Transition from a symmetric to an increasingly asymmetric meridional ocean circulation. The stream function plots represent results from an idealized 2D model of thermo-solutal convection in a rectangular domain for a prescribed value of the Rayleigh number and increasing values of the nondimensional intensity γ of the salinity flux at the surface. (a) $\gamma = 0.40$. (b) $\gamma = 0.50$. (c) $\gamma = 0.55$. From Quon and Ghil, 1992.

did indeed find the Atlantic Ocean to be multistable [see, e.g., Rahmstorf *et al.* (2005)], while several of the GCMs used in recent IPCC ARs did not show such a behavior, with an exception coming in the study by Hawkins *et al.* (2011); see Fig. 24. Thus, a failure of high-end models in the hierarchy to confirm results obtained on the hierarchy's lower rungs does not necessarily imply that it is the simpler models that are wrong. To the contrary, such a failure might well indicate that the high-end models, no matter how detailed, may still be rather imperfect; see Ghil (2015) for a summary.

Internal variability of the THC, with smaller and more regular excursions than the large and totally irregular jumps associated with bistability, was studied intensively in the late 1980s and the 1990s. These studies placed themselves on various rungs of the modeling hierarchy, from box models

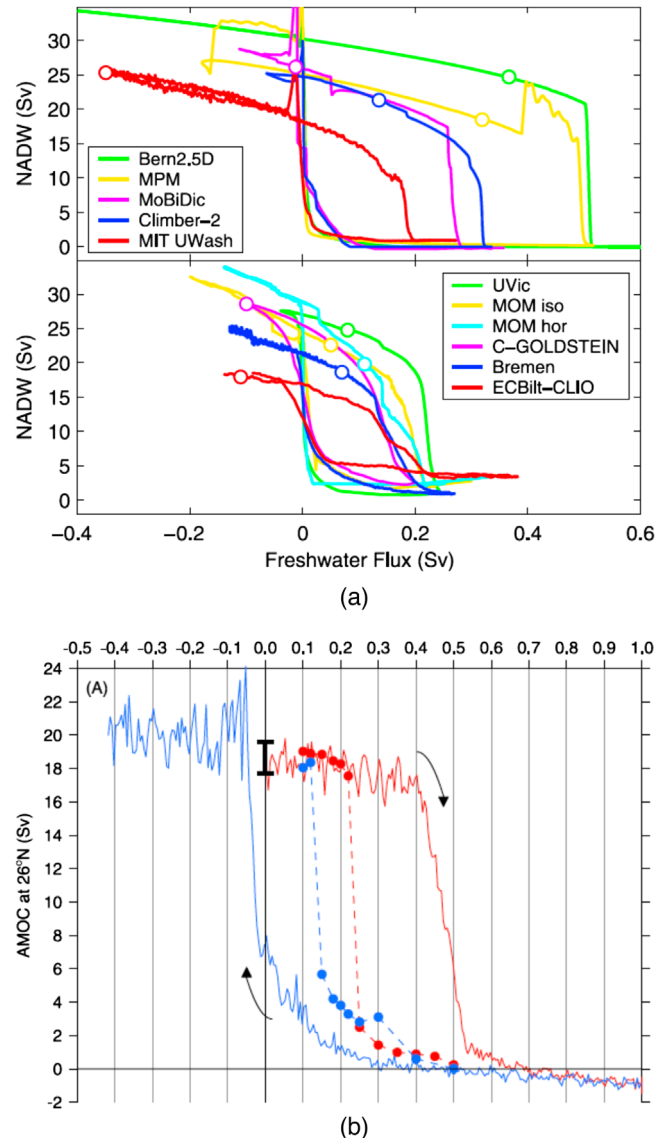


FIG. 24. Multistability of the THC for (a) Earth models of intermediate complexity, and (b) an IPCC-class climate model. Parameter controlling the freshwater input in the North Atlantic basin on the abscissa and the THC's intensity on the ordinate. (a) From Rahmstorf *et al.*, 2005. (b) From Hawkins *et al.* (2011).

through 2D models and all the way to ocean GCMs. A summary of the different kinds of oscillatory variability found in the latter appears in Table I. Such oscillatory behavior seems to more closely match the instrumentally recorded THC variability, as well as the paleoclimatic records for the recent geological past, than bistability.

The (multi)millennial oscillations interact with variability in the surface features and processes shown in Fig. 22. Chen and Ghil (1996), in particular, studied some of the interactions between atmospheric processes and the THC. They used a so-called hybrid coupled model, namely, a 2D EBM, coupled to a rectangular-box version of the North Atlantic rendered by a low-resolution ocean GCM. This hybrid model's regime diagram is shown in Fig. 25(a). A steady state is stable for higher values of the coupling parameter λ_{ao} or of the EBM's

TABLE I. Oscillations in the ocean's thermohaline circulation. Anomalies are defined as the difference between the monthly mean value of a variable and its climatological mean. See also Ghil (1994).

| Timescale | Phenomena | Mechanism |
|------------|---|---|
| Decadal | Local migration of surface anomalies in the northwest corner of the ocean basin Gyre advection in midlatitudes | Localized surface density anomalies due to surface coupling Gyre advection |
| Centennial | Loop-type, meridional circulation | Conveyor-belt advection of density anomalies |
| Millennial | Relaxation oscillation, with "flushes" and superimposed decadal fluctuations | Bottom water warming due to the strong braking effect of salinity forcing |

diffusion parameter d . Interdecadal oscillations with a period of 40–50 yr are self-sustained and stable for lower values of these parameters.

The self-sustained THC oscillations in question are characterized by a pair of vortices of opposite sign that grow and decay in quadrature with each other in the ocean's upper layers. Their centers follow each other counterclockwise through the northwestern quadrant of the model's rectangular domain. Both the period and the spatiotemporal characteristics of the oscillation are thus rather similar to those seen in a fully coupled GCM with realistic geometry (Delworth, Manabe, and Stouffer, 1993). The transition from a stable equilibrium to a stable limit cycle via *Hopf bifurcation* in this hybrid coupled model is shown in Fig. 25(b), and we elaborate upon it in Sec. III.D.2.

D. Bistability, oscillations, and bifurcations

In Secs. III.A, III.B, and III.C.1 we introduced bistability of steady-state solutions via saddle-node and pitchfork bifurcations, while in Sec. III.C.2 we mentioned oscillatory solutions

and Hopf bifurcation as the typical way the latter are reached as a model parameter changes. We start here by summarizing the bifurcations of steady-state solutions, often referred to as equilibria, and then introduce and discuss the normal forms of Hopf bifurcation, both supercritical and subcritical.

1. Bistability and steady-state bifurcations

Section III.B introduced EBMs and explained how the present climate and a totally ice-covered Earth could result as coexisting stable steady states over a certain parameter range. The normal forms of a *supercritical* and a *subcritical* saddle-node bifurcation were given as Eqs. (15) and (16), respectively. Here the criticality is defined as the existence of the two equilibria, stable and unstable, to the right or the left of the *critical* or bifurcation point.

An S-shaped bifurcation curve, such as the one that appears in Fig. 21 for the 1D EBM of Eq. (14), can be obtained easily by soldering smoothly together the back-to-back saddle-node bifurcations of Eqs. (15) and (16). While there is no generic normal form for such a curve, the following is a simple example:

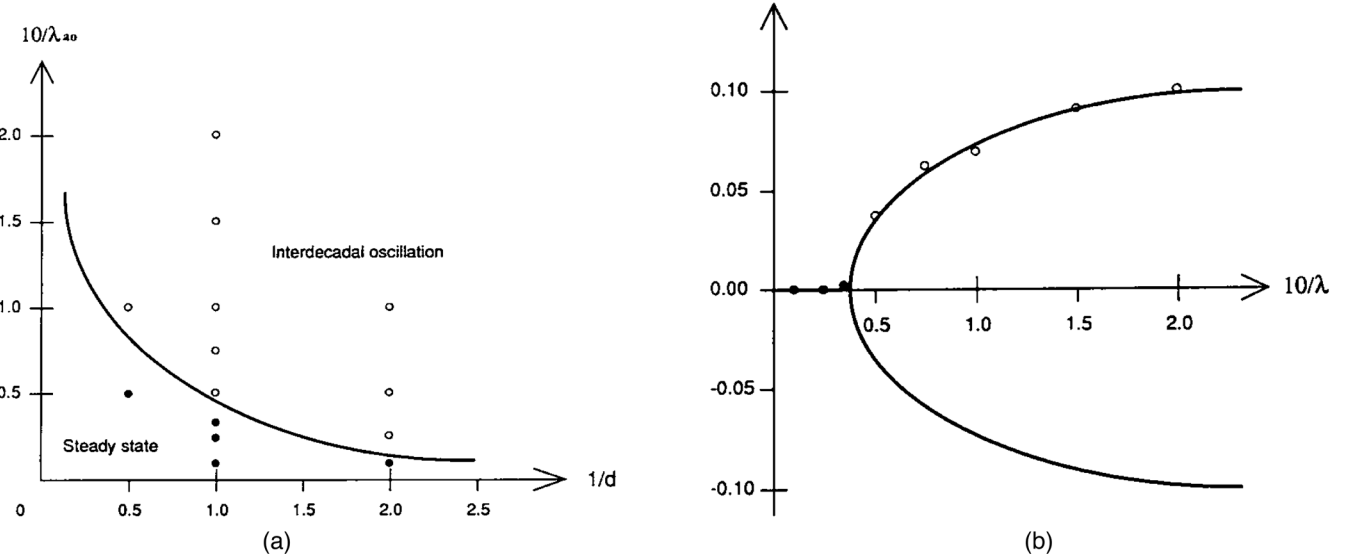


FIG. 25. Dependence of THC solutions on two parameters in a hybrid coupled model; the two parameters are the atmosphere-ocean coupling coefficient λ_{ao} and the atmospheric thermal diffusion coefficient d . (a) Schematic regime diagram. The solid circles stand for the model's stable steady states, the open circles stand for stable limit cycles, and the solid curve is the estimated neutral stability curve between the former and the latter. (b) Hopf bifurcation curve at fixed $d = 1.0$ and varying λ_{ao} ; this curve is obtained by fitting a parabola to the model's numerical-simulation results, shown as filled and open circles. From Chen and Ghil, 1996.

$$\dot{X} = \mu - X^2, \quad (18a)$$

$$\dot{X} = (\mu - \mu_0) + (X - X_0)^2, \quad (18b)$$

with $\mu_0 = 1$ and $X_0 = -1/2$.

Note that both the subcritical and supercritical saddle-node bifurcations are *structurally stable*, i.e., they persist as the system of evolution equations, whether a system of ordinary or partial differential equations, is smoothly perturbed (Andronov and Pontryagin, 1937; Guckenheimer and Holmes, 1983; Temam, 1997; Arnold, 2003) by a small amount. This robustness is the reason why saddle-node bifurcations, and other elementary bifurcations referred to as *codimension 1*, i.e., depending on a single parameter, like the Hopf bifurcation, are so important and can, in practice, be a guide through the hierarchy of models, in the climate sciences and elsewhere. A striking example was provided in Sec. III.B for the supercritical saddle-node bifurcation that can be found in the 3D GCM of Wetherald and Manabe (1975) (Fig. 5 therein), as well as the 1D EBM reproduced in Fig. 21.

The next kind of bifurcation that leads to bistability of stationary states is the pitchfork bifurcation introduced in Sec. III.C.1 in connection with the THC, and whose normal form is given by Eq. (17). This bifurcation, however, arises only in the presence of a mirror symmetry in the model under study, as seen in Fig. (23a). One suspects, therefore, that it is not structurally stable with respect to perturbations of the dynamics that do not preserve this symmetry.

A simple example is given by the following perturbed pitchfork bifurcation:

$$\dot{X} = f(X; \mu, \epsilon) = X(\mu - X^2) + \epsilon, \quad (19)$$

where ϵ is a small parameter. The bifurcation diagrams for $\epsilon = 0$ and $+0.1$ are given in Figs. 26(a) and 26(b), respectively. A nonzero value of ϵ breaks the $X \rightarrow -X$ symmetry of Eq. (17) since it is no longer the case that $f(X) = f(-X)$. Hence, the pitchfork breaks up into a continuous uppermost branch that is stable for all X values, and a supercritical saddle-node bifurcation whose lower branch is stable. If $\epsilon < 0$, it will be the lowermost branch that is stable for all X values (not shown), and the upper branch of the saddle-node bifurcation above it that is stable. In both cases, above a critical value associated with the saddle-node bifurcation three solution branches exist, with the middle one that is unstable and the other two that are stable.

One way that the symmetric pitchfork bifurcation present in 2D models of the THC can be broken, as illustrated in Fig. 26, is simply by considering 3D models with zonally asymmetric basin boundaries. Perturbed pitchfork bifurcations were also found in shallow-water models of the wind-driven ocean circulation; see, e.g., Jiang, Jin, and Ghil (1995), Speich, Dijkstra, and Ghil (1995b), and Ghil (2017).

2. Oscillatory instabilities and Hopf bifurcations

In spite of the considerable detail and 3D character of the ocean GCM involved in the hybrid coupled model of Chen and Ghil (1996), it is clear that the numerically obtained bifurcation diagram in Fig. 25(b) is of a simple,

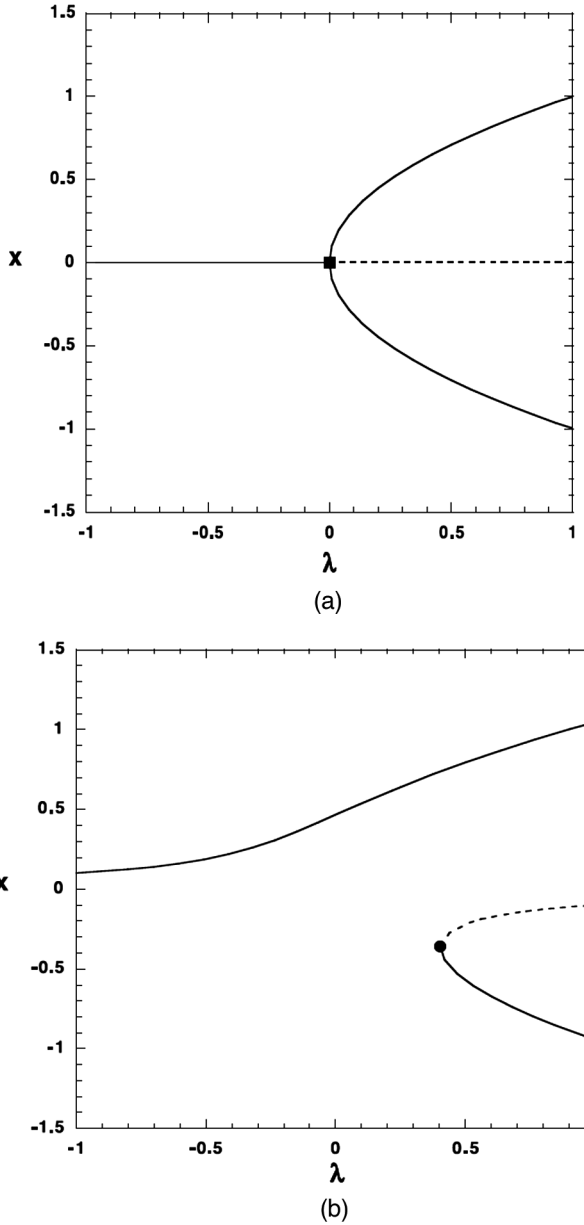


FIG. 26. Bifurcation diagram of the pitchfork bifurcation in Eq. (19) (a) for $\epsilon = 0$, and (b) for $\epsilon = 0.1$. Solid lines indicate stable solutions, and dashed lines indicate unstable ones. From Dijkstra and Ghil, 2005.

fundamental type. The normal form of such a Hopf bifurcation is given by

$$\dot{z} = (\mu + i\omega)z + c(z\bar{z})z, \quad (20)$$

where $z = x + iy$ is a complex variable, while c and ω are non-negative and μ is a real parameter. For small z , Eq. (20) describes a rotation in the complex plane with an increasing radius $|z|$ when $\mu > 0$, i.e., it contains the possibility of an oscillatory instability, while the cubic term corresponds to an increasing modification of this simple rotation away from the origin.

The previous parsimonious complex notation follows Arnold (1983) and Ghil and Childress (1987) and is more

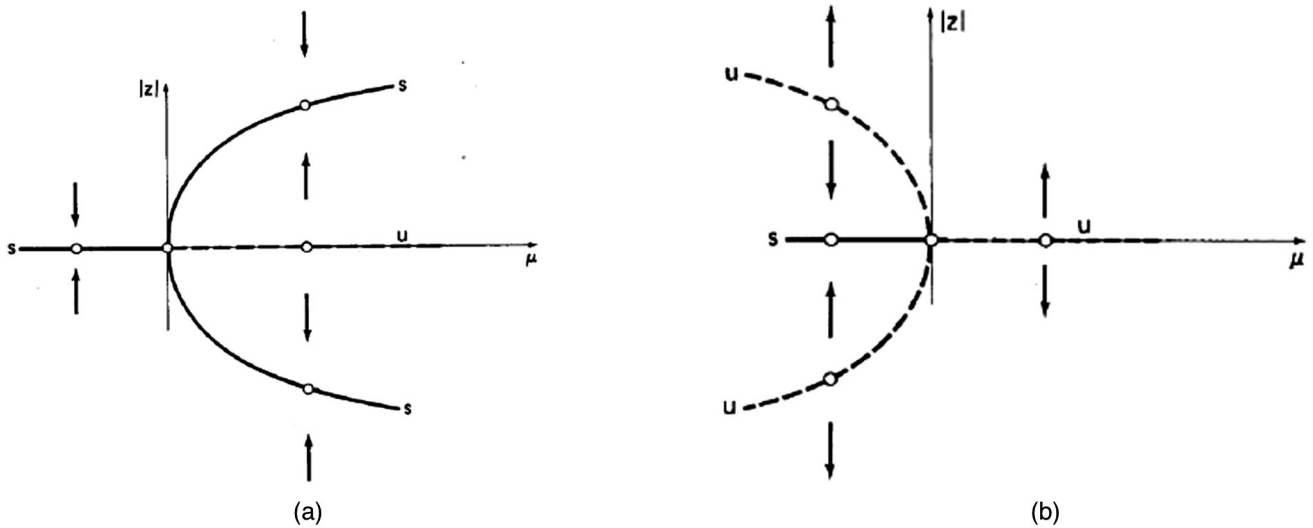


FIG. 27. Bifurcation diagram of the Hopf bifurcation in Eq. (20). (a) Supercritical Hopf bifurcation for $c = -1$. (b) Subcritical Hopf bifurcation for $c = +1$. Solid lines indicate stable solutions (s), and dashed lines indicate unstable ones (u); it is common to plot $|z| = -\mu^{1/2}$ along with $|z| = \mu^{1/2}$ to emphasize that one is actually projecting onto the $(|z|, \mu)$ plane a paraboloid-shaped, one-parameter family of limit cycles with given $r = |z| = \mu^{1/2}$ and $0 \leq \theta < 2\pi$. From Ghil and Childress, 1987.

suggestive and transparent than the more common one that separately uses the two real variables x and y ; see, e.g., Guckenheimer and Holmes (1983). The advantages of the former are apparent when introducing polar variables via $z = \rho^{1/2}e^{i\theta}$, with $\rho = z\bar{z} \geq 0$. One can then separate the flow induced by Eq. (20) into a constant rotation with angular velocity ω and a radius $r = \rho^{1/2}$ that either increases or decreases as $\dot{\rho} \gtrless 0$ according to

$$\dot{\rho} = 2\rho(\mu + c\rho), \quad (21a)$$

$$\dot{\theta} = \omega. \quad (21b)$$

Equation (21a) is quadratic in ρ and has the two roots $\rho = 0$ and $-\mu/c$. The former corresponds to a fixed point at the origin $z = 0$ in Eq. (20), while the latter exists only when $c\mu < 0$.

We thus anticipate a solution that is a circle with radius $r = (-\mu/c)^{1/2}$ when $c\mu \neq 0$ and the two parameters have opposite signs. The simpler case is that of the nonzero radii given by Eq. (21a) for positive stability parameter μ and negative saturation parameter c : it corresponds to the supercritical Hopf bifurcation sketched in Fig. 27(a). In this case, the stable fixed point at the origin loses its stability as μ changes sign and transmits it to a limit cycle of parabolically increasing radius.

The opposite case of $c > 0$ is plotted in Fig. 27(b): it corresponds to subcritical Hopf bifurcation. Here, in fact, the stability of the fixed point is also lost at $\mu = 0$ but there is no oscillatory solution for $\mu > 0$ at all since the higher-order terms in either Eq. (20) or Eq. (21a) cannot stabilize the linearly unstable oscillatory solution, which spirals out to infinity. It is not just that the parabolas in Figs. 27(a) and 27(b) point in opposite directions, as for the saddle-node bifurcations in Eqs. (18a) and (18b) or Eqs. (15) and (16), but the two figures are topologically distinct.

E. Main modes of variability

The atmosphere, ocean, and the coupled ocean-atmosphere climate system have many modes of variability, as initially discussed in Secs. II.A–II.C. We review here some of the most important ones and comment on the general features of such modes.

1. Modes of variability and extended-range prediction

Several large-scale spatial patterns of atmospheric covariance have been studied, starting in the second half of the 19th century. Lorenz (1967) and Wallace and Gutzler (1981) provided good reviews of the earlier studies. The earliest work tended to emphasize “centers of action,” where the variability is strongest (Teisserenc de Bort, 1881), while more recently, it is so-called teleconnections between such centers of action that have been emphasized. J. Namias (1910–1997) played a key role in developing the interest in such teleconnections by applying systematically the use of their spatiotemporal properties to the development of operational extended-range weather forecasting; see, e.g., Namias (1968).

Returning to the discussion of prediction in Sec. II.D, it is important to recall John Von Neumann’s (1903–1957) important distinction (Von Neumann, 1960) between weather and climate prediction. To wit, short-term NWP is the easiest, i.e., it is a pure initial-value problem. Long-term climate prediction is next easiest, it corresponds to studying the system’s asymptotic behavior, while intermediate-term prediction is hardest: both initial and boundary values are important. Von Neumann’s role in solving the NWP problem by integrating the discretized equations that govern large-scale atmospheric motions (Bjerknes, 1904; Richardson, 1922; Charney, Fjørtoft, and Von Neumann, 1950) is well known. In fact, he also played a key role in convening the conference on the Dynamics of Climate that was held at Princeton’s

Institute for Advanced Studies in October 1955, and whose proceedings (Pfeffer, 1960) were finally published three years after Von Neumann's death.

Today routine NWP is quite skillful for several days, but we also know that detailed prediction of the weather is limited in theory by the exponential growth of small errors (Lorenz, 1963), and by their turbulent cascading from small to large scales (Thompson, 1957; Lorenz, 1969a, 1969b; Leith and Kraichnan, 1972). The theoretical limit of detailed prediction, in the sense of predicting future values of temperature, wind, and precipitation at a certain point, or within a small volume, in time and space, is of the order of 10–15 days (Tribbia and Anthes, 1987; Epstein, 1988).

In the sense of Von Neumann (1960), short-term predictions are being improved by meteorologists and oceanographers through more-and-more-accurate discretizations of the governing equations, increased horizontal and vertical resolution of the numerical models, improved observations and data assimilation methodologies, and improved parametrization of subgrid-scale processes.

Important strides in solving the theoretical problems of the climate system's asymptotic behavior are being taken by the use of idealized models, either by simplifying the governing equations in terms of the number of subsystems and of active physical processes, e.g., by eliminating phase transitions or chemical processes in the atmosphere, or by systematic model reduction to small or intermediate-size sets of ordinary differential or stochastic differential equations; see, e.g., Palmer and Williams (2009) and Chang *et al.* (2015). We return to the latter in Secs. IV and V.

What then, if anything, how, and how accurately can climate-related scalars or fields be predicted beyond the limits of NWP? In other words, what can be done about the gap between short-term and asymptotic prediction of climate? These issues have been actively pursued for the last three decades; see, e.g., Tribbia and Anthes (1987), Epstein (1988), and Ghil and Robertson (2002). Atmospheric, oceanic, and coupled modes of variability play an important role in extended- and long-range forecasting.

The key idea is that a mode that is stationary or oscillatory can, by its persistence or periodicity, contribute a fraction of variance that is predictable for the mode's characteristic time or, at least, for a substantial fraction thereof. We start, therefore, with a review of some of the most promising modes of variability.

2. Coupled atmosphere-ocean modes of variability

The best known of all of these modes is the ENSO [see Philander (1990), Dijkstra (2005), and references therein], mentioned in Sec. II.B. The ENSO phenomenon is particularly strong over the tropical Pacific, but it affects temperatures and precipitations far away and over a large area of the globe. Some of the best documented and statistically most significant ones of these teleconnections are illustrated in Fig. 28. As an example, destructive droughts over northeast Brazil and southeast Africa and cold spells over Florida are often associated with particularly strong warm ENSO episodes.

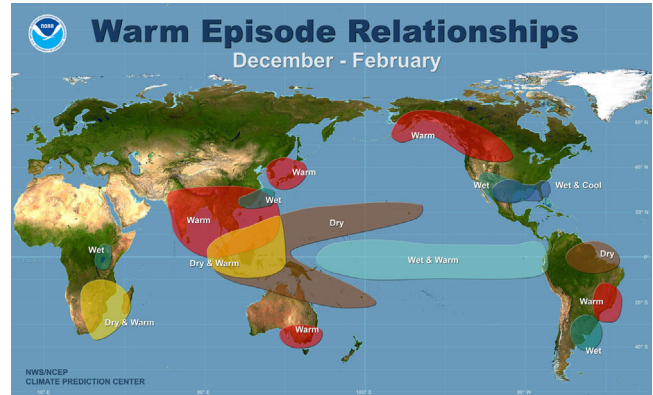


FIG. 28. Teleconnection pattern for a warm ENSO episode, during the boreal winter months December–February. We indicate warm-vs-cold and wet-vs-dry anomalies, with an anomaly being defined as the difference between a monthly mean value of a variable and its climatological mean.¹⁹

Such strong episodes recurred every 2–7 yr during the instrumental record of roughly 150 yr, and the ENSO phenomenon, with its alternation of warm episodes (El Niños) and cold ones (La Niñas), is quite irregular. Still, there is a marked tendency for year-to-year alternation of not necessarily strong El Niños and La Niñas; this alternation is associated with a well-known quasibiennial near periodicity; see, e.g., Rasmusson, Wang, and Ropelewski (1990) and Ghil *et al.* (2002).

An even larger variance, accompanied by lesser regularity, is associated with a quasiquadrennial mode (Jiang, Neelin, and Ghil, 1995; Ghil *et al.*, 2002), sometimes just called the low-frequency ENSO mode. The positive interference of these two modes generates large ENSO events that visually coincide with the instrumentally recorded ones; see Jiang, Neelin, and Ghil (1995), Fig. 9.

These ENSO features have been used since 1992 for real-time forecasting that essentially relies on predicting the oscillatory modes of two scalar indices that capture much of the ENSO variability, namely, the Southern Oscillation Index and the so-called Niño-3 index, obtained by averaging mean-monthly SSTs over an area of the eastern tropical Pacific. For the time being, such a data-driven forecast appears to still be quite competitive with those made by high-end, detailed GCMs (Barnston *et al.*, 2012).

3. Atmospheric low-frequency variability

As discussed in Sec. II.A, datasets for the atmosphere are both longer and more plentiful than for the ocean. Thus, there are quite a few modes of variability that have been detected and described, especially for the Northern Hemisphere, where both the human population and the datasets are denser.

As discussed in Sec. II.B in connection with Fig. 12, atmospheric phenomena are designated as having low, or intraseasonal, frequency if their characteristic time is longer than the life cycle of a midlatitude weather system but still

¹⁹From https://www.met.no/ams/wim_2014/9b.html.

shorter than a season. We are thus discussing here intrinsic variability, as opposed to the externally forced seasonal cycle, with the latter being easier to understand. More recently one is also referring to this variability as *subseasonal*; see, e.g., Robertson and Vitart (2018).

There are essentially two approaches for describing this intrinsic subseasonal variability: (i) episodic or intermittent, and (ii) oscillatory. The two approaches are complementary, as we shall see, and they have been named the *particle* and *wave* descriptions by a crude analogy with quantum mechanics (Ghil and Robertson, 2002); see also Sec. I.A

The key ingredient of the particle approach is provided by so-called persistent anomalies or regimes. The best known among these are blocking and zonal flows, which were mentioned in Sec. II.B. Other well-known persistent features, especially during boreal winter, are the positive and negative phases of the North Atlantic Oscillation (NAO) and the Pacific North American (PNA) pattern. A rich literature exists on the reliable identification, description, and modeling of these patterns; see Ghil *et al.* (2019) and references therein. In the Southern Hemisphere, there has also been some interest in an approximate counterpart of the PNA called the Pacific South American (PSA) pattern (Mo and Ghil, 1987).

The key ingredient of the wave approach is provided by oscillatory modes that do not necessarily possess exact periodicities, but instead the broad spectral peaks that were illustrated in Fig. 12 and discussed to some extent in Sec. II.B. Probably the best known example of this type in the subseasonal band is the Madden-Julian oscillation (MJO) (Madden and Julian, 1971). It has a near periodicity of roughly 50 days and affects winds and precipitation in the Tropics, being strongest in the Indo-Pacific sector. Like the much lower-frequency ENSO phenomenon, important extratropical effects have been documented; see, e.g., Maloney and Hartmann (2000).

In spite of the considerable amount of observational, theoretical, and modeling work dedicated to the MJO, it is still incompletely understood and not well simulated or predicted. Some of the reasons for these difficulties include the key role played in its mechanism by transitions among liquid and gaseous phases of water in tropical clouds, its multiscale character, and the pronounced interactions with the ocean (Zhang, 2005).

Two extratropical modes in the subseasonal band are the Branstator-Kushnir wave (Branstator, 1987; Kushnir, 1987) and the 40-day mode associated with the topographic instability first described by Charney and DeVore (1979) in a low-order model. The Branstator-Kushnir wave is, like the MJO, an eastward-traveling wave, while the 40-day mode is a standing wave anchored by the topography.

Charney and DeVore (1979) emphasized the bimodality of the solutions of a model version with only three Fourier modes, with one stable steady state being zonal and the other being blocked, and did not pursue further the fact that in a more highly resolved version of the model oscillatory solutions did appear. Legras and Ghil (1985), Ghil and Childress (1987), and Jin and Ghil (1990) did clarify the role of the higher meridional modes in the Hopf bifurcation that gives rise to the oscillatory solutions. The potential role of these results in the controversy surrounding the effect of

anthropogenic polar amplification on blocking frequency was mentioned in Sec. II.B.2.

While midlatitude weather systems, like tropical ones, involve precipitation, their large-scale properties seem to be much less affected by wet processes; the former arise essentially from purely dynamical as opposed to largely thermodynamical mechanisms. For simplicity, we thus try to illustrate in further detail the complementarity of the wave and particle approaches for the extratropical topographic oscillation.

Given the recent interest in the physical literature for synchronization in continuous media [see Duane *et al.* (2017) and references therein], it might be a challenging notion for this readership that one can accommodate in a fairly narrow frequency band, between roughly 0.1 and 0.01 day⁻¹, three distinct oscillatory modes that do not seem to synchronize: in the Tropics the MJO, with a period of ≈ 50 days, and in midlatitudes the Branstator-Kushnir wave, with a period of ≈ 30 days, along with the topographic oscillatory mode, with a period of ≈ 40 days; see, for instance, Dickey, Ghil, and Marcus (1991), Fig. 11. Not only are these three frequencies fairly close, i.e., the detuning is fairly small, but the characteristic wavelengths of all three of these oscillatory modes are quite large with respect to the radius of Earth, and several teleconnections mentioned so far extend across continents and oceans; see Fig. 28.

Let us now concentrate on the topographic wave mode and its relationship with the blocking and zonal particles. Ghil *et al.* (2019) reviewed the evidence provided by a hierarchy of models for the presence of a Hopf bifurcation that arises from the interaction of the large-scale westerly flow in midlatitudes with the topography of the Northern Hemisphere.

Certain spatial features of the phases of this mode do present striking similarities to the blocked and zonal flows that appear not just as the two stable equilibria in the highly idealized model of Charney and DeVore (1979) but also as unstable, though long-lived, patterns in much more realistic models, like the three-level quasigeostrophic (QG3) model originally formulated by Marshall and Molteni (1993). The latter model is still widely used to study the nonlinear dynamics of large-scale, midlatitude atmospheric flows; see, e.g., Kondrashov, Ide, and Ghil (2004) and Lucarini and Gritsun (2020).

We summarize here the relevant conclusions of the Ghil *et al.* (2019) review on the observational, theoretical, and modeling literature of multiple regimes and oscillatory modes of subseasonal variability. Four complementary approaches to explaining this variability are illustrated in Fig. 29.

One approach to persistent anomalies in midlatitude atmospheric flows on subseasonal timescales is to consider them simply as due to a slowing down of Rossby waves or their linear interference (Lindzen, 1986). This approach is illustrated in Fig. 29(c): zonal flow Z and blocked flow B are simply slow phases of an harmonic oscillation, like the neighborhood of $t = \pi/2$ or $3\pi/2$ for a sine wave $\sin(t)$; otherwise, they are due to an interference of two or more linear waves, like the one occurring for a sum $A \sin(t) + B \sin(3t)$ near $t = (2k+1)\pi/2$. A more ambitious, quasilinear version

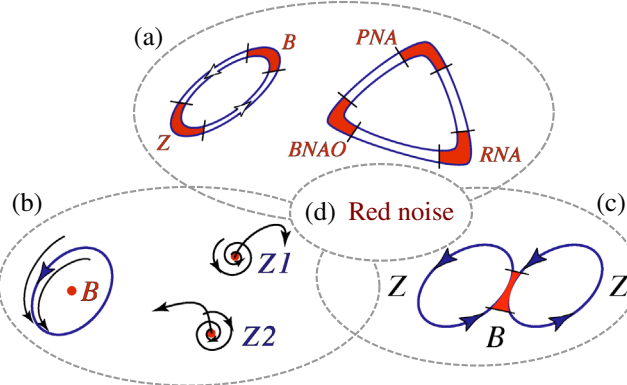


FIG. 29. Schematic overview of atmospheric low-frequency variability (LFV) mechanisms; see the text for details. From [Ghil et al., 2019](#).

of this approach is to study long-lived resonant wave triads between a topographic Rossby wave and two free Rossby waves ([Egger, 1978](#); [Trevisan and Buzzi, 1980](#); [Ghil and Childress, 1987](#)). Neither version of this line of thought, though, explains the organization of the persistent anomalies into distinct flow regimes.

[Rossby \(1939\)](#) initiated a different, genuinely nonlinear approach by suggesting that multiple equilibria may explain preferred atmospheric flow patterns. They drew an analogy between such equilibria and hydraulic jumps, and formulated simple models in which similar transitions between faster and slower atmospheric flows could occur. This multiple-equilibria approach was then pursued vigorously in the 1980s ([Charney and DeVore, 1979](#); [Charney, Shukla, and Mo, 1981](#); [Legras and Ghil, 1985](#); [Ghil and Childress, 1987](#)), and it is illustrated in Fig. 29(a): one version of the sketch illustrates models that concentrated on the *B-Z* dichotomy ([Charney and DeVore, 1979](#); [Charney, Shukla, and Mo, 1981](#); [Benzi et al., 1986](#)), the other on models [see, e.g., [Legras and Ghil \(1985\)](#)] that allowed for the presence of additional clusters, found by [Kimoto and Ghil \(1993a\)](#) and [Smyth, Ide, and Ghil \(1999\)](#) among others in observations. The latter include opposite phases of the NAO and PNA anomalies [PNA, RNA, and BNAO in Fig. 29(a)]. The LFV dynamics in this approach is given by the preferred transition paths between the two or more regimes; see Table 1 in [Ghil et al. \(2019\)](#) and references therein.

A third approach is associated with the idea of oscillatory instabilities of one or more of the multiple fixed points that can play the role of regime centroids. Thus, [Legras and Ghil \(1985\)](#) found a 40-day oscillation arising by Hopf bifurcation off their blocked regime *B*, as illustrated in Fig. 29(b).

An ambiguity arises, though, between this point of view and the complementary possibility that the regimes are just slow phases of such an oscillation, caused itself by the interaction of the midlatitude jet with topography that gives rise to a supercritical Hopf bifurcation. Thus, [Kimoto and Ghil \(1993a, 1993b\)](#) found in their observational data closed paths within a Markov chain whose states resembled well-known phases of an intraseasonal oscillation. Such a possibility was confirmed in the QG3 model by [Kondrashov, Ide, and Ghil \(2004\)](#). Furthermore, multiple regimes and intraseasonal

oscillations can coexist in a two-layer model on the sphere within the scenario of “chaotic itinerary” ([Itoh and Kimoto, 1996, 1997](#)).

[Lucarini and Gritsun \(2020\)](#) observed that blockings occur when the system’s trajectory is in the neighborhood of a specific class of unstable periodic orbits (UPOs). UPOs in general are natural modes of variability that cover a chaotic system’s attractor ([Cvitanović, 1988](#); [Cvitanović and Eckhardt, 1991](#)). Here the UPOs that correspond to blockings have a higher degree of instability than UPOs associated with zonal flow; thus, blockings are associated with anomalously unstable atmospheric states, as suggested theoretically by [Legras and Ghil \(1985\)](#) and confirmed experimentally by [Weeks et al. \(1997\)](#). Different regimes may be associated with different bundles of UPOs, a conjecture that could also explain the efficacy of Markov chains in describing the transitions between qualitatively different regimes.

Figure 29(d) refers to the role of stochastic processes in S2S variability and prediction, whether it be noise that is white in time, as in [Hasselmann \(1976\)](#) or in linear inverse models ([Penland, 1989, 1996](#); [Penland and Ghil, 1993](#); [Penland and Sardeshmukh, 1995](#)), or red in time, as in certain nonlinear data-driven models ([Kravtsov, Kondrashov, and Ghil, 2005, 2009](#); [Kondrashov, Kravtsov, and Ghil, 2006](#); [Kondrashov et al., 2013](#); [Kondrashov, Chekroun, and Ghil, 2015](#)) or even non-Gaussian ones ([Sardeshmukh and Penland, 2015](#)). Stochastic processes may enter into models situated on various rungs of the modeling hierarchy, from the simplest conceptual models to high-resolution GCMs. In the former, they may enter via stochastic forcing, whether additive or multiplicative, Gaussian or not [see, e.g., [Kondrashov, Chekroun, and Ghil \(2015\)](#)], while in the latter they may enter via stochastic parametrizations of subgrid-scale processes; see, e.g., [Palmer and Williams \(2009\)](#) and references therein.

Figure 29 summarizes some of the key dynamical mechanisms of midlatitude subseasonal variability, as discussed in this section and in [Ghil et al. \(2019\)](#), without attempting to provide a definitive answer as to which approach to modeling and prediction of this variability will be the most productive in the near future.

F. Internal variability and routes to chaos

In this section, we illustrate the wind-driven ocean circulation a sequence of successive bifurcations that lead from a highly symmetric, steady-state circulation to much more finely structured, irregular, possibly chaotic oscillations. Various issues arise in pursuing such a bifurcation sequence across a hierarchy of models and on to the observational data.

Midlatitude oceanic gyres appear clearly in Fig. 30 in the four major extratropical ocean basins, namely, the North and South Atlantic and the North and South Pacific. The large subtropical ocean gyres are formed by a poleward-flowing western boundary current, an equatorward-flowing eastern boundary current, and the roughly zonally flowing currents that connect these two coastal currents off the equator and on the poleward basin side, respectively. These gyres are characterized by so-called anticyclonic rotation, clockwise in the Northern Hemisphere and counterclockwise in the Southern Hemisphere. In the North Pacific and the North Atlantic, they

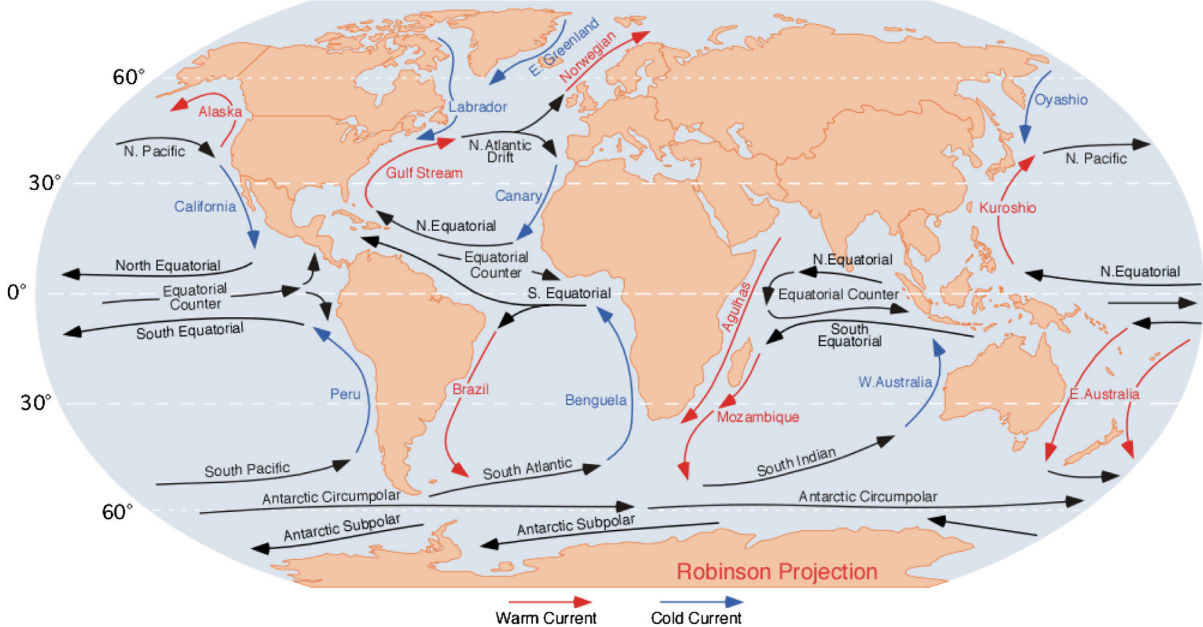


FIG. 30. A map of the main oceanic currents: warm currents in red and cold ones in blue. From Ghil, Chekroun, and Simonnet, 2008.

are accompanied by smaller, cyclonically rotating gyres, while in the Southern Hemisphere such subpolar gyres are missing and replaced by the Antarctic Circumpolar Current (ACC).

The basic phenomenology of these gyres and the detailed physical mechanisms that give rise to it were described in several books [see, e.g., Sverdrup, Johnson, and Fleming (1946), Gill (1982), Ghil and Childress (1987), Pedlosky (1996), Vallis (2006), and Cushman-Roisin and Beckers (2011)] and review papers (Dijkstra and Ghil, 2005; Ghil, 2017). The sharp western boundary currents, like the Gulf Stream in the North Atlantic, the Kuroshio and its cross-basin extension in the North Pacific, and the Brazil Current in the South Atlantic, as well as the more diffuse eastern boundary currents, like the Canaries Current in the North Atlantic and the California and Peru currents in the North and South Pacific, respectively, play a major role in carrying heat poleward and colder waters equatorward. Hence, these gyres' interannual and interdecadal variability is a major contributor to climate variability.

To illustrate the bifurcation sequence that might lead to this oceanic LFV, we use a highly idealized model of the wind-driven double-gyre circulation in a rectangular geometry. Note that the counterparts of synoptic weather systems in the ocean are eddies and meanders that have much shorter spatial scales than in the atmosphere, but considerably longer timescales: $\mathcal{O}(100)$ km in the ocean versus $\mathcal{O}(1000)$ km in the atmosphere, but of the order of several months in time versus of the order of merely several days. Thus, the definition we used for LFV in the atmosphere (see Sec. II.E.3) corresponds in the ocean to a timescale of years to decades.

1. A simple model of the double-gyre circulation

The simplest model that includes several of the most pertinent mechanisms described in Sec. II.B is governed by the barotropic quasigeostrophic equations. We consider an idealized, rectangular basin geometry and simplified forcing

that mimics the distribution of vorticity due to the wind stress sketched by Simonnet, Ghil, and Dijkstra (2005) in their Fig. 2. In this idealized model, the amounts of subpolar and subtropical vorticity injected into the basin are equal and the rectangular domain $\Omega = (0, L_x) \times (0, L_y)$ is symmetric about the axis of zero wind-stress curl $y = L_y/2$.

The barotropic 2D quasigeostrophic equations in this idealized setting are

$$\partial_t q + J(\psi, q) - \nu \Delta^2 \psi + \mu \Delta \psi = -\tau \sin\left(\frac{2\pi y}{L_y}\right), \quad (22a)$$

$$q = \Delta \psi - \lambda_R^{-2} \psi + \beta y. \quad (22b)$$

Here x points east and y points north, while q and ψ are the potential vorticity and the stream function, respectively, and the Jacobian J gives the advection of potential vorticity by the flow, as discussed in Sec. II.C.3, so $J(\psi, q) = \psi_x q_y - \psi_y q_x = \mathbf{u} \cdot \nabla q$.

The physical parameters are the strength of the planetary vorticity gradient $\beta = \partial f / \partial y$, the Rossby radius of deformation λ_R^{-2} , the eddy-viscosity coefficient ν , the bottom friction coefficient μ , and the wind-stress intensity τ . One considers here free-slip boundary conditions $\psi = \Delta^2 \psi = 0$; the qualitative results described later do not depend on the choice of homogeneous boundary condition (Jiang, Jin, and Ghil, 1995; Dijkstra and Ghil, 2005).

The nonlinear system of PDEs (22) is an infinite-dimensional dynamical system, and one can thus study its bifurcations as the parameters change. Two key parameters are the wind-stress intensity τ and the eddy viscosity ν : as τ increases, the solutions become rougher, while an increase in ν renders them smoother.

An important property of Eq. (22) is its mirror symmetry along the $y = L_y/2$ axis. This symmetry can be expressed as invariance with respect to the discrete \mathbb{Z}_2 group \mathcal{S} ,

$$\mathcal{S}[\psi(x, y)] = -\psi(x, L_y - y).$$

Any solution of Eq. (22) is thus accompanied by its mirror-conjugated solution. Hence, the prevailing bifurcations are of either the symmetry-breaking or the Hopf type.

2. Bifurcations in the double-gyre problem

The development of a comprehensive nonlinear theory of the double-gyre circulation over the last two decades has gone through four main steps. These four steps can be followed through the bifurcation tree in Fig. 31.

a. Symmetry-breaking bifurcation

The “trunk” of the bifurcation tree is plotted as the solid blue line in the lower part of Fig. 31. When the forcing τ is weak or the dissipation ν is large, there is only one steady solution, which is antisymmetric with respect to the midaxis of the basin. This solution exhibits two large gyres, along with their β -induced western boundary currents. Away from the western boundary, such a near-linear solution (not shown) is dominated by so-called Sverdrup balance between wind-stress

curl and the meridional mass transport (Sverdrup, 1947; Gill, 1982).

The first generic bifurcation of this quasigeostrophic model was found to be a genuine pitchfork bifurcation that breaks the system’s symmetry as the nonlinearity becomes large enough with increasing wind-stress intensity τ (Cessi and Ierley, 1995; Jiang, Jin, and Ghil, 1995). As τ increases, the near-linear Sverdrup solution that lies along the solid blue line in the figure develops an eastward jet along the midaxis, which penetrates farther into the domain and also forms two intense recirculation vortices, on either side of the jet and near the western boundary of the domain.

The resulting more intense and hence more nonlinear solution is still antisymmetric about the midaxis, but it loses its stability for some critical value of the wind-stress intensity $\tau = \tau_p$. This value is indicated by the solid square on the symmetry axis of Fig. 31 and is labeled “Pitchfork” in the figure.

A pair of mirror-symmetric solutions emerges and it is plotted as the two red solid lines in the figure’s middle part. The stream function fields associated with the two stable steady-state branches have a rather different vorticity distribution, and they are plotted in the two small panels in the upper left and upper right of Fig. 31. In particular, the jet in such a solution exhibits a large, stationary meander, reminiscent of the semipermanent one that occurs in the Gulf Stream, just downstream of Cape Hatteras. These asymmetric flows are characterized by one recirculation vortex being stronger in intensity than the other; accordingly, the eastward jet is deflected either to the southeast, as is the case in the observations for the North Atlantic, or to the northeast.

b. Gyre modes

The next step in the theoretical treatment of the problem was taken in part concurrently with the first one that we mentioned (Jiang, Jin, and Ghil, 1995) and in part shortly thereafter (Speich, Dijkstra, and Ghil, 1995a; Dijkstra and Katsman, 1997; Sheremet, Ierley, and Kamenkovich, 1997). It involved the study of time-periodic instabilities that arise through Hopf bifurcation from either an antisymmetric or an asymmetric steady flow. Some of these studies treated wind-driven circulation models limited to a stand-alone, single gyre (Pedlosky, 1996; Sheremet, Ierley, and Kamenkovich, 1997); such a model concentrates on the larger subtropical gyre while neglecting the smaller subpolar one.

The overall idea was to develop a full generic picture of the time-dependent behavior of the solutions in more turbulent regimes by classifying the various instabilities in a comprehensive way. However, it quickly appeared that a particular kind of instability leads to so-called gyre modes (Jiang, Jin, and Ghil, 1995; Speich, Dijkstra, and Ghil, 1995a) and was prevalent across the full hierarchy of models of the double-gyre circulation; furthermore, this instability triggers the lowest nonzero frequency present in all such models (Dijkstra, 2005; Dijkstra and Ghil, 2005).

These gyre modes always appear after the first pitchfork bifurcation, and it took several years to understand their

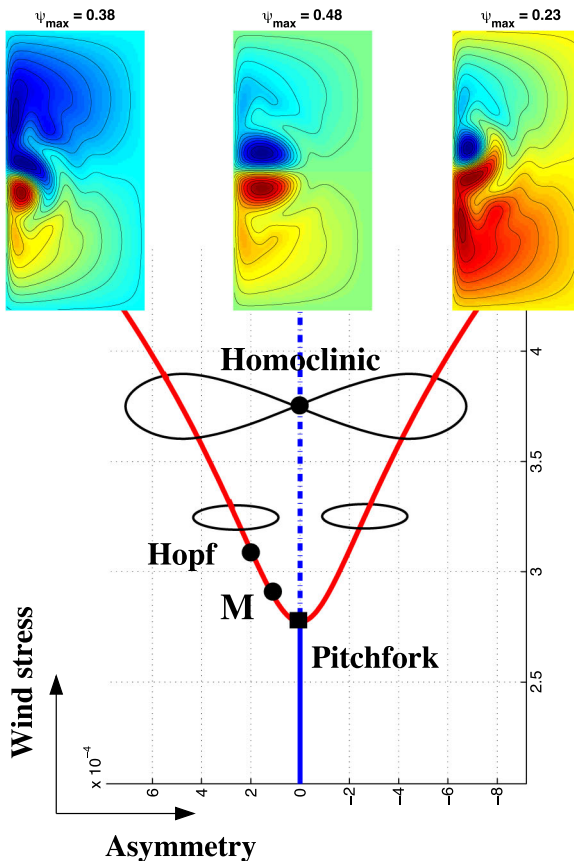


FIG. 31. Generic bifurcation diagram for the barotropic quasi-geostrophic model of the double-gyre problem: the asymmetry of the solution is plotted versus the intensity of the wind stress τ . The stream function field is plotted for a steady-state solution associated with each of the three branches; positive values are in red and negative ones are in blue. From Simonnet, Ghil, and Dijkstra, 2005.

genesis: gyre modes arise as two eigenvalues merge: one of the two is associated with a symmetric eigenfunction and responsible for the pitchfork bifurcation, and the other one is associated with an antisymmetric eigenfunction (Simonnet and Dijkstra, 2002). This merging is marked by a solid circle on the left branch of antisymmetric stationary solutions and is labeled as **M** in Fig. 31.

Such a merging phenomenon is not a bifurcation in the term's usual meaning: Although it corresponds to a topological change in phase space, the oscillatory behavior at and near **M** is damped. Nevertheless, this oscillatory eigenmode is eventually destabilized through a Hopf bifurcation, which is indicated in Fig. 31 by a heavy dot marked "Hopf," from which a stylized limit cycle emerges. A mirror-symmetric **M** and Hopf bifurcation also occur on the right branch of stationary solutions, but they have been omitted for visual clarity. This merging is as generic as the pitchfork bifurcation in the figure and arises in much more complex situations and models; see, e.g., Simonnet *et al.* (2003b) and Simonnet (2005).

In fact, such a merging is quite common in small-dimensional dynamical systems with symmetry, as exemplified by the unfolding of codimension-2 bifurcations of the Bogdanov-Takens type (Guckenheimer and Holmes, 1983). In particular, the fact that gyre modes trigger the longest multi-annual periodicity of the model is due to the frequency of this mode growing quadratically with the control parameter from zero, i.e., from the infinite period, until nonlinear saturation sets in; see, e.g., Simonnet and Dijkstra (2002) and Simonnet, Dijkstra, and Ghil (2009).

More generally, Hopf bifurcations give rise to features that recur more or less periodically in fully turbulent planetary-scale flows, atmospheric, oceanic, and coupled (Ghil and Childress, 1987; Dijkstra, 2005; Dijkstra and Ghil, 2005; Ghil, 2015, 2017). It is precisely this kind of near-periodic recurrence that is identified in the climate sciences as LFV.

c. Global bifurcations

The bifurcations studied thus far, in this section as well as the preceding ones, are collectively known as local bifurcations: they result from an instability of a specific solution that arises at a particular value of a control parameter. This term is meant to distinguish them from the global bifurcations to be studied in this subsection.

The importance of the gyre modes was further confirmed through an even more puzzling discovery. Several other authors realized, independently of one other, that the low-frequency dynamics of their respective double-gyre models was driven by intense relaxation oscillations of the jet (Simonnet *et al.*, 1998, 2003a, 2003b; Meacham, 2000; Chang *et al.*, 2001; Nadiga and Luce, 2001; Simonnet, Ghil, and Dijkstra, 2005). These relaxation oscillations, previously described by Jiang, Jin, and Ghil (1995) and Speich, Dijkstra, and Ghil (1995b), were now attributed to a homoclinic bifurcation, which is no longer due to a linear instability of an existing solution but to a so-called homoclinic reconnection, whose character is global in phase space (Guckenheimer and Holmes, 1983; Ghil and Childress, 1987). In effect, the quasigeostrophic model reviewed here

undergoes a genuine homoclinic bifurcation that is generic across the full hierarchy of double-gyre models.

This bifurcation is due to the growth and eventual merging of the two limit cycles, each of which arises from either one of the two mutually symmetric Hopf bifurcations. The corresponding bifurcation is marked in Fig. 31 by a solid circle and labeled "Homoclinic"; the reconnecting orbit itself is illustrated in the figure by a stylized lemniscate and plotted accurately by Simonnet, Ghil, and Dijkstra (2005) in their Fig. 2. This global bifurcation is associated with chaotic behavior of the flow due to the Shilnikov phenomenon (Nadiga and Luce, 2001; Simonnet, Ghil, and Dijkstra, 2005), which induces Smale horseshoes in phase space.

The connection between such homoclinic bifurcations and gyre modes was not immediately obvious, but Simonnet, Ghil, and Dijkstra (2005) emphasized that the two were part of a single global dynamical phenomenon. The homoclinic bifurcation indeed results from the unfolding of the gyre modes' limit cycles. This familiar dynamical scenario is again well illustrated by the unfolding of a codimension-2 Bogdanov-Takens bifurcation, where the homoclinic orbits emerge naturally.

Since homoclinic orbits have an infinite period, it was natural to hypothesize that the gyre-mode mechanism in this broader, global-bifurcation context gave rise to the observed 7- and 14-yr North Atlantic oscillations. Although this hypothesis may appear a little farfetched given the simplicity of the double-gyre models analyzed so far, it is reinforced by results with much more detailed models in the hierarchy; see, e.g., Dijkstra (2005), Dijkstra and Ghil (2005), and Vannitsem *et al.* (2015).

The successive-bifurcation theory there appears to be fairly complete for barotropic, single-layer models of the double-gyre circulation. This theory also provides a self-consistent, plausible explanation for the climatically important 7- and 14-yr oscillations of the oceanic circulation and the related atmospheric phenomena in and around the North Atlantic basin (Plaut, Ghil, and Vautard, 1995; Moron, Vautard, and Ghil, 1998; Wunsch, 1999; Da Costa and Colin de Verdière, 2002; Simonnet *et al.*, 2003b; Feliks, Ghil, and Simonnet, 2004, 2007; Dijkstra, 2005; Dijkstra and Ghil, 2005; Kondrashov, Feliks, and Ghil, 2005; Simonnet, Ghil, and Dijkstra, 2005; Feliks, Ghil, and Robertson, 2010, 2011). Moreover, the dominant 7- and 14-yr modes of this theory survive perturbation by seasonal-cycle changes in the intensity and meridional position of the westerly winds (Sushama, Ghil, and Ide, 2007).

In baroclinic models with two or more active layers of different density, baroclinic instabilities (Gill, 1982; Ghil and Childress, 1987; Pedlosky, 1987; Dijkstra and Ghil, 2005; Berloff, Hogg, and Dewar, 2007; Feliks, Ghil, and Simonnet, 2007; Kravtsov *et al.*, 2006) surely play a fundamental role, as they do in the observed dynamics of the ocean. However, it is not known to what extent baroclinic instabilities can destroy gyre-mode dynamics. The difficulty lies in a deeper understanding of the so-called rectification process (Katsman, Dijkstra, and Drijfhout, 1998), which arises from the nonzero mean effect of the baroclinic eddying and meandering of the flow on its barotropic component.

Roughly speaking, rectification drives the dynamics further away from any stationary solutions. In this situation, dynamical-systems theory by itself cannot be used as a full explanation of complex observed behavior resulting from successive bifurcations that are rooted in simple stationary or periodic solutions.

Therefore, other tools from statistical mechanics and non-equilibrium thermodynamics have to be considered (Robert and Sommeria, 1991; Chavanis and Sommeria, 1996; Farrell and Ioannou, 1996; Bouchet and Sommeria, 2002; Majda and Wang, 2006; Lucarini and Sarno, 2011; Lucarini, Blender *et al.*, 2014), and they are discussed in Secs. IV and V. Combining these tools with those of the successive-bifurcation approach could lead to a more complete physical characterization of gyre modes in realistic models. Preparing the ground for combining dynamical-systems tools and statistical-physics tools in this way is one of the main purposes of our review.

G. Multiple scales: Stochastic and memory effects

In Sec. II.B, we illustrated in Fig. 12 the multiplicity of timescales that are present in the climate spectrum. We also pointed out that this multiplicity of scales gives rise to the need for a hierarchy of models that enable the study of separate scales of motion and of the phenomena associated with each, as well as of the interactions between two or more scales; see Fig. 11. Here we discuss several ways in which one can address these issues, using the theory of stochastic processes and taking into account non-Markovian effects.

1. Fast scales and their deterministic parametrization

Let us concentrate, for the sake of definiteness, on variability within a particular range of frequencies f in the climatic power spectrum of Fig. 12(a), say, seasonal to centennial, i.e., $10^{-2} \text{ yr}^{-1} = f_1 \leq f \leq f_2 = 10^0 \text{ yr}^{-1}$, and write a model of this variability as

$$\dot{\mathbf{z}} = \mathbf{H}(\mathbf{z}; \boldsymbol{\mu}). \quad (23)$$

Here \mathbf{z} is the vector of the system's variables and $\boldsymbol{\mu}$ is the vector of the system's parameters. We saw that oscillatory modes of both the THC (see Sec. III.D) and the wind-driven circulation (see Sec. III.F) lie in this range. How should one then take into account the slower timescales to the left of this range $f_0 < f < f_1$, and the faster ones to the right $f_2 < f < f_3$, where $0 \leq f_0 < 10^{-2} \text{ yr}^{-1}$ and $1 < f_3 < \infty$?

A time-honored approach in physical modeling is to describe variability to the left as a prescribed slow evolution of parameters

$$\boldsymbol{\mu} = \boldsymbol{\mu}(et), \quad 0 < e \ll 1, \quad (24)$$

where e is small and et is, therefore, a slow time. One might, for instance, consider a particular $\boldsymbol{\mu} = \boldsymbol{\mu}(et)$ in Eq. (24) to represent a slow change in the solar constant or in the height of the topography.

To the right, one might approximate the more rapid fluctuations as being extremely fast with respect to those of

main interest or even infinitely fast. There are two distinct approaches based on these ideas: the first one is purely deterministic, and the second one introduces a noise process and thus stochastic considerations.

The standard slow-fast formulation of a system of differential equations when assuming a large but finite separation of timescales is given, for $e \neq 0$, by

$$x' = eF(x, y; e), \quad (25a)$$

$$y' = G(x, y; e). \quad (25b)$$

Here $\mathbf{z} = (x, y)^T$, with x the slow variable and y the fast variable and $\mathbf{H} = (F, G)^T$, while $(\cdot)^T$ designates the transpose and $(\cdot)' = d(\cdot)/dt$ stands for differentiation with respect to the fast time t .

As long as $e \neq 0$, the system (25) is equivalent to the so-called slow system,

$$\dot{x} = F(x, y; e), \quad (26a)$$

$$\epsilon \dot{y} = G(x, y; e), \quad (26b)$$

in which the dot stands for differentiation $d(\cdot)/d\tau$ with respect to the slow time $\tau = et$.

The classical way of dealing with such problems has been using matched asymptotic expansions; see, e.g., Grasman (1987) and Lagerstrom (1988). This methodology arose originally from dealing with boundary layers in fluid dynamics, with the inner problem referring to the fast variations in the boundary layer, while the outer problem refers to the more slowly varying free flow outside this layer.

More recently a point of view inspired by dynamical-systems theory (Fenichel, 1979) led to geometric singular perturbation theory; see, e.g., Jones (1995). In this approach, one considers the invariant manifolds that arise in the two complementary limits obtained by letting $e \rightarrow 0$ in the fast and slow systems, respectively.

In the fast system (25), the limit is given by

$$x' = 0, \quad (27a)$$

$$y' = G(x, y; 0), \quad (27b)$$

while in the slow one it makes sense only if the right-hand side of Eq. (26b) is identically zero; if so, the latter limit is given by

$$\dot{x} = F(x, y; 0), \quad (28a)$$

$$0 = G(x, y; 0). \quad (28b)$$

The algebraic equation $G(x, y; 0) = 0$ defines the critical manifold \mathcal{M}_c on which the solutions of the reduced problem $\dot{x} = F(x, y; 0)$ evolve; here $y = Y_G(x)$ are the explicit solutions of the implicit equation (28a).

The splitting of the full, slow-fast system given by either Eq. (25) or Eq. (26) into the two systems (27) and (28) has proven to be helpful in the study of relaxation oscillations; see, e.g., Grasman (1987). We saw such sawtooth-shaped,

slow-fast oscillations arise in both the THC (Sec. III.C.2) and the wind-driven circulation of the ocean (Sec. III.F.2).

Another important application of this methodology is in the reduction of large multiscale problems to much smaller ones. In the systems (25) and (26), we considered both x and y to be scalar variables. We saw in Fig. 11, though, that the characteristic spatial and temporal scales of atmospheric, oceanic, and coupled climate phenomena are highly correlated with each other; large-scale motions tend to be slow and smaller-scale ones faster. Thus, it is much more judicious to consider $\mathbf{z} = (\mathbf{X}^T, \mathbf{Y}^T)^T$, with $\mathbf{X} \in \mathbb{R}^m$, $\mathbf{Y} \in \mathbb{R}^n$, and $n \gg m$; i.e., the number of small and fast degrees of freedom is much larger than that of the large and slow ones.

This setup corresponds conceptually to the parametrization problem, which we defined in Sec. II.B as finding a representation of the unresolved subgrid-scale processes described by $\mathbf{Y} \in \mathbb{R}^n$ in terms of the resolved, larger-scale ones described by $\mathbf{X} \in \mathbb{R}^m$. A paradigmatic example is that of parametrizing cloud processes, with spatial scales of 1 km and smaller and with temporal scales of 1 h and less, given the large-scale fields characterized by lengths of tens and hundreds of kilometers and by durations of substantial fractions of a day and longer. In this case, the critical manifold appears to be S shaped, as for the periodically forced Van der Pol oscillator [see, e.g., Guckenheimer, Hoffman, and Weckesser (2003), Fig. 2.1], with jumps that occur between the branch on which convection, and hence rain, is prevalent, and the one on which the mean vertical stratification is stable, and thus no rain is possible. Next we discuss specifically the parametrization of convective processes and of clouds in this perspective.

2. An example: Convective parametrization

Clouds have a dramatic role in climate modeling and in determining the climate's sensitivity to natural and anthropogenic perturbations; see, e.g., IPCC (2001, 2014a). A substantial literature exists, therefore, on cloud observations, modeling, and simulation; see, e.g., Emanuel (1994) and references therein. See our earlier discussion in Secs. II.C.2 and III.G.1. One of the oldest, best known, and most widely used cumulus parametrizations is the Arakawa and Schubert (1974) one. Cumulus convection occurs due to moist convective instability, which converts the potential energy of the large-scale mean state into the kinetic energy of the cumulus clouds. A fundamental parameter in this process is the fractional entrainment rate λ of a cumulus updraft. In the Arakawa-Schubert (AS) parametrization of moist atmospheric convection, the key idea is that an ensemble of cumulus clouds is in quasiequilibrium with the large-scale environment.

The cloud work function $A(\lambda)$ changes in time according to

$$\dot{A}(\lambda) = J \otimes M_B(\lambda) + F(\lambda). \quad (29)$$

Here $M_B(\lambda)$ is the non-negative mass flux through the cloud base and $J \otimes M_B$ is a weighted average over cloud types, with J standing for the weights in the averaging integral, while F is the large-scale forcing.

The dot stands for differentiation with respect to the slow time $\tau = et$ as in Eq. (26a). The quasiequilibrium assumption

in the AS parametrization corresponds simply to the critical manifold equation (28a), which becomes

$$0 = J \otimes M_B(\lambda) + F(\lambda). \quad (30)$$

In this case, the small parameter that corresponds to the ϵ of the general slow-fast formulation is the reciprocal of the adjustment time τ_{adj} of a cloud ensemble to the mean state $\epsilon \sim 1/\tau_{\text{adj}}$.

Pan and Randall (1998) proposed an equation that corresponds to the behavior of a cumulus ensemble off the critical manifold given by Eq. (30), which they termed a prognostic closure. In their formulation, one computes a cumulus kinetic energy K from

$$\dot{K} = B + S - D. \quad (31)$$

Here B is the buoyancy production term, S is the shear production term, and D is the vertically integrated dissipation rate. The main parameters on which the behavior of the slow-fast system given by Eqs. (30) and (31) depends are

$$\alpha = M_B^2/K, \quad \tau_D = K/D. \quad (32)$$

While Pan and Randall (1998) did not determine α , τ_D , or τ_{adj} explicitly, they provided qualitative arguments based on the physics of cumulus convection that make the quasiequilibrium limit plausible.

3. Stochastic parametrizations

It is of broader interest, though, to consider now the slow-fast formulation of a system of differential equations in the limit case of infinite separation of timescales, i.e., when the fast motions have zero decorrelation time. In this case, one has to introduce a white-noise process and the associated stochastic considerations.

The basic idea relies on the Einstein (1905) explanation of Brownian motion, in which a large particle is immersed in a fluid formed of many small ones. Let the large particle move along a straight line with velocity $u = u(t)$, subject to a random force $\eta(t)$ and to linear friction $-\lambda u$, with coefficient λ . The equation of motion is

$$du = -\lambda u dt + \eta(t). \quad (33)$$

The random force $\eta(t)$ is assumed to be “white noise,” i.e., it has mean zero $\mathcal{E}[\eta(t; \omega)] = 0$ and autocorrelation $\mathcal{E}[\eta(t; \omega)\eta(t+s; \omega)] = \sigma^2 \delta(s)$, where $\delta(s)$ is a Dirac function, σ^2 is the variance of the white-noise process, ω labels the realization of the random process, and \mathcal{E} is the expectation operator, which averages over the realizations ω . Alternative notations for the latter are an overbar in climate sciences and angle brackets in quantum mechanics, $\mathcal{E}[F] := \bar{F} := \langle F \rangle$.

Equation (33), with $\eta = \sigma dW$, is a linear stochastic differential equation (SDE) of a form that is now referred to as a Langevin equation, where $W(t)$ is a normalized Wiener process, also called Brownian motion. It was introduced into climate dynamics by Hasselmann (1976), who identified slow “climate” variations with the motion of the large particle and

fast “weather” fluctuations with the motions of the small fluid particles. He also thought of weather as associated with the atmosphere and climate as associated with the ocean, cryosphere, and land vegetation.

Specifically, Hasselmann (1976) assumed that in a system like Eq. (23) and without formally introducing the timescale separation parameter ϵ one would have $\tau_x \ll \tau_y$, where τ_x and τ_y are the characteristic times of the fast x and slow y variables, respectively. From this assumption and relying also upon the results of Taylor (1921), he then derived a linear SDE for the deviations y'_j of the slow variables \mathbf{Y} from a reference state \mathbf{Y}_0 and the properties of the corresponding covariance matrix and spectral densities. In particular, the red-noise character of the spectrum $S = S(f)$, with $S \sim f^{-2}$ for many oceanic observed time series, lent considerable credence to the thermal-flywheel role that Hasselmann (1976) attributed to the ocean in the climate system.

In light of recent mathematical results on extremely large timescale separation in slow-fast deterministic systems, let us consider a relatively simple, but still sufficiently relevant and instructive, case in which the reduction to a SDE can be rigorously derived; see Pavliotis and Stuart (2008), Melbourne and Stuart (2011), and Gottwald and Melbourne (2013). Their deterministic system of ordinary differential equations (ODEs) is a small modification of Eq. (26), namely,

$$\dot{x} = \epsilon^{-1} f_0(y^{(\epsilon)}) + f_1(x^{(\epsilon)}, y^{(\epsilon)}), \quad x^{(\epsilon)}(0) = x_0, \quad (34a)$$

$$\dot{y}^{(\epsilon)} = \epsilon^{-2} g(y^{(\epsilon)}), \quad y^{(\epsilon)}(0) = y_0, \quad (34b)$$

where $x^{(\epsilon)} \in \mathbb{R}^d$ and $y^{(\epsilon)} \in \mathbb{R}^{d'}$.

The formal difference with respect to the situation studied in Sec. III.G.1 is that $F(x, y; \epsilon)$ of Eq. (26a) has been expanded in ϵ as $F(x, y; \epsilon) = f_0(y^{(\epsilon)}) + \epsilon f_1(x^{(\epsilon)}, y^{(\epsilon)})$, while $G(x, y; \epsilon)$ of Eq. (26b) has been both simplified, in becoming x independent, and “accelerated,” to read $G(x, y; \epsilon) = \epsilon^{-2} g(y^{(\epsilon)})$. The basic idea is that the chaotic and fast $y^{(\epsilon)}$ induces, as $\epsilon \rightarrow 0$, a white-noise driving of the slow x . Note that one needs $d' \geq 3$ for the autonomous Eq. (34b) to have chaotic solutions.

Melbourne and Stuart (2011) assumed merely that the fast equation (34b) has a compact attractor $\Lambda \in \mathbb{R}^{d'}$ that supports an invariant measure μ , and that $\mathcal{E}_\mu[f_0(x)] = 0$, along with certain boundedness and regularity conditions on $f(x, y)$. They then rigorously showed that

$$x^{(\epsilon)}(t) \xrightarrow[p]{} X(t) \quad \text{as } \epsilon \rightarrow 0,$$

where the convergence is with respect to the appropriate probability measure p and $X(t)$ is the solution of the SDE

$$X(t) = x_0 + \int_0^t \bar{F}[X(s)]ds + \sigma W(t). \quad (35)$$

Here W is the Brownian motion with variance σ^2 , such that the white noise in Eq. (33) is given by $\eta = \sigma dW$. Moreover, $\bar{F}(X) = \mathcal{E}_\mu[F(x, \cdot)]$ with respect to μ .

Fundamental mathematical issues associated with the previous diffusive limit of slow-fast systems were explored by Papanicolaou and Kohler (1974), and early results in the

physical literature include Beck (1990) and Just *et al.* (2001). Many aspects of the applications to climate modeling were covered by Palmer and Williams (2009). More specifically, Berner *et al.* (2017) and Franzke *et al.* (2015) discussed issues of stochastic parametrization of subgrid-scale processes.

To conclude this section, it is of interest to consider in a broader perspective the potential for a unified theory of nonautonomous dynamical systems in which the fast processes may be modeled as either deterministic or stochastic. The theory of purely deterministic, skew-product flows was laid on a solid basis by Sell (1967, 1971) and, more recently, by Kloeden and Rasmussen (2011). Random dynamical systems were extensively covered by Arnold (1998), with many recent results in an active field.

Berger and Siegmund (2003) pointed out, “Quite often, results for random dynamical systems and continuous skew-product flows are structurally similar,” and thus open the way to a unified theory. They outline both commonalities and distinctions between the two broad classes of nonautonomous dynamical systems, to shed further light on existing results, as well as to stimulate the development of common concepts and methods.

Caraballo and Han (2017) provided a solid and accessible introduction to random dynamical systems, as well as to deterministically nonautonomous ones, along with several interesting applications. They also considered the two distinct types of formulation of the deterministic ones, the so-called process formulation and the skew-product flow one. System (34), for instance, is a particular case of a master-slave system

$$\dot{x} = f(x, y), \quad \dot{y} = g(y), \quad \text{with } x \in \mathbb{R}^d, \quad y \in \mathbb{R}^{d'}, \quad (36)$$

that induces a skew-product flow, where $y(t)$ is the driving force for $x(t)$.

These developments bear following since the climate sciences offer a rich source of relevant problems and could thus lead to novel and powerful applications of the unified theory. Caraballo and Han (2017) already studied the Lorenz (1984) model, in which seasonal forcing acting on deterministic subseasonal variability can induce interannual variability. Other applications are discussed later, especially in Sec. IV.E.

4. Modeling memory effects

While the study of differential equations goes back to Isaac Newton, the interest for explicitly including delays in evolution equations that govern physical and biological processes is relatively recent. A mid-20th-century reference is Bellman and Cooke (1963), followed by Driver (1977) and Hale (1977). Delay-differential equations (DDEs) were introduced into the climate sciences by Bhattacharya, Ghil, and Vulis (1982) and have been used widely in studying ENSO; see, for instance, Tziperman *et al.* (1994a), and Ghil, Chekroun, and Stepan (2015) and references therein.

As we shall see, memory effects can play a key role when there is little separation between scales, in contrast to the assumptions of Hasselmann (1976) and of other authors mentioned in Secs. III.G.2 and III.G.3. Moreover, when properly incorporated in the mathematical formulation of

the climate problem at hand, relying on such effects can lead to highly efficient and accurate model reduction methods.

a. The Mori-Zwanzig formalism

In statistical physics, the Mori-Zwanzig (MZ) (Zwanzig, 1961; Mori, 1965) formalism arose from describing the interaction of a Hamiltonian many-particle system with a heat bath. Today, though, it is being used in a large number of applications that include dissipative systems.

The fundamental idea is illustrated by the following simple linear system of two ODEs (E and Lu, 2011):

$$\dot{x} = a_{11}x + a_{12}y, \quad (37a)$$

$$\dot{y} = a_{21}x + a_{22}y. \quad (37b)$$

The sole assumption is that we are interested in the details of the behavior of $x(t)$, but only in the statistics of y ; one thinks of y as fluctuating faster than x , but this is not actually required for the formalism outlined later to work. One considers x as a slowly varying parameter in solving Eq. (37b) for y by using the variation-of-constants formula

$$y(t) = e^{a_{22}t}y(0) + \int_0^t e^{a_{22}(t-s)}a_{21}x(s)ds$$

and plugs this result back into Eq. (37) to yield

$$\dot{x} = a_{11}x + \int_0^t K(t-s)x(s)ds + f(t). \quad (38)$$

Equation (38) is a generalized Langevin equation (GLE) in which $K(t) = a_{12}\exp(a_{22}t)a_{21}$ is the memory *kernel* and $f(t) = a_{12}\exp(a_{22}t)y(0)$ is the *noise* term since one thinks of $y(0)$ as randomly drawn from the rapidly fluctuating $y(t)$. The essential difference with respect to Eq. (33) is the convolution integral in Eq. (38), which expresses the delayed action of the slow variable x on the fast variable y .

The MZ formalism consists, in a general, nonlinear set of Markovian evolution equations with a large or even infinite number of degrees of freedom, in selecting the variables one is interested in via a projection operator and deriving the generalized form of the GLE in Eq. (38). Examples of Markovian evolution equations are systems of ODEs or PDEs for which an instantaneous initial state carries all of the information from the past.

In this general case, the memory term involves repeated convolutions between decaying memory kernels and the resolved modes, and the GLE there is a non-Markovian, stochastic integrodifferential system that is difficult to solve without further simplifications. Among the latter, the short-term memory approximation [see, e.g., Chorin and Stinis (2007)] posits rapidly decaying memory and is equivalent to assuming a relatively large separation of scales, as in Secs. III.G.1 and III.G.3.

Kondrashov, Chekroun, and Ghil (2015) showed that there is a way to approximate the GLE in a broad setting, efficiently and accurately, using a set of Markovian SDEs without the need for pronounced scale separation and in the presence of so-called intermediate-range memory. This way relies on a methodology that was developed at first quite independently

of the MZ formalism, namely, empirical model reduction (EMR) (Kondrashov *et al.*, 2005; Kravtsov, Kondrashov, and Ghil, 2005, 2009).

b. EMR methodology

The purpose of EMR development was to derive relatively simple nonlinear, stochastic-dynamic models from time series of observations or of long simulations with high-end models such as GCMs. An EMR model can be compactly written as

$$\dot{\mathbf{x}} = -\mathbf{A}\mathbf{x} + \mathbf{B}(\mathbf{x}, \mathbf{x}) + \mathbf{L}(\mathbf{x}, \mathbf{r}_t^l, \xi_t, t), \quad 0 \leq l \leq L-1. \quad (39)$$

Here \mathbf{x} typically represents the resolved and most energetic modes. Most often, these are chosen by first selecting a suitable basis of empirical orthogonal functions (Preisendorfer, 1988) or other data-adaptive basis [see, e.g., Kravtsov, Kondrashov, and Ghil (2009) and references therein], and retaining a set of principal components that capture a satisfactory fraction of the total variance in the dataset.

The terms $-\mathbf{A}\mathbf{x}$ and $\mathbf{B}(\mathbf{x}, \mathbf{x})$ represent, respectively, the linear dissipation and the quadratic self-interactions of these modes, while \mathbf{L} is a time-dependent operator that is bilinear in the resolved variables \mathbf{x} and the unresolved ones \mathbf{r}_t^l . These interactions take a prescribed form in the EMR formulation of Eq. (39) and arise by integrating recursively, from the lowest level L to the top level $l = 0$, the “matrioshka” of linear SDEs

$$d\mathbf{r}_t^l = \mathbf{M}_l(\mathbf{x}, \mathbf{r}_t^0, \dots, \mathbf{r}_t^{l-1})dt + \mathbf{r}_t^{l+1}dt.$$

At each level l , the coupling between the variable \mathbf{r}_t^l and the previous-level variables $(\mathbf{x}, \mathbf{r}_t^0, \dots, \mathbf{r}_t^{l-1})$ is modeled by $L-1$ rectangular matrices \mathbf{M}_l of increasing order.

In practice, the matrices \mathbf{A} , \mathbf{M}_l , and the quadratic terms \mathbf{B} are estimated by a recursive least-square procedure, which is stopped when the L th-level residual noise $\mathbf{r}^{L-1} = \xi_t$ has a vanishing lag 1 autocorrelation. The stochastic residuals \mathbf{r}_t^l obtained in this recursive minimization procedure are ordered in decreasing order of decorrelation time, from \mathbf{r}_t^0 to ξ_t .

Note that the integral terms arising in the \mathbf{L} operator are convolution integrals between the macrostate variables \mathbf{x} and memory kernels that decay according to the dissipative properties of the matrices \mathbf{M}_l . These decay times are not necessarily short, and one can thus treat the case of intermediate-range memory in the MZ terminology. Furthermore, Kondrashov *et al.* (2005) noted that any external forcing, such as the seasonal cycle, can typically be introduced as a time dependence in the linear part \mathbf{A} of the main level of Eq. (39).

c. Role of memory effects in EMR

We propose here a simple analytic example that should help one understand the general description of EMR in the previous paragraphs, as well as the connection to the MZ formalism. The model is given by

$$dx = [f(x) + r]dt, \quad (40a)$$

$$dr = (\gamma x - ar)dt + dW_t, \quad (40b)$$

where f is a nonlinear function, $W_t = W_t(\omega)$ is a standard Wiener process as in Eq. (33), $\alpha > 0$, and γ is real. We are interested in x , which is slow, and want to parametrize r , which is fast.

Proceeding with Eq. (40) as we did with the system (37), but now for a fixed realization $\omega \in \Omega$, we get

$$r(t; \omega) = e^{-\alpha t} r_0 + \gamma \int_0^t e^{-\alpha(t-s)} x(s) ds + W_t(\omega),$$

where $r(t_0; \omega) = r_0$. Substituting this back into Eq. (40a) yields the following randomly forced integrodifferential equation:

$$\dot{x} = f(x) + e^{-\alpha t} r_0 + \gamma \int_0^t e^{-\alpha(t-s)} x(s) ds + W_t(\omega), \quad (41)$$

which is the analog of Eq. (38) in the stochastic-dynamic context of Eq. (40).

Kondrashov, Chekroun, and Ghil (2015) rigorously proved that the EMR (39) is equivalent to a suitable generalization of the GLE (41). Pavliotis (2014) defines as *quasi-Markovian* a stochastic process where the noise in the GLE can be described by adding a finite number of auxiliary variables, as in the case of the EMR approach. Thus, the EMR methodology can be seen as an efficient implementation of the MZ formalism, i.e., an efficient solution of the associated GLE, even in the absence of large-scale separation. This result explains the remarkable success of EMR in producing reduced models that capture the multimodality as well as the nontrivial power spectrum of phenomena merely known from time series of observations or of high-end model simulations.

In the remainder of this section, we give two examples of this success and further references to many more. Alternative approaches to efficient solutions of the GLE can be found, for instance, in Chorin, Hald, and Kupferman (2002).

d. EMR applications

We choose here an EMR model to simulate Northern Hemisphere midlatitude flow (Kravtsov, Kondrashov, and Ghil, 2005) and a real-time ENSO prediction model (Kondrashov *et al.*, 2005). Further examples of successful application of the methodology appear in Kravtsov, Kondrashov, and Ghil (2009) and Kravtsov *et al.* (2011) and elsewhere.

Kravtsov, Kondrashov, and Ghil (2005) introduced the EMR methodology and illustrated it at first with quadratically nonlinear models of the general form given here in Eq. (39). The applications were to the Lorenz (1963) convection model, the classical double-well potential in one space dimension, and a triple-well potential in two dimensions with an exponential shape for the wells. More challenging was a real-data application to geopotential height data for 44 boreal winters (1 December 1949–31 March 1993). The dataset consisted of $44 \times 90 = 3960$ daily maps of winter data, defined as 90-day sequences starting on 1 December of each year. The best EMR fit for the data required the use of nine principal components and of $L = 3$ levels.

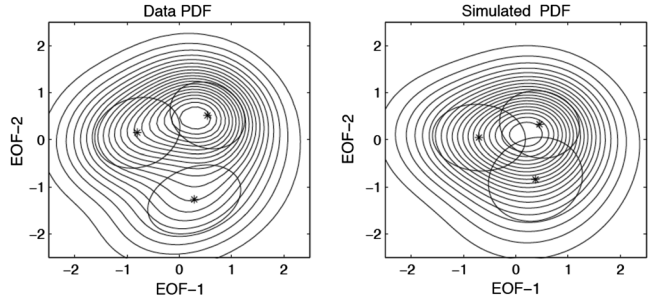


FIG. 32. Multimodal probability density function (PDF) for the Northern Hemisphere's geopotential height anomalies of 44 boreal winters; see Smyth, Ide, and Ghil (1999) for details of the dataset and of the mixture model methodology for computing the PDFs. PDF (a) of the observed height anomalies and (b) of the anomalies given by the EMR model. Adapted from Kravtsov, Kondrashov, and Ghil, 2005.

The probability density functions (PDFs) for the observed and the EMR model-generated datasets are plotted in Fig. 32. The EMR captures the three modes obtained with a Gaussian mixture model; see Smyth, Ide, and Ghil (1999) and Ghil and Robertson (2002). These three modes correspond to three clusters found by Cheng and Wallace (1993) using extremely different methods on a somewhat different dataset. The maps of the corresponding centroids appear as Fig. 1 in Ghil and Robertson (2002) and are discussed therein; they agree quite well with those of Cheng and Wallace (1993); see Smyth, Ide, and Ghil (1999), Fig. 9.

Kondrashov *et al.* (2005) fitted the global SST field between 30°S and 60°N over the time interval January 1950–September 2003 by using linear and quadratic EMR models with one and two noise levels $L = 1, 2$, based on monthly SST anomaly maps and allowing a seasonal dependence of the dissipative terms in Eq. (39). Their results when using $L = 2$ were much better for both linear and quadratic models, which shows the role of memory effects in EMR modeling and the connection with the MZ formalism that was already explained.

The use of the EMR models in prediction was tested by so-called hindcasting, or retrospective forecasting, i.e., a protocol, also called “no look-ahead”, in which the data available past a certain time instant are eliminated when constructing the model to be used in the forecast to be evaluated. The results of these tests are plotted in Fig. 33 for $L = 2$ and a linear versus a quadratic model. The light-black rectangle in the eastern tropical Pacific corresponds to the region (5°S–5°N, 150°–90°W) over which SST anomalies are averaged to obtain the Niño-3 index mentioned in Sec. III.E.2.

Climate forecast skill is measured mainly via root-mean-square errors and anomaly correlations. The former skill scores were given by Kondrashov *et al.* (2005) in their Fig. 2(d) and clearly indicate the superiority of the quadratic model. The latter appear in Fig. 33 too.

Anomaly correlations of roughly 0.5–0.6 (red in Fig. 33) are considered quite useful in climate prediction, and the red area is substantially larger in Fig. 33(b), covering most of the tropical Pacific and Indian oceans. Concerning actual real-time forecasts, Barnston *et al.* (2012) found that, over the 2002–2011 interval of their evaluation, the EMR-based

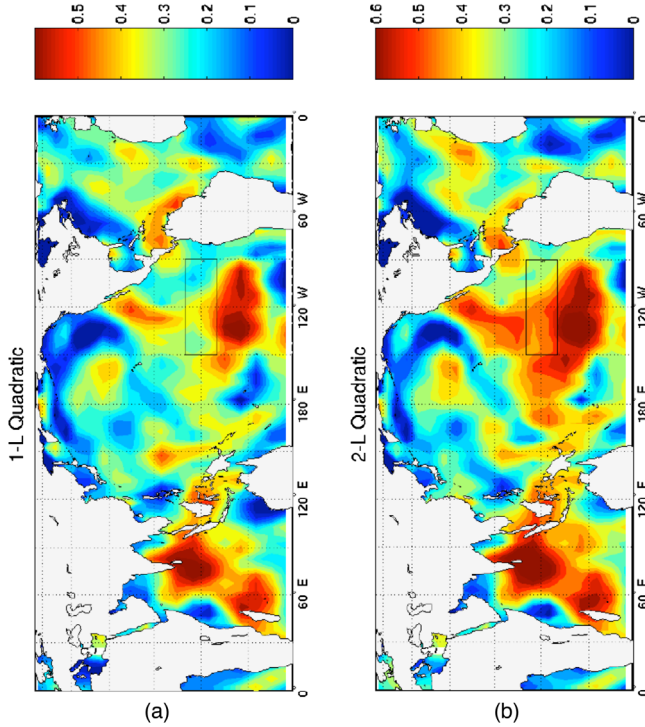


FIG. 33. Validation of forecast skill of the EMR-based ENSO model of Kondrashov *et al.* (2005) via anomaly correlation maps of SSTs at 9-month lead time. (a) Using a quadratic EMR model with $L = 1$. (b) Using a quadratic model with $L = 2$. Adapted from Kondrashov *et al.*, 2005.

forecasts of University of California–Los Angeles’s Theoretical Climate Dynamics group were at the top of the eight statistical models being evaluated and exceeded in skill by only a few of the 12 dynamical, high-end models in the group that participated in the ENSO forecast plume of the International Research Institute for Climate and Society.²⁰

e. Explicit derivation of the parametrized equations

The EMR methodology is data driven, so it allows one to construct bottom up an effective dynamics able to account for the observed data. Wouters and Lucarini (2012, 2013) showed that the MZ formalism can also be used to derive the parametrizations in a top-down manner in a general way. Assume that the system of interest is described by the following evolution equations:

$$\dot{\mathbf{X}} = f_{\mathbf{X}}(\mathbf{X}) + \epsilon \Psi_{\mathbf{X}}(\mathbf{X}, \mathbf{Y}), \quad (42a)$$

$$\dot{\mathbf{Y}} = f_{\mathbf{Y}}(\mathbf{Y}) + \epsilon \Psi_{\mathbf{Y}}(\mathbf{X}, \mathbf{Y}). \quad (42b)$$

Here again $\mathbf{X} \in \mathbb{R}^m$, $\mathbf{Y} \in \mathbb{R}^n$, \mathbf{X} is the set of large-scale, energetic variables of interest, and, typically, $n \gg m$.

We assume, furthermore, that ϵ is a small parameter describing the strength of the coupling between the two sets of variables, and that if $\epsilon = 0$ the dynamics is chaotic for both

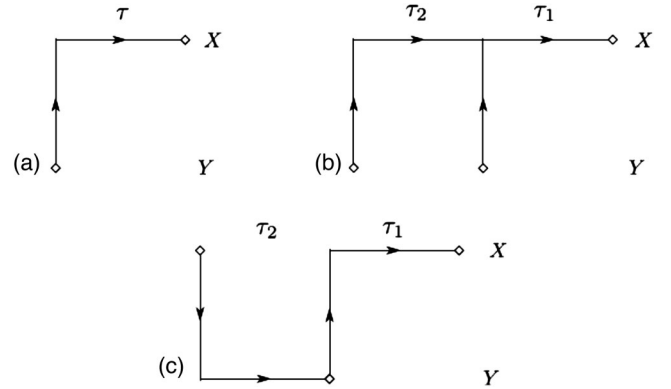


FIG. 34. Schematic representation of the three terms contributing to the parametrization of the fast variables \mathbf{X} in Eq. (43). (a) Mean-field term M . (b) Stochastic term S . (c) Memory term with kernel K . The symbols (τ, τ_1, τ_2) denote the delays involved in these effects. From Wouters and Lucarini, 2013.

the \mathbf{X} and \mathbf{Y} variables. By expanding the MZ projection operator, it is possible to derive the following expression for the projected dynamics on the \mathbf{X} variables, which is valid up to order $O(\epsilon^3)$:

$$\dot{\mathbf{X}} = f_{\mathbf{X}}(\mathbf{X}) + \epsilon M(\mathbf{X}) + \epsilon S(\mathbf{X}) + \epsilon^2 \int K(\mathbf{X}, t-s) ds. \quad (43)$$

This equation provides the explicit expression of the mean-field, deterministic term M , the time-correlation properties of the stochastic term S , which is, in general, multiplicative, and the integration kernel K , which defines the non-Markovian contribution.

Figure 34 provides a schematic diagram of the three terms of the parametrization: the M term comes from a time averaging of the effects of the \mathbf{Y} variables on the \mathbf{X} variables, the S term results from the fluctuations of the forcing of the \mathbf{Y} variables on the \mathbf{X} variables, and the non-Markovian contribution represents the self-interaction of the \mathbf{X} variables on themselves at a later time, mediated by the \mathbf{Y} variables.

These terms are derived using the statistical properties of the uncoupled dynamics of the \mathbf{Y} variables at $\epsilon = 0$. In the limit of infinite timescale separation between the \mathbf{X} and \mathbf{Y} variables, the non-Markovian term drops out and the stochastic term becomes a white-noise contribution, where one needs to use the Stratonovich definition of the stochastic integral (Pavliotis and Stuart, 2008). If instead $\Psi_{\mathbf{Y}} = 0$ in the master-slave skew-product system (42), the non-Markovian term is identically zero, as expected.

A surprising property of the surrogate dynamics given by Eq. (43) is that the expectation value of any observable $\phi(\mathbf{X})$ is the same as for the full dynamics governed by Eq. (42) up to third order in ϵ (Wouters and Lucarini, 2013). This property is due to the fact that one can derive Eq. (43) by treating the weak coupling using Ruelle response theory (Ruelle, 1998, 1999, 2009); see Sec. IV.E.3. As a result, the average model error due to the use of parametrized dynamics is under control; see the discussion by Hu, Bódai, and Lucarini (2019). Moreover, Vissio and Lucarini (2018a, 2018b) showed by explicit examples that this top-down approach can, in some cases, help derive scale-adaptive parametrizations, while

²⁰See https://iri.columbia.edu/our-expertise/climate/forecasts/enso/current/?enso_tab=enso-sst_table.

Demaeyer and Vannitsem (2017) demonstrated its effectiveness in an intermediate-complexity climate model.

Finally, note that there is an alternative route to construct parametrizations in slow-fast systems where the timescale separation is finite. Wouters and Gottwald (2019a, 2019b) recently proposed the idea of avoiding the need to add memory terms in the surrogate dynamics by using the formalism of Edgeworth expansions. This approach allows one to describe corrections to the Gaussian limiting behavior of slow-fast systems and is able to capture the feedbacks between the slow and fast variables.

IV. CLIMATE SENSITIVITY AND RESPONSE

A central goal of the climate sciences is to predict the impact of changes in the system's internal or external parameters, such as the greenhouse gas (GHG) concentration or the solar constant, on its statistical properties. A key concept in doing so is climate sensitivity, which aims to measure the response of the climate system to external perturbations of Earth's radiative balance. As we see later, this measure is being used for projecting, for instance, mean temperature changes over the coming century as a response to increasing concentrations of atmospheric GHGs. While a good start, accurate and flexible predictions of climate changes require more sophisticated concepts and methods.

A. A simple framework for climate sensitivity

To illustrate the main ideas, let us consider the simple EBM introduced in Eq. (13) of Sec. III.A, where the net radiation $R = R_i - R_o$ at the top of the atmosphere is related to the corresponding average temperature T near the Earth's surface by $R = R(T)$. This simple, 0D EBM includes both longwave and shortwave processes so that $c dT/dt = R(T)$, as in Eq. (13a).

Following Peixoto and Oort (1992) and Zaliapin and Ghil (2010), we assume, furthermore, that there are N climatic variables $\{\alpha_k = \alpha_k(T), k = 1, \dots, N\}$ that are to a first approximation directly affected by the temperature change only and that can, in turn, affect the radiative balance. Hence, one can write $R = R(T, \alpha_1(T), \dots, \alpha_N(T))$. Let us assume, furthermore, that for a certain reference temperature $T = T_0$ one has $R(T_0) = 0$, which corresponds to steady-state conditions.

The simplest framework for climate sensitivity is to think of the difference in global annual mean surface air temperature ΔT between two statistical steady states that have distinct CO₂ concentration levels. We then assume that changing the CO₂ concentration corresponds to applying an extra net radiative forcing $\Delta \tilde{R}$ to the system, and we look for the corresponding change ΔT in the average temperature so that $R(T_0 + \Delta T) + \Delta \tilde{R} = 0$.

For small ΔT and smooth $R = R(T)$, the Taylor expansion yields

$$\begin{aligned} \Delta \tilde{R} &= -\frac{dR}{dT}\Big|_{T=T_0} \Delta T + \mathcal{O}((\Delta T)^2) = -\frac{\partial R}{\partial T}\Big|_{T=T_0} \Delta T \\ &\quad - \sum_{k=1}^N \frac{\partial R}{\partial \alpha_k} \frac{\partial \alpha_k}{\partial T}\Big|_{T=T_0} \Delta T + \mathcal{O}((\Delta T)^2). \end{aligned} \quad (44)$$

Here $\mathcal{O}(x)$ is a function such that $\mathcal{O}(x) \leq Cx$ as soon as $0 < x < \epsilon$ for some positive constants C and ϵ . While the higher-order terms in ΔT are usually small, they can become important where the smooth dependence of R on T breaks down. Specifically, rapid climate change may ensue when the system crosses a tipping point, as we explain later.

Introducing the notations

$$\frac{1}{\lambda_0(T_0)} = -\frac{\partial R}{\partial T}\Big|_{T=T_0}, \quad (45a)$$

$$f_k(T_0) = -\lambda_0(T_0) \frac{\partial R}{\partial \alpha_k} \frac{\partial \alpha_k}{\partial T}\Big|_{T=T_0}, \quad (45b)$$

for the “reference sensitivity” λ_0 and the “feedback factors” f_k at the reference state $T = T_0$, we obtain

$$\Delta \tilde{R} = \frac{1 - \sum_{k=1}^N f_k(T_0)}{\lambda_0(T_0)} \Delta T + \mathcal{O}((\Delta T)^2), \quad (46)$$

which readily leads to

$$\Delta \tilde{R} = \Lambda(T_0) \Delta T + \mathcal{O}((\Delta T)^2). \quad (47)$$

Here

$$\Lambda(T_0) = -\frac{dR}{dT}\Big|_{T=T_0} = \frac{\lambda_0(T_0)}{1 - \sum_{k=1}^N f_k(T_0)} \quad (48)$$

is the linear gain factor, which can be defined as long as $\sum_{k=1}^N f_k(T_0) \neq 1$; note that if the sum of the feedback factors exceeds unity, i.e., $\sum_{k=1}^N f_k(T_0) > 1$, the system is unstable.

Referring again to Eq. (13), the feedback associated with the dependence of α on the temperature in Eq. (13b) is usually taken to be the ice-albedo feedback [see Sec. III.A], while the dependence of the emissivity m on the temperature in Eq. (13c) is associated with the changes in the atmospheric opacity. For the latter one, the standard reference sensitivity associated with deviations from Planck's law for black-body radiation is $\lambda_0(T_0) = -\partial R/\partial T|_{T=T_0} = 4\sigma m(T_0)T_0^3$.

More specifically, feedbacks that can contribute to changes in reflectivity in Eq. (13b) include, aside from the incremental presence of snow and ice, the climate-vegetation feedback; see, e.g., Watson and Lovelock (1983), Zeng and Neelin (2000), Rombouts and Ghil (2015), and references therein. The feedbacks that can affect the sensitivity of emitted radiation in Eq. (13c) include atmospheric alteration in water vapor content and cloud cover, as well as in GHGs and aerosol concentration.

In climate studies, different measures of climate sensitivity are used. The so-called equilibrium climate sensitivity (ECS) denotes the globally and annually averaged surface air temperature increase that would result from sustained doubling of the concentration of carbon dioxide in Earth's atmosphere versus that of the reference state after the climate system reaches a new steady-state equilibrium (Charney *et al.*, 1979). The ECS was used extensively by the IPCC's first three assessment reports, up to IPCC (2001).

Taking the linear approximation in Eqs. (44)–(47), one has

$$\begin{aligned} \text{ECS} &= \Lambda(T_0) \Delta \tilde{R}_{2 \times \text{CO}_2} \\ &= \frac{\lambda_0(T_0)}{1 - \sum_{k=1}^N f_k(T_0)} \Delta \tilde{R}_{2 \times \text{CO}_2}. \end{aligned} \quad (49)$$

Note that the radiative forcing is, to a good approximation, proportional to the logarithm of the CO_2 concentration. Hence, in the linear-response regime and for a given reference state T_0 the long-term globally averaged surface air temperature change resulting from a quadrupling of the CO_2 concentration is twice as large as the ECS; see Fig. 35.

The concept of climate sensitivity can be generalized to describe the linear dependence of the long-term average of any climatic observable with respect to the radiative forcing due to changes in CO_2 or in other GHGs, as well as to changes in solar radiation, aerosol concentration, or any other sudden changes in the forcing (Ghil, 1976, 2015; Lucarini, Fraedrich, and Lunkeit, 2010b; von der Heydt *et al.*, 2016).

B. Climate sensitivity: Uncertainties and ambiguities

The ECS is widely considered to be the most important indicator in understanding climate response to natural and anthropogenic forcings. It is usually estimated from instrumental data coming from the industrial age, from proxy paleoclimatic data, and from climate models of different levels of complexity. In climate models, the ECS results from a nontrivial combination of several model parameters that enter the feedback factors $\{f_k\}$ in Eq. (45b), and it requires careful tuning. Despite many years of intense research, major uncertainties still exist in estimating it from past climatic data, as well as substantial discrepancies among different climate

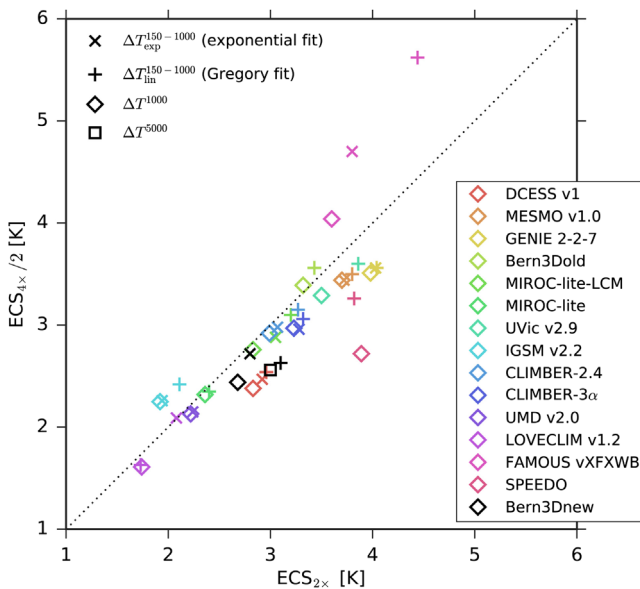


FIG. 35. Test of the linear scaling of the long-term climate response with respect to the CO_2 concentration increase in 15 GCMs. On the abscissa, standard ECS, as in Eq. (49); on the ordinate, long-term response of the globally averaged surface air temperature to quadrupling of the CO_2 concentration. From Pfister and Stocker, 2017.

models (IPCC, 2001, 2007, 2014a). In fact, Charney *et al.* (1979) estimated the ECS uncertainty as 1.5–4.5 K for CO_2 doubling, and this range of uncertainties has increased rather than decreasing over the four intervening decades.

The basic reason for these uncertainties lies in the high sensitivity of the ECS to the strength of the feedbacks f_k as a result of the factor $1/\{1 - \sum_{k=1}^N f_k(T_0)\}$ in Eq. (48). Efforts to reduce the uncertainty in ECS values for the current climate include adopting ultra-high-resolution GCMs (Satoh *et al.*, 2018), in which one may better account for feedbacks that act on a larger range of scales, as well as applying so-called emergent constraints, i.e., relations that are rigorously valid for simple stochastic models, to climate datasets (Cox, Huntingford, and Williamson, 2018), where one hopes to take advantage of general, and possibly universal, relationships between climatic variables.

In particular, the largest uncertainty in defining the ECS for the current climate state is associated with the difficulty in estimating correctly the strength of the two main feedbacks associated with clouds (Bony *et al.*, 2015; Schneider *et al.*, 2017). A warmer climate leads to increased presence of water vapor in the atmosphere, and, in turn, to more clouds. An increased cloud cover leads, on the one hand, to an increase in the climate system's albedo (cooling effect) and, on the other hand, to a more efficient trapping of longwave radiation near the surface (warming effect). The balance between the two feedbacks changes substantially according to the type of cloud, with the cooling effect dominant for low-lying clouds, while the warming effect is dominant for high-altitude ones. This is a striking example of the multiscale nature of the climate system: an extremely small-scale, short-lived dynamical process, cloud formation, has a substantial effect on the planet's global and long-term energy budget.

Despite the previous highly simplified description, it should be clear that the ECS is a state-dependent indicator. This state dependence is further supported by the evidence in Figs. 36 and 37. In particular, we have as follows.

- Both the Planck response and the strength of the feedbacks that determine the gain factor Λ in Eq. (48) depend on the reference state T_0 . As an example, in warmer climates where sea ice is absent, the positive ice-albedo feedback is greatly reduced, thus contributing to a smaller climate sensitivity. On the other hand, in warmer climates the atmosphere is more opaque as a result of the presence of more water vapor, leading to a strong enhancement of the greenhouse effect.
- The radiative forcing is only approximately linear with the logarithm of the CO_2 concentration, so $\Delta \tilde{R}_{2 \times \text{CO}_2}$ depends on the concentration's reference value. In fact, this dependence is weak across a large range of CO_2 concentrations, but it is greatly strengthened by optical saturation effects in the CO_2 absorption bands.
- Near the moist greenhouse threshold, which corresponds to a tipping point of the Earth system, the ECS is greatly strengthened. Figure 36 shows that for a solar irradiance comparable or stronger than the

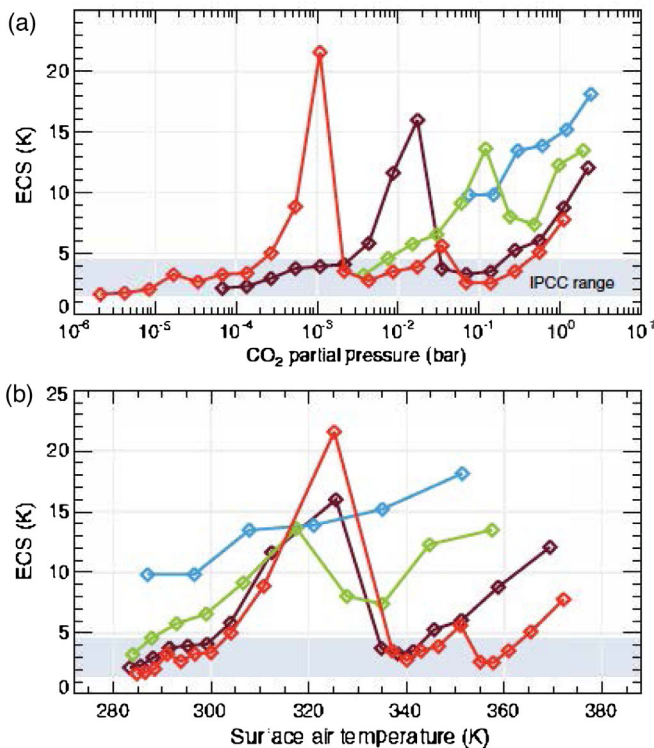


FIG. 36. Estimates of the state dependence of the ECS using the Community Earth System Model (CESM). The four curves correspond to CESM simulations with four multiples of the solar constant Q_0 ; in the notation of Eq. (13), $\mu = 0.75, 0.875, 1.0$, and 1.1 for the blue, green, brown, and red curves. (a) ECS as a function of CO_2 partial pressure ($\mu = 0.75, 0.875, 1.0$, and 1.1 from the rightmost to the leftmost curve, respectively). (b) ECS as a function of global mean surface air temperature ($\mu = 0.75, 0.875, 1.0$, and 1.1 from the uppermost to the lowermost curve, respectively). The temperatures shown in (b) are an average between the base and doubled- CO_2 state. The shaded regions in (a) and (b) indicate the IPCC estimated range for ECS. From Wolf, Haqq-Misra, and Toon, 2018; see also Gómez-Leal *et al.* (2018).

present one, the peak in the value of the ECS is realized at a surface temperature of about 320 K, which corresponds to a lower CO_2 concentration in the case of weaker irradiance; see the discussion by Gómez-Leal *et al.* (2018). Note that reaching the moist greenhouse threshold for lower values of the solar irradiance requires exceedingly high CO_2 concentrations.

- Recently Schneider, Kaul, and Pressel (2019), using extremely high-resolution simulations that represent explicitly convective processes, proposed a mechanism of instability of stratocumulus clouds occurring at high CO_2 concentrations that greatly enhances the ECS and eventually leads to an abrupt transition to a much warmer climatic regime.

While useful, the ECS concept faces practical difficulties because its definition assumes that after the forcing is applied the climate reaches a new steady state after all transients have died out. Since the climate is multiscale in both time and space, it is extremely nontrivial to define an effective cutoff

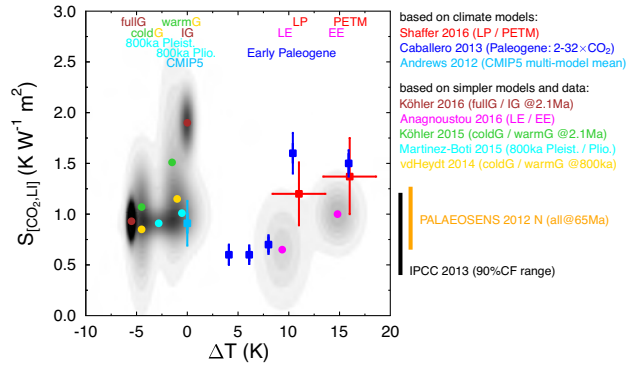


FIG. 37. State dependence of the ECS: estimates from proxy data and climate models. The large number of datasets, models, and acronyms is detailed by von der Heydt *et al.* (2016). The ΔT on the x axis refers to the difference of the given T_0 from the preindustrial value T_{00} , i.e., $T_0 = T_{00} + \Delta T$; the $S_{[\text{CO}_2, \text{LI}]}$ on the y axis refers to sensitivity with respect to CO_2 concentration corrected for land-ice albedo feedback. Mean values: for data, color-coded circles with shaded probability density functions; for models, squares with error bars. From von der Heydt *et al.*, 2016.

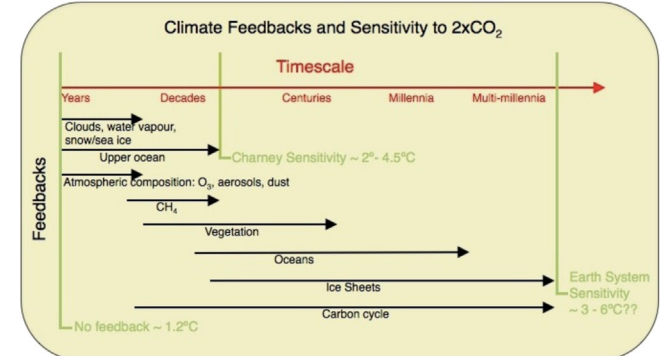


FIG. 38. Dependence of the effective ECS on the reference timescale. Consideration of longer timescales entails taking into account a larger set of slow climate processes.

timescale able to include all transient behavior. Thus, a timescale of 100 yr is long compared to atmospheric processes, but short with respect to oceanic ones that involve the deep ocean. While a timescale of 5000 yr is long compared to oceanic processes, it is short with respect to cryospheric ones that involve the dynamics of the Antarctic ice sheets. Therefore, one needs to associate each ECS estimate from observational or model data to a reference timescale; see Fig. 38²¹ for an illustrative cartoon, and a discussion by Rohling *et al.* (2012) and von der Heydt *et al.* (2016).

C. Transient climate response (TCR)

TCR has recently gained popularity in the study of climate change and climate variability because of its ability to help capture the evolution in time of climate change by addressing the transient rather than asymptotic response of the climate

²¹From <http://www.realclimate.org/index.php/archives/2013/01/on-sensitivity-part-i/>.

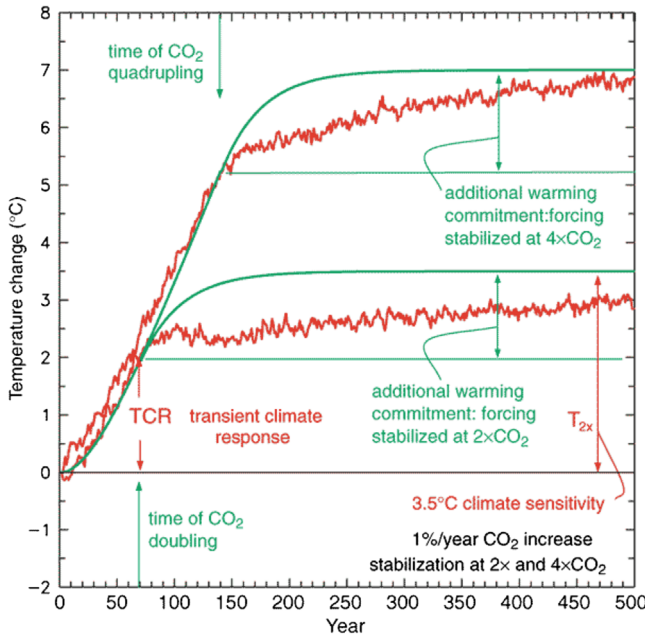


FIG. 39. Transient climate response (TCR) estimates from two climate models: (i) a coupled atmosphere-ocean GCM, red (nonsmooth) curves, and (ii) a simple illustrative model with no energy exchange with the deep ocean, green (smooth) curves. Time on abscissa from start of CO_2 concentration increase at preindustrial levels, with change in global mean temperature on the ordinate. The “additional warming commitment” corresponds to temperature stabilization at a given CO_2 level, i.e., at $2 \times \text{CO}_2$ or $4 \times \text{CO}_2$. From IPCC, 2001.

system to perturbations in the CO_2 concentration. TCR is defined as the change in the globally averaged surface air temperature recorded at the time at which CO_2 has doubled due to an increase at a 1% annual rate, i.e., roughly after 70 yr, having started at a given reference value T_0 (Otto *et al.*, 2013). This operational definition agrees well with the standard IPCC-like simulation protocols, and TCR is therefore better suited than ECS to test model outputs against observational datasets from the industrial era.

As shown in Fig. 39, the TCR is found to have been lower than the ECS because of the climate system’s thermal inertia,

which is dominated by the ocean’s heat capacity. A smaller effective heat capacity c in Eq. (13a), and hence a shorter relaxation time, would result in the TCR catching up much faster with the ECS, as is the case in regular diffusion processes; see Fig. 40(a). Assuming linearity in the response, a relationship must clearly exist between ECS and TCR. Thus far this inference has been based, by and large, on heuristic arguments of timescale separation between climate feedbacks, not rigorous derivations (Otto *et al.*, 2013); it is derived more systematically in Sec. IV.E.

D. Beyond climate sensitivity

The standard viewpoint on climate sensitivity previously discussed is associated with the idea that the climate is in equilibrium in the absence of external perturbations. In the setting of deterministic, autonomous dynamical systems, this view can be described by the change in the position of a fixed point $\mathbf{X}_0 = \mathbf{X}_0(\mu)$ as a function of a parameter μ .

We illustrate in Fig. 40 the difference between the ways that a change in a parameter can affect a climate model’s behavior in the case of equilibrium solutions [see Fig. 40(a)] versus more complex dynamical behavior [see Figs. 40(b) and 40(c)]. Assume that the climate state is periodic, i.e., it lies on a limit cycle, rather than being a fixed point, as in Fig. 40(a). In this case, climate sensitivity can no longer be defined by a single scalar $\partial\bar{T}/\partial\mu$ but needs four scalars, the sensitivity of the mean temperature along with that of the limit cycle’s frequency, amplitude, and phase, or more, e.g., the orbit’s ellipticity too.

But the internal climate variability can be better described in terms of strange attractors than by fixed points or limit cycles. Moreover, the presence of time-dependent forcing, deterministic as well as stochastic, introduces additional complexities into the proper definition of climate sensitivity. It is thus apparent that a rigorous definition of climate sensitivity requires considerably more effort.

Ghil (2015) proposed measuring the change in the overall properties of the attractor before and after the change in forcing by computing the *Wasserstein distance* d_W between the two invariant measures. The Wasserstein distance or “earth mover’s distance” d_W quantifies the minimum effort in morphing one

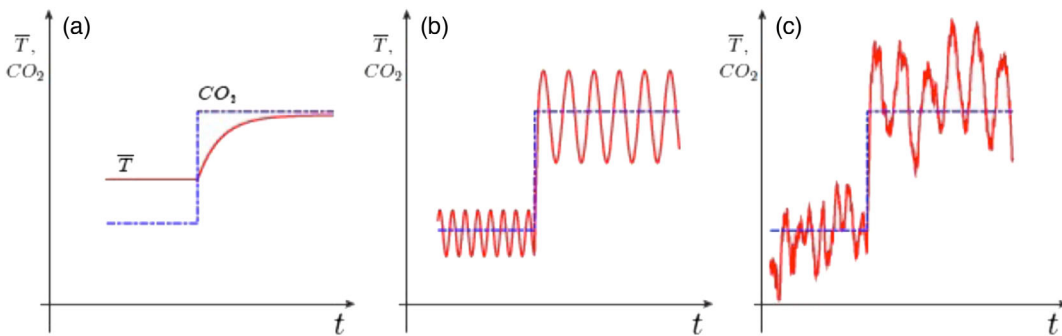


FIG. 40. Climate sensitivity (a) for an equilibrium model, (b) for a nonequilibrium, oscillatory model, and (c) for a nonequilibrium model featuring chaotic dynamics and stochastic perturbations. As a forcing (atmospheric CO_2 concentration, blue dash-dotted line) changes suddenly, global temperature (red thick solid line) undergoes a transition. (a) Only the mean temperature \bar{T} changes. (b) The amplitude, frequency, and phase of the oscillation change too. (c) All details of the invariant measure, as well as the correlations at all orders, are affected. From Ghil, 2017.

measure into another one of equal mass on a metric space, like an n -dimensional Euclidean space (Dobrushin, 1970).

Monge (1781) originally introduced this distance to study a problem of military relevance. Roughly speaking, d_W represents the total work needed to move the “dirt” (i.e., the measure) from a trench you are digging to another one you are filling, over the distance between the two trenches. In general, the shape of the two trenches and the depth along the trench, i.e., the support of the measure and its density, can differ. Robin, Yiou, and Naveau (2017) and Vissio and Lucarini (2018b) recently showed the effectiveness of applying this idea to climate problems.

E. A general framework for climate response

A major use of state-of-the-art climate models is to produce projections of climate change taking into account different possible future scenarios of emission of greenhouse gases and pollutants like aerosols, as well as changes in land use, which has substantial impacts on the terrestrial carbon cycle. Not only are projections needed for quantities like the global average surface air temperature, but detailed information on spatially and temporally is needed for a multitude of practical needs; see, for instance, Fig. 18.

The ECS concept is well suited for describing the properties of equilibrium solutions of heuristically simplified equations for the climate system, like Eq. (13a), and has clear intuitive appeal, as in Fig. 40(a). But it also has the following basic scientific limitations:

- It addresses long-term climatic changes only and no detailed temporal information, an issue only partially addressed by the information provided by the TCR.
- It addresses changes in the globally averaged surface air temperature only and no spatial information at the regional scale or at different levels of the atmosphere, the ocean, or the soil.
- It cannot discriminate between radiative forcings resulting from different physical and chemical processes, e.g., differences resulting from changes in aerosol versus GHG concentration: these two forcings impact shortwave and longwave radiation differently and their effects depend in distinct ways on the atmospheric level.

We thus try to address these shortcomings by taking the complementary points of view of nonequilibrium statistical mechanics and dynamical-systems theory. The setting of nonautonomous and of stochastically forced dynamical systems allows one to examine the interaction of internal climate variability with the forcing, whether natural or anthropogenic; it also helps provide a general definition of climate response that takes into account the climate system’s nonequilibrium behavior, its time-dependent forcing, and its spatial patterns.

1. Pullback attractors (PBAs)

The climate system experiences forcings that vary on many different timescales [see, e.g., Saltzman (2001)], and its feedbacks also act on multiple timescales ; see, e.g., Ghil and Childress (1987). Hence, defining rigorously what climate

response to forcing, versus intrinsic variability, actually requires some care. Observed variations can be related to the presence of natural periodicities such as the daily and the seasonal cycle and orbital forcings; to rapid, impulsive forcings such as volcanic eruptions; or to slow modulations to the parameters of the system, as in the case of anthropogenic climate change.

For starters, consider a dynamical system in continuous time

$$\dot{x} = F(x, t) \quad (50)$$

on a compact manifold $\mathcal{Y} \subset \mathbb{R}^d$; here $x(t) = \phi(t, t_0)x(t_0)$, with initial state $x(t_0) = x_0 \in \mathcal{Y}$. The evolution operator $\phi(t, t_0)$ is assumed to be defined for all $t \geq t_0$, with $\phi(s, s) = \mathbf{1}$, and it thus generates a two-parameter semigroup. In the autonomous case, time-translational invariance reduces the latter to a one-parameter semigroup since $\forall t \geq s \phi(t, s) = \phi(t - s)$. In the nonautonomous case, in other terms there is an absolute clock.

We are interested in forced and dissipative systems such that, with probability 1, initial states in the remote past are attracted at time t toward $\mathbf{A}(t)$, a time-dependent family of geometrical sets that define the system’s PBA. In the autonomous case, $\mathbf{A}(t) \equiv \mathbf{A}_0$ is the time-independent attractor of the system, and it is known to support, under suitable conditions, a physical measure $\mu(dx)$ (Eckmann and Ruelle, 1985; Ledrappier and Young, 1988).²²

Such a PBA can also be constructed when random forcing is present [see, e.g., Arnold (1988) and references therein],

$$dx = F(x, t)dt + g(x)d\eta, \quad (51)$$

where $\eta = \eta(t; \omega)$ is a Wiener process, while ω labels the particular realization of this random process and $d\eta(t)$ is commonly referred to as white noise. The noise can be multiplicative, and one then uses the Itô calculus for the integration of Eq. (51).

In the random case, the PBA $\mathbf{A}(t; \omega)$ is commonly referred to as a random attractor. A more detailed and mathematically rigorous discussion of these concepts appears in Chekroun, Simonnet, and Ghil (2011), Carvalho, Langa, and Robinson (2013), and the appendix of Ghil, Chekroun, and Simonnet (2008). Careful numerical applications of PBAs to explain the wind-driven circulation and the THC are now available (Sevăruec and Fedorov, 2015; Pierini, Ghil, and Chekroun, 2016; Pierini, Chekroun, and Ghil, 2018).

In the purely deterministic case, the theory of nonautonomous dynamical systems goes back to the skew-product flows of Sell (1967, 1971). A concept that is closely related to

²² Among invariant measures, a natural measure is one obtained by flowing a volume forward in time, and a physical measure is one for which the time average equals the ensemble average almost surely with respect to the Lebesgue measure; moreover, physical implies natural. A particular class of invariant measures of interest are Sinai-Ruelle-Bowen (SRB) measures [see, e.g., Young (2002)], and an important result is that, for a system with no null Lyapunov exponents, except the one corresponding to the flow, an ergodic SRB measure is physical.

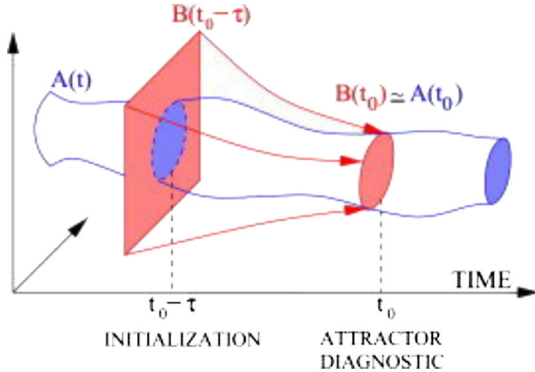


FIG. 41. A cartoon depicting the pullback attractor (PBA) for a nonautonomous system as in Eq. (50). The set \mathbf{B} of finite Lebesgue measure, initialized at time $t = t_0 - \tau$, evolves toward the set $\mathbf{A}(t_0)$. The construction is exact in the limit $\tau \rightarrow \infty$; for a random attractor, see Ghil, Chekroun, and Simonnet (2008), Figs. A.1 and A.2. Adapted from Sevellec and Fedorov, 2015.

PBAs is that of snapshot attractors; it was introduced in a more intuitive and less rigorous manner to the physical literature by Romeiras, Grebogi, and Ott (1990). Snapshot attractors have also been used for studying time-dependent problems of climatic relevance (Bódai, Károlyi, and Tél, 2011, 2013; Bódai and Tél, 2012; Drótós, Bódai, and Tél, 2015).

Note that in the most recent IPCC reports (IPCC, 2001, 2007, 2014a) and according to the standard protocols described in Sec. II.D.2, future climate projections are virtually always performed using as initial states the final states of sufficiently long simulations of historical climate conditions. As a result, it is reasonable to assume that the pullback time τ , as defined in Fig. 41, is large enough, and that the covariance properties of the associated $\mathbf{A}(t)$ sets are therefore well approximated.

2. Fluctuation dissipation and climate change

The fluctuation-dissipation theorem (FDT) has its roots in the classical theory of many-particle systems in thermodynamic equilibrium. The idea is simple: the system's return to equilibrium will be the same whether the perturbation that modified its state is due to a small external force or to an internal, random fluctuation. The FDT thus relates natural and forced fluctuations of a system; see, e.g., Kubo (1957, 1966). It is a cornerstone of statistical mechanics and has applications in many areas; see, Marconi *et al.* (2008) and references therein.

We emphasized in Sec. III.B that even when the climate system is in a steady state it is not at all in thermodynamic equilibrium; see, e.g., Lucarini and Ragone (2011) and Ghil (2019). Still, Leith (1975) showed that the FDT applies to a 2D or QG turbulent flow with two integral invariants, kinetic energy E and enstrophy Z , under some additional assumptions of normal distribution of the realizations and stationarity. Soon thereafter, Bell (1980) showed that the FDT still seemed to work for a highly truncated version of such a model, even in the presence of dissipative terms that invalidate the thermodynamic equilibrium assumption.

The FDT has been applied to the output of climate models to predict the climate response to a steplike increase of the

solar irradiance (North, Bell, and Hardin, 1993), as well as to increases in atmospheric CO₂ concentration (Cionni, Visconti, and Sassi, 2004; Langen and Alexeev, 2005), while Gritsun and Branstator (2007) and Gritsun, Branstator, and Majda (2008) used it to predict the response of an atmospheric model to localized heating anomalies. Most recently Cox, Huntingford, and Williamson (2018) tried to reduce the uncertainty in the ECS discussed in Sec. IV.B by a systematic FDT application to an ensemble of model outputs, as well as to the observed instrumental climate variability.

The FDT-based response of the system to perturbations in the previous examples reproduces the actual changes at a good qualitative rather than strictly quantitative level. An important limitation of these insightful studies is the use of a severely simplified version of the FDT that is heuristically constructed by taking a Gaussian approximation for the invariant measure of the unperturbed system. This approximation amounts to treating the climate as being in thermodynamic equilibrium; see also Majda, Gershgorin, and Yuan (2010), who specifically addressed the applicability of the FDT in a reduced phase space.

To address the problem of Gaussian approximation, Cooper and Haynes (2011) proposed constructing a kernel-based approximation of the actual invariant measure of the unperturbed system and then used Eq. (56) to construct the system's Green's function. This approach has been applied successfully in an extremely low-dimensional system, but its robustness may be limited by the kernel's arbitrary cutoff not being able to account for the smaller scales of the invariant measure's fine structure.

3. Ruelle response theory

FDT generalizations to systems out of equilibrium have been developed since the early 1950s; see, e.g., Kubo (1966). But a particularly fruitful change in point of view was provided by Ruelle (1998, 1999, 2009), who considered the problem in the setting of dynamical-systems theory, rather than that of statistical mechanics. The former point of view is justified in this context by the so-called chaotic hypothesis (Gallavotti and Cohen, 1995), which states, roughly, that chaotic systems with many degrees of freedom possess a physically relevant invariant measure, as discussed in Sec. IV.E.1.

It is common in practice to assume that a time-dependent measure $\mu_t(dx)$ associated with the evolution of the dynamical system given by Eq. (50) does exist. Still, computing the expectation value of measurable observables with respect to this measure is in general far from trivial and requires setting up a large ensemble of initial states in the Lebesgue measurable set \mathbf{B} mentioned earlier. Moreover, PBAs and the physical measures they support set the stage for predicting the system's sensitivity to small changes in the forcing or the dynamics.

Ruelle's response theory allows one to compute the change in the measure $\mu(dx)$ of an autonomous Axiom A system due to weak perturbations of intensity ϵ applied to the dynamics, in terms of the unperturbed system's properties. The basic idea behind it is that the invariant measure of such a system, although supported on a strange attractor, is differentiable with respect to ϵ . Baladi (2008) reviewed extensions of response

theory and provided a complementary approach to it, while [Lucarini \(2016\)](#) estimated its radius of convergence in ϵ .

The establishment of a rigorous response theory is somewhat simpler in a sense if one considers stochastic instead of strictly deterministic processes ([Haller, 2010](#)). Recently, [Wormell \(2019\)](#) clarified the link between the deterministic and stochastic perspectives.

The nonautonomous version of the Ruelle response theory allows one to calculate the time-dependent measure $\mu_t(dx)$ on the PBA by computing the time-dependent corrections to it with respect to a reference state $x(t) = \tilde{x}(t)$. This provides a fairly general formulation for the climate system's response to perturbations.

Let us assume that we can write

$$\dot{x} = F(x, t) = F(x) + \epsilon X(x, t), \quad (52)$$

where $\forall t \in \mathbb{R}$ and $\forall x \in \mathcal{Y} \subset \mathbb{R}^d$, $|\epsilon X(x, t)| \ll |F(x)|$. Hence, we can take $F(x)$ as the background dynamics and $\epsilon X(x, t)$ as a perturbation. We treat here only the case of deterministic dynamics; see [Lucarini \(2012\)](#) for stochastic perturbations. As shown by [Lucarini, Ragone, and Lunkeit \(2017\)](#), we can restrict our analysis without loss of generality to the separable case of $F(x, t) = F(x) + \epsilon X(x)T(t)$.

To evaluate the expectation value $\langle \Psi \rangle^\epsilon(t)$ of a measurable observable $\Psi(x)$ with respect to the measure $\mu_t(dx)$ of the system governed by Eq. (50), one writes

$$\langle \Psi \rangle^\epsilon(t) = \int \Psi(x) \mu_t(dx) = \langle \Psi \rangle_0 + \sum_{j=1}^{\infty} \epsilon^j \langle \Psi \rangle_0^{(j)}(t). \quad (53)$$

Here $\langle \Psi \rangle_0 = \int \Psi(x) \bar{\mu}(dx)$ is the expectation value of Ψ with respect to the SRB invariant measure $\bar{\mu}(dx)$ of the autonomous dynamical system $\dot{x} = F(x)$. We restrict ourselves here to the linear correction term, which can be written as

$$\begin{aligned} \langle \Psi \rangle_0^{(1)}(t) &= \int \int_0^\infty \Lambda S_0^\tau \Psi(x) T(t - \tau) d\tau \bar{\mu}(dx); \\ &= \int_0^\infty G_{\Psi, X}^{(1)}(\tau) T(t - \tau) d\tau. \end{aligned} \quad (54)$$

The Green's function $G_{\Psi, X}^{(1)}(\tau)$ in Eq. (54) is given by

$$G_{\Psi, X}^{(1)}(\tau) = \int \Theta(\tau) \Lambda S_0^\tau \Psi(x) \bar{\mu}(dx), \quad (55)$$

where $\Lambda(\bullet) = X \cdot \nabla(\bullet)$ and $S_0^t(\bullet) = \exp(tF \cdot \nabla)(\bullet)$ is the semigroup of unperturbed Koopman operators,²³ (\cdot) denotes the inner product in \mathcal{Y} , and the Heaviside distribution $\Theta(\tau)$ enforces causality. If the unperturbed invariant measure $\bar{\mu}(dx)$ is smooth with respect to the standard Lebesgue measure, one has $\bar{\mu}(dx) = \tilde{\mu}(x)dx$, with $\tilde{\mu}(x)$ the density, and the Green's function can be written as follows:

²³In discrete-time dynamics given by $x_{k+1} = g(x_k)$, the Koopman operator is a linear operator acting on observables $h: \mathcal{Y} \rightarrow \mathbb{R}$ via $Uh(x) = h(g(x))$. In continuous-time dynamics like Eq. (50), this operator is replaced by a semigroup of operators, as in Eq. (55); see [Budivsić, Mohr, and Mezić \(2012\)](#).

$$\begin{aligned} G_{\Psi, X}^{(1)}(\tau) &= \Theta(\tau) \int \frac{-\nabla \cdot [\tilde{\mu}(x)X]}{\tilde{\mu}(x)} S_0^\tau \Psi(x) \tilde{\mu}(x) dx \\ &= \Theta(\tau) \mathcal{C}(\Phi, S_0^\tau \Psi). \end{aligned} \quad (56)$$

Here $\Phi = -\{\nabla \cdot [\tilde{\mu}(x)X]\}/\tilde{\mu}(x)$ and $\mathcal{C}(A, S_0^\tau B)$ is the τ -lagged correlation between the variables A and B , and the average of Φ vanishes. Note that Eq. (56) is the appropriate generalization of the FDT for the nonautonomous, out-of-equilibrium system (52).

Given any specific choice of the forcing's time dependency $T(t)$ in Eqs. (52)–(54) and measuring the linear correction term $\langle \Psi \rangle_0^{(1)}(t)$ from a set of experiments, the same equations allow one to derive the appropriate Green's function. Therefore, using the output of a specific set of experiments or of GCM simulations, we achieve predictive power for any temporal pattern of the forcing $X(x)$.

Consider now the Fourier transform of Eq. (54):

$$\langle \Psi \rangle_0^{(1)}(\omega) = \chi_{\Psi, X}^{(1)}(\omega) T(\omega), \quad (57)$$

where we introduce the susceptibility $\chi_{\Psi, X}^{(1)}(\omega) = \mathcal{F}[G_{\Psi, X}^{(1)}]$, defined as the Fourier transform of the Green's function $G_{\Psi, X}^{(1)}(t)$. Under suitable integrability conditions, the fact that the Green's function $G_{\Psi, X}^{(1)}$ is causal is equivalent to saying that its susceptibility obeys the so-called Kramers-Kronig relations ([Ruelle, 2009; Lucarini and Sarno, 2011](#)); these provide integral constraints that link the real and imaginary parts so that $\chi_{\Psi, X}^{(1)}(\omega) = i\mathcal{P}(1/\omega) \star \chi_{\Psi, X}^{(1)}(\omega)$, where $i = \sqrt{-1}$, \star indicates the convolution product, and \mathcal{P} stands for integration by parts. Extensions to the case of higher-order susceptibilities are also available ([Lucarini et al., 2005; Lucarini, 2008a, 2009a; Lucarini and Colangeli, 2012](#)).

Instead of studying merely individual trajectories, one can study the evolution of ensembles of trajectories to obtain probabilistic estimates. The evolution of the measure ρ driven by the dynamical system $\dot{x} = F(x)$ is described by the transfer or Perron-Frobenius operator \mathcal{L}_0^t ([Baladi, 2000; Villani, 2009; Chekroun et al., 2014](#)), which is the adjoint of the Koopman or composition operator S_0^t ; it is defined as follows:

$$\int \mathcal{L}_0^t \rho(x) \Psi(x) dx = \int \rho(x) S_0^t \Psi(x) dx. \quad (58)$$

Assuming that no degeneracies are present, the generator of the semigroup $\{\mathcal{L}_0^t\}$ is the so-called Liouville operator L and it satisfies $\partial_t \rho = -\nabla(\rho F) = L\rho$.

Let $\{(\sigma_k, \rho_k): k = 1, \dots, \infty\}$ be the eigenpairs of L . Then the eigenvalues of \mathcal{L}_0^t are given by $\{\exp(\sigma_k t)\}$, with the same eigenvectors $\{\rho_k\}$. Correspondingly, the invariant measure $\bar{\mu}$ is the eigenvector having the null eigenvalue $\sigma_1 = 0$ for L or $\forall t \geq 0$ unit eigenvalue of \mathcal{L}_0^t . Note that $\forall k \geq 2 \Re(\sigma_k) < 0$, which implies exponential decay of correlations for all the system's smooth observables, with an asymptotic rate that is given by the largest value of $\Re(\sigma_k)$, $k \geq 2$. Moreover, the presence of a small spectral gap between the unit eigenvalue of \mathcal{L}_0^t and its other eigenvalues within the unit disk leads to a

small radius of expansion for Ruelle's perturbative approach (Chekroun *et al.*, 2014; Lucarini, 2016).

It turns out that if one neglects the essential part of the spectrum, the susceptibility can be written as

$$\chi_{\Psi,X}^{(1)}(\omega) = \sum_{k=1}^{\infty} \frac{\alpha_k \{\Psi, X\}}{\omega - \sigma_k}, \quad (59)$$

where the factor α_k evaluates how the response of the system to the forcing X for the observable Ψ projects on the eigenvector $\{\rho_k\}$. The constants $\pi_k = i\sigma_k$ are usually referred to as Ruelle-Pollicott poles (Pollicott, 1985; Ruelle, 1986). Note that Eq. (59) implies that the Green's function corresponding to the susceptibility can be written as a weighted sum of exponential functions if one neglects possible degeneracies.²⁴

4. Climate change prediction via Ruelle response theory

A somewhat different approach to constructing the climate response to forcings focuses on computing it directly from Eq. (55) without relying on the applicability of the FDT, which fails in certain cases of geophysical relevance; see, e.g., Gritsun and Lucarini (2017). The difficulty in applying this direct approach lies in the fact that the formula contains contributions from both stable and unstable directions in the tangent space (Ruelle, 2009).

Evaluating the contribution of the unstable directions is especially hard; hence, Abramov and Majda (2007) proposed a blended approach that also uses the FDT. Using adjoint methods in the direct approach has yielded promising results (Wang, 2013). Faced with the so-called cold-start problem of climate simulations, Hasselmann *et al.* (1993) suggested a heuristic approach to computing a climate model's Green's function and applied it to study the relaxation to steady state of a coupled GCM's globally averaged surface temperatures.

Lucarini and Sarno (2011), Ragone, Lucarini, and Lunkeit (2016), and Lucarini, Ragone, and Lunkeit (2017) proposed evaluating the Green's function using an experimental but rigorous approach suggested by standard optics laboratory practice (Lucarini *et al.*, 2005). The idea is to use a set of carefully selected probe experiments, typically, steplike increases of the parameter of interest, to construct the Green's function and then, exploiting Eq. (55), use this operator to predict the response of the system to a temporal pattern of interest for the forcing.

Given a set of forced climate simulations and a background unperturbed one, such an approach allows one to construct the Green's function's response operators for as many observables

as desired, global as well as local in space. Such a tool kit allows one to treat a continuum of scenarios of temporal patterns forcings, thus providing a general framework for improving climate change projections given in the form shown in Fig. 18.

The idea is to consider the set of equations describing an unperturbed climate evolution in the form $\dot{x} = F(x)$, with the vector field $X = X(x)$ in Eq. (52) as the 3D radiative forcing associated with the increase of CO₂ concentration, and $\epsilon T(t)$ its time modulation. By plugging $T(t) = \epsilon \Theta(t)$ into Eq. (54), we have, for any climatic observable Ψ ,

$$\frac{d}{dt} \langle \Psi \rangle_0^{(1)}(t) = \epsilon G_{\Psi,[\text{CO}_2]}^{(1)}(t). \quad (60)$$

We estimate $\langle \Psi \rangle_0^{(1)}(t)$ by taking the system's average of response over an ensemble of initial states and use the previous equation to derive our estimate of $G_{\Psi,[\text{CO}_2]}^{(1)}(t)$ by assuming linearity in the response.

Note that these Green's functions are specifically related to changes in the atmospheric CO₂ concentration, rather than to a generic radiative forcing. Indeed, for each climatic variable, the response to changes in the solar irradiance, e.g., via modulation of the parameter μ in Eq. (13), is different from the impact of changes in the CO₂ concentration because the details of the radiative forcing are extremely different in the two cases. Thus, geoengineering proposals that aim to reduce solar irradiance by injecting sulphate aerosols into the stratosphere [see, e.g., Smith and Wagner (2018)] rely on flawed scientific reasoning (Lucarini, 2013; Bódai, Lucarini, and Lunkeit, 2020), are of dubious practical help (Proctor *et al.*, 2018), and are hardly defensible from an ethical perspective (Lawrence *et al.*, 2018).

Ragone, Lucarini, and Lunkeit (2016) derived, moreover, a closed formula relating the TCR and the ECS. Indeed, with the definition of TCR(τ) given at the beginning of Sec. IV.C, one gets

$$\begin{aligned} & \text{ECS} - \text{TCR}(\tau) \\ &= \text{INR}(\tau) \\ &= \Delta \tilde{R}_{2 \times \text{CO}_2} \times \mathcal{P} \int_{-\infty}^{\infty} \chi_{T_s,[\text{CO}_2]}^{(1)}(\omega') \\ & \quad \times \frac{1 + [\sin(\omega' \tau/2)/(\omega' \tau/2)] \exp[-i\omega' \tau/2]}{2\pi i \omega} d\omega'. \end{aligned} \quad (61)$$

The difference between ECS and TCR is a weighted integral of the susceptibility, accounting for the contribution of processes and feedbacks occurring at different timescales. The integral in Eq. (61) yields $\chi_{T_s,[\text{CO}_2]}^{(1)}(0)$ if $\tau \rightarrow 0$ [i.e., TCR(0) = 0], decreases with τ , and vanishes in the limit $\tau \rightarrow \infty$. INR(τ) is a measure of the system's inertia at the timescale τ due to the overall contribution of the internal physical processes and characteristic timescales of the relevant climatic subsystems.

Figure 42 illustrates a climate prediction obtained by applying the previously mentioned response theory to the

²⁴Note that Eq. (59) mirrors the quantum-mechanical expressions for the electric susceptibility of atoms or molecules. In the latter case, the summation involves all eigenstate pairs of the system's unperturbed Hamiltonian operator; in each term, the pole's imaginary part corresponds to the energy difference between the pair of considered eigenstates, and the real part is the so-called linewidth of the transition, whose inverse is the lifetime. Finally, the numerator is its so-called dipole strength (Cohen-Tannoudji, Dupont-Roc, and Grynberg, 2007).

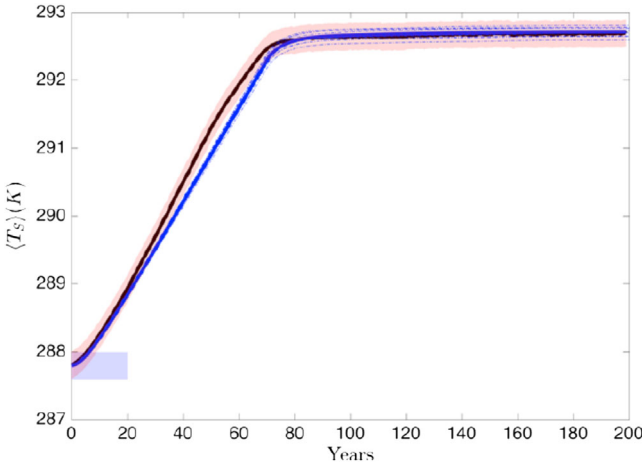


FIG. 42. Comparison between the climate model simulation (black line) and response theory prediction (blue line) for a TCR experiment using PlaSim, a GCM of intermediate complexity. The CO₂ concentration was ramped up by 1% per year to double its initial value. The upper and lower limit of the light-shaded bands are computed as 2 standard deviations of the ensemble distribution. From Lucarini, Ragone, and Lunkeit, 2017.

open-source model PlaSim,²⁵ an atmospheric GCM of intermediate complexity coupled with a mixed-layer ocean model (Fraedrich *et al.*, 2005; Fraedrich, 2012). The figure shows good agreement between (a) the ensemble average of 200 simulations where the CO₂ concentration is increased at the rate of 1% until doubling (black curve), and then kept constant, and (b) the prediction done by convolving the Green's function of Eq. (60) with the time pattern of the forcing (blue curve). Note that the temperature increase predicted at year 70, when doubling of the CO₂ is reached, gives as estimate the TCR $\simeq 4.1$ K (blue curve). The true value of the TCR $\simeq 4.3$ K is given by the black line. The TCR is indeed smaller than the ECS $\simeq 4.8$ K, which corresponds to a good approximation to the temperature increase predicted at year 200.

The power of response theory lies in the fact that once the Green's function of interest has been computed one can predict the future evolution of bespoke observables, defined as needed. Furthermore, Lucarini (2018) showed that it is possible to use certain classes of observables as surrogate forcings of other observables, in the spirit of the linear feedback analysis of Eq. (44). Given the notoriously more difficult prediction of precipitation, Lucarini, Ragone, and Lunkeit (2017) found that predictions of changes in the globally averaged precipitation can be as good as those of the temperature.

Proceeding from global predictions to more localized ones, Fig. 43 shows the outcome of predicting the change in the zonal averages of the surface temperature. It is clear that response theory does a good job in reproducing the spatial patterns of temperature change, except for an underestimate of the temperature change in the high latitudes on the scale of few decades. Indeed, such a mishap is due the strong polar amplification of the warming due to the ice-albedo

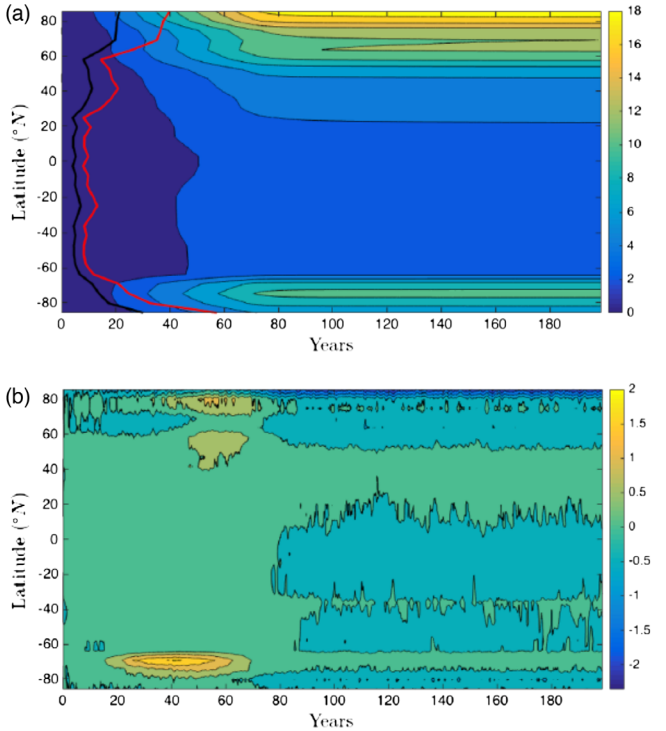


FIG. 43. Patterns of climate response for the zonal average of the surface temperature. (a) Prediction via response theory (red and black lines are not relevant in this context). (b) Difference between the ensemble average of the direct numerical simulations and the predictions obtained using the response theory. From Lucarini, Ragone, and Lunkeit, 2017.

feedback, which can be qualitatively captured only by a linear approach like the one used by Lucarini, Ragone, and Lunkeit (2017). A major limitation of the investigations by Ragone, Lucarini and Lunkeit (2016) and Lucarini, Ragone, and Lunkeit (2017) was the use of a model unable to represent explicitly the dynamical processes of the global ocean. More recently, Lembo, Lucarini, and Ragone (2020) proved the effectiveness of response theory in predicting the future climate response to CO₂ on a vast range of temporal scales, from interannual to centennial, and for very diverse climatic variables, including those representing the strength of the Atlantic Ocean's meridional overturning circulation and of the ACC.

5. Slow correlation decay and sensitive parameter dependence

Equation (59) implies that resonant amplification occurs if the forcing acts as a frequency ω that is close to the imaginary part of a subdominant Ruelle-Pollicott pole π_k , $k \geq 2$, that has a small real part and corresponds therewith to a sharp spectral feature, i.e., for some $k \geq 2$,

$$|\omega - \Im(\pi_k)| \ll \omega, \quad |\Re(\pi_k)| \ll \omega, \quad (62)$$

because the system's susceptibility is greatly enhanced at such an ω . Conditions (62) are easily satisfied for a broadband forcing and a system that has a small spectral gap. Conversely, as discussed after Eq. (58), the presence of a small spectral gap is associated with a slow decay of correlation for smooth

²⁵See <http://tiny.cc/zgk0bz>.

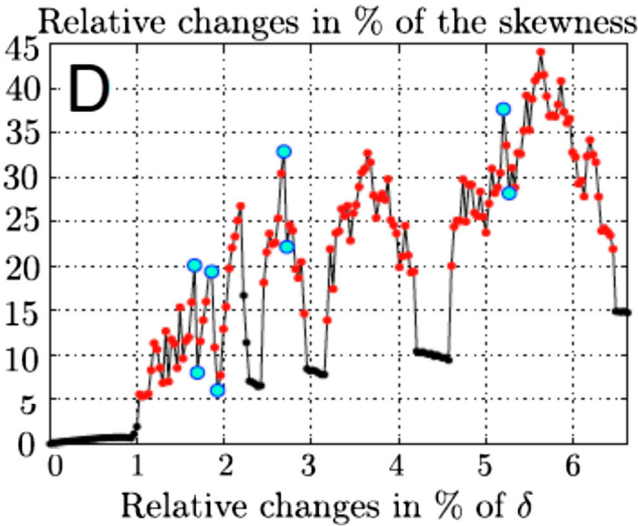


FIG. 44. Rough dependence (red dots) of the skewness of the equatorial ocean temperature's distribution with respect to changes in the parameter δ that controls the travel time of equatorially trapped waves in a simplified ENSO model; see text for details. Black points refer to nonchaotic windows where the parameter dependence is smooth; cyan points indicate particularly sharp jumps in the parameter dependence. From Chekroun *et al.*, 2014.

observables. We now provide two examples that show how linear response breaks down for forced systems possessing slow decay of correlations due to a small spectral gap in the unperturbed dynamics.

The first example is due to Chekroun *et al.* (2014), who investigated the response of the highly simplified ENSO model of Jin and Neelin (1993), to which Jin, Neelin, and Ghil (1994) added periodic forcing that led to chaotic behavior. Chekroun *et al.* focused on how the response changes when one varies the model parameter δ that controls the travel time of the equatorially trapped waves, which play an essential role in the ENSO mechanism. As shown in Fig. 44, Chekroun *et al.* (2014) found that when the spectral gap is small the system exhibits rough dependence of its properties with respect to small modulations of the parameters since Ruelle's perturbative expansion breaks down even for an extremely small intensity of the forcing.

The second example shows the importance of correlation slowdown near saddle-node bifurcation points in the PlaSim model discussed in Sec. IV.E.4. This intermediate-complexity model is multistable: its bifurcation diagram with respect to the solar insolation parameter μ is similar to Fig. 21; see Lucarini, Fraedrich, and Lunkeit (2010a) and Lucarini *et al.* (2013). PlaSim's bifurcation diagram is reproduced in Fig. 45(a), where the present climate $S = S_0 = 1360 \text{ W m}^{-2}$ is denoted by a bullet and the bifurcation points associated with the transition from the warm to the snowball state W-SB and from the snowball to the warm state SB-W are indicated by solid arrowheads. For a comparison with Fig. 21, note that $\mu = S/S_0$ there.

Tantet *et al.* (2018) investigated PlaSim's response to changes in the solar irradiance for $S < S_0$. They found that as the W-SB transition nears, the lag correlation for a

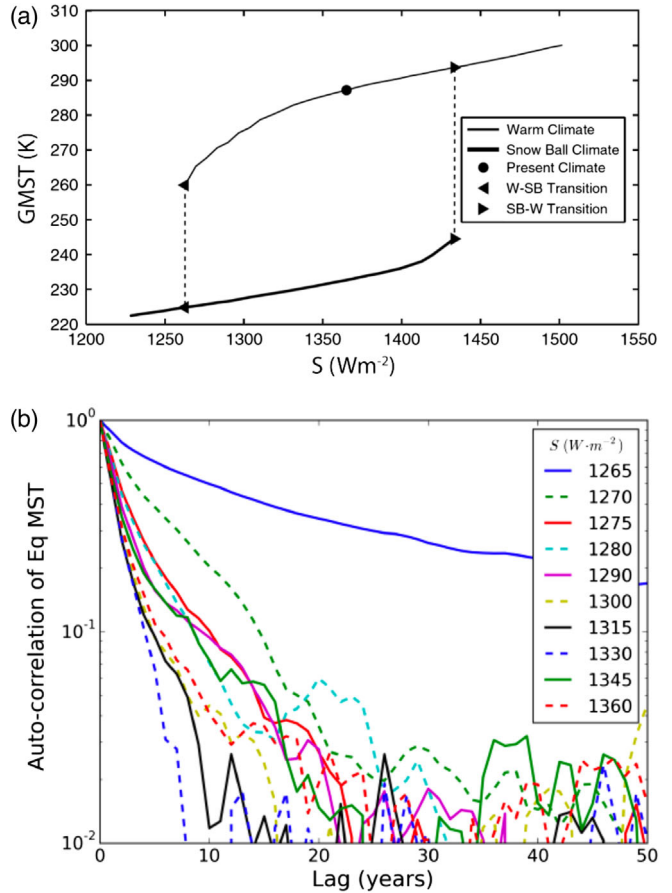


FIG. 45. Slowdown of correlations near a saddle-node bifurcation point in the PlaSim model. (a) The model's bifurcation diagram as a function of the value of the solar irradiance S . The critical transitions warm to snowball and snowball to warm as well as the present-day conditions are indicated. From Lucarini, Fraedrich, and Lunkeit, 2010a. (b) Decay of correlation of the equatorial mean surface temperature for various values of the solar irradiance S . The decay becomes considerably slower as S approaches the critical value of $S \approx 1265 \text{ W m}^{-2}$. From Tantet *et al.*, 2018.

large-scale observable, namely the average equatorial near-surface air temperature, decays more and more slowly as a result of a narrowing spectral gap. Indeed, near the saddle-node bifurcations, the response of the system to perturbations is significantly amplified and, by definition, becomes singular exactly at the bifurcation point.

More generally, Scheffer *et al.* (2009) proposed a set of “early warning signals” (EWSs) that occur when a dynamical system approaches a critical transition. Correlation slowdown is one of the main signals, and it is verified in the Tantet *et al.* (2018) case for the back-to-back saddle-node bifurcations that make up the backbone of the PlaSim model's hysteresis cycle. Colon, Claessen, and Ghil (2015), though, found that in a predator-prey system—modeled either by a set of coupled ODEs or by an agent-based model—more complex critical transitions can behave differently than in the simplest saddle-node case.

Biggs, Carpenter, and Brock (2009) provided a broader perspective on EWSs in the generic codimension-1

bifurcations in multidimensional systems. The literature on EWSs, their successes, their failures, when they work and when they do not, is rich and beyond the scope of this review.

These considerations naturally lead us to an investigation of the climate system's global stability properties and its critical transitions, which are the subject of Sec. V.

V. CRITICAL TRANSITIONS AND EDGE STATES

In Sec. III, we introduced several types of bifurcations that involve transitions between two or more regimes: saddle-node bifurcations whose pairing can lead to coexistence of two stable steady states (fixed points), pitchfork bifurcations that in the presence of a mirror symmetry can lead from one stable symmetric steady state to the coexistence of two steady states that are mirror images of each other, Hopf bifurcations that lead from a stable steady state to a stable periodic solution (limit cycle) and then again from the stable limit cycle to a stable torus on which an infinity of quasiperiodic solutions live, and nonlocal bifurcations associated with the existence of homoclinic and heteroclinic orbits that lead to chaotic regimes.

Successive-bifurcation scenarios (Eckmann, 1981; Ghil and Childress, 1987; Dijkstra and Ghil, 2005; Dijkstra, 2013) that involve several of these bifurcations and additional ones lead from solutions with high symmetry in space and time to successively more complex and chaotic ones. We saw in Sec. III that such bifurcation scenarios shed considerable light on the phenomenology of large-scale atmospheric, oceanic, and coupled ocean-atmosphere flows. Finally, in Secs. III.G and IV.E, we introduced stochastic effects into the nonlinearly deterministic setting recalled previously and outlined the role of PBAs and of the invariant measures they support in the theory of nonautonomous and random dynamical systems (NDSs and RDSs).

Recently the interest in bifurcations in the climate and environmental sciences has significantly increased due to the introduction of the concept of tipping points from the social sciences (Gladwell, 2000; Lenton *et al.*, 2008). A tipping point sounds a lot more threatening than a bifurcation point, especially when dealing with a hurricane or dramatic and irreversible climate change.

Beyond the linguistic effectiveness of the term, it does also generalize the bifurcation concept in the context of open systems that are modeled mathematically by NDSs or RDSs. As we saw in Secs. III and II, the climate system, as well as its subsystems, namely, the atmosphere, ocean, biosphere, and cryosphere, are open and exchange time-dependent fluxes of mass, energy, and momentum with each other and with outer space. Hence, it is quite appropriate to consider this generalization. Following Ashwin *et al.*

(2012), one distinguishes among three kinds of tipping points, as shown in Table II.

The investigation of systems possessing multiple attractors, which may include fixed points, limit cycles, strange attractors, and PBAs or random attractors, is an active area of research encompassing mathematics as well as the natural and socioeconomic sciences. Feudel, Pisarchik, and Showalter (2018), for instance, provide a review that introduces a special issue of the journal Chaos on the topic and sketch several interesting examples. More generally, Kuehn (2011) studied tipping points and critical transitions in the NDS and RDS context.

This section is devoted to providing a general framework for the study of multistability in the Earth system, to forced transitions between different regimes when multistability is present, and to the critical transitions taking place at classical bifurcation and more general tipping points. Recall, for motivation, two cases of multistability in the climate system.

First, Earth as a whole has boundary conditions that arise from its space environment in the solar system that are compatible with at least two competing stable regimes: today's relatively ice-free and warm climate and a deep-freeze or snowball climate; see Sec. III.A. Second, the ocean's THC is, over a broad range of the parameters that control its heat and freshwater budget, bistable, with the current active state coexisting with a greatly reduced or even reversed circulation; see Sec. III.C.

To illustrate the main mathematical and physical aspects of the problem, we choose at first the specific example of coexistence between the warmer Holocene-like state and the much colder snowball state of Earth, as discussed in Secs. III.A and IV.E.5; see, in particular, Figs. 21 and 45(a).

A. Bistability for gradient flows and EBMs

The theory of SDEs and of RDSs provides a comprehensive framework for deriving the probability of occurrence of coexisting regimes in multistable systems and for estimating the probability of stochastic-forcing-triggered transitions between them. A good starting point is gradient flow in the presence of additive white noise.

The governing SDE in this case is

$$dx = -\nabla_x V(x)dt + \epsilon dW, \quad (63)$$

where $x \in \mathbb{R}^d$, the potential $V: \mathbb{R}^d \rightarrow \mathbb{R}$ is sufficiently smooth, and dW is a vector of d independent increments of Brownian motion, while ϵ determines the strength of the noise. The Fokker-Planck equation associated with Eq. (63) describes the evolution of the PDF $p_\epsilon(x, t)$ of an ensemble of trajectories obeying the SDE.

TABLE II. Tipping points in open systems; see also Ashwin *et al.* (2012) and Fig. 46.

| Type | Cause | Mechanism |
|-------------|-------------------------|--|
| B tipping | Bifurcation-due tipping | Slow change in a parameter leads to the system's passage through a classical bifurcation |
| N tipping | Noise-induced tipping | Random fluctuations lead to the system crossing an attractor basin boundary |
| R tipping | Rate-induced tipping | Because of rapid changes in the forcing, the system loses track of a slow change in its attractors |

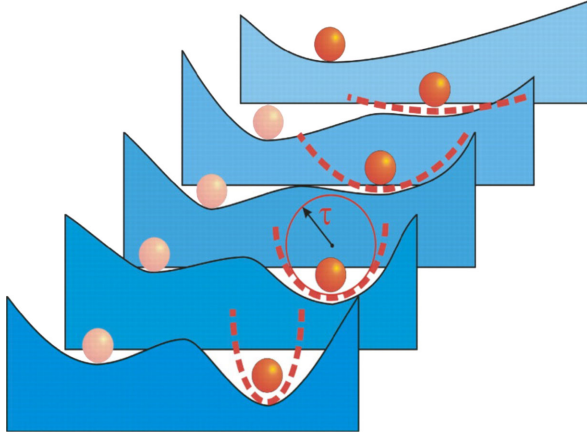


FIG. 46. Schematic diagram of B tipping. As a control parameter is slowly changed, the number of stable equilibria is reduced from 2 to 1. From Lenton *et al.*, 2008.

The stationary solution corresponding to the latter equation's invariant measure $\lim_{t \rightarrow \infty} p_\epsilon(x, t) = p_\epsilon(x)$ is given by a large-deviation law (Varadhan, 1966)

$$p_\epsilon(x) = \frac{1}{Z} \exp \left(-\frac{2V(x)}{\epsilon^2} \right), \quad (64)$$

where Z is a normalization constant. The local minima of the potential V are the stable fixed points of the deterministic dynamics. One obtains them by setting $\epsilon = 0$ in the SDE (63), and they correspond to the local maxima of p . Thus, for instance, the double-well potential of Fig. 20 corresponds to a bimodal PDF.

The mountain pass lemma [see, e.g., Bisgard (2015)] states that the two minima of V that give rise to the two stable fixed points have to be separated by an unstable one of the saddle type, which is a maximum of V in one direction and a minimum in all other ones. Such a saddle looks like a mountain pass on a topographic map (hence the name of the lemma). Ghil and Childress (1987) discussed in their Sec. 10.4 its application to 1D EBMs.

In the limit of weak noise, trajectories starting near a local minimum of V located at $x = x_1$ typically wait a long time before moving to the neighborhood of a different local minimum of V . The transitions are most likely to occur through the lowest energy saddle $x = x_s$ that links the initial basin of attraction to any other basin. Call the corresponding local minimum $x = x_2$.

The optimal path linking x_1 to x_s minimizes the Freidlin and Wentzell (1984) action and is called an instanton. In the weak-noise limit $\epsilon \rightarrow 0$, the persistence time inside the basin of attraction of $x = x_1$ is

$$\bar{\tau}_\epsilon \propto \exp \left(\frac{2[V(x_s) - V(x_1)]}{\epsilon^2} \right), \quad (65)$$

which is referred to as the Kramers (1940) formula.

Assume now, for simplicity, that we deal with a bistable system, as in Fig. 20. If the potential V depends on a slowly varying control parameter ϕ , a B tipping would involve, for

instance, the number of local minima decreasing from 2 to 1, as a local minimum merges with a saddle point at $\phi = \phi_c$. This merging is illustrated in Fig. 46 for a simple 1D case like that of the 0D EBM governed by Eq. (13).²⁶

When the system nears the tipping point, the persistence time in the shallow, metastable minimum is reduced because $\Delta V \equiv V_s - V_1 \rightarrow 0$. Another flag anticipating the tipping point is the increase of the autocorrelation time τ in the metastable state, which is proportional to the inverse of the second derivative of the potential evaluated at the minimum $\bar{\tau}_\epsilon \propto 1/V''_{x_1}$.

These two easily observable phenomena are the simplest manifestation of the slowing-down process (Scheffer *et al.*, 2009), which was discussed in Sec. IV.E.5 when describing the findings of Tantet *et al.* (2018). As indicated in footnote 28 there, the warning signals of the tipping-point approach have been studied mostly in the B -tipping case for saddle-node bifurcations. Much remains to be done in this context for more complex situations that may involve N -tipping, R -tipping, or global bifurcations rather than local ones. For instance, Ditlevsen and Johnsen (2010) analyzed a high-resolution ice-core record and excluded the possibility of interpreting Dansgaard-Oeschger events as B tipping by noting the lack of the two early warning signals mentioned previously. Their results leave us with the alternative of interpreting the associated irregular oscillations [see, e.g., Boers, Ghil, and Rousseau (2018)] either as the result of N tipping for an S-shaped back-to-back saddle-node bifurcation or as B tipping for a Hopf bifurcation; see Fig. 29 and its discussion in Sec. III.E.3 for similar ambiguities in interpreting changes in atmospheric LFV.

Returning to the right-hand side of the 0D EBM of Eq. (13), it can be written as minus the derivative of a potential $V(T)$; see Ghil (1976). The gain factor Λ given in Eq. (47), as well as the ECS, is proportional to the inverse of the second derivative of the potential V evaluated at the local minimum defining the reference climate T_0 , $ECS \propto \Lambda \propto 1/V''_{T_0}$. Hence, near the critical transition a small forcing in the right direction can lead the system to jump to the other basin of attraction, even in the absence of noise. Note, though, that near such a transition the linear stability analysis performed in Eqs. (46) and (47) is no longer valid, and an accurate quantitative analysis of climate response requires taking into account the essential nonlinearity in the problem; see the Zaliapin and Ghil (2010) comments on Roe and Baker (2007).

Determining the saddle point that potentially connects, via instantons, two local minima is not at all trivial when looking at high- or even infinite-dimensional systems. Figure 47 reports the findings of Bódai *et al.* (2015) on the Ghil (1976) 1D EBM. Figure 47(a) shows the bifurcation diagram of the model, in which the control variable is the globally averaged surface air temperature \bar{T} , and the tuning parameter is the insolation parameter $\mu = S/S_0$ introduced in Eq. (13b).

Figure 47(b) shows the zonally averaged temperatures of the 1D model's steady states for the reference conditions $T = T(x)$ at $\mu = 1$. The red and blue lines represent the two

²⁶Note that the number of dimensions in phase space is 1, while that of the model in physical space is 0.

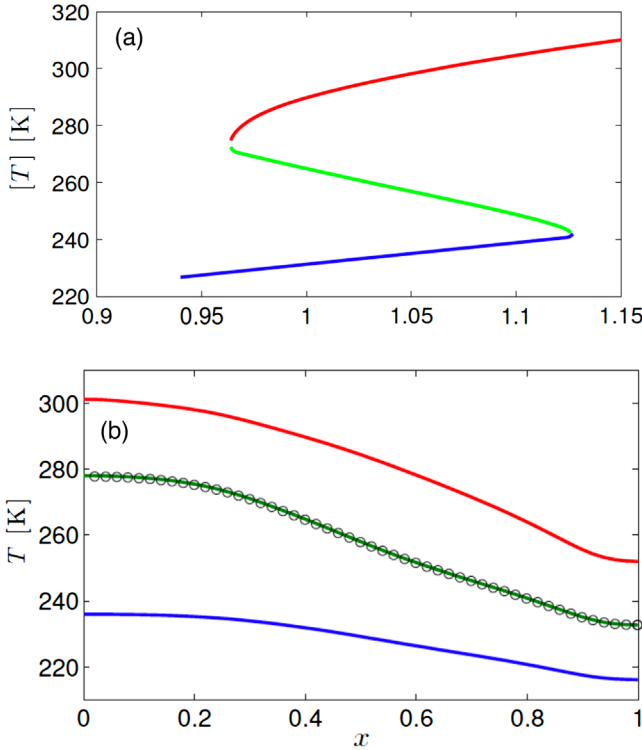


FIG. 47. Bistability for the Ghil-Sellers 1D EBM. (a) Simplified bifurcation diagram for the Ghil (1976) 1D EBM; compare Figs. 21 and 45. The red, blue, and green lines correspond to the globally averaged surface air temperature for the warm, snowball, and melancholia states, respectively, as a function of the relative solar irradiance μ ; see also Arcoya, Diaz, and Tello (1998). (b) Meridional temperature profile for the warm state (red line), snowball state (blue line), and M state (green line) for this model under present-day conditions ($\mu = 1$), with the sine of latitude on the x axis; compare to Ghil (1976), Fig. 3(a). The circles indicate the M -state estimate obtained using the edge tracking method. Adapted from Bódai *et al.*, 2015.

stable solutions, warm W and snowball SB, respectively, while the green line is the unstable solution lying between. Note that at each tipping point the unstable state comes in contact with a stable one and then both disappear, in accordance with the scenario of basin boundary crisis (Ott, 2002). In fact, the lack of stability of the steady-state solution described by the green line is apparent by observing that \bar{T} in Fig. 47(a) decreases with increasing solar radiation, as opposed to the W and SB states, which is clearly not physical (Ghil, 1976; North, Cahalan, and Coakley, 1981) and can be loosely interpreted as the result of a negative heat capacity; see Bódai *et al.* (2015).

B. Finding the edge states

In one phase space dimension, every first-order system $\dot{x} = f(x; \mu)$ is a gradient system since one can always write $V(x; \mu) = -\int f(\xi, \mu) d\xi$. This is not so in two or more dimensions, and one might wonder whether it is possible to compute unstable solutions for more general multistable systems with no gradient property. Scott, Marotzke, and Stone (1999) presented an example of such an unstable stationary

solution in a simple box model of the THC featuring competing stable solutions and no gradient structure. Moreover, the actual computation of the unstable steady state in Fig. 3(a) of Ghil (1976) relied not on the system's potential $V(T(x))$ but on its 1D character in physical space and on a shooting method to solve the Sturm-Liouville equation that results when setting $\partial T(x, t)/\partial t \equiv 0$ in the Ghil-Sellers model. Neither of these approaches (Ghil, 1976; Scott, Marotzke, and Stone, 1999) can easily be extended to more general systems.

In the remainder of this section, we discuss a more general paradigm of multistability for deterministic systems and, subsequently, how this paradigm may be useful for studying the problem of noise-induced transitions between competing states without the simplifying assumption of a gradient, as in Eq. (63).

One can formally introduce general multistable systems as follows. We consider a smooth autonomous continuous-time dynamical system acting on a smooth finite-dimensional compact manifold \mathcal{M} , described by an ODE system of the form $\dot{x} = F(x)$. The system is multistable if it possesses more than one asymptotically stable state, defined by the attractors $\{\Omega_j : j = 1, \dots, J\}$. The asymptotic state of an orbit is determined by its initial state, and the phase space is partitioned between the basins of attraction $\{B_j\}$ of the attractors $\{\Omega_j\}$ and the boundaries $\{\partial B_\ell : \ell = 1, \dots, L\}$ separating these basins.

The basin boundaries can be strange geometrical objects with a codimension smaller than 1. Orbits initialized on the basin boundaries $\{\partial B_\ell\}$ are attracted toward invariant saddles $\{\Pi_{\ell k} : \ell = 1, \dots, L; k = 1, \dots, k_\ell\}$, where we allow for the existence of k_ℓ separate saddles in the basin boundary ∂B_ℓ ; these saddles are often referred to as edge states; see Skufca, Yorke, and Eckhardt (2006) and Schneider, Eckhardt, and Yorke (2007).²⁷ For nongradient flows, the edge states, like the asymptotic states, can feature chaotic dynamics (Grebogi, Ott, and Yorke, 1983; Robert *et al.*, 2000; Ott, 2002; Vollmer, Schneider, and Eckhardt, 2009). Lucarini and Bódai (2017, 2019, 2020) refer to the chaotic edge states as melancholia (M) states. Hence, we cannot expect to easily find edge states and, *a fortiori*, M states for such general multistable systems.

The edge tracking algorithm by Skufca, Yorke, and Eckhardt (2006) and Schneider, Eckhardt, and Yorke (2007) allows one to do so by constructing a shadowing trajectory that leads an orbit starting on the basin boundary toward the corresponding edge state; see Fig. 48. Therein, one uses a bisection method to control the instability associated with the trajectories' divergence from the basin boundary. Bódai *et al.* (2015) first used edge tracking in a geophysical context to reproduce the unstable solution of Ghil (1976) with this more easily generalizable approach; compare to the green line and circles in Fig. 47(b).

Lucarini and Bódai (2017) computed M states for an intermediate-complexity climate model with $O(10^5)$ degrees of freedom that couples PUMA, an atmospheric primitive

²⁷Note that edge states refer to solutions separating long-lived turbulence and laminar flow, rather than the interface between truly separated attractor basins.

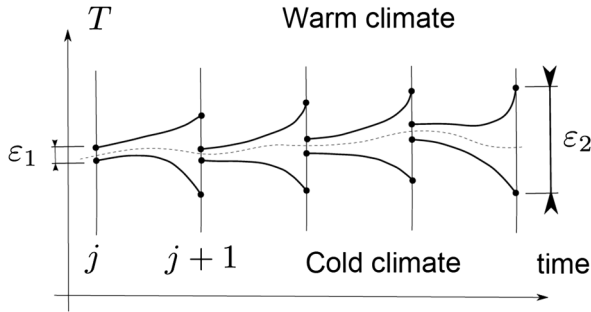


FIG. 48. Schematic diagram of the edge tracking algorithm proposed by Skufca, Yorke, and Eckhardt (2006) and Schneider, Eckhardt, and Yorke (2007) as applied to the 1D EBM of Fig. 47. From Bódai *et al.*, 2015.

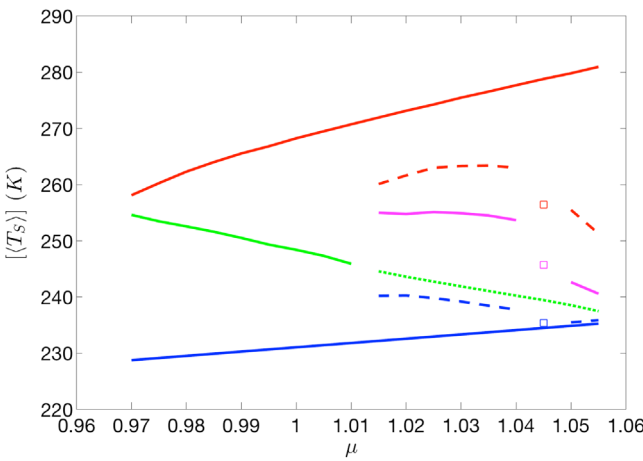


FIG. 49. Bifurcation diagram for the intermediate-complexity climate model in Lucarini and Bódai (2017), drawn for the long-term, globally averaged ocean temperatures $\langle T_S \rangle$. Bistability is found for a large range of values of the control parameter $\mu = S/S_0$. The relevant solid lines are in red for the warm W states, in blue for the snowball SB states, and in green for the melancholia M states, as in Fig. 47. From Lucarini and Bódai, 2019.

equation model (Frisius *et al.*, 1998) with a modified version of the 1D EBM of Ghil (1976) that acts as a surrogate ocean and contributes to meridional heat transport. Figure 49 shows the bifurcation diagram of this climate model, where the $W \rightarrow SB$ tipping point is located near $\mu = 0.98$, while the $SB \rightarrow W$ tipping point is located near $\mu = 1.06$. Just as in the 1D EBM of Fig. 47, the tipping points are associated with basin boundary crises (Ott, 2002).

Over a wide range of μ values, the edge state features chaotic dynamics that arises from the atmospheric model's baroclinic instability; it leads to weather variability and to a limited predictability horizon. Since this instability is much faster than the climatic one due to the ice-albedo feedback, the basin boundary is a fractal set with near-zero codimension, in agreement with results obtained in low-dimensional cases (Grebogi, Ott, and Yorke, 1983; Lai and Tél, 2011). In other words, the basin boundary has almost full Lebesgue measure. As a result, near the basin boundary there is virtually no

predictability on the asymptotic state of the system because infinitesimally close initial states have a high probability of belonging to separate basins of attraction.

C. Invariant measures and noise-induced transitions

As mentioned previously, transitions across the basin boundaries of competing attractors are possible and quite likely in the presence of stochastic perturbations. Noise-induced escape from an attractor has, in fact, long been studied in the natural sciences; see, e.g., Hanggi (1986), Kautz (1987), and Grassberger (1989).

Let us generalize Eq. (63) as follows:

$$dx = F(x)dt + \epsilon s(x)dW. \quad (66)$$

Here $x \in \mathbb{R}^d$, $F(x)dt$ is the drift term given by a vector flow field that admits multiple steady states, as previously discussed, and dW are the increments of a d -dimensional Brownian motion. The volatility matrix $s(x) \in \mathbb{R}^{d \times d}$ is such that $s(x)^T s(x)$ is the covariance matrix of the noise. Finally, the parameter $\epsilon \geq 0$ controls the noise intensity.

Recent extensions of the classical Freidlin and Wentzell (1984) theory (Graham, Hamm, and Tél, 1991; Hamm, Tél, and Graham, 1994; Lai and Tél, 2011) yield results that closely mirror those summarized earlier in the case of gradient flows with additive noise [see Eqs. (64) and (65)], given suitable assumptions on the drift term and the volatility; see, e.g., Lucarini and Bódai (2019, 2020). In the weak-noise limit given by $\epsilon \rightarrow 0$, the invariant measure of the system can be written as a large-deviation law. Formally, one must replace $V(x)$ with a general quasipotential $\Phi(x)$, which depends in a nontrivial way on $F(x)$ and $s(x)$. Moreover, the constant Z in Eq. (64) is replaced by a function $\zeta(x)$, which is relatively unimportant because the behavior of the system depends mostly on the properties of $\Phi(x)$.

Certain general properties of $\Phi(x)$ apply to all choices of the noise law, and once a noise law is chosen one can derive how the properties of the system change as a function of the parameter ϵ . In general, regardless of the noise law, $\Phi(x)$ has local minima supported on the attractors $\{\Omega_j : j = 1, \dots, J\}$ of the deterministic dynamics. Correspondingly, the invariant measure has local maxima on the attractor. Moreover, $\Phi(x)$ has a constant value on the support of each edge state Π_ℓ and each attractor Ω_j .

In the simplest case of $J = 2$ attractors and $L = 1$ edge state in the basin boundary, in the weak-noise limit transitions away from either attractor basin take place exponentially more likely along the instanton connecting the corresponding attractor with the edge state Π_1 . As for the gradient flows in Sec. V.A, instantons can be calculated as minimizers of a suitably defined action (Kautz, 1987; Grassberger, 1989; Kraut and Feudel, 2002; Beri *et al.*, 2005).

Consider now the case in which more than one edge state separates a given Ω_j from the other attractors $\{\Omega_k : k \neq j\}$. Let us denote then by Π_j the edge state for which the value of Φ is lowest. In this case, the most probable exit path connects Ω_j with Π_j , while the other escape channels are basically switched off in the weak-noise limit.

Note that if the attractors and the edge states are more complex sets than isolated points, the instantons connecting them are not unique because, in principle, any point of the attractor can be linked by an instanton to any point of the edge state because the quasipotential is constant on Ω_j and Π_j . Indeed, the edge states are the gateways for the noise-induced escapes from the deterministic basins of attraction, as illustrated in the bistable example with nongradient flow given later.

[Lucarini and Bódai \(2019\)](#) introduced stochastic forcing into the climate model studied by [Lucarini and Bódai \(2017\)](#) as a fluctuating factor of the form $1 + \epsilon dW/dt$, where dW is a Brownian motion that modulates the solar insolation parameter μ . This forcing yields a multiplicative noise law because the energy input into the system depends on the product of μ times the co-albedo $(1 - \alpha)$, where the albedo $\alpha = \alpha(T)$ depends explicitly on the surface air temperature $T = T(x, t)$, which is a state variable of the model; compare with Eq. (13b).

In Fig. 50, we reproduce the estimate by [Lucarini and Bódai \(2019\)](#) of a 2D projection of the invariant measure for $\mu = 1$ from a climate simulation of $\approx 6.0 \times 10^4$ yr with fluctuations in the solar insolation of 1.5% on the scale of 100 yr. The simulation features 92 SB \rightarrow W and W \rightarrow SB transitions, and the measure is projected onto the $([T_S], \Delta T_S)$ plane; here $[T_S]$ is the globally averaged surface air temperature and ΔT_S measures the temperature difference between the surface temperature in the low- and high-latitude regions.

The peaks of the PDFs are close to the W and SB attractors, and the agreement improves even further when considering the two marginal PDFs (top left and bottom right insets). Both

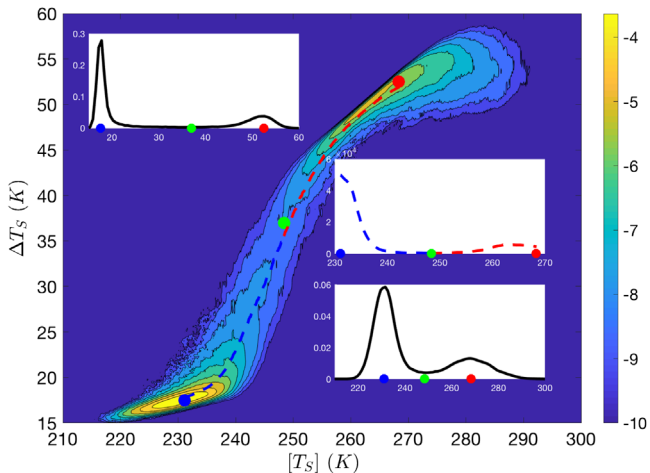


FIG. 50. Invariant measure of the transitions between the two stable regimes of the stochastically perturbed climate model by [Lucarini and Bódai \(2017\)](#) via the M state separating them for $\mu = 1$. (Main panel) Projection of this invariant measure on the reduced space $(T_S, [\Delta T_S])$. W attractor, red dot; SB attractor, blue dot; M state, green dot. Red and blue dashed lines plot the $W \rightarrow SB$ and $SB \rightarrow W$ instantons, respectively. (Top left inset) Marginal PDF with respect to ΔT_S . (Bottom right inset) Marginal PDF with respect to $[T_S]$. (Center right inset) Probability along the two instantons. From [Lucarini and Bódai, 2019](#).

the $W \rightarrow SB$ and $SB \rightarrow W$ instantons can be estimated: their starting and final points agree well with the attractors and the M state. The instantons follow a path of monotonic descent that closely tracks the crests of the PDF, with the minimum occurring at the M state.

These features are all in excellent agreement with the theoretical predictions for multistable systems with a generalized quasipotential.

D. Nearing critical transitions

The general framework outlined in Sec. V.C is also useful for studying the properties of such systems near a critical transition; see, e.g., [Lucarini and Bódai \(2019\)](#). In Fig. 49, it is clear that $\mu = 0.98$ is close to the $W \rightarrow SB$ tipping point. One finds that at low noise intensities, i.e., at a relative μ fluctuation less than or equal to 1.4% on a centennial scale, it is extremely hard to escape from the SB state. This finding happens to agree with snowball-state simulations that used more detailed models as well; see, e.g., [Crowley, Hyde, and Peltier \(2001\)](#), [Pierrehumbert \(2004\)](#), and [Ghil \(2019\)](#).

Let us then focus on the escape from the W state. [Lucarini and Bódai \(2019\)](#) estimated the expected value of the transition time from the W to the SB state using 50 simulations per noise strength value. These values grow exponentially with the inverse of the square of the parameter ϵ , as predicted by the theory; see Fig. 51(a). Note that the difference between the quasipotential value Φ at the M state and at the W state is equal to half the slope of the straight line, which is in agreement with Eq. (65).

Finally, the escape transition paths from the W state to the M state are plotted in Fig. 51(b). In the weak-noise case of relative μ fluctuation smaller than 1% on a centennial scale, the highest densities of these paths lie quite close to the instanton connecting the W attractor to the M state and follow a path of decreasing probability.

These encouraging results suggest that the underlying methodology of edge tracking and instanton estimation could be applied to observational and reanalysis datasets. As discussed in Sec. III.E.3, the episodic, or particle, approach to atmospheric LFV results in a Markov chain of regimes $\{R_j : j = 1, \dots, J\}$ that involves preferential transition paths $\{\Theta_{j,k} : j = 1, \dots, J; k = 1, \dots, J\}$ between them. Heretofore, these transition paths, as well as the regimes themselves, were estimated by purely statistical methods; see [Ghil et al. \(2019\)](#) and Fig. 29(a). [Deloncle et al. \(2007\)](#) and [Kondrashov et al. \(2007\)](#) applied a random-forest algorithm (Breiman, 2001) to find the best real-time predictors of the next regime in a Markov chain, conditional upon the one currently occupied. The results were quite satisfying for the QG3 model by [Marshall and Molteni \(1993\)](#), and encouraging for an observational dataset of 55 winters of Northern Hemisphere 700-hPa geopotential height anomalies; see [Deloncle et al. \(2007\)](#) and [Kondrashov et al. \(2007\)](#).

E. Chaos-to-chaos transition

Thus far we have seen that critical transitions associated with saddle-node bifurcations and mild generalizations thereof are fairly well understood by now. We conclude this

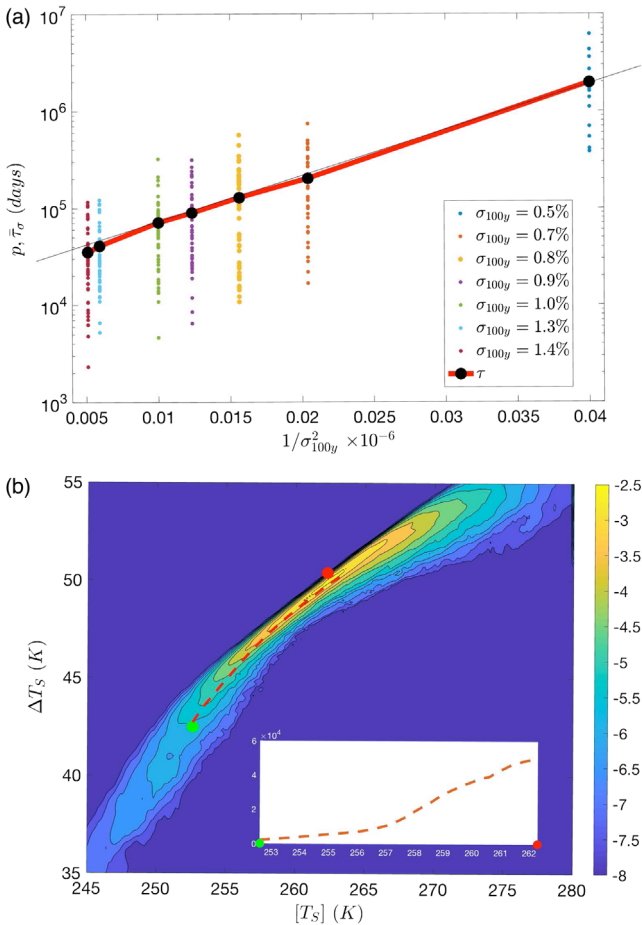


FIG. 51. Escape from the W attractor near the $W \rightarrow \text{SB}$ critical transition of the stochastically perturbed climate model by Lucarini and Bódai (2017) for $\mu = 0.98$. (a) The expected value of the transition time obeys Eq. (65) in the weak-noise regime; the diagram is in log-linear coordinates and σ on the x axis is the relative fluctuation of the solar insolation μ . (b) Estimate of the $W \rightarrow \text{SB}$ instanton and, in the inset, logarithm of the empirical density; both use 50 trajectories that escape to the SB state. From Lucarini and Bódai, 2019.

section and the main part of the text with a somewhat more exotic example of chaos-to-chaos transition for a DDE system with and without stochastic perturbations.

We saw in Secs. II.B.1 and III.E.2 that ENSO plays a key role in the global climate on interannual-to-interdecadal scales. Hence, a large number of relatively simple models thereof exist to better understand its main features. Important mechanisms involved are air-sea interaction, equatorial wave dynamics, and radiative forcing by the seasonal cycle (Bjerknes, 1969). In particular, the role of wave dynamics has been captured by introducing one or two delays into the governing equations of some of the simpler models; see, e.g., Tziperman *et al.* (1994b), and Ghil, Zaliapin, and Thompson (2008) and references therein.

Chekroun, Ghil, and Neelin (2018) studied the PBA of the seasonally forced Tziperman *et al.* (1994b) model both with and without stochastic perturbations. The model has two delays, associated with a positive and a negative feedback; these delays are based on the basin-crossing times of the

eastward-traveling Kelvin waves and the westward-traveling Rossby waves. The control parameter a is the intensity of the positive feedback, and the PBA undergoes a crisis that consists of a chaos-to-chaos transition; they refer to it as a strange PBA since model behavior is chaotic within it in the purely deterministic case.

The changes in the invariant, time-dependent measure μ_t supported on this ENSO model's PBA are illustrated in Figs. 52(a)–52(d) as a function of the control parameter a . The PBA experiences a critical transition at a value a_* , as illustrated in Fig. 52, where $h(t)$ is the thermocline depth anomaly from seasonal depth values at the domain's eastern boundary, with t in years. Here $a = (1.12 + \delta)/180$ and $0.015700 < \delta_* < 0.015707$.

The transition in the Kolmogorov-Smirnov metric of the invariant measure's dependence on the parameter a , i.e., in $\mu_t = \mu_t(a)$, is quite sharp according to Chekroun, Ghil, and Neelin (2018), Fig. 3 (not shown). The singular support of the measure is in full agreement with rigorous mathematical results, as well as with the numerical results (Chekroun, Simonnet, and Ghil, 2011; Ghil, 2017) on the random attractor of the stochastically perturbed Lorenz (1963) convection model.

The change in the PBA is associated with the population lying toward the ends of the elongated filaments apparent in Figs. 52(a)–52(d). This population is due to the occurrence of large warm El Niño and cold La Niña events. Thus, $\mu_t(a)$ encodes faithfully the disappearance of such extreme events as $a \nearrow a_*$.

Note that Mukhin, Loskutov *et al.* (2015) and Mukhin, Kondrashov *et al.* (2015) used neural-network methodology to predict such transitions between two types of chaotic regimes in inverse models learned from time series simulated by ENSO models of increasing complexity. The ENSO models were subjected to a linear change in a parameter meant to represent gradual global warming. Transitions between regimes in the inverse model did occur out of sample, even when the training interval did not contain both types of behavior.

Returning to the results of Chekroun, Ghil, and Neelin (2018), they found that perturbing the Tziperman *et al.* (1994b) model by small additive noise eliminated the crisis. The explanation of this numerical observation is tied to the role played in ENSO dynamics by the interaction between the intrinsic frequency of the coupled ocean-atmosphere system [see, e.g., Neelin *et al.* (1998)] and the seasonal forcing (Jin, Neelin, and Ghil, 1994, 1996; Tziperman *et al.*, 1994b; Ghil, Zaliapin, and Thompson, 2008). This interaction induces the devil's staircase in model frequency, which has plausible counterparts in observations (Ghil and Robertson, 2000).

As shown by Ghil, Chekroun, and Simonnet (2008) in their Appendix B, the devil's staircase step that corresponds to a rational rotation number can be smoothed out by a sufficiently intense noise. In fact, the narrower the devil's staircase step is, the less robust is it to noise perturbations, while wider ones are the most robust. The effect of noise on the paradigmatic example of such a staircase, the standard circle map, was examined in greater depth by Marangio *et al.* (2019).

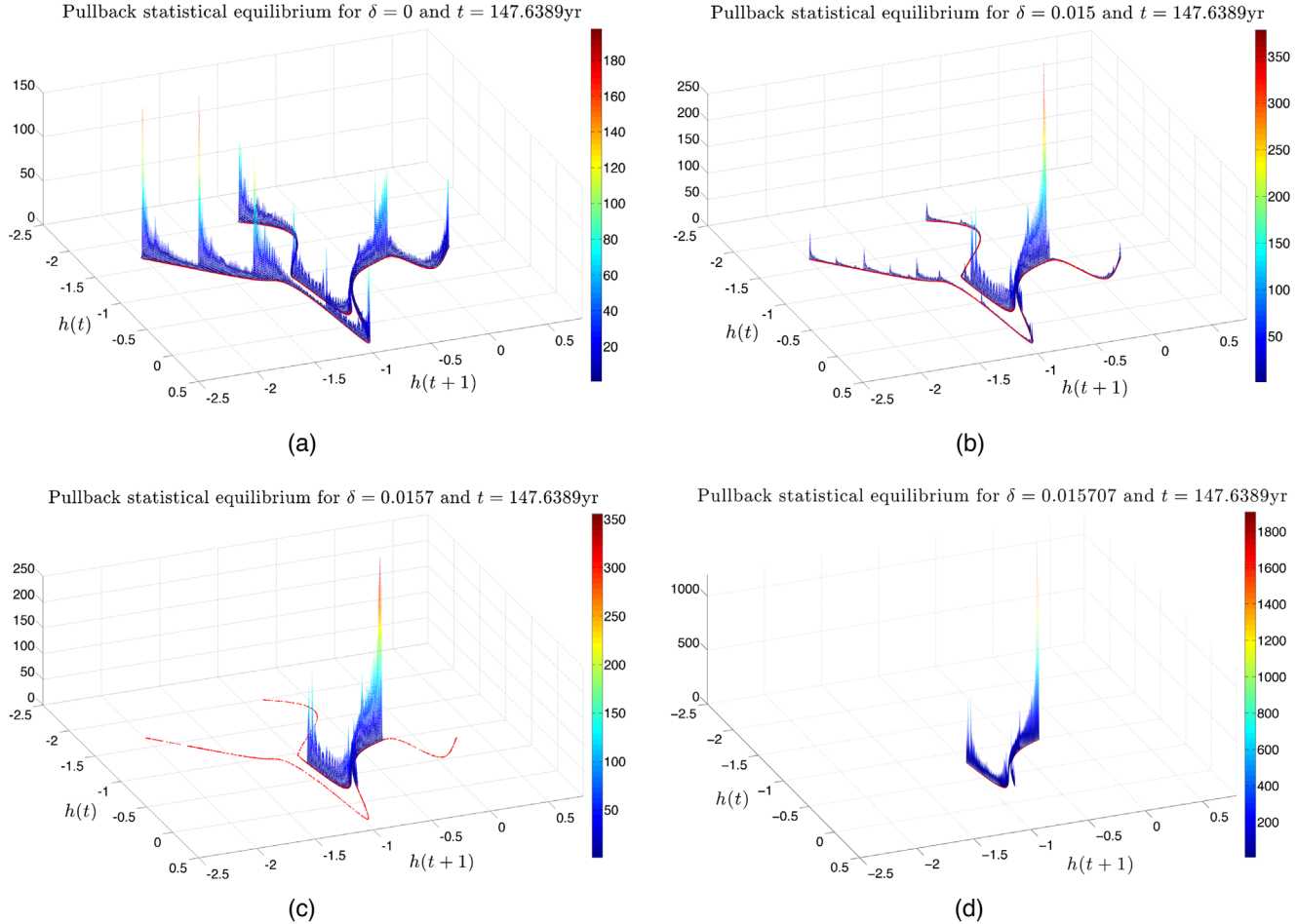


FIG. 52. Embedding of the invariant, time-dependent measure μ_t supported on the PBA associated with the highly idealized ENSO DDE model by Tziperman *et al.* (1994b). The embedding is shown within the $(h(t), h(t+1))$ plane for $a = (1.12 + \delta)/180$, $t \approx 147.64$ yr, and (a) $\delta = 0.0$, (b) $\delta = 0.015\ 00$, (c) $\delta = 0.0157$, and (d) $\delta = 0.015\ 707$. The red curves on the $(h(t), h(t+1))$ plane in the four panels represent the singular support of the measure. From Chekroun, Ghil, and Neelin, 2018.

This example is just one step on the long road of using the tools of nonautonomous and random dynamical systems for a better understanding of major climatic phenomena and processes. Note, however, that the model, while relatively simple, is actually infinite dimensional because of the dependence of a DDE solution on a full interval of initial values on the real axis.

VI. CONCLUSIONS

The goal of this review is to highlight some of the key physical and mathematical ingredients that can help address the description, understanding, and prediction of climate variability and climate change. Complementary aspects of observations, theory, and numerics were taken into consideration. We leaned heavily on dynamical-systems theory and nonequilibrium statistical mechanics and tried to present a coherent picture of the time dependence of the climate system, its multiscale nature, and its multistability.

We emphasized the complex interplay between intrinsic climate variability and the climate's response to perturbations. The topic is, in fact, relevant for three problems of significant scientific relevance: (a) anthropogenic climate change,

(b) coevolution of Earth's climate and the biosphere, and (c) the quest for life on other planets, along with the habitability of our own planet.

The presentation also aimed to show the extent to which basic mathematical and physical tools could help solve the main challenges inherent to the climate sciences. These challenges cannot be overcome merely by increasing the resolution of numerical models and including in them more and more physical and biogeochemical processes. In addition, a balanced interplay of observations, modeling, and theory is definitely needed to achieve the necessary progress.

This review is far from exhaustive: we had to make hard personal choices on the topics to be covered. We want to briefly mention here several additional approaches to the problems at hand that have been developed in recent years.

- *Network theory* [see, e.g., Barrat, Barthelemy, and Vespignani (2008) and Newman (2010)] has provided a novel viewpoint for constructing a parsimonious yet efficient representation of many complex processes taking place in the Earth system; see, e.g., Tsonis and Roebber (2004), Tsonis, Swanson, and Roebber (2006), and Donges *et al.* (2009). Gozolchiani,

Havlin, and Yamasaki (2011) and Wang *et al.* (2013) provided examples of the use of networks for capturing specific climatic processes, while Boers *et al.* (2014) provided an example of applying network theory to climate prediction.

- *Extreme value theory (EVT)* [see, e.g., Embrechts, Klüppelberg, and Mikosch (1999) and Coles (2001)] has been used extensively in studying the statistical properties of rare hydrometeorological events, such as the occurrence of intense rain or extreme temperatures; see Katz, Parlange, and Naveau (2002), Ghil *et al.* (2011), and references therein. Yet this classical methodology has been almost entirely neglected in IPCC reports dedicated to the study of extremes; see IPCC (2012). Recently, though, rapid advances in EVT theory for general observables of chaotic deterministic dynamical systems (Holland *et al.*, 2012; Lucarini, Kuna *et al.*, 2014; Lucarini *et al.*, 2016) have led to the derivation of indicators of weather regimes based on extreme value statistics in the recurrence of atmospheric fields. In addition to the mere classification of such regimes, as mentioned at the end of Sec. V.D, this approach allows one to infer higher or lower instability of these regimes, and hence their lower or higher predictability (Faranda, Messori, and Yiou, 2017; Hochman *et al.*, 2019).
- *Large-deviation theory* [see, e.g., Varadhan (1984) and Touchette (2009)] was first used in the context of geophysical fluid dynamics for studying the self-organization and the multistability of turbulent flows and, specifically, of jet structures (Bouchet and Venaille, 2012; Bouchet, Laurie, and Zaboronski, 2014); see also Secs. V.A and V.C. More recently it has been applied successfully to the study of weather and climate extremes. First, it has helped formulate rare event algorithms able to nudge a climate model toward representing preferentially the class of extreme events of interest (Ragone, Wouters, and Bouchet, 2018). Second, it has provided a solid theoretical and numerical basis for the study of spatially extended or temporally persistent temperature extremes (Gálfy, Lucarini, and Wouters, 2019). Large-deviation theory has also recently been used to study multiscale and coupled atmosphere-ocean instabilities in a hierarchy of climate models (Vannitsem and Lucarini, 2016; De Cruz *et al.*, 2018).
- *Detection and attribution studies.* In a complex system like the climate, inferring causal relationships among events and phenomena is far from obvious. Nonetheless, doing so for well-defined weather and climate events is essential for building simplified models and, at a practical level, for causal attribution of weather- and climate-related events. This is quite important in the case of detection and attribution studies of anthropogenic climate change, especially

when aiming to go beyond changes in mean climate properties, such as globally averaged temperatures, and on to determining to what extent the occurrence of an individual extreme event (e.g., of a hurricane or an extended drought) can be attributed to climate change (Allen, 2003; Adam, 2011).

Methodologies based on the causal counterfactual theory of Pearl (2009) are being increasingly recognized as a key instrument for providing a more rigorous basis for detection and attribution studies; see, e.g., Hannart, Pearl *et al.* (2016). They also seem better suited for defining reliably the link between anthropogenic climate forcing and individual events (Hannart and Naveau, 2018). Combining these methods with those of data assimilation, discussed in Sec. II.A, appears to be well suited to refine the distinction between the factual and counterfactual world that separates causation from the lack thereof; see, e.g., Hannart, Carrassi *et al.* (2016).

- Beyond linear-response theory. As shown in Sec. IV.E, linear-response theory can provide a systematic improvement upon the standard methodology of forward integration of model ensembles with perturbed initial states and parameters. While it does apply to systems out of thermodynamic equilibrium, it is still limited by its linearity to fairly small perturbations in parameters. In Sec. IV.D, we mentioned that one can use the Wasserstein distance to measure arbitrary changes between two invariant measures, whether supported on a time-independent, classical attractor or a time-dependent PBA. One might thus want to apply the PBA-based methodologies herein directly to observational datasets or to the simulations of IPCC-class models, either instead of or in combination with previously tested statistical methods.

In Sec. V.E, we showed that the PBA of an intermediate but still infinite-dimensional ENSO model can undergo a chaos-to-chaos transition that involves major changes in its invariant measure. Moreover, these changes could be connected to a physically quite significant change in model behavior, namely, in the number and size of extreme events, i.e., of the largest warm and cold events. Thus, exploring similarly interesting changes in model PBAs and in the time-dependent invariant measures supported by them appears to be a promising road toward a deeper understanding of climate variability and its interaction with both natural and anthropogenic forcing.

In this review, we have pointed out several open scientific problems; see Ghil (2019) for a historical perspective. An important matter that was left practically untouched, aside from the brief discussion of ENSO and its prediction in Sec. III.E.2, is the tropical atmosphere. Half of Earth's surface lies in the Tropics, between 30° N and 30° S, and much of humanity lives there. As one gets closer to the Equator, the

quasigeostrophic approximation collapses and moist processes take on a much greater importance. Four of the classical references are Palmer (1951), Riehl (1954), Krishnamurti, Stefanova, and Misra (1979), and Yanai (1975). The current literature is too plethoric to marshal here.

We have also alluded, in Sec. I.B, to the increasing importance of the issues discussed herein for the economic well-being of our society and for the political decisions needed to mitigate climate change as well as adapt to it; see, for instance, IPCC (2014a, 2014b). A prudent way to address such decisions requires better estimates of the uncertainties involved; see, e.g., Barnett, Brock, and Hansen (2020). Ghil (2020) provided an introduction to recent efforts at including the nonlinearities and stochasticities discussed herein in coupled climate-economy models for uncertainty quantification.

More broadly, we alluded at the end of Sec. I to the lack of a proper definition of climate and to the efforts to provide a mathematically rigorous definition that would distinguish it from weather. We also mentioned in Sec. III.E.1 the distinction made by Von Neumann (1960) between the short-, medium-, and long-term prediction problem in the climate sciences.

At an even higher level of abstraction, one might wish to recall the parallel drawn by H. Poincaré between the deterministic unpredictability of weather and that of the position of the planets on the ecliptic; see Poincaré (1902), pp. 69 and 70. Harking back to these two giants of both physics and mathematics, we could say that (i) the astronomical ephemerides are the analog of weather and of its short-term prediction, (ii) the problem of climate corresponds to that of the long-term stability of the solar system, and (iii) the secular variations of the orbital configurations in the Solar System are the appropriate counterpart of the slow evolution of the climate system's low-frequency modes of variability (Chown, 2004).

Making these analogies stick at a level that might help determine more reliably climate sensitivity to human activities is a worthwhile effort for the best mathematicians, physicists, and climate scientists.

LIST OF SYMBOLS AND ABBREVIATIONS

| | |
|-------|---|
| ACC | Antarctic Circumpolar Current |
| AR | assessment report |
| AS | Arakawa-Schubert (parametrization) |
| CMIP | Climate Model Intercomparison Project |
| CNs | complex networks |
| DDE | delay-differential equation |
| DNS | direct numerical simulation |
| EBM | energy balance model |
| ECMWF | European Centre for Mid-range Weather Forecasts |
| ECS | equilibrium climate sensitivity |
| ENSO | El Niño–Southern Oscillation |
| EMS | empirical model reduction |
| EWS | early warning signal |
| FDT | fluctuation-dissipation theorem |
| GCM | general circulation model |

| | |
|-------|---|
| GCM | global climate model |
| GFD | geophysical fluid dynamics |
| GHGs | greenhouse gases |
| GLE | generalized Langevin equation |
| IPCC | Intergovernmental Panel on Climate Change |
| LFV | low-frequency variability |
| MJO | Madden-Julian oscillation |
| MOC | meridional overturning circulation |
| MZ | Mori-Zwanzig |
| NAO | North Atlantic Oscillation |
| NCAR | National Center for Atmospheric Research |
| NCEP | National Center for Environmental Prediction |
| NDS | nonautonomous dynamical system |
| NWP | numerical weather prediction |
| NSEs | Navier-Stokes equations |
| ODE | ordinary differential equation |
| PBA | pullback attractor |
| PCMDI | Program for Climate Model Diagnostics and Intercomparison |
| PDE | partial differential equation |
| PNA | Pacific North American (pattern) |
| PSA | Pacific South American (pattern) |
| QG | quasigeostrophic (flow, model) |
| RDS | random dynamical system |
| SDE | stochastic differential equation |
| SPM | Summary for Policy Makers |
| TCR | transient climate response |
| THC | thermohaline circulation |
| UNEP | United Nations Environmental Programme |
| WCRP | World Climate Research Programme |
| WMO | World Meteorological Organization |

ACKNOWLEDGMENTS

We benefited immensely from discussions with many colleagues and friends in the last few years, but we especially want to thank T. Bódai, N. Boers, F. Bouchet, W. A. Brock, M. D. Chekroun, J. I. Díaz, H. A. Dijkstra, D. Faranda, A. Feigin, U. Feudel, K. Fraedrich, G. Froyland, G. Gallavotti, G. Gottwald, A. Gritsun, A. Groth, D. Holm, B. Hoskins, F.-F. Jin, D. Kondrashov, S. Kravtsov, J. Kurths, J. C. McWilliams, J. D. Neelin, S. Pierini, F. Ragone, D. Ruelle, A. Speranza, H. Swinney, O. Talagrand, A. Tantet, S. Vannitsem, J. Yorke, J. Wouters, and I. Zaliapin. Two anonymous reviewers provided constructive comments. M. Cucchi suggested corrections in key formulas when inspecting an earlier version of the manuscript. This review is TiPES contribution no. 19; the TiPES (Tipping Points in the Earth System) project has received funding from the European Union's Horizon 2020 research and innovation program under Grant Agreement No. 820970. This activity has been supported by the EIT Climate-KIC. EIT Climate-KIC is supported by EIT, a body of the European Union. VL also acknowledges the financial

support provided by Horizon 2020 through the projects CRESCENDO (Grant No. 641816) and Blue-Action (Grant No. 727852), and by the Royal Society (Grant No. IEC R2 170001).

REFERENCES

- Abramov, R. V., and A. J. Majda, 2007, “Blended response algorithms for linear fluctuation-dissipation for complex nonlinear dynamical systems,” *Nonlinearity* **20**, 2793–2821.
- Adam, D., 2011, “Climate change in court,” *Nat. Clim. Change* **1**, 127–130.
- Allen, M., 2003, “Liability for climate change,” *Nature (London)* **421**, 891–892.
- Andersen, K. K., *et al.* (North Greenland Ice Core Project Collaboration), 2004, “High-resolution record of Northern Hemisphere climate extending into the last interglacial period,” *Nature (London)* **431**, 147–151.
- Andronov, A. A., and L. S. Pontryagin, 1937, “Structurally stable systems,” *Dokl. Akad. Nauk SSSR* **14**, 247–251.
- Arakawa, A., and W. H. Schubert, 1974, “Interaction of a cumulus cloud ensemble with the large-scale environment. Part I,” *J. Atmos. Sci.* **31**, 674–701.
- Arcaya, D., J. I. Diaz, and L. Tello, 1998, “S-shaped bifurcation branch in a quasilinear multivalued model arising in climatology,” *J. Differ. Equations* **150**, 215–225.
- Arnold, L., 1998, *Random Dynamical Systems* (Springer-Verlag, New York).
- Arnold, Ludwig, 1988, *Random Dynamical Systems* (Springer, New York).
- Arnold, V., 1983, *Geometric Methods in the Theory of Ordinary Differential Equations* (Springer, New York).
- Arnold, V. I., 2003, *Catastrophe Theory* (Springer Nature, Berlin).
- Ashwin, P., S. Wieczorek, R. Vitolo, and P. Cox, 2012, “Tipping points in open systems: Bifurcation, noise-induced and rate-dependent examples in the climate system,” *Phil. Trans. R. Soc. A* **370**, 1166–1184.
- Baladi, V., 2000, *Positive Transfer Operators and Decay of Correlations* (World Scientific, Singapore).
- Baladi, V., 2008, “Linear response despite critical points,” *Nonlinearity* **21**, T81.
- Balmaseda, M. A., *et al.*, 2015, “The ocean reanalyses intercomparison project (ORA-IP),” *J. Oper. Oceanogr.* **8**, s80–s97.
- Barenblatt, G. I., 1987, *Dimensional Analysis* (Gordon and Breach, New York).
- Barnes, E. A., and J. A. Screen, 2015, “The impact of Arctic warming on the midlatitude jetstream: Can it? Has it? Will it?,” *WIREs Clim. Change* **6**, 277–286.
- Barnett, M., W. Brock, and L. P. Hansen, 2020, “Pricing uncertainty induced by climate change,” *Rev. Financ. Stud.* **33**, 1024–1066.
- Barnston, A. G., M. K. Tippett, M. L. Heureux, S. Li, and D. G. DeWitt, 2012, “Skill of real-time seasonal ENSO model predictions during 2002–2011—Is our capability improving?,” *Bull. Am. Meteorol. Soc.* **93**, 631–651.
- Barrat, A., M. Barthélémy, and A. Vespignani, 2008, *Dynamical Processes in Complex Networks* (Cambridge University Press, Cambridge, England).
- Batchelor, G., 1974, *Introduction to Fluid Dynamics* (Cambridge University Press, Cambridge, England).
- Beck, C., 1990, “Brownian motion from deterministic dynamics,” *Physica (Amsterdam)* **169A**, 324–336.
- Bell, T. L., 1980, “Climate sensitivity from fluctuation dissipation: Some simple model tests,” *J. Atmos. Sci.* **37**, 1700–1707.
- Bellenger, H., E. Guilyardi, J. Leloup, M. Lengaigne, and J. Vialard, 2014, “Enso representation in climate models: From CMIP3 to CMIP5,” *Clim. Dyn.* **42**, 1999–2018.
- Bellman, R. E., and K. L. Cooke, 1963, *Differential-Difference Equations* (Rand Corporation, Santa Monica, CA).
- Bengtsson, L., M. Ghil, and E. Källén, 1981, *Dynamic Meteorology: Data Assimilation Methods* (Springer, New York).
- Bensid, S., and J. I. Diaz, 2019, “On the exact number of monotone solutions of a simplified Budyko climate model and their different stability,” *Discrete Contin. Dyn. Syst. B* **24**, 1033.
- Benzi, R., P. Malguzzi, A. Speranza, and A. Sutera, 1986, “The statistical properties of general atmospheric circulation: Observational evidence and a minimal theory of bimodality,” *Q. J. R. Meteorol. Soc.* **112**, 661–674.
- Benzi, R., and A. Speranza, 1989, “Statistical properties of low-frequency variability in the Northern Hemisphere,” *J. Clim.* **2**, 367–379.
- Berger, A., and S. Siegmund, 2003, “On the gap between random dynamical systems and continuous skew products,” *J. Dyn. Differ. Equations* **15**, 237–279.
- Beri, S., R. Mannella, D. G. Luchinsky, A. N. Silchenko, and P. V. E. McClintock, 2005, “Solution of the boundary value problem for optimal escape in continuous stochastic systems and maps,” *Phys. Rev. E* **72**, 036131.
- Berloff, P., A. Hogg, and W. K. Dewar, 2007, “The turbulent oscillator: A mechanism of low-frequency variability of the wind-driven ocean gyres,” *J. Phys. Oceanogr.* **37**, 2363–2386.
- Berner, J., *et al.*, 2017, “Stochastic parameterization: Toward a new view of weather and climate models,” *Bull. Am. Meteorol. Soc.* **98**, 565–588.
- Bhattacharya, K., M. Ghil, and I. L. Vulis, 1982, “Internal variability of an energy-balance model with delayed albedo effects,” *J. Atmos. Sci.* **39**, 1747–1773.
- Biggs, R., S. R. Carpenter, and W. A. Brock, 2009, “Turning back from the brink: Detecting an impending regime shift in time to avert it,” *Proc. Natl. Acad. Sci. U.S.A.* **106**, 826–831.
- Bisgard, J., 2015, “Mountain passes and saddle points,” *SIAM Rev.* **57**, 275–292.
- Bjerknes, J. P., 1969, “Atmospheric teleconnections from the equatorial Pacific,” *Mon. Weather Rev.* **97**, 163–172.
- Bjerknes, V., 1904, “Das Problem der Wettervorhersage, betrachtet vom Standpunkte der Mechanik und der Physik,” *Meteorol. Z.* **21**, 1–7 [“The problem of weather prediction, considered from the viewpoints of mechanics and physics,” *Meteorol. Z.* **18**, 663–667 (2009)].
- Bódai, T., G. Károlyi, and T. Tél, 2013, “Driving a conceptual model climate by different processes: Snapshot attractors and extreme events,” *Phys. Rev. E* **87**, 022822.
- Bódai, T., Gy. Károlyi, and T. Tél, 2011, “A chaotically driven model climate: Extreme events and snapshot attractors,” *Nonlinear Processes Geophys.* **18**, 573–580.
- Bódai, T., V. Lucarini, and F. Lunkeit, 2020, “Can we use linear response theory to assess geoengineering strategies?,” *Chaos* **30**, 023124.
- Bódai, T., V. Lucarini, F. Lunkeit, and R. Boschi, 2015, “Global instability in the Ghil-Sellers model,” *Clim. Dyn.* **44**, 3361–3381.
- Bódai, T., and T. Tél, 2012, “Annual variability in a conceptual climate model: Snapshot attractors, hysteresis in extreme events, and climate sensitivity,” *Chaos* **22**, 023110.

- Boers, N., B. Bookhagen, H. M. J. Barbosa, N. Marwan, J. Kurths, and J. A. Marengo, 2014, "Prediction of extreme floods in the Eastern Central Andes based on a complex networks approach," *Nat. Commun.* **5**, 5199.
- Boers, N., M. Ghil, and D.-D. Rousseau, 2018, "Ocean circulation, ice shelf, and sea ice interactions explain Dansgaard-Oeschger cycles," *Proc. Natl. Acad. Sci. U.S.A.* **115**, E11005–E11014.
- Boiseau, M., M. Ghil, and A. Juillet-Leclerc, 1999, "Trends and interdecadal variability from South-Central Pacific coral records," *Geophys. Res. Lett.* **26**, 2881–2884.
- Bond, G., W. Showers, M. Cheseby, R. Lotti, P. Almasi, P. deMenocal, P. Priori, H. Cullen, I. Hajdas, and G. Bonani, 1997, "A pervasive millennial-scale cycle in the North Atlantic Holocene and glacial climates," *Science* **278**, 1257–1265.
- Bony, S., et al., 2015, "Clouds, circulation and climate sensitivity," *Nat. Geosci.* **8**, 261–268.
- Boos, W. R., and J. V. Hurley, 2013, "Thermodynamic bias in the multimodel mean boreal summer monsoon," *J. Clim.* **26**.
- Bouchet, F., J. Laurie, and O. Zaboronski, 2014, "Langevin dynamics, large deviations and instantons for the quasi-geostrophic model and two-dimensional Euler equations," *J. Stat. Phys.* **156**, 1066–1092.
- Bouchet, F., and J. Sommeria, 2002, "Emergence of intense jets and Jupiter's Great Red Spot as maximum-entropy structures," *J. Fluid Mech.* **464**, 165–207.
- Bouchet, F., and A. Venaille, 2012, "Statistical mechanics of two-dimensional and geophysical flows," *Phys. Rep.* **515**, 227–295.
- Branstator, G., 1987, "A striking example of the atmosphere's leading traveling pattern," *J. Atmos. Sci.* **44**, 2310–2323.
- Breiman, L., 2001, "Random forests," *Mach. Learn.* **45**, 5–32.
- Broecker, W. S., 1991, "The great ocean conveyor," *Oceanography* **4**, 79–89.
- Bryan, F. O., 1986, "High-latitude salinity effects and interhemispheric thermohaline circulations," *Nature (London)* **323**, 301–304.
- Budivsić, M., R. Mohr, and I. Mezić, 2012, "Applied Koopmanism," *Chaos* **22**, 047510.
- Budyko, M. I., 1969, "The effect of solar radiation variations on the climate of the Earth," *Tellus* **21**, 611–619.
- Cane, M. A., and S. E. Zebiak, 1985, "A theory for El Niño and the Southern Oscillation," *Science* **228**, 1085–1087.
- Caraballo, T., and X. Han, 2017, *Applied Nonautonomous and Random Dynamical Systems: Applied Dynamical Systems* (Springer Science+Business Media, New York).
- Carrassi, A., M. Bocquet, L. Bertino, and G. Evensen, 2018, "Data assimilation in the geosciences: An overview of methods, issues, and perspectives," *WIREs Clim. Change* **9**, e535.
- Carton, J. A., and B. S. Giese, 2008, "A reanalysis of ocean climate using Simple Ocean Data Assimilation (SODA)," *Mon. Weather Rev.* **136**, 2999–3017.
- Carvalho, A. N., J. Langa, and J. C. Robinson, 2013, "The pullback attractor," in *Attractors for Infinite-Dimensional Non-autonomous Dynamical Systems*, Applied Mathematical Sciences Vol. 182 (Springer New York), pp. 3–22.
- Cessi, P., 2019, "The global overturning circulation," *Annu. Rev. Mar. Sci.* **11**, 249–270.
- Cessi, P., and G. R. Ierley, 1995, "Symmetry-breaking multiple equilibria in quasi-geostrophic, wind-driven flows," *J. Phys. Oceanogr.* **25**, 1196–1205.
- Cessi, P., and W. R. Young, 1992, "Multiple equilibria in two-dimensional thermohaline circulation," *J. Fluid Mech.* **241**, 291–309.
- Chang, C. P., M. Ghil, M. Latif, and J. M. Wallace, Eds., 2015, *Climate Change: Multidecadal and Beyond* (World Scientific, Singapore).
- Chang, K-II, M. Ghil, K. Ide, and C-C. A. Lai, 2001, "Transition to aperiodic variability in a wind-driven double-gyre circulation model," *J. Phys. Oceanogr.* **31**, 1260–1286.
- Charney, J. G., 1947, "The dynamics of long waves in a baroclinic westerly current," *J. Meteorol.* **4**, 136–162.
- Charney, J. G., 1971, "Geostrophic turbulence," *J. Atmos. Sci.* **28**, 1087–1095.
- Charney, J. G., A. Arakawa, D. J. Baker, B. Bolin, R. E. Dickinson, R. M. Goody, C. E. Leith, H. M. Stommel, and C. I. Wunsch, 1979, *Carbon Dioxide and Climate: A Scientific Assessment* (National Academy of Sciences, Washington, DC).
- Charney, J. G., and J. G. DeVore, 1979, "Multiple flow equilibria in the atmosphere and blocking," *J. Atmos. Sci.* **36**, 1205–1216.
- Charney, J. G., R. Fjørtoft, and J. von Neumann, 1950, "Numerical integration of the barotropic vorticity equation," *Tellus* **2**, 237–254.
- Charney, J. G., M. Hale, and R. Jastrow, 1969, "Use of incomplete historical data to infer the present state of the atmosphere," *J. Atmos. Sci.* **26**, 1160–1163.
- Charney, J. G., J. Shukla, and K. C. Mo, 1981, "Comparison of a barotropic blocking theory with observation," *J. Atmos. Sci.* **38**, 762–779.
- Chavanis, P. H., and J. Sommeria, 1996, "Classification of self-organized vortices in two-dimensional turbulence: The case of a bounded domain," *J. Fluid Mech.* **314**, 267–297.
- Chekroun, M. D., M. Ghil, and J. D. Neelin, 2018, "Pullback attractor crisis in a delay differential ENSO model," in *Advances in Non-linear Geosciences*, edited by A. Tsonis (Springer, New York), pp. 1–33.
- Chekroun, M. D., J. D. Neelin, D. Kondrashov, J. C. McWilliams, and M. Ghil, 2014, "Rough parameter dependence in climate models and the role of Ruelle-Pollicott resonances," *Proc. Natl. Acad. Sci. U.S.A.* **111**, 1684–1690.
- Chekroun, M. D., E. Simonnet, and M. Ghil, 2011, "Stochastic climate dynamics: Random attractors and time-dependent invariant measures," *Physica (Amsterdam)* **240D**, 1685–1700.
- Chen, F., and M. Ghil, 1996, "Interdecadal variability in a hybrid coupled ocean-atmosphere model," *J. Phys. Oceanogr.* **26**, 1561–1578.
- Cheng, X., and J. M. Wallace, 1993, "Cluster analysis of the Northern Hemisphere wintertime 500 pHa height field: Spatial patterns," *J. Atmos. Sci.* **50**, 2674–2696.
- Chorin, A., and P. Stinis, 2007, "Problem reduction, renormalization, and memory," *Commun. Appl. Math. Comput. Sci.* **1**, 1–27.
- Chorin, A. J., O. H. Hald, and R. Kupferman, 2002, "Optimal prediction with memory," *Physica (Amsterdam)* **166D**, 239–257.
- Chown, M., 2004, "Chaotic heavens," *New Sci.* **181**, 32–35.
- Cionni, I., G. Visconti, and F. Sassi, 2004, "Fluctuation dissipation theorem in a general circulation model," *Geophys. Res. Lett.* **31**, <https://doi.org/10.1029/2004GL019739>.
- Cohen-Tannoudji, C., J. Dupont-Roc, and G. Grynberg, 2007, *Photons and Atoms: Introduction to Quantum Electrodynamics* (Wiley, New York).
- Coles, S., 2001, *An Introduction to Statistical Modeling of Extreme Values* (Springer Science+Business Media, New York).
- Colon, C., D. Claessen, and M. Ghil, 2015, "Bifurcation analysis of an agent-based model for predator-prey interactions," *Ecol. Modell.* **317**, 93–106.
- Compo, G. P., et al., 2011, "The twentieth century reanalysis project," *Q. J. R. Meteorol. Soc.* **137**, 1–28.
- Cooper, F. C., and P. H. Haynes, 2011, "Climate sensitivity via a nonparametric fluctuation-dissipation theorem," *J. Atmos. Sci.* **68**, 937–953.

- Cox, P. M., C. Huntingford, and M. S. Williamson, 2018, "Emergent constraint on equilibrium climate sensitivity from global temperature variability," *Nature (London)* **553**, 319–322.
- Cronin, T. N., 2010, *Paleoclimates: Understanding Climate Change Past and Present* (Columbia University Press, New York).
- Crowley, T. J., W. T. Hyde, and W. R. Peltier, 2001, "CO₂ levels required for deglaciation of a 'near-snowball' Earth," *Geophys. Res. Lett.* **28**, 283–286.
- Cushman-Roisin, B., and J.-M. Beckers, 2011, *Introduction to Geophysical Fluid Dynamics: Physical and Numerical Aspects* (Academic Press, New York), p. 875.
- Cvitanović, Predrag, 1988, "Invariant measurement of strange sets in terms of cycles," *Phys. Rev. Lett.* **61**, 2729–2732.
- Cvitanović, P., and B. Eckhardt, 1991, "Periodic orbit expansions for classical smooth flows," *J. Phys. A* **24**, L237.
- Da Costa, E. D., and A. C. Colin de Verdiére, 2002, "The 7.7 year North Atlantic Oscillation," *Q. J. R. Meteorol. Soc.* **128**, 797–817.
- Dansgaard, W., et al., 1993, "Evidence for general instability of past climate from a 250-kyr ice-core record," *Nature (London)* **364**, 218–220.
- Davini, P., and F. D'Andrea, 2016, "Northern Hemisphere atmospheric blocking representation in global climate models: Twenty years of improvements?," *J. Clim.* **29**, 8823–8840.
- De Cruz, L., S. Schubert, J. Demaeyer, V. Lucarini, and S. Vannitsem, 2018, "Exploring the Lyapunov instability properties of high-dimensional atmospheric and climate models," *Nonlinear Processes Geophys.* **25**, 387–412.
- Dee, D. P., et al., 2011, "The ERA-Interim reanalysis: Configuration and performance of the data assimilation system," *Q. J. R. Meteorol. Soc.* **137**, 553–597.
- de Groot, S. R., and P. Mazur, 1984, *Non-Equilibrium Thermodynamics* (Dover, New York).
- Dell'Aquila, A., V. Lucarini, P. M. Ruti, and S. Calmanti, 2005, "Hayashi spectra of the Northern Hemisphere mid-latitude atmospheric variability in the NCEP and ERA-40 reanalyses," *Clim. Dyn.* **25**, 639–652.
- Dell'Aquila, A., P. M. Ruti, S. Calmanti, and V. Lucarini, 2007, "Southern Hemisphere midlatitude atmospheric variability of the NCEP-NCAR and ECMWF reanalyses," *J. Geophys. Res.* **112**, D08106.
- Deloncle, A., R. Berk, F. D'Andrea, and M. Ghil, 2007, "Weather regime prediction using statistical learning," *J. Atmos. Sci.* **64**, 1619–1635.
- Delworth, T., S. Manabe, and R. J. Stouffer, 1993, "Interdecadal variations of the thermohaline circulation in a coupled ocean-atmosphere model," *J. Clim.* **6**, 1993–2011.
- Delworth, T. L., and M. E. Mann, 2000, "Observed and simulated multidecadal variability in the Northern Hemisphere," *Clim. Dyn.* **16**, 661–676.
- Demaeyer, J., and S. Vannitsem, 2017, "Stochastic parametrization of subgrid-scale processes in coupled ocean-atmosphere systems: Benefits and limitations of response theory," *Q. J. R. Meteorol. Soc.* **143**, 881–896.
- Dickey, J. O., M. Ghil, and S. L. Marcus, 1991, "Extratropical aspects of the 40–50 day oscillation in length-of-day and atmospheric angular momentum," *J. Geophys. Res.* **96**, 22643–22658.
- Dijkstra, H. A., 2005, *Nonlinear Physical Oceanography: A Dynamical Systems Approach to the Large Scale Ocean Circulation and El Niño*, 2nd ed. (Springer Science+Business Media, Berlin).
- Dijkstra, H. A., 2007, "Characterization of the multiple equilibria regime in a global ocean model," *Tellus A* **59**, 695–705.
- Dijkstra, H. A., 2013, *Nonlinear Climate Dynamics* (Cambridge University Press, Cambridge, England).
- Dijkstra, H. A., and G. Burgers, 2002, "Fluid mechanics of El Niño variability," *Annu. Rev. Fluid Mech.* **34**, 531–558.
- Dijkstra, H. A., and M. Ghil, 2005, "Low-frequency variability of the large-scale ocean circulation: A dynamical systems approach," *Rev. Geophys.* **43**, RG3002.
- Dijkstra, H. A., and C. A. Katsman, 1997, "Temporal variability of the wind-driven quasi-geostrophic double gyre ocean circulation: Basic bifurcation diagrams," *Geophys. Astrophys. Fluid Dyn.* **85**, 195–232.
- Ditlevsen, P. D., and S. J. Johnsen, 2010, "Tipping points: Early warning and wishful thinking," *Geophys. Res. Lett.* **37**.
- Doblas-Reyes, Francisco J., Javier Garcia-Serrano, Fabian Lienert, Aida Pinto Biescas, and Luis R. L. Rodrigues, 2013, "Seasonal climate predictability and forecasting: status and prospects," *WIREs Clim. Change* **4**, 245–268.
- Dobrushin, R., 1970, "Prescribing a system of random variables by conditional distributions," *Theory Probab. Appl.* **15**, 458–486.
- Donges, J. F., Y. Zou, N. Marwan, and J. Kurths, 2009, "Complex networks in climate dynamics," *Eur. Phys. J. Special Topics* **174**, 157–179.
- Driver, R. D., 1977, *Ordinary and Delay Differential Equations* (Springer-Verlag, New York).
- Drótos, G., T. Bódai, and T. Tél, 2015, "Probabilistic concepts in a changing climate: A snapshot attractor picture," *J. Clim.* **28**, 3275–3288.
- Duane, G. S., C. Grabow, F. Selten, and M. Ghil, 2017, "Introduction to focus issue: Synchronization in large networks and continuous media-data, models, and supermodels," *Chaos* **27**, 126601.
- Duplessy, J-C, and N. J. Shackleton, 1985, "Response of global deep-water circulation to Earth's climatic change 135 000–107 000 years ago," *Nature (London)* **316**, 500–507.
- E, W., and J. Lu, 2011, "Multiscale modeling," *Scholarpedia* **6**, 11527.
- Eade, R., D. Smith, A. Scaife, E. Wallace, N. Dunstone, L. Hermanson, and N. Robinson, 2014, "Do seasonal-to-decadal climate predictions underestimate the predictability of the real world?," *Geophys. Res. Lett.* **41**, 5620–5628.
- Eady, E. T., 1949, "Long waves and cyclone waves," *Tellus* **1**, 33–52.
- Eckmann, J. P., 1981, "Roads to turbulence in dissipative dynamical systems," *Rev. Mod. Phys.* **53**, 643–654.
- Eckmann, J. P., and D. Ruelle, 1985, "Ergodic theory of chaos and strange attractors," *Rev. Mod. Phys.* **57**, 617–656.
- Edwards, P. N., 2010, *A Vast Machine: Computer Models, Climate Data, and the Politics of Global Warming* (MIT Press, Cambridge, MA).
- Egger, J., 1978, "Dynamics of blocking highs," *J. Atmos. Sci.* **35**, 1788–1801.
- Einstein, A., 1905, "On the movement of small particles suspended in a stationary liquid demanded by the molecular-kinetic theory of heat," *Ann. Phys. (Berlin)* **322**, 549–560 [reprinted in *Investigations on the Theory of the Brownian Movement*, edited by R. Furth, and A. D. Cowper (Dover, New York, 1956), p. 122].
- Emanuel, K. A., 1994, *Atmospheric Convection* (Oxford University Press, New York).
- Embrechts, P., C. Klüppelberg, and T. Mikosch, 1999, *Modelling Extremal Events for Insurance and Finance* (Springer-Verlag, New York).
- Epstein, E. S., 1988, "Long-range weather prediction: Limits of predictability and beyond," *Weather Forecast.* **3**, 69–75.

- Esper, J., E. R. Cook, and F. H. Schweingruber, 2002, "Low-frequency signals in long tree-ring chronologies and the reconstruction of past temperature variability," *Science* **295**, 2250–2253.
- Eyring, V., S. Bony, G. A. Meehl, C. A. Senior, B. Stevens, R. J. Stouffer, and K. E. Taylor, 2016, "Overview of the Coupled Model Intercomparison Project Phase 6 (CMIP6) experimental design and organization," *Geosci. Model Dev.* **9**, 1937–1958.
- Eyring, V., et al., 2016, "ESMValTool (v1.0)—A community diagnostic and performance metrics tool for routine evaluation of Earth system models in CMIP," *Geosci. Model Dev.* **9**, 1747–1802.
- Eyring, V., et al., 2019, "ESMValTool v2.0—Extended set of large-scale diagnostics for quasi-operational and comprehensive evaluation of earth system models in CMIP," *Geosci. Model Dev.* **2019**, 1–81.
- Faranda, D., G. Messori, and P. Yiou, 2017, "Dynamical proxies of North Atlantic predictability and extremes," *Sci. Rep.* **7**, 41278.
- Farrell, B. F., and P. J. Ioannou, 1996, "Generalized stability theory. I: Autonomous operators," *J. Atmos. Sci.* **53**, 2025–2040.
- Feliks, Y., M. Ghil, and A. W. Robertson, 2010, "Oscillatory climate modes in the Eastern Mediterranean and their synchronization with the North Atlantic Oscillation," *J. Clim.* **23**, 4060–4079.
- Feliks, Y., M. Ghil, and A. W. Robertson, 2011, "The atmospheric circulation over the North Atlantic as induced by the SST field," *J. Clim.* **24**, 522–542.
- Feliks, Y., M. Ghil, and E. Simonnet, 2004, "Low-frequency variability in the mid-latitude atmosphere induced by an oceanic thermal front," *J. Atmos. Sci.* **61**, 961–981.
- Feliks, Y., M. Ghil, and E. Simonnet, 2007, "Low-frequency variability in the mid-latitude baroclinic atmosphere induced by an oceanic thermal front," *J. Atmos. Sci.* **64**, 97–116.
- Fenichel, N., 1979, "Geometric singular perturbation theory for ordinary differential equations," *J. Differ. Equations* **31**, 53–98.
- Ferranti, L., S. Corti, and M. Janousek, 2015, "Flow-dependent verification of the ECMWF ensemble over the Euro-Atlantic sector," *Q. J. R. Meteorol. Soc.* **141**, 916–924.
- Feudel, U., A. N. Pisarchik, and K. Showalter, 2018, "Multistability and tipping: From mathematics and physics to climate and brain—Minireview and preface to the focus issue," *Chaos* **28**, 033501.
- Fraedrich, K., 2012, "A suite of user-friendly global climate models: Hysteresis experiments," *Eur. Phys. J. Plus* **127**, 53.
- Fraedrich, K., and H. Bottger, 1978, "A wavenumber frequency analysis of the 500 mb geopotential at 50° N," *J. Atmos. Sci.* **35**, 745–750.
- Fraedrich, K., H. Jansen, E. Kirk, U. Luksch, and F. Lunkeit, 2005, "The planet simulator: Towards a user friendly mode," *Meteorol. Z.* **14**, 299–304.
- Francis, J. A., and S. J. Vavrus, 2012, "Evidence linking Arctic amplification to extreme weather in mid-latitudes," *Geophys. Res. Lett.* **39**, L06801.
- Franzke, C. L. E., T. J. O'Kane, J. Berner, P. D. Williams, and V. Lucarini, 2015, "Stochastic climate theory and modeling," *WIREs Clim. Change* **6**, 63–78.
- Freidlin, M. I., and A. D. Wentzell, 1984, *Random Perturbations of Dynamical Systems* (Springer, New York).
- Frisius, T., F. Lunkeit, K. Fraedrich, and I. N. James, 1998, "Storm-track organization and variability in a simplified atmospheric global circulation model," *Q. J. R. Meteorol. Soc.* **124**, 1019–1043.
- Gálfy, V. M., V. Lucarini, and J. Wouters, 2019, "A large deviation theory-based analysis of heat waves and cold spells in a simplified model of the general circulation of the atmosphere," *J. Stat. Mech.* **033404**.
- Gallavotti, G., and E. G. D. Cohen, 1995, "Dynamical ensembles in stationary states," *J. Stat. Phys.* **80**, 931–970.
- Ghil, M., 1976, "Climate stability for a Sellers-type model," *J. Atmos. Sci.* **33**, 3–20.
- Ghil, M., 1989, "Meteorological data assimilation for oceanographers. Part I: Description and theoretical framework," *Dyn. Atmos. Oceans* **13**, 171–218.
- Ghil, M., 1994, "Cryothermodynamics: The chaotic dynamics of paleoclimate," *Physica (Amsterdam)* **77D**, 130–159.
- Ghil, M., 2001, "Hilbert problems for the geosciences in the 21st century," *Nonlinear Processes Geophys.* **8**, 211–222.
- Ghil, M., 2002, "Natural climate variability," in *Encyclopedia of Global Environmental Change*, Vol. 1, edited by T. E. Munn, M. MacCracken, and J. Perry (J. Wiley & Sons, New York), pp. 544–549.
- Ghil, M., 2015, "A mathematical theory of climate sensitivity or, How to deal with both anthropogenic forcing and natural variability?" in *Climate Change: Multidecadal and Beyond*, edited by C. P. Chang, M. Ghil, M. Latif, and J. M. Wallace (World Scientific, Singapore), pp. 31–51.
- Ghil, M., 2017, "The wind-driven ocean circulation: Applying dynamical systems theory to a climate problem," *Discrete Contin. Dyn. Syst. A* **37**, 189–228.
- Ghil, M., 2019, "A century of nonlinearity in the geosciences," *Earth Space Sci.* **6**, 1007–1042.
- Ghil, M., 2020, "Hilbert problems for the geosciences in the 21st century—20 years later," *Nonlinear Processes Geophys.* (in press), <https://doi.org/10.5194/npg-2020-13>.
- Ghil, M., M. D. Chekroun, and E. Simonnet, 2008, "Climate dynamics and fluid mechanics: Natural variability and related uncertainties," *Physica (Amsterdam)* **237D**, 2111–2126.
- Ghil, M., M. D. Chekroun, and G. Stepan, 2015, "A collection on 'Climate dynamics: Multiple scales and memory effects. Introduction,'" *Proc. R. Soc. A* **471**, 20150097.
- Ghil, M., and S. Childress, 1987, *Topics in Geophysical Fluid Dynamics: Atmospheric Dynamics, Dynamo Theory, and Climate Dynamics* (Springer-Verlag, Berlin).
- Ghil, M., A. Groth, D. Kondrashov, and A. W. Robertson, 2019, "Extratropical sub-seasonal-to-seasonal oscillations and multiple regimes: The dynamical systems view," in *Sub-seasonal to Seasonal Prediction: The Gap between Weather and Climate Forecasting*, edited by A. W. Robertson and F. Vitart (Elsevier, New York), Chap. 6, 119–142.
- Ghil, M., M. Hale, and R. Atlas, 1979, "Time-continuous assimilation of remote-sounding data and its effect on weather forecasting," *Mon. Weather Rev.* **107**, 140–171.
- Ghil, M., M. Kimoto, and J. D. Neelin, 1991, "Nonlinear dynamics and predictability in the atmospheric sciences," *Rev. Geophys.* **29**, 46–55.
- Ghil, M., and P. Malanotte-Rizzoli, 1991, "Data assimilation in meteorology and oceanography," in *Advances in Geophysics*, Vol. 33 (Academic Press, New York), pp. 141–266.
- Ghil, M., and K. C. Mo, 1991, "Intraseasonal oscillations in the global atmosphere. Part 1: Northern Hemisphere and tropics," *J. Atmos. Sci.* **48**, 752–779.
- Ghil, M., A. Mulhaupt, and P. Pestiaux, 1987, "Deep water formation and Quaternary glaciations," *Clim. Dyn.* **2**, 1–10.
- Ghil, M., and A. W. Robertson, 2000, "Solving problems with GCMs: General circulation models and their role in the climate modeling hierarchy," in *General Circulation Model Development: Past, Present and Future*, edited by D. A. Randall (Academic Press, New York), pp. 285–325.

- Ghil, M., and A. W. Robertson, 2002, ‘Waves’ vs. ‘particles’ in the atmosphere’s phase space: A pathway to long-range forecasting?,” *Proc. Natl. Acad. Sci. U.S.A.* **99**, 2493–2500.
- Ghil, M., I. Zaliapin, and S. Thompson, 2008, “A delay differential model of ENSO variability: Parametric instability and the distribution of extremes,” *Nonlinear Processes Geophys.* **15**, 417–433.
- Ghil, M., *et al.*, 2002, “Advanced spectral methods for climatic time series,” *Rev. Geophys.* **40**, 3–1–3–41.
- Ghil, M., *et al.*, 2011, “Extreme events: Dynamics, statistics and prediction,” *Nonlinear Processes Geophys.* **18**, 295–350.
- Gildor, H., and E. Tziperman, 2001, “A sea ice climate switch mechanism for the 100-kyr glacial cycles,” *J. Geophys. Res.* **106**, 9117–9133.
- Gill, A. E., 1982, *Atmosphere-Ocean Dynamics* (Academic Press, New York).
- Ginelli, F., P. Poggi, A. Turchi, H. Chaté, R. Livi, and A. Politi, 2007, “Characterizing Dynamics with Covariant Lyapunov Vectors,” *Phys. Rev. Lett.* **99**, 130601.
- Gladwell, M., 2000, *The Tipping Point: How Little Things Can Make a Big Difference* (Little, Brown, Boston).
- Gleckler, P. J., C. Doutriaux, P. J. Durack, K. E. Taylor, Y. Zhang, D. N. Williams, E. Mason, and J. Servonnat, 2016, “A more powerful reality test for climate models,” *EOS Trans. Am. Geophys. Union* **97**, <https://eos.org/science-updates/a-more-powerful-reality-test-for-climate-models>.
- Gómez-Leal, I., L. Kaltenegger, V. Lucarini, and F. Lunkeit, 2018, “Climate sensitivity to carbon dioxide and the moist greenhouse threshold of earth-like planets under an increasing solar forcing,” *Astrophys. J.* **869**, 129.
- Goody, R., 2000, “Sources and sinks of climate entropy,” *Q. J. R. Meteorol. Soc.* **126**, 1953–1970.
- Gottwald, G. A., and I. Melbourne, 2013, “Homogenization for deterministic maps and multiplicative noise,” *Proc. R. Soc. A* **469**, 20130201.
- Gozolchiani, A., S. Havlin, and K. Yamasaki, 2011, “Emergence of El Niño as an Autonomous Component in the Climate Network,” *Phys. Rev. Lett.* **107**, 148501.
- Graham, R., A. Hamm, and T. Tél, 1991, “Nonequilibrium Potentials for Dynamical Systems with Fractal Attractors or Repellers,” *Phys. Rev. Lett.* **66**, 3089–3092.
- Grasman, J., 1987, *Asymptotic Methods for Relaxation Oscillations and Applications* (Springer Science+Business Media, New York).
- Grassberger, P., 1989, “Noise-induced escape from attractors,” *J. Phys. A* **22**, 3283.
- Grebogi, C., E. Ott, and J. A. Yorke, 1983, “Fractal Basin Boundaries, Long-Lived Chaotic Transients, and Unstable-Unstable Pair Bifurcation,” *Phys. Rev. Lett.* **50**, 935–938.
- Gritsun, A., G. Branstator, and A. J. Majda, 2008, “Climate response of linear and quadratic functionals using the fluctuation-dissipation theorem,” *J. Atmos. Sci.* **65**.
- Gritsun, Andrey, and Grant Branstrator, 2007, “Climate response using a three-dimensional operator based on the fluctuation-dissipation theorem,” *J. Atmos. Sci.* **64**, 2558–2575.
- Gritsun, Andrey, and Valerio Lucarini, 2017, “Fluctuations, response, and resonances in a simple atmospheric model,” *Physica (Amsterdam)* **349D**, 62–76.
- Guckenheimer, J., and P. Holmes, 1983, *Nonlinear Oscillations, Dynamical Systems and Bifurcations of Vector Fields*, 2nd ed. (Springer-Verlag, Berlin).
- Guckenheimer, John, Kathleen Hoffman, and Warren Weckesser, 2003, “The forced van der Pol equation I: The slow flow and its bifurcations,” *SIAM J. Appl. Dyn. Syst.* **2**, 1–35.
- Haines, K., 1994, “Low-frequency variability in atmospheric middle latitudes,” *Surv. Geophys.* **15**, 1–61.
- Hale, J. K., 1977, *Theory of Functional Differential Equations* (Springer-Verlag, New York).
- Hamm, A., T. Tél, and R. Graham, 1994, “Noise-induced attractor explosions near tangent bifurcations,” *Phys. Lett. A* **185**, 313–320.
- Hanggi, P., 1986, “Escape from a metastable state,” *J. Stat. Phys.* **42**, 105–148.
- Hannart, A., A. Carrassi, M. Bocquet, M. Ghil, P. Naveau, M. Pulido, J. Ruiz, and P. Tandeo, 2016, “DADA: Data assimilation for the detection and attribution of weather and climate-related events,” *Clim. Change* **136**, 155–174.
- Hairer, M., and A. J. Majda, 2010, “A simple framework to justify linear response theory,” *Nonlinearity* **23**, 909–922.
- Hannart, A., and P. Naveau, 2018, “Probabilities of causation of climate changes,” *J. Clim.* **31**, 5507–5524.
- Hannart, A., J. Pearl, F. E. L. Otto, P. Naveau, and M. Ghil, 2016, “Causal counterfactual theory for the attribution of weather and climate-related events,” *Bull. Am. Meteorol. Soc.* **97**, 99–110.
- Hassanzadeh, P., Z. Kuang, and B. F. Farrell, 2014, “Responses of midlatitude blocks and wave amplitude to changes in the meridional temperature gradient in an idealized dry GCM,” *Geophys. Res. Lett.* **41**, 5223–5232.
- Hasselmann, K., 1976, “Stochastic climate models. I: Theory,” *Tellus* **28**, 473–485.
- Hasselmann, K., R. Sausen, E. Maier-Reimer, and R. Voss, 1993, “On the cold start problem in transient simulations with coupled atmosphere-ocean models,” *Clim. Dyn.* **9**, 53–61.
- Hasson, S., V. Lucarini, and S. Pascale, 2013, “Hydrological cycle over South and Southeast Asian river basins as simulated by PCMDI/CMIP3 experiments,” *Earth Syst. Dyn.* **4**, 199–217.
- Hawkins, E., R. S. Smith, L. C. Allison, J. M. Gregory, T. J. Woollings, H. Pohlmann, and B. Cuevas, 2011, “Bistability of the Atlantic overturning circulation in a global climate model and links to ocean freshwater transport,” *Geophys. Res. Lett.* **38**, L10605.
- Hayashi, Y., 1971, “A generalized method for resolving disturbances into progressive and retrogressive waves by space Fourier and time cross-spectral analysis,” *J. Meteorol. Soc. Jpn.* **49**, 125–128.
- Heinrich, H., 1988, “Origin and consequences of cyclic ice rafting in the northeast Atlantic Ocean during the past 130 000 years,” *Quat. Res.* **29**, 142–152.
- Held, I. M., 2001, “The partitioning of the poleward energy transport between the tropical ocean and atmosphere,” *J. Atmos. Sci.* **58**, 943–948.
- Held, I. M., 2005, “The gap between simulation and understanding in climate modeling,” *Bull. Am. Meteorol. Soc.* **86**, 1609–1614.
- Held, I. M., and M. J. Suarez, 1974, “Simple albedo feedback models of the ice caps,” *Tellus* **26**, 613–629.
- Hochman, A., P. Alpert, T. Harpaz, H. Saaroni, and G. Messori, 2019, “A new dynamical systems perspective on atmospheric predictability: Eastern Mediterranean weather regimes as a case study,” *Sci. Adv.* **5**.
- Hoffman, P. F., A. J. Kaufman, G. P. Halverson, and D. P. Schrag, 1998, “On the initiation of a snowball Earth,” *Science* **281**, 1342–1346.
- Hoffman, P. F., and D. P. Schrag, 2002, “The snowball Earth hypothesis: Testing the limits of global change,” *Terra Nova* **14**, 129.
- Holland, Mark P., Renato Vitolo, Pau Rabassa, Alef E. Sterk, and Henk W. Broer, 2012, “Extreme value laws in dynamical

- systems under physical observables," *Physica (Amsterdam)* **241D**, 497–513.
- Holton, J. R., and G. J. Hakim, 2013, *An Introduction to Dynamic Meteorology*, 4th ed. (Academic Press, San Diego).
- Hoskins, B. J., M. E. McIntyre, and A. W. Robertson, 1985, "On the use and significance of isentropic potential vorticity maps," *Q. J. R. Meteorol. Soc.* **111**, 877–946.
- Hu, G., T. Bódai, and V. Lucarini, 2019, "Effects of stochastic parametrization on extreme value statistics," *Chaos* **29**, 083102.
- Huybers, P., 2005, "Comment on ‘Hockey sticks, principal components, and spurious significance’ by S. McIntyre and R. McKittrick," *Geophys. Res. Lett.* **32**, L20705.
- Imbrie, J., and K. P. Imbrie, 1986, *Ice Ages: Solving the Mystery*, 2nd ed. (Harvard University Press, Cambridge, MA).
- IPCC, 2001, *Climate Change 2001: The Scientific Basis. Contribution of Working Group I to the Third Assessment Report of the Intergovernmental Panel on Climate Change*, edited by J. T. Houghton *et al.* (Cambridge University Press, Cambridge, England).
- IPCC, 2007, *Climate Change 2007—The Physical Science Basis: Working Group I Contribution to the Fourth Assessment Report of the IPCC*, edited by S. Solomon *et al.* (Cambridge University Press, Cambridge, England).
- IPCC, 2012, *Managing the Risks of Extreme Events and Disasters to Advance Climate Change Adaptation. A Special Report of Working Groups I and II of the Intergovernmental Panel on Climate Change*, edited by C. B. Field *et al.* (Cambridge University Press, Cambridge, England).
- IPCC, 2014a, *Climate Change 2013: The Physical Science Basis. Contribution of Working Group I to the Fifth Assessment Report of the Intergovernmental Panel on Climate Change*, edited by T. Stocker *et al.* (Cambridge University Press, Cambridge, England).
- IPCC, 2014b, *Climate Change 2014. Impacts, Adaptation and Vulnerability. Contribution of Working Group II to the Fifth Assessment Report of the Intergovernmental Panel on Climate Change*, edited by C. B. Field *et al.* (Cambridge University Press, Cambridge, England).
- IPCC, 2014c, *Climate Change 2014. Mitigation of Climate Change. Contribution of Working Group III to the Fifth Assessment Report of the Intergovernmental Panel on Climate Change*, edited by O. Edenhofer *et al.* (Cambridge University Press, Cambridge, England).
- Itoh, H., and M. Kimoto, 1996, "Multiple attractors and chaotic itinerancy in a quasigeostrophic model with realistic topography: Implications for weather regimes and low-frequency variability," *J. Atmos. Sci.* **53**, 2217–2231.
- Itoh, H., and M. Kimoto, 1997, "Chaotic itinerancy with preferred transition routes appearing in an atmospheric model," *Physica (Amsterdam)* **109D**, 274–292.
- Jiang, N., J. D. Neelin, and M. Ghil, 1995, "Quasi-quadrennial and quasi-biennial variability in the equatorial Pacific," *Clim. Dyn.* **12**, 101–112.
- Jiang, S., F.-F. Jin, and M. Ghil, 1995, "Multiple equilibria and aperiodic solutions in a wind-driven double-gyre, shallow-water model," *J. Phys. Oceanogr.* **25**, 764–786.
- Jin, F.-F., and M. Ghil, 1990, "Intraseasonal oscillations in the extratropics: Hopf bifurcation and topographic instabilities," *J. Atmos. Sci.* **47**, 3007–3022.
- Jin, F.-F., and J. D. Neelin, 1993, "Modes of interannual tropical ocean-atmosphere interaction—A unified view. I: Numerical results," *J. Atmos. Sci.* **50**, 3477–3503.
- Jin, F.-F., J. D. Neelin, and M. Ghil, 1994, "El Niño on the devil’s staircase: Annual subharmonic steps to chaos," *Science* **264**, 70–72.
- Jin, F.-F., J. D. Neelin, and M. Ghil, 1996, "El Niño/Southern Oscillation and the annual cycle: Subharmonic frequency-locking and aperiodicity," *Physica (Amsterdam)* **98D**, 442–465.
- Jones, C. K. R. T., 1995, "Geometric singular perturbation theory," in *Dynamical Systems*, Lecture Notes in Mathematics Vol. 1609, edited by R. Johnson (Springer, New York), pp. 44–118.
- Jouzel, J., *et al.*, 1993, "Extending the Vostok ice-core record of paleoclimate to the penultimate glacial period," *Nature (London)* **364**, 407–412.
- Just, W., H. Kantz, C. Rödenbeck, and M. Helm, 2001, "Stochastic modelling: Replacing fast degrees of freedom by noise," *J. Phys. A* **34**, 3199–3213.
- Kalnay, E., 2003, *Atmospheric Modeling, Data Assimilation and Predictability* (Cambridge University Press, Cambridge, England).
- Karamperidou, C., P. N. Di Nezio, A. Timmermann, F.-F. Jin, and K. M. Cobb, 2015, "The response of ENSO flavors to mid-Holocene climate: Implications for proxy interpretation," *Paleoceanography* **30**, 527–547.
- Karspeck, Alicia R., *et al.*, 2018, "A global coupled ensemble data assimilation system using the community earth system model and the data assimilation research testbed," *Q. J. R. Meteorol. Soc.* **144**, 2404–2430.
- Katsman, C. A., H. A. Dijkstra, and S. S. Drijfhout, 1998, "The rectification of the wind-driven circulation due to its instabilities," *J. Mar. Res.* **56**, 559–587.
- Katz, R. W., M. B. Parlange, and P. Naveau, 2002, "Statistics of extremes in hydrology," *Adv. Water Res.* **25**, 1287–1304.
- Kautz, R. L., 1987, "Activation energy for thermally induced escape from a basin of attraction," *Phys. Lett. A* **125**, 315–319.
- Kennett, J. P., and L. D. Stott, 1991, "Abrupt deep-sea warming, palaeoceanographic changes and benthic extinctions at the end of the Palaeocene," *Nature (London)* **353**, 225–229.
- Kharin, V. V., F. W. Zwiers, and X. Zhang, 2005, "Intercomparison of near surface temperature and precipitation extremes in AMIP-2 simulations, reanalyses and observations," *J. Clim.* **18**, 5201–5223.
- Kim, Y.-H., and M.-H Kim, 2013, "Examination of the global Lorenz energy cycle using MERRA and NCEP-reanalysis 2," *Clim. Dyn.* **40**, 1499–1513.
- Kimoto, M., and M. Ghil, 1993a, "Multiple flow regimes in the Northern Hemisphere winter. Part I: Methodology and hemispheric regimes," *J. Atmos. Sci.* **50**, 2625–2643.
- Kimoto, M., and M. Ghil, 1993b, "Multiple flow regimes in the Northern Hemisphere winter. Part II: Sectorial regimes and preferred transitions," *J. Atmos. Sci.* **50**, 2645–2673.
- Kistler, R., *et al.*, 2001, "The NCEP-NCAR 50-year reanalysis: Monthly means CD-ROM and documentation," *Bull. Am. Meteorol. Soc.* **82**, 247–267.
- Kleidon, A., 2009, "Non-equilibrium thermodynamics and maximum entropy production," *Naturwissenschaften* **96**, 653–677.
- Kleidon, A., 2010, "Life, hierarchy, and the thermodynamic machinery of planet Earth," *Phys. Life Rev.* **7**, 424–460.
- Kleidon, A., and R. Lorenz, 2005, Eds., *Non-equilibrium Thermodynamics and the Production of Entropy* (Springer, Berlin).
- Klein, R., 2010, "Scale-dependent models for atmospheric flows," *Annu. Rev. Fluid Mech.* **42**, 249–274.
- Kloeden, P. E., and M. Rasmussen, 2011, *Nonautonomous Dynamical Systems* (American Mathematical Society, Providence).
- Kondrashov, D., M. D. Chekroun, and M. Ghil, 2015, "Data-driven non-Markovian closure models," *Physica (Amsterdam)* **297D**, 33–55.

- Kondrashov, D., M. D. Chekroun, A. W. Robertson, and M. Ghil, 2013, “Low-order stochastic model and ‘past-noise forecasting’ of the Madden-Julian oscillation,” *Geophys. Res. Lett.* **40**, 5305–5310.
- Kondrashov, D., Y. Feliks, and M. Ghil, 2005, “Oscillatory modes of extended Nile River records (A.D. 622–1922),” *Geophys. Res. Lett.* **32**, L10702.
- Kondrashov, D., K. Ide, and M. Ghil, 2004, “Weather regimes and preferred transition paths in a three-level quasigeostrophic model,” *J. Atmos. Sci.* **61**, 568–587.
- Kondrashov, D., S. Kravtsov, and M. Ghil, 2006, “Empirical mode reduction in a model of extratropical low-frequency variability,” *J. Atmos. Sci.* **63**, 1859–1877.
- Kondrashov, D., S. Kravtsov, A. W. Robertson, and M. Ghil, 2005, “A hierarchy of data-based ENSO models,” *J. Clim.* **18**, 4425–4444.
- Kondrashov, D., J. Shen, R. Berk, F. DAndrea, and M. Ghil, 2007, “Predicting weather regime transitions in northern hemisphere datasets,” *Clim. Dyn.* **29**, 535–551.
- Kramers, H. A., 1940, “Brownian motion in a field of force and the diffusion model of chemical reactions,” *Physica (Amsterdam)* **7**, 284–304.
- Kraut, S., and U. Feudel, 2002, “Multistability, noise, and attractor hopping: The crucial role of chaotic saddles,” *Phys. Rev. E* **66**, 015207.
- Kravtsov, S., P. Berloff, W. K. Dewar, M. Ghil, and J. C. McWilliams, 2006, “Dynamical origin of low-frequency variability in a highly nonlinear mid-latitude coupled model,” *J. Clim.* **19**, 6391–6408.
- Kravtsov, S., D. Kondrashov, and M. Ghil, 2005, “Multi-level regression modeling of nonlinear processes: Derivation and applications to climatic variability,” *J. Clim.* **18**, 4404–4424.
- Kravtsov, S., D. Kondrashov, and M. Ghil, 2009, “Empirical model reduction and the modeling hierarchy in climate dynamics and the geosciences,” in *Stochastic Physics and Climate Modelling*, edited by T. N. Palmer and P. Williams (Cambridge University Press, Cambridge, England), pp. 35–72.
- Kravtsov, S., D. Kondrashov, Igor Kamenkovich, and M. Ghil, 2011, “An empirical stochastic model of sea-surface temperatures and surface winds over the Southern Ocean,” *Ocean Sci.* **7**, 755–770.
- Krishnamurti, T. N., L. Stefanova, and V. Misra, 1979, *Tropical Meteorology: An Introduction* (Springer, New York).
- Kubo, R., 1957, “Statistical-mechanical theory of irreversible processes. I. General theory and simple applications to magnetic and conduction problems,” *J. Phys. Soc. Jpn.* **12**, 570–586.
- Kubo, R., 1966, “The fluctuation-dissipation theorem,” *Rep. Prog. Phys.* **29**, 255–284.
- Kuehn, C., 2011, “A mathematical framework for critical transitions: Bifurcations, fast-slow systems and stochastic dynamics,” *Physica (Amsterdam)* **240D**, 1020–1035.
- Kuhlbrodt, T., A. Griesel, M. Montoya, A. Levermann, M. Hofmann, and S. Rahmstorf, 2007, “On the driving processes of the Atlantic meridional overturning circulation,” *Rev. Geophys.* **45**, RG2001.
- Kushnir, Y., 1987, “Retrograding wintertime low-frequency disturbances over the North Pacific ocean,” *J. Atmos. Sci.* **44**, 2727–2742.
- Kushnir, Y., 1994, “Interdecadal variations in North Atlantic sea surface temperature and associated atmospheric conditions,” *J. Phys. Oceanogr.* **7**, 141–157.
- Lagerstrom, P. A., 1988, *Matched Asymptotic Expansions: Ideas and Techniques* (Springer Science+Business Media, New York).
- Lai, Y-C, and T. Tél, 2011, *Transient Chaos* (Springer, New York).
- Laloyaux, P., et al., 2018, “CERA-20C: A coupled reanalysis of the twentieth century,” *J. Adv. Model. Earth Syst.* **10**, 1172–1195.
- Lamb, H. H., 1972, *Climate: Present, Past and Future* (Methuen, London).
- Langen, P. L., and V. A. Alexeev, 2005, “Estimating 2X CO₂ warming in an aquaplanet GCM using the fluctuation-dissipation theorem,” *Geophys. Res. Lett.* **32**, L23708.
- Lawrence, M. G., S. Schäfer, H. Muri, V. Scott, A. Oschlies, N. E. Vaughan, O. Boucher, H. Schmidt, J. Haywood, and J. Scheffran, 2018, “Evaluating climate geoengineering proposals in the context of the Paris Agreement temperature goals,” *Nat. Commun.* **9**, 3734.
- /Ledrappier, F., and L.-S. Young, 1988, “Entropy formula for random transformations,” *Prob. Theory Relat. Fields* **80**, 217–240.
- Lee, T., T. Awaji, M. A. Balmaseda, E. Greiner, and D. Stammer, 2009, “Ocean state estimation for climate research,” *Oceanography* **22**, 160–167.
- Legras, B., and M. Ghil, 1985, “Persistent anomalies, blocking, and variations in atmospheric predictability,” *J. Atmos. Sci.* **42**, 433–471.
- Leith, C. E., 1975, “Climate response and fluctuation dissipation,” *J. Atmos. Sci.* **32**, 2022–2026.
- Leith, C. E., and R. H. Kraichnan, 1972, “Predictability of turbulent flows,” *J. Atmos. Sci.* **29**, 1041–1058.
- Lembo, V., V. Lucarini, and F. Ragone, 2020, “Beyond forcing scenarios: Predicting climate change through response operators in a coupled general circulation model,” *Sci. Rep.* **10**, 8668.
- Lembo, V., F. Lunkeit, and V. Lucarini, 2019, “TheDiaTo (v1.0)—A new diagnostic tool for water, energy and entropy budgets in climate models,” *Geosci. Model Dev.* **12**, 3805–3834.
- Lenton, T. M., H. Held, E. Kriegler, J. W. Hall, W. Lucht, S. Rahmstorf, and H. J. Schellnhuber, 2008, “Tipping elements in the Earth’s climate system,” *Proc. Natl. Acad. Sci. U.S.A.* **105**, 1786–1793.
- Li, Z-X, K. Ide, H. Le Treut, and M. Ghil, 1997, “Atmospheric radiative equilibria in a simple column model,” *Clim. Dyn.* **13**, 429–440.
- Lindzen, R. S., 1986, “Stationary planetary waves, blocking, and interannual variability,” in *Advances in Geophysics*, Vol. 29 (Elsevier, New York), pp. 251–273.
- Liu, J., J. A. Curry, H. Wang, M. Song, and R. M. Horton, 2012, “Impact of declining Arctic sea ice on winter snowfall,” *Proc. Natl. Acad. Sci. U.S.A.* **109**, 4074–4079.
- Lorenz, E. N., 1955, “Available potential energy and the maintenance of the general circulation,” *Tellus* **7**, 157–167.
- Lorenz, E. N., 1963, “Deterministic nonperiodic flow,” *J. Atmos. Sci.* **20**, 130–141.
- Lorenz, E. N., 1967, *The Nature and Theory of the General Circulation of the Atmosphere* (World Meteorological Organization, Geneva).
- Lorenz, E. N., 1969a, “The predictability of a flow which possesses many scales of motion,” *Tellus* **21**, 289–307.
- Lorenz, E. N., 1969b, “Three approaches to atmospheric predictability,” *Bull. Am. Meteorol. Soc.* **50**, 345–349.
- Lorenz, E. N., 1976, “Nondeterministic theories of climatic change,” *Quat. Res.* **6**, 495–506.
- Lorenz, E. N., 1979, “Forced and free variations of weather and climate,” *J. Atmos. Sci.* **36**, 1367–1376.
- Lorenz, E. N., 1984, “Irregularity: A fundamental property of the atmosphere,” *Tellus A* **36A**, 98–110.
- Lorenz, E. N., 1996, “Predictability: A problem partly solved,” in *Seminar on Predictability, 4–8 September 1995* (European Centre for Medium-range Weather Forecasts, Reading, England), pp. 1–18.
- Lu, Z., Z. Fu, L. Hua, N. Yuan, and L. Chen, 2018, “Evaluation of ENSO simulations in CMIP5 models: A new perspective based on

- percolation phase transition in complex networks," *Sci. Rep.* **8**, 14912.
- Lucarini, V., 2002, "Towards a definition of climate science," *Intl. J. Environ. Pollution* **18**, 413–422.
- Lucarini, V., 2008a, "Response theory for equilibrium and non-equilibrium statistical mechanics: Causality and generalized kramers-kronig relations," *J. Stat. Phys.* **131**, 543–558.
- Lucarini, V., 2008b, "Validation of climate models," in *Encyclopedia of Global Warming and Climate Change*, edited by G. Philander (SAGEThousand Oaks, CA), pp. 1053–1057.
- Lucarini, V., 2009a, "Evidence of dispersion relations for the non-linear response of the Lorenz 63 system," *J. Stat. Phys.* **134**, 381–400.
- Lucarini, V., 2009b, "Thermodynamic efficiency and entropy production in the climate system," *Phys. Rev. E* **80**, 021118.
- Lucarini, V., 2012, "Stochastic perturbations to dynamical systems: A response theory approach," *J. Stat. Phys.* **146**, 774–786.
- Lucarini, V., 2013, "Modeling complexity: The case of climate science," in *Models, Simulations, and the Reduction of Complexity*, edited by U. Gähde, S. Hartmann, and J. H. Wolf (De Gruyter, Berlin), pp. 229–254.
- Lucarini, V., 2016, "Response operators for Markov processes in a finite state space: Radius of convergence and link to the response theory for Axiom A systems," *J. Stat. Phys.* **162**, 312–333.
- Lucarini, V., 2018, "Revising and extending the linear response theory for statistical mechanical systems: Evaluating observables as predictors and predictands," *J. Stat. Phys.* **173**, 1698–1721.
- Lucarini, V., R. Blender, C. Herbert, F. Ragone, S. Pascale, and J. Wouters, 2014, "Mathematical and physical ideas for climate science," *Rev. Geophys.* **52**, 809–859.
- Lucarini, V., and T. Bódai, 2017, "Edge states in the climate system: Exploring global instabilities and critical transitions," *Nonlinearity* **30**, R32.
- Lucarini, V., and T. Bódai, 2019, "Transitions across Melancholia States in a Climate Model: Reconciling the Deterministic and Stochastic Points of View," *Phys. Rev. Lett.* **122**, 158701.
- Lucarini, V., and T. Bódai, 2020, "Global stability properties of the climate: Melancholia states, invariant measures, and phase transitions," *Nonlinearity* (to be published), <https://doi.org/10.1088/1361-6544/ab86cc>.
- Lucarini, V., S. Calmanti, and V. Artale, 2005, "Destabilization of the thermohaline circulation by transient changes in the hydrological cycle," *Clim. Dyn.* **24**, 253–262.
- Lucarini, V., S. Calmanti, and V. Artale, 2007, "Experimental mathematics: Dependence of the stability properties of a two-dimensional model of the Atlantic Ocean circulation on the boundary conditions," *Russ. J. Math. Phys.* **14**, 224–231.
- Lucarini, V., and M. Colangeli, 2012, "Beyond the linear fluctuation-dissipation theorem: The role of causality," *J. Stat. Mech.* P05013.
- Lucarini, V., D. Faranda, A. C. G. M. M. de Freitas, J. M. M. de Freitas, M. Holland, T. Kuna, M. Nicol, M. Todd, and S. Vaienti, 2016, *Extremes and Recurrence in Dynamical Systems* (Wiley, New York).
- Lucarini, V., K. Fraedrich, and F. Lunkeit, 2010a, "Thermodynamic analysis of snowball Earth hysteresis experiment: Efficiency, entropy production, and irreversibility," *Q. J. R. Meteorol. Soc.* **136**, 2–11.
- Lucarini, V., K. Fraedrich, and F. Lunkeit, 2010b, "Thermodynamics of climate change: Generalized sensitivities," *Atmos. Chem. Phys.* **10**, 9729–9737.
- Lucarini, V., and A. Gritsun, 2020, "A new mathematical framework for atmospheric blocking events," *Clim. Dyn.* **54**, 575–598.
- Lucarini, V., T. Kuna, D. Faranda, and J. Wouters, 2014, "Towards a general theory of extremes for observables of chaotic dynamical systems," *J. Stat. Phys.* **154**.
- Lucarini, V., S. Pascale, V. Boschi, E. Kirk, and N. Iro, 2013, "Habitability and multistability in Earth-like planets," *Astron. Nachr.* **334**, 576–588.
- Lucarini, V., and F. Ragone, 2011, "Energetics of climate models: Net energy balance and meridional enthalpy transport," *Rev. Geophys.* **49**, RG1001.
- Lucarini, V., F. Ragone, and F. Lunkeit, 2017, "Predicting climate change using response theory: Global averages and spatial patterns," *J. Stat. Phys.* **166**, 1036–1064.
- Lucarini, V., J. J. Saarinen, K.-E. Peiponen, and E. M. Vartiainen, 2005, *Kramers-Kronig relations in Optical Materials Research* (Springer, New York).
- Lucarini, V., and S. Sarno, 2011, "A statistical mechanical approach for the computation of the climatic response to general forcings," *Nonlinear Processes Geophys.* **18**, 7–28.
- Lucarini, Valerio, and Peter H. Stone, 2005, "Thermohaline circulation stability: A box model study. Part I: Uncoupled model," *J. Clim.* **18**, 501–513.
- Lynch, P., 2008, "The ENIAC forecasts: A re-creation," *Bull. Am. Meteorol. Soc.* **89**, 45–55.
- Madden, R. A., and P. R. Julian, 1971, "Detection of a 40–50 day oscillation in the zonal wind in the tropical Pacific," *J. Atmos. Sci.* **28**, 702–708.
- Majda, A. J., B. Gershgorin, and Y. Yuan, 2010, "Low-frequency climate response and fluctuation–Dissipation theorems: Theory and practice," *J. Atmos. Sci.* **67**, 1186–1201.
- Majda, A. J., and X. Wang, 2006, *Nonlinear Dynamics and Statistical Theories for Basic Geophysical Flows* (Cambridge University Press, Cambridge, England).
- Maloney, E. D., and D. L. Hartmann, 2000, "Modulation of hurricane activity in the Gulf of Mexico by the Madden-Julian oscillation," *Science* **287**, 2002–2004.
- Manabe, Syukuro, and Robert F. Strickler, 1964, "Thermal equilibrium of the atmosphere with a convective adjustment," *J. Atmos. Sci.* **21**, 361–385.
- Mann, M. E., R. S. Bradley, and M. K. Hughes, 1998, "Global-scale temperature patterns and climate forcing over the past six centuries," *Nature (London)* **392**, 779–787.
- Mann, M. E., R. S. Bradley, and M. K. Hughes, 1999, "Northern Hemisphere temperatures during the past millennium: Inferences, uncertainties, and limitations," *Geophys. Res. Lett.* **26**, 759–762.
- Mann, M. E., Z. Zhang, M. K. Hughes, R. S. Bradley, S. K. Miller, F. Rutherford, and S. Ni, 2008, "Proxy-based reconstructions of hemispheric and global surface temperature variations over the past two millennia," *Proc. Natl. Acad. Sci. U.S.A.* **105**, 13252–13257.
- Marangio, L., J. Sedro, S. Galatolo, A. Di Garbo, and M. Ghil, 2019, "Arnold maps with noise: Differentiability and non-monotonicity of the rotation number," [arXiv:1904.11744](https://arxiv.org/abs/1904.11744).
- Marconi, U Marini Bettolo, A. Puglisi, L. Rondoni, and A. Vulpiani, 2008, "Fluctuation-dissipation: Response theory in statistical physics," *Phys. Rep.* **461**, 111.
- Marotzke, J., 2000, "Abrupt climate change and thermohaline circulation: Mechanisms and predictability," *Proc. Natl. Acad. Sci. U.S.A.* **97**, 1347–1350.
- Marques, C. A. F., A. Rocha, and J. Corte-Real, 2010, "Comparative energetic of ERA-40, JRA-25 and NCEP-R2 reanalysis, in the wave number domain," *Dyn. Atmos. Oceans* **50**, 375–399.

- Marques, C. A. F., A. Rocha, J. Corte-Real, J. M. Castanheira, J. Ferreira, and P. Melo-Goncalves, 2009, “Global atmospheric energetic from NCEP-reanalysis 2 and ECMWF-ERA40 reanalysis,” *Int. J. Climatol.* **29**, 159–174.
- Marshall, J., C. Hill, L. Perelman, and A.. Adcroft, 1997, “Hydrostatic, quasi-hydrostatic, and non-hydrostatic ocean modelling,” *J. Geophys. Res.* **102**, 5733–5752.
- Marshall, J., and F. Molteni, 1993, “Toward a dynamical understanding of atmospheric weather regimes,” *J. Atmos. Sci.* **50**, 1792.
- Martinson, D. G., K. Bryan, M. Ghil, M. M. Hall, T. R. Karl, E. S. Sarachik, S. Sorooshian, and L. D. Talley, 1995, Eds., *Natural Climate Variability on Decade-to-Century Time Scales* (National Academies Press, Washington, DC).
- McIntyre, S., and R. McKittrick, 2005, “Hockey sticks, principal components, and spurious significance,” *Geophys. Res. Lett.* **32**, L03710.
- McWilliams, J. C., 2006, *Fundamentals of Geophysical Fluids* (Cambridge University Press, Cambridge, England).
- McWilliams, J. C., 2019, “A perspective on the legacy of Edward Lorenz,” *Earth Space Sci.* (in press).
- Meacham, S. P., 2000, “Low frequency variability of the wind-driven circulation,” *J. Phys. Oceanogr.* **30**, 269–293.
- Meehl, G. A., *et al.*, 2014, “Decadal climate prediction: An update from the trenches,” *Bull. Am. Meteorol. Soc.* **95**, 243–267.
- Melbourne, I., and A. M. Stuart, 2011, “A note on diffusion limits of chaotic skew-product flows,” *Nonlinearity* **24**, 1361–1367.
- Merkin, V. G., D. Kondrashov, M. Ghil, and B. J. Anderson, 2016, “Data assimilation of low-altitude magnetic perturbations into a global magnetosphere model,” *Space Weather* **14**, 165–184.
- Merryfield, William J *et al.*, 2020, “Current and emerging developments in subseasonal to decadal prediction,” *Bull. Am. Meteorol. Soc.* (in press).
- Mitchell, J. M., 1976, “An overview of climate variability and its causal mechanisms,” *Quat. Res.* **6**, 481–493.
- Mo, K. C., and M. Ghil, 1987, “Statistics and dynamics of persistent anomalies,” *J. Atmos. Sci.* **44**, 877–902.
- Molteni, F. M., 2002, “Weather regimes and multiple equilibria,” in *Encyclopedia of Atmospheric Sciences*, edited by J. R. Holton (Academic Press, New York), pp. 2577–2586.
- Monge, G., 1781, “An essay on the theory of excavation and embankment,” *Hist. Acad. R. Sci.* **1**, 666–704.
- Mori, H., 1965, “Transport, collective motion, and Brownian motion,” *Prog. Theor. Phys.* **33**, 423–455.
- Moron, V., R. Vautard, and M. Ghil, 1998, “Trends, interdecadal and interannual oscillations in global sea-surface temperature,” *Clim. Dyn.* **14**, 545–569.
- Mukhin, D., D. Kondrashov, E. Loskutov, A. Gavrilov, A. Feigin, and M. Ghil, 2015, “Predicting critical transitions in ENSO models. Part II: Spatially dependent models,” *J. Clim.* **28**, 1962–1976.
- Mukhin, D., E. Loskutov, A. Mukhina, A. Feigin, I. Zaliapin, and M. Ghil, 2015, “Predicting critical transitions in ENSO Models. Part I: Methodology and simple models with memory,” *J. Clim.* **28**, 1940–1961.
- Munk, W., and C. Wunsch, 1982, “Observing the ocean in the 1990s,” *Phil. Trans. R. Soc. A* **307**, 439–464.
- NAC, 1986, *NASA Advisory Council: Earth System Science Overview*, edited by F. Bretherton *et al.* (National Aeronautics and Space Administration, Washington, DC).
- Nadiga, B. T., and B. Luce, 2001, “Global bifurcation of Shilnikov type in a double-gyre model,” *J. Phys. Oceanogr.* **31**, 2669–2690.
- Namias, J., 1968, “Long-range weather forecasting: History, current status and outlook,” *Bull. Am. Meteorol. Soc.* **49**, 438–470.
- Neelin, J. D., D. S. Battisti, A. C. Hirst, F.-F. Jin, Y. Wakata, T. Yamagata, and S. E. Zebiak, 1998, “ENSO Theory,” *J. Geophys. Res.* **103**, 14261.
- Neelin, J. D., M. Latif, and F.-F. Jin, 1994, “Dynamics of coupled ocean-atmosphere models: The tropical problem,” *Annu. Rev. Fluid Mech.* **26**, 617–659.
- Newman, Mark, 2010, *Networks: An Introduction* (Oxford University Press, Oxford).
- North, G. R., 1975, “Analytical solution to a simple climate model with diffusive heat transport,” *J. Atmos. Sci.* **32**, 1301–1307.
- North, G. R., R. E. Bell, and J. W. Hardin, 1993, “Fluctuation dissipation in a general circulation model,” *Clim. Dyn.* **8**, 259–264.
- North, G. R., R. F. Cahalan, and J. A. Coakley, 1981, “Energy balance climate models,” *Rev. Geophys. Space Phys.* **19**, 91.
- North, G. R., L. Howard, D. Pollard, and B. Wielicki, 1979, “Variational formulation of Budyko-Sellers climate models,” *J. Atmos. Sci.* **36**, 255–259.
- NRC, 2006, *National Research Council: Surface Temperature Reconstructions for the Last 2000 Years* (National Academies Press, Washington, DC).
- Onogi, K., *et al.*, 2007, “The JRA-25 reanalysis,” *J. Meteorol. Soc. Jpn.* **85**, 369–432.
- Onsager, L., 1931, “Reciprocal relations in irreversible processes. I,” *Phys. Rev.* **37**, 405–426.
- Ott, E., 2002, *Chaos in Dynamical Systems* (Cambridge University Press, Cambridge, England).
- Otto, A., *et al.*, 2013, “Energy budget constraints on climate response,” *Nat. Geosci.* **6**, 415–416.
- PAGES 2k Consortium, 2013, “Continental-scale temperature variability during the past two millennia,” *Nat. Geosci.* **6**, 339–346.
- Palmer, C. E., 1951, “Tropical meteorology,” in *Compendium of Meteorology* (Springer, New York), pp. 859–880.
- Palmer, T., 2017, “The primacy of doubt: Evolution of numerical weather prediction from determinism to probability,” *J. Adv. Model. Earth Syst.* **9**, 730–734.
- Palmer, T. N., F. J. Doblas-Reyes, A. Weisheimer, and M. J. Rodwell, 2008, “Toward seamless prediction: Calibration of climate change projections using seasonal forecasts,” *Bull. Am. Meteorol. Soc.* **89**, 459–470.
- Palmer, T. N., and P. Williams, 2009, Eds., *Stochastic Physics and Climate Modelling* (Cambridge University Press, Cambridge, England).
- Pan, D-M, and D. A. Randall, 1998, “A cumulus parameterization with a prognostic closure,” *Q. J. R. Meteorol. Soc.* **124**, 949–981.
- Papanicolaou, G. C., and W. Kohler, 1974, “Asymptotic theory of mixing stochastic ordinary differential equations,” *Commun. Pure Appl. Math.* **27**, 641–668.
- Parker, W. S., 2010, “Whose probabilities? Predicting climate change with ensembles of models,” *Philos. Sci.* **77**, 985–997.
- Paterson, W. S. B., 1981, *The Physics of Glaciers*, 2nd ed. (Pergamon Press, Oxford).
- Pauluis, O., and I M. Held, 2002, “Entropy budget of an atmosphere in radiative-convective equilibrium. Part I: Maximum work and frictional dissipation,” *J. Atmos. Sci.* **59**, 125–139.
- Pavliotis, G. A., 2014, *Stochastic Processes and Applications: Diffusion Processes, the Fokker-Planck and Langevin Equations*, Texts in Applied Mathematics (Springer, New York).
- Pavliotis, G. A., and A. M. Stuart, 2008, *Multiscale Methods* (Springer, New York).

- Pearl, J., 2009, *Causality: Models, Reasoning, and Inference* (Cambridge University Press, Cambridge, England).
- Pedlosky, J., 1987, *Geophysical Fluid Dynamics*, 2nd ed. (Springer-Verlag, New York).
- Pedlosky, J., 1996, *Ocean Circulation Theory* (Springer, New York).
- Peixoto, J. P., and A. H. Oort, 1992, *Physics of Climate* (AIP Press, New York).
- Penland, C., 1989, "Random forcing and forecasting using principal oscillation pattern analysis," *Mon. Weather Rev.* **117**, 2165–2185.
- Penland, C., 1996, "A stochastic model of IndoPacific sea surface temperature anomalies," *Physica (Amsterdam)* **98D**, 534–558.
- Penland, C., and M. Ghil, 1993, "Forecasting Northern Hemisphere 700-mb geopotential height anomalies using empirical normal modes," *Mon. Weather Rev.* **121**, 2355–2372.
- Penland, C., and P. D. Sardeshmukh, 1995, "The optimal growth of tropical sea surface temperature anomalies," *J. Clim.* **8**, 1999–2024.
- Penny, S. G., and T. M. Hamill, 2017, "Coupled data assimilation for integrated Earth system analysis and prediction," *Bull. Am. Meteorol. Soc.* **98**, ES169–ES172.
- Pfeffer, R. L., 1960, Ed., *Dynamics of Climate* (Pergamon Press, New York).
- Pfister, P. L., and T. F. Stocker, 2017, "State-dependence of the climate sensitivity in earth system models of intermediate complexity," *Geophys. Res. Lett.* **44**, 10 643–10 653.
- Philander, S. G. H., 1990, *El Niño and the Southern Oscillation*. (Academic Press, New York).
- Pierini, S., M. D. Chekroun, and M. Ghil, 2018, "The onset of chaos in nonautonomous dissipative dynamical systems: A low-order ocean-model case study," *Nonlinear Processes Geophys.* **25**, 671–692.
- Pierini, S., M. Ghil, and M. D. Chekroun, 2016, "Exploring the pullback attractors of a low-order quasigeostrophic ocean model: The deterministic case," *J. Clim.* **29**, 4185–4202.
- Pierrehumbert, R. T., 2004, "High levels of atmospheric carbon dioxide necessary for the termination of global glaciation," *Nature (London)* **429**, 646.
- Plant, R. S., and J. I. Yano, 2016, *Parameterization of Atmospheric Convection*, Vol. 1 (Imperial College Press, London).
- Plaut, G., M. Ghil, and R. Vautard, 1995, "Interannual and interdecadal variability in 335 years of Central England temperature," *Science* **268**, 710–713.
- Poincaré, H., 1902, *La Science et l'Hypothèse*, translated in 1905 into English as *Science and Hypothesis*; versions of this translation are (i) downloadable for free as Gutenberg Project EBook No. 37157, published in 2011, and (ii) available online as a Wikisource book, https://en.wikisource.org/wiki/Science_and_Hypothesis, published in 2017.
- Poincaré, H., 1908, *Science et Méthode* (Ernest Flammarion, Paris).
- Poli, P., et al., 2016, "ERA-20C: An atmospheric reanalysis of the twentieth century," *J. Clim.* **29**, 4083–4097.
- Pollicott, M., 1985, "On the rate of mixing of Axiom A flows," *Invent. Math.* **81**, 413–426.
- Pratt, R. W., 1976, "The interpretation of space-time spectral quantities," *J. Atmos. Sci.* **33**, 1060–1066.
- Preisendorfer, R. W., 1988, *Principal Component Analysis in Meteorology and Oceanography* (Elsevier, Amsterdam).
- Prigogine, I., 1961, *Thermodynamics of Irreversible Processes* (Interscience, New York).
- Proctor, J., S. Hsiang, J. Burney, M. Burke, and W. Schlenker, 2018, "Estimating global agricultural effects of geoengineering using volcanic eruptions," *Nature (London)* **560**, 480–483.
- Quon, C., and M. Ghil, 1992, "Multiple equilibria in thermosolutal convection due to salt-flux boundary conditions," *J. Fluid Mech.* **245**, 449–484.
- Ragone, F., V. Lucarini, and F. Lunkeit, 2016, "A new framework for climate sensitivity and prediction: A modelling perspective," *Clim. Dyn.* **46**, 1459–1471.
- Ragone, F., J. Wouters, and F. Bouchet, 2018, "Computation of extreme heat waves in climate models using a large deviation algorithm," *Proc. Natl. Acad. Sci. U.S.A.* **115**, 24–29.
- Rahmstorf, Stefan, et al., 2005, "Thermohaline circulation hysteresis: A model intercomparison," *Geophys. Res. Lett.* **32**, <https://doi.org/10.1029/2005GL023655>.
- Ramanathan, V., and J. A. Coakley, 1978, "Climate modeling through radiative-convective models," *Rev. Geophys.* **16**, 465–489.
- Randall, D. A., 2000, Ed., *General Circulation Model Development: Past, Present and Future* (Academic Press, New York).
- Rasmusson, E., X. Wang, and C. Ropelewski, 1990, "The biennial component of ENSO variability," *J. Mar. Syst.* **1**, 71–96.
- Richardson, L. F., 1922, *Weather Prediction by Numerical Process* (Cambridge University Press, Cambridge, England).
- Riehl, H., 1954, *Tropical Meteorology* (McGraw-Hill, New York).
- Robert, C., K. T. Alligood, E. Ott, and J. A. Yorke, 2000, "Explosions of chaotic sets," *Physica (Amsterdam)* **144D**, 44–61.
- Robert, R., and J. Sommeria, 1991, "Statistical equilibrium states for two-dimensional flows," *J. Fluid Mech.* **229**, 291–310.
- Robertson, A. W., and F. Vitart, Eds., 2018, *The Gap Between Weather and Climate Forecasting: Sub-seasonal to Seasonal Prediction* (Elsevier, Amsterdam).
- Robin, Y., P. Yiou, and P. Naveau, 2017, "Detecting changes in forced climate attractors with Wasserstein distance," *Nonlinear Processes Geophys.* **24**, 393–405.
- Robinson, I. S., 2010, *Discovering the Ocean From Space: The Unique Applications of Satellite Oceanography* (Praxis Publishing, Chichester, England).
- Roe, G. H., and M. B. Baker, 2007, "Why is climate sensitivity so unpredictable?," *Science* **318**, 629–632.
- Rohling, E. J., et al. (PALAEOSENS Project Collaboration), 2012, "Making sense of palaeoclimate sensitivity," *Nature (London)* **491**, 683.
- Rombouts, J., and M. Ghil, 2015, "Oscillations in a simple climate–vegetation model," *Nonlinear Processes Geophys.* **22**, 275–288.
- Romeiras, F. J., C. Grebogi, and E. Ott, 1990, "Multifractal properties of snapshot attractors of random maps," *Phys. Rev. A* **41**, 784.
- Rooth, C., 1982, "Hydrology and ocean circulation," *Prog. Oceanogr.* **11**, 131–149.
- Roques, L., M. D. Chekroun, M. Cristofol, S. Soubeyrand, and M. Ghil, 2014, "Parameter estimation for energy balance models with memory," *Proc. R. Soc. A* **470**, 20140349.
- Rossby, C.-G., 1939, "Relation between variations in the intensity of the zonal circulation of the atmosphere and the displacements of the semi-permanent centers of action," *J. Mar. Res.* **2**, 38–55.
- Rothman, D. H., J. M. Hayes, and R. E. Summons, 2003, "Dynamics of the Neoproterozoic carbon cycle," *Proc. Natl. Acad. Sci. U.S.A.* **100**, 8124–8129.
- Ruelle, D., 1986, "Resonances of Chaotic Dynamical Systems," *Phys. Rev. Lett.* **56**, 405–407.
- Ruelle, D., 1998, "General linear response formula in statistical mechanics, and the fluctuation-dissipation theorem far from equilibrium," *Phys. Lett. A* **245**, 220–224.
- Ruelle, D., 1999, "Smooth dynamics and new theoretical ideas in nonequilibrium statistical mechanics," *J. Stat. Phys.* **95**, 393–468.
- Ruelle, D., 2009, "A review of linear response theory for general differentiable dynamical systems," *Nonlinearity* **22**, 855–870.

- Ruti, P. M., V. Lucarini, A. Dell'Aquila, S. Calmant, and A. Speranza, 2006, "Does the subtropical jet catalyze the midlatitude atmospheric regimes?", *Geophys. Res. Lett.* **33**, L06814.
- Salmon, Rick, 1998, *Lectures on Geophysical Fluid Dynamics* (Oxford University Press, Oxford).
- Saltzman, B., 2001, *Dynamical Paleoclimatology: Generalized Theory of Global Climate Change* (Academic Press, New York).
- Sardeshmukh, P. D., and C. Penland, 2015, "Understanding the distinctively skewed and heavy tailed character of atmospheric and oceanic probability distributions," *Chaos* **25**, 036410.
- Satoh, M., A. T. Noda, T. Seiki, Y.-W. Chen, C. Kodama, Y. Yamada, N. Kuba, and Y. Sato, 2018, "Toward reduction of the uncertainties in climate sensitivity due to cloud processes using a global non-hydrostatic atmospheric model," *Prog. Earth Planet. Sci.* **5**, 67.
- Scheffer, M., J. Bascompte, W. A. Brock, V. Brovkin, S. R. Carpenter, V. Dakos, H. Held, Egbert H. Van Nes, M. Rietkerk, and G. Sugihara, 2009, "Early-warning signals for critical transitions," *Nature (London)* **461**, 53–59.
- Schneider, S. H., and R. E. Dickinson, 1974, "Climate modelling," *Rev. Geophys.* **12**, 447–493.
- Schneider, T., J. Teixeira, C. S. Bretherton, F. Brient, K. G. Pressel, C. Schär, and A. P. Siebesma, 2017, "Climate goals and computing the future of clouds," *Nat. Clim. Change* **7**, <https://doi.org/10.1038/nclimate3190>.
- Schneider, T. M., B. Eckhardt, and J. A. Yorke, 2007, "Turbulence Transition and the Edge of Chaos in Pipe Flow," *Phys. Rev. Lett.* **99**, 034502.
- Schneider, Tapio, Colleen M. Kaul, and Kyle G. Pressel, 2019, "Possible climate transitions from breakup of stratocumulus decks under greenhouse warming," *Nat. Geosci.* **12**, 163–167.
- Schubert, Sebastian, and Valerio Lucarini, 2016, "Dynamical analysis of blocking events: Spatial and temporal fluctuations of covariant Lyapunov vectors," *Q. J. R. Meteorol. Soc.* **142**, 2143–2158.
- Scott, J. R., J. Marotzke, and P. H. Stone, 1999, "Interhemispheric thermohaline circulation in a coupled box model," *J. Phys. Oceanogr.* **29**, 351–365.
- Sell, G. R., 1967, "Nonautonomous differential equations and topological dynamics. I. The basic theory," *Trans. Am. Math. Soc.* **127**, 241–262.
- Sell, G. R., 1971, *Topological Dynamics and Ordinary Differential Equations* (Van Nostrand Reinhold, New York).
- Sellers, W. D., 1969, "A global climatic model based on the energy balance of the earth atmosphere," *J. Appl. Meteorol.* **8**, 392–400.
- Sevellec, F., and A. V. Fedorov, 2015, "Unstable AMOC during glacial intervals and millennial variability: The role of mean sea ice extent," *Earth Planet. Sci. Lett.* **429**, 60–68.
- Sheremet, V. A., G. R. Ierley, and V. M. Kamenkovich, 1997, "Eigenanalysis of the two-dimensional wind-driven ocean circulation problem," *J. Mar. Res.* **55**, 57–92.
- Simonnet, E., 2005, "Quantization of the low-frequency variability of the double-gyre circulation," *J. Phys. Oceanogr.* **35**, 2268–2290.
- Simonnet, E., and H. A. Dijkstra, 2002, "Spontaneous generation of low-frequency modes of variability in the wind-driven ocean circulation," *J. Phys. Oceanogr.* **32**, 1747–1762.
- Simonnet, E., M. Ghil, and H. A. Dijkstra, 2005, "Homoclinic bifurcations in the quasi-geostrophic double-gyre circulation," *J. Mar. Res.* **63**, 931–956.
- Simonnet, E., M. Ghil, K. Ide, R. Temam, and S. Wang, 2003a, "Low-frequency variability in shallow-water models of the wind-driven ocean circulation. Part I: Steady-state solutions," *J. Phys. Oceanogr.* **33**, 712–728.
- Simonnet, E., M. Ghil, K. Ide, R. Temam, and S. Wang, 2003b, "Low-frequency variability in shallow-water models of the wind-driven ocean circulation. Part II: Time dependent solutions," *J. Phys. Oceanogr.* **33**, 729–752.
- Simonnet, E., R. Temam, S. Wang, M. Ghil, and K. Ide, 1998, "Successive bifurcations in a shallow-water ocean model," *Lect. Notes Phys.* **515**, 225–230.
- Simonnet, S., H. A. Dijkstra, and M. Ghil, 2009, "Bifurcation analysis of ocean, atmosphere and climate models," in *Computational Methods for the Ocean and the Atmosphere*, edited by R. Temam and J. J. Tribbia (North-Holland, Amsterdam), pp. 187–229.
- Skufca, J. D., J. A. Yorke, and B. Eckhardt, 2006, "Edge of Chaos in a Parallel Shear Flow," *Phys. Rev. Lett.* **96**, 174101.
- Slingo, J., and T. N. Palmer, 2011, "Uncertainty in weather and climate prediction," *Phil. Trans. R. Soc. A* **369**, 4751–4767.
- Smith, W., and G. Wagner, 2018, "Stratospheric aerosol injection tactics and costs in the first 15 years of deployment," *Environ. Res. Lett.* **13**, 124001.
- Smyth, P., K. Ide, and M. Ghil, 1999, "Multiple regimes in Northern Hemisphere height fields via mixture model clustering," *J. Atmos. Sci.* **56**, 3704–3723.
- Speich, S., H. A. Dijkstra, and M. Ghil, 1995a, "Successive bifurcations in a shallow-water model applied to the wind-driven ocean circulation," *Nonlinear Processes Geophys.* **2**, 241–268.
- Speich, S., H. A. Dijkstra, and M. Ghil, 1995b, "Successive bifurcations of a shallow-water model with applications to the wind driven circulation," *Nonlinear Processes Geophys.* **2**, 241–268.
- Speranza, A., 1983, "Deterministic and statistical properties of the westerlies," *Pure Appl. Geophys.* **121**, 511–562.
- Stommel, H., 1961, "Thermohaline convection with two stable regimes of flow," *Tellus* **13**, 224–230.
- Stommel, H., 1963, "Varieties of oceanographic experience," *Science* **139**, 572–576.
- Sushama, L., M. Ghil, and K. Ide, 2007, "Spatio-temporal variability in a mid-latitude ocean basin subject to periodic wind forcing," *Atmosphere-Ocean* **45**, 227–250.
- Sverdrup, H. U., 1947, "Wind-driven currents in a baroclinic ocean with application to the equatorial current in the eastern Pacific," *Proc. Natl. Acad. Sci. U.S.A.* **33**, 318–326.
- Sverdrup, H. U., M. W. Johnson, and R. H. Fleming, 1946, *The Oceans: Their Physics, Chemistry and General Biology* (Prentice-Hall, Englewood Cliffs, NJ).
- Swinbank, R., P. Friederichs, and S. Wahl, 2016, "Forecasting high-impact weather using ensemble prediction systems," in *Dynamics and Predictability of Large-Scale, High-Impact Weather and Climate Events*, Special Publications of the International Union of Geodesy and Geophysics, edited by J. Li, R. Swinbank, R. Grotjahn, and H. Volkert (Cambridge University Press, Cambridge, England), pp. 95–112.
- Tantet, A., V. Lucarini, F. Lunkeit, and H. A. Dijkstra, 2018, "Crisis of the chaotic attractor of a climate model: A transfer operator approach," *Nonlinearity* **31**, 2221–2251.
- Taricco, C., M. Ghil, S. Alessio, and G. Vivaldo, 2009, "Two millennia of climate variability in the Central Mediterranean," *Clim. Past* **5**, 171–181.
- Taylor, G. I., 1921, "Diffusion by continuous movements," *Proc. London Math. Soc.* **s2-20**, 196–212.
- Tebaldi, C., and R. Knutti, 2007, "The use of the multi-model ensemble in probabilistic climate projections," *Phil. Trans. R. Soc. A* **365**, 2053–2075.

- Teisserenc de Bort, L., 1881, "Study of the winter of 1879-80 and investigations on the position of atmospheric centers of action in abnormal winters," *Ann. Bur. Cent. Météor. France* **4**, 17–62.
- Temam, R., 1984, *Navier-Stokes Equations: Theory and Numerical Analysis* (North-Holland, Amsterdam).
- Temam, R., 1997, *Infinite-Dimensional Dynamical Systems in Mechanics and Physics*, 2nd ed. (Springer Nature, New York).
- Thompson, P. D., 1957, "Uncertainty of initial state as a factor in the predictability of large scale atmospheric flow patterns," *Tellus* **9**, 275–295.
- Thual, O., and J. C. McWilliams, 1992, "The catastrophe structure of thermohaline convection in a two-dimensional fluid model and a comparison with low-order box models," *Geophys. Astrophys. Fluid Dyn.* **64**, 67–95.
- Titz, S., T. Kuhlbrodt, S. Rahmstorf, and U. Feudel, 2002, "On freshwater-dependent bifurcations in box models of the interhemispheric thermohaline circulation," *Tellus A* **54**, 89–98.
- Torralba, V., F. J. Doblas-Reyes, D. MacLeod, I. Christel, and M. Davis, 2017, "Seasonal climate prediction: A new source of information for the management of wind energy resources," *J. Appl. Meteorol. Climatol.* **56**, 1231–1247.
- Touchette, H., 2009, "The large deviation approach to statistical mechanics," *Phys. Rep.* **478**, 1–69.
- Trenberth, K. E., and J. M. Caron, 2001, "Estimates of meridional atmosphere and ocean heat transports," *J. Clim.* **14**, 3433–3443.
- Trenberth, Kevin E., John T. Fasullo, and Jeffrey Kiehl, 2009, "Earth's global energy budget," *Bull. Am. Meteorol. Soc.* **90**, 311–324.
- Trevisan, A., and A. Buzzi, 1980, "Stationary response of barotropic weakly non-linear Rossby waves to quasi-resonant orographic forcing," *J. Atmos. Sci.* **37**, 947–957.
- Tribbia, J. J., and R. A. Anthes, 1987, "Scientific basis of modern weather prediction," *Science* **237**, 493–499.
- Tsonis, A. A., and P. J. Roebber, 2004, "The architecture of the climate network," *Physica (Amsterdam)* **333A**, 497–504.
- Tsonis, A. A., K. L. Swanson, and P. J. Roebber, 2006, "What do networks have to do with climate?," *Bull. Am. Meteorol. Soc.* **87**, 585–595.
- Turco, R. P., O. B. Toon, T. P. Ackerman, J. B. Pollack, and C. Sagan, 1983, "Nuclear winter: Global consequences of multiple nuclear explosions," *Science* **222**, 1283–1292.
- Turner, A. G., and H. Annamalai, 2012, "Climate change and the South Asian summer monsoon," *Nat. Clim. Change* **2**, 587–595.
- Tziperman, E., L. Stone, M. A. Cane, and H. Jarosh, 1994a, "El Niño chaos: Overlapping of resonances between the seasonal cycle and the Pacific ocean-atmosphere oscillator," *Science* **264**, 72–74.
- Tziperman, E., L. Stone, M. A. Cane, and H. Jarosh, 1994b, "El Niño chaos: Overlapping of resonances between the seasonal cycle and the Pacific ocean-atmosphere oscillator," *Science* **264**, 72–74.
- Vallis, G. K., 2006, *Atmospheric and Oceanic Fluid Dynamics: Fundamentals and Large-Scale Circulation* (Cambridge University Press, Cambridge, England).
- Vannitsem, S., J. Demaeyer, L. De Cruz, and M. Ghil, 2015, "Low-frequency variability and heat transport in a low-order nonlinear coupled ocean-atmosphere model," *Physica (Amsterdam)* **309D**, 71–85.
- Vannitsem, S., and V. Lucarini, 2016, "Statistical and dynamical properties of covariant Lyapunov vectors in a coupled atmosphere-ocean model—Multiscale effects, geometric degeneracy, and error dynamics," *J. Phys. A* **49**, 224001.
- Varadhan, S. R. S., 1966, "Asymptotic probabilities and differential equations," *Commun. Pure Appl. Math.* **19**, 261–286.
- Varadhan, S. R. S., 1984, *Large Deviations and Applications* (SIAM, Philadelphia).
- Veronis, G., 1963, "An analysis of the wind-driven ocean circulation with a limited number of Fourier components," *J. Atmos. Sci.* **20**, 577–593.
- Villani, C., 2009, *Optimal Transport: Old and New* (Springer Science+Business Media, New York).
- Vissio, G., and V. Lucarini, 2018a, "A proof of concept for scale-adaptive parametrizations: The case of the Lorenz '96 model," *Q. J. R. Meteorol. Soc.* **144**, 63–75.
- Vissio, G., and V. Lucarini, 2018b, "Evaluating a stochastic parametrization for a fast-slow system using the Wasserstein distance," *Nonlinear Processes Geophys.* **25**, 413–427.
- Vollmer, J., T. M. Schneider, and B. Eckhardt, 2009, "Basin boundary, edge of chaos and edge state in a two-dimensional model," *New J. Phys.* **11**, 013040.
- von der Heydt, Anna S., et al., 2016, "Lessons on climate sensitivity from past climate changes," *Curr. Clim. Change Rep.* **2**, 148–158.
- Von Neumann, J., 1960, "Some remarks on the problem of forecasting climatic fluctuations," in *Dynamics of Climate*, edited by R. L. Pfeffer (Pergamon Press, New York), pp. 9–11.
- Wallace, J. M., and D. S. Gutzler, 1981, "Teleconnections in the geopotential height field during the Northern Hemisphere winter," *Mon. Weather Rev.* **109**, 784–812.
- Walsh, J. E., 2014, "Intensified warming of the Arctic: Causes and impacts on middle latitudes," *Global Planet. Change* **117**, 52–63.
- Wang, Q., 2013, "Forward and adjoint sensitivity computation of chaotic dynamical systems," *J. Comput. Phys.* **235**, 1–13.
- Wang, Y., A. Gozolchiani, Y. Ashkenazy, Y. Berezin, O. Guez, and S. Havlin, 2013, "Dominant Imprint of Rossby Waves in the Climate Network," *Phys. Rev. Lett.* **111**, 138501.
- Washington, W. M., and C. L. Parkinson, 2005, *An Introduction to Three-dimensional Climate Modeling* (University Science Books, Sausalito, CA).
- Watson, A. J., and J. E. Lovelock, 1983, "Biological homeostasis of the global environment: The parable of Daisyworld," *Tellus B* **35B**, 284–289.
- Weeks, E. R., Y. Tian, J. S. Urbach, K. Ide, H. L. Swinney, and M. Ghil, 1997, "Transitions between blocked and zonal flows in a rotating annulus with topography," *Science* **278**, 1598–1601.
- Wester, P., A. Mishra, A. Mukherji, and A. B. Shrestha., Eds, 2019, *The Hindu Kush Himalaya Assessment—Mountains, Climate Change, Sustainability and People* (Springer Nature, Cham, Switzerland).
- Wetherald, R. T., and S. Manabe, 1975, "The effect of changing the solar constant on the climate of a general circulation model," *J. Atmos. Sci.* **32**, 2044–2059.
- Wiener, N., 1949, *Extrapolation, Interpolation and Smoothing of Stationary Time Series, with Engineering Applications* (MIT Press, Cambridge, MA).
- Wolf, E. T., J. Haqq-Misra, and O. B. Toon, 2018, "Evaluating climate sensitivity to CO₂ across Earth's history," *J. Geophys. Res.* **123**, 11 861–11 874.
- Woollings, T., D. Barriopedro, J. Methven, S.-W. Son, O. Martius, B. Harvey, J. Sillmann, A. R. Lupo, and S. Seneviratne, 2018, "Blocking and its response to climate change," *Curr. Clim. Change Rep.* **4**, 287–300.
- Wormell, C. L., and G. A. Gottwald, 2019, "Linear response for macroscopic observables in high-dimensional systems," *Chaos* **29**, 113127.

- Wouters, J., and G. A. Gottwald, 2019a, “Edgeworth expansions for slow-fast systems with finite time-scale separation,” *Proc. R. Soc. A* **475**, 20180358.
- Wouters, J., and G. A. Gottwald, 2019b, “Stochastic model reduction for slow-fast systems with moderate time scale separation,” *Multiscale Model. Simul.* **17**, 1172–1188.
- Wouters, J., and V. Lucarini, 2012, “Disentangling multi-level systems: Averaging, correlations and memory,” *J. Stat. Mech.* P03003.
- Wouters, J., and V. Lucarini, 2013, “Multi-level dynamical systems: Connecting the Ruelle response theory and the Mori-Zwanzig approach,” *J. Stat. Phys.* **151**, 850–860.
- Wunsch, C., 1999, “The interpretation of short climate records, with comments on the North Atlantic and Southern Oscillations,” *Bull. Am. Meteorol. Soc.* **80**, 245–255.
- Wunsch, C., 2002, “What is the thermohaline circulation?,” *Science* **298**, 1179–1180.
- Wunsch, C., 2013, “The past and future ocean circulation from a contemporary perspective,” in *Ocean Circulation: Mechanisms and Impacts—Past and Future Changes of Meridional Overturning* (American Geophysical Union, Washington, DC), pp. 53–74.
- Yanai, M., 1975, “Tropical meteorology,” *Rev. Geophys.* **13**, 685–710.
- Young, L-S, 2002, “What are SRB measures, and which dynamical systems have them?” *J. Stat. Phys.* **108**, 733–754.
- Zaliapin, I., and M. Ghil, 2010, “Another look at climate sensitivity,” *Nonlinear Processes Geophys.* **17**, 113–122.
- Zeng, N., and J. D. Neelin, 2000, “The role of vegetation–climate interaction and interannual variability in shaping the African savanna,” *J. Clim.* **13**, 2665–2670.
- Zhang, C., 2005, “Madden-Julian oscillation,” *Rev. Geophys.* **43**, RG2003.
- Zilitinkevich, S. S., 1975, “Resistance laws and prediction equations for depth of planetary boundary-layer,” *J. Atmos. Sci.* **32**, 741–752.
- Zwanzig, R., 1961, “Memory effects in irreversible thermodynamics,” *Phys. Rev.* **124**, 983–992.